Theoretical Studies on Superconducting and Normal State Properties of Some Fe-based Superconductors

By

Smritijit Sen

PHYS03201104010

Raja Ramanna Centre for Advanced Technology, Indore

A thesis submitted to the

Board of Studies in Physical Sciences

In partial fulfilment of requirements

for the Degree of

DOCTOR OF PHILOSOPHY

of

HOMI BHABHA NATIONAL INSTITUTE

April, 2017

Homi Bhabha National Institute

Recommendations of the Viva Voce Committee

As members of the Viva Voce Committee, we certify that we have read the dissertation prepared by Smritijit Sen entitled "Theoretical Studies on Superconducting and Normal State Properties of Some Fe-based Superconductors" and recommend that it may be accepted as fulfilling the thesis requirement for the award of Degree of Doctor of Philosophy.

Chairman - Prof. S. B. Roy	S B Roy	**Date:** 24.4.17
Guide / Convener - Prof. Haranath Ghosh	Haranath Ghosh	**Date:** 24/04/2017
Examiner - Prof. Saurabh Basu	Saurabh Basu	**Date:** 24/04/2017
External Member - Prof. G. Ravikumar		**Date:** 24/04/2017
Member 1- Prof. Arup Banerjee	Arup Banerjee	**Date:** 24/04/2017
Member 2- Prof. S. R. Mishra	S R Mishra	**Date:** 24.04.2017
Member 3- Prof. Vinit Kumar	Vinit Kumar	**Date:** 24.4.2017
Member 4- Prof. T. K. Sharma		**Date:** 24/04/2017
Member 5- Prof. A. Moorti	Anand Moorti	**Date:** 24/04/2017.

Final approval and acceptance of this thesis is contingent upon the candidate's submission of the final copies of the thesis to HBNI.

I hereby certify that I have read this thesis prepared under my direction and recommend that it may be accepted as fulfilling the thesis requirement.

Date: 24.04.2017

Place: RRCAT, Indore

Haranath Ghosh
Guide

STATEMENT BY AUTHOR

This dissertation has been submitted in partial fulfilment of requirements for an advanced degree at Homi Bhabha National Institute (HBNI) and is deposited in the Library to be made available to borrowers under rules of the HBNI.

Brief quotations from this dissertation are allowable without special permission, provided that accurate acknowledgement of source is made. Requests for permission for extended quotation from or reproduction of this manuscript in whole or in part may be granted by the Competent Authority of HBNI when in his or her judgement the proposed use of the material is in the interests of scholarship. In all other instances, however, permission must be obtained from the author.

Smritijit Sen

Smritijit Sen

DECLARATION

I, hereby declare that the investigation presented in the thesis has been carried out by me. The work is original and has not been submitted earlier as a whole or in part for a degree / diploma at this or any other Institution / University.

Smritijit Sen

Smritijit Sen

List of Publications arising from the thesis

- Journal

1. Origin of structural and magnetic transitions in $BaFe_{2-x}Ru_xAs_2$ materials., **Smritijit Sen**, Haranath Ghosh, A. K. Sinha and A. Bharathi, Superconductor Science and Technology, **27** (2014) 122003 (Fast Track Communication).
2. Intra-inter band pairing, order parameter symmetry in Fe-based superconductors: A model study., **Smritijit Sen** and Haranath Ghosh, Journal of Alloys and Compounds, **618** (2015) 102.
3. Structural investigations in $BaFe_{2-x}Ru_xAs_2$ as a function of Ru and temperature., Shilpam Sharma, A. Bharathi, K. Vinod, C. S. Sundar, V. Srihari, **Smritijit Sen**, Haranath Ghosh, Anil K. Sinha and S. K. Deb, Acta Crystallographica B, **71** (2015) 61.
4. Fermiology of 122 family of Fe-based superconductors: An ab-initio study., **Smritijit Sen** and Haranath Ghosh, Physics Letters A, **379** (2015) 843.
5. Nematicity, magnetic fluctuation and ferro-spin-orbital ordering in $BaFe_2As_2$ family., **Smritijit Sen** and Haranath Ghosh, Journal of Alloys and Compounds, **675** (2016) 416.
6. Role of Sn impurity on electronic topological transitions in 122 Fe-based superconductors., Haranath Ghosh and **Smritijit Sen**, Journal of Alloys and Compounds, **677** (2016) 245.
7. Electronic structures of doped $BaFe_2As_2$ materials: virtual crystal approximation versus super-cell approach., **Smritijit Sen** and Haranath Ghosh, European Physical Journal B, **89** (2016) 277.
8. Electronic origin of structural transition in 122 Fe based superconductors., Haranath Ghosh, **Smritijit Sen**, Abyay Ghosh, Journal of Physics and Chemistry of Solids **102** (2017) 157–167

9. Superconductivity on the verge of electronic topological transition in Fe based superconductors., Haranath Ghosh and **Smritijit Sen**,Journal of Physics and Chemistry of Solids **103** (2017) 170–178

- **Chapters in books**

  1. Iron based superconductors: A brief overview., Haranath Ghosh and **Smritijit Sen**, ISBN: 978-3-659-38098-3, LAP LAMBERT Academic Publishing, Germany, pp.**264** (40 printed pages) (2012).

- **Conferences**

  1. Specific heat and Characteristics ratio of some Fe-based superconductors: A model study., Haranath Ghosh, **Smritijit Sen** and H. Purwar, AIP Conference Proceedings, **1591** (2014) 1621
  2. Influence of spin structure on anion height and electronic structures in the orthorhombic phase of $BaFe_2As_2$., **Smritijit Sen** and Haranath Ghosh, AIP Conference Proceedings, **1728** (2016) 020180.
  3. Stoner factors of various doped 122 Fe-based superconductors: An ab-initio study., **Smritijit Sen** and Haranath Ghosh, Conference Proceedings, PRLC-CMP (2016), PRL, Ahmedabad.

Smritijit Sen

Smritijit Sen

Dedicated

to

My Parents

ACKNOWLEDGEMENTS

First and foremost, I express my unfeigned gratitude and deep sense of indebtedness to my thesis supervisor Dr. Haranth Ghosh for his invaluable guidance, motivation, patience, endless encouragement and his continuous support paired with stimulating enthusiasm. I am highly obliged to him for the constructive criticism, valuable suggestions, critical reading and deep involvement in all of my scientific communications including the present thesis.

I would like to acknowledge HBNI and RRCAT for the financial support during my PhD days.

I would like to take this opportunity to thank Dr. A. K. Sinha and Dr. A. Bharathi for providing the experimental data. I am extremely grateful to all the members of my Ph.D doctoral committee for monitoring the progress of my research work over these years. I specially thank Dr. S. B. Roy, chairman of the doctoral committee for his valuable suggestions and comments. I extend my sincere thanks to Dr. P. A. Naik and Dr. P. D. Gupta for their constant support and encouragement. I am also thankful to Dr. Arup Banerjee, Head HRDS for his valuable suggestions and comments. I would like to thank Mr. P. Thander and the scientific computing group, Computer Centre, RRCAT for providing computational facility and help. I am also thankful to all the members of ISUD and HRDS for providing enjoyable and stimulating working atmosphere. My special thanks are also to Mr. Tufan Roy, Mr. Gangadhar Das, Arijit Chakraborty, Arup Ratan Jana, Mr. Debashis Mondal, Dr. C. Kamal, Mr. Sudheer and Dr. Harishchandra Singh for their help and

company during this period. I would also like to acknowledge Abyay and Soumyadeep for their help in writing the thesis in a smooth way.

It is my pleasure to thank all my friends, specially Yashvir, Paro, DJ and Gopal for their help, positive support and fruitful advices at several stages of my PhD days.

Finally, I would like to convey my deepest regards to my parents and sister for their never-ending love and affection to me.

Contents

Synopsis

High temperature superconductivity is a remarkable macroscopic quantum phenomena and without doubt is one of the most important unsolved problems of condensed matter physics. Discovery of iron-based superconductors unwrapped a new era of superconductivity which indulges researchers to resolve the unsettled mysteries of high-temperature superconductivity that remains so far unexplained. These new types of superconductors have conducting layers of iron and pnictogen (Pn)/chalcogen (Ch) (typically arsenic/selenium) and seems to show great potentials as the next generation high temperature superconductors [1]. Dominance of Fe electrons at the Fermi surface (FS) and unusual Fermiology, that can be modulated by doping, temperature, pressure makes normal and superconducting state properties of iron-based superconductors quite unique compared to other classes of superconductors [2]. Fe-based high temperature superconductors exhibit a number of exotic properties like anti-ferromagnetism, structural transition, nematicity, orbital ordering *etc.*, which are also known to condensed matter community with reference to cuprates superconductors as close proximity to superconductivity. Therefore, studying on the above mentioned properties for Fe-based superconductors may also reveal the mechanism of such phases in the other classes of high T_c superconductors and strongly correlated electron. Understanding such phases through theoretical studies via model Hamiltonian as well as first principles methods like density functional theory, is the main purpose of the current thesis.

This thesis comprises of eight chapters that addresses the above mentioned issues, are organized as follows.

Chapter 1: Introduction.

In this chapter a brief introduction to Fe-based superconductors in terms of their crystal structures, basic physical properties, phase diagram *etc.*, is presented. Fe-based superconductors are broadly classified into six families, among them 122 family is the most studied family, both experimentally as well as theoretically. One of the most interesting aspects of these Fe-based superconductors (SCs) from a fundamental point of view, is that superconductivity may arise from magnetic fluctuation or orbital fluctuation. However the glue to the electron-electron attraction or more precisely pairing mechanism in these Fe-based SCs is far from being settled. Phase diagrams of Fe-based SCs establish the existence of various exotic phases like inter orbital spin density wave (SDW), orbital order, nematic order, structural transition *etc.*, which are highly sensitive to temperature, pressure and doping. But microscopic origin of these phases are not well understood. Fe-As (pnictides) or Fe-Se (chalcogenides) planes are back bone structures of these superconductors where As/Se atoms are placed above and below the Fe plane. Height of this As/Se atom from Fe plane defines 'anion height', which is closely related to z_{As} *i.e.*, the fractional co-ordinate of As atom, plays a major role in most of the exotic phases discussed above.

Experimental studies on the superconducting gaps in iron-based superconductors reveal that there are two nearly isotropic gaps with characteristics ratios $2\Delta_{SC}(k)/k_BT_c$ = 2.5 ± 1.5 (for small gap on the outer Γ-barrel) and 7±2 (on the inner Γ-barrel and the propeller-like structure around the X point, for large gap) which is considerably different from the conventional BCS characteristic ratio 3.5 [3]. The behaviour of specific heat of these iron-based superconductors is also distinctly different ($\Delta C/T_c$ proportional to T_c^2) from other classes of SCs where, $\Delta C/T_c$ proportional to T_c. All these experimental features are explained using the minimal two band model of Fe-based SCs, considering combined intra-inter band pairing picture in chapter 3. Apart from its novel superconductivity as mentioned earlier, Fe-based SCs display a number of exotic normal state properties like structural transition, spin nematic phase, ferro-orbital ordering *etc*. Origin of structural transition and microscopic relationship between the orbital order, structural transition and nematic order in 122 family of Fe-based superconductors are presented in chapters 4 and 5. Angle resolved photo electron spectroscopy (ARPES) measurement revealed multi-band and quasi two dimensional nature of FSs of Fe-based 122 superconducting systems. The shape of a Fermi surface is very crucial as it determines the degree of nesting in Fe-based SCs which in turn gives rise to magnetic as well as orbital ordering. Superconductivity emerges in these systems due to the suppression of magnetic order. Moreover, Lifshitz transitions/electronic topological transitions are also experimentally observed in Fe-based 122 systems as a function of doping and pressure [4,5,6]. A detailed study of FS topology and electronic topological transitions in 122 Fe-based SCs and its consequences are presented in chapters 6 and 7.

Part of this chapter is published as a book chapter, "Iron based superconductors: A brief overview", Haranath Ghosh and Smritijit Sen, ISBN: 978-3-659-38098-3, LAP LAMBERT Academic Publishing, Germany, pp.264 (2012).

Chapter 2: Theoretical methods.

This chapter describes two methods; (i) Study of Fe-based materials through minimal model Hamiltonian and (ii) First principles studies using density functional theory.

First principles band structure calculations in Fe-based superconducting systems reveal that the density of states near Fermi level dominantly have Fe-3d character. Among all the five Fe orbitals, 3d_{yz},3d_{xz} have the largest contribution to the density of states at the Fermi level [7]. Moreover, S. Raghu *et al.*,[8] suggested a minimal two-band model that generates a topologically similar FS as observed experimentally. We consider two orbitals (d_{xz},d_{yz}) per site on a two dimensional square lattice of iron. We take the mean field model Hamiltonian within the two band picture as [9],

$$\begin{aligned} H &= \sum_{k,\sigma}^{FBZ} \varepsilon_k^e C_{k,\sigma}^\dagger C_{k,\sigma} + \sum_{k,\sigma}^{FBZ} \varepsilon_k^h f_{k,\sigma}^\dagger f_{k,\sigma} + \Delta_{SDW} \sum_{k,\sigma}^{FBZ} (C_{k,\sigma}^\dagger \sigma_{\sigma,\sigma'}^z f_{k+Q,\sigma'} + h.c.) \\ & -i \sum_{k,\sigma}^{FBZ} \Delta_{ODW} (C_{k,\sigma}^\dagger f_{k+Q,\sigma} - f_{k+Q,\sigma}^\dagger C_{k,\sigma}) + \sum_{k}^{FBZ} \Delta_{SC}(k)(C_{-k,\downarrow} C_{k,\uparrow} + f_{-k,\downarrow} f_{k,\uparrow} + h.c.) \end{aligned}$$

The first two terms of the above model Hamiltonian represent kinetic (band) energies in the electronic ($C_{k,\sigma}$ being the annihilation operator of an electron with spin σ) and hole ($f_{k,\sigma}$ being the annihilation operator of a hole) bands. The electronic and hole band dispersions are obtained as, [8,9,10] $\varepsilon_k^{e/h} = \epsilon_+(k) \pm \sqrt{\epsilon_-^2(k) + \epsilon_{xy}^2(k)} - \mu$ where $\epsilon_+(k) = -(t_1 + t_2)(\cos k_x + \cos k_y) - 4t_3 \cos k_x \cos k_y$. The order parameters $\Delta_{SDW}, \Delta_{ODW}$ represent respectively the spin density wave (SDW) and orbital density wave (ODW) that involves ordering between the electron and hole like bands that are nested by the nesting wave vector Q = (0, π) or (π,0). These ingredients in our model that the electron-like FS nests with the hole-like one and vice versa, is justified as it is consistent with recent experimental findings [11]. In ref [11] weak z-direction dispersion among the hole FSs and electron FSs are found resulting quasi-2d nested nature. The fifth term represent effective superconductivity (SC) where $\Delta_{SC}(k) = (\Delta_{SC}^e(k) - \Delta_{SC}^h(k))$; $\Delta_{SC}^{e/h}$ being superconducting order parameter around the electronic and hole FSs respectively (see further detail in chapter 2).

Ab initio density functional theory (DFT) [12] based electronic structure calculations are used to study the properties of several materials including the Fe-based superconductors. It is a popular tool to study the electronic structure of matter in which the ground state electron density of a system is used as a basic variable instead of lengthy quantum many-body wave function. The theoretical foundation for the density functional theory was laid by P. Hohenberg and W. Kohn in 1964 [12]. A brief descriptions of DFT methods for calculating electronic structure are presented in this chapter.

Parent compounds of 122 Fe-based systems are not superconducting at ambient pressure but it shows magnetic order in the form of spin density wave (SDW). Superconductivity appears in these systems when the SDW order is suppressed and that can be accomplished either by applying hydrostatic pressure or chemical pressure *i.e.*, by doping. Superconductivity can also be developed by doping on any of the three sites. To treat such disordered or doped systems within first principles method there exist two very popular approaches: super-cell method and virtual crystal approximation (VCA). A detail comparative study of electronic structures of various doped $BaFe_2As_2$ systems through first principles simulation by implementing doping effect via virtual crystal approximation (VCA) and super-cell approaches is also presented in this chapter.

Chapter 3: Model studies of Fe based superconductors.

Within two-band model a detailed study of BCS characteristic ratio and electronic specific heat of Fe-based superconductors is presented. Three scenarios of superconducting pairings are considered (i) intra-band pairing (ii) inter-band pairing and (iii) intra-inter band pairing. Superconductivity within all the above scenarios are studied in presence of inter-orbital SDW and ODW order together with different allowed superconducting pairing symmetries. The intra-band pairing leads to two distinct T_cs and characteristic ratios similar to the weak coupling BCS theory and hence not found suitable for Fe-based superconductors. In the solely inter-band pairing picture, single global T_c is achieved and larger $2\Delta_{SC}/k_BT_c$ consistent with experimental findings are seen. This picture still suffers from drawbacks in the followings: (a) $\Delta^{large}/\Delta^{small} \leqslant 2$, (b) $2\Delta_{SC}^{small}/k_BT_c$ exceeds experimental findings, (c) $\Delta C/T_c \propto T_c^2$ with negative proportionality constant. In the third scenario with combined intra-inter band pairing all the above mentioned shortcomings are overcome. In all the above scenarios coupled gap equations involving SDW, ODW and SC-gaps are presented. Nature of quasi-particle in the above three pictures are also pointed out. The larger value of $2\Delta_{SC}/k_BT_c$ is found to be primarily due to the presence of inter-band pairing which is consistent with the earlier theoretical prediction [13]. Within the combined intra-inter band pairing for sign changing order parameters we find that the temperature dependence of specific heat jump is very different from other classes of superconductors. Calculated "Characteristics ratios" and $\Delta C/T_c$ variation with T_c matches very well with experimental findings [3,14,15] in case of $s^{\pm}$ pairing symmetry (for both electron and hole doping). Therefore, it is concluded that the combined intra and inter band pairing reproduces essential important features from experiment.

Content of this chapter is published in J. of Alloys and Compounds, **618** (2015) 102.

Chapter 4: Origin of magneto-structural transition in 122 family of Fe-based superconductors.

In this chapter intimate structural correlation to electronic structure and origin of magneto-structural transition in Fe-based superconductors are demonstrated. Using temperature and doping dependent lattice parameters on Ru-doped $BaFe_2As_2$, we show through detailed first principles simulations that the electronic structure carries the 'finger prints' of structural parameters like z_{As}, Fe-As bond distance and reproduces the experimentally observed angle resolved photo emission spectroscopy data [16] that have so far remained unexplained. Below the structural transition an orbital order develops between the d_{xz} and d_{yz} orbitals of Fe. On the other hand, temperature-dependent modifications of the d_{xz} and d_{yz} bands cause loss of nesting, in turn causing suppression of spin density wave transition. Total band energies at high symmetric Γ and X points of the d_{xz} and d_{yz} bands become non-degenerate at the structural transition whose temperature dependence is very similar to that of the observed two Fe-Fe distances (or a(T) and b(T)); whereas the differences of band energies at the high symmetry points like Γ, X of the said bands, give rise to an orbital order that follows the temperature as well as doping dependence of the orthorhombicity parameter. An universal correlation among the orbital ordering, orthorhombicity (*i.e.,* structural transition) and structural parameters is established in a number of 122 (including Ru doped 122) Fe-based materials as a function of both temperature as well as doping. Therefore, orbital fluctuations play a dominant role in the magneto-structural transition in 122 family of Fe-based SCs.

Contents of this chapter are published in Acta Crystallographica B, **71** (2015) 61 and Superconductor Science and Technology, **27** (2014) 122003 (Fast Track Communication).

Chapter 5: Nematicity and ferro-spin-orbital ordering in 122 Fe-based superconductors.

We take a relook to the nature of orbital ordering, its temperature, doping dependencies *etc.,* that are established in the previous chapter. Through detailed electronic structure simulations, it has been shown that the electronic orbital ordering (between d_{xz} and d_{yz} bands) takes place due to local breaking of in-plane symmetry that generates two non-equivalent *a*, *b* directions in 122 family of Fe-based superconductors. Orbital ordering is strongly anisotropic and the temperature dependence of the corner zone orbital order maps to that of the orthorhombicity parameter. Orbital anisotropy results in two distinct spin density wave nesting wave vectors and causes inter-orbital charge and spin fluctuations. The microscopic relationship between the orbital order, structural transition and nematic order in 122 family of Fe-based superconductors is presented in this chapter. Temperature dependence of the orbital order is proportional to the nematic order and it sets in at a temperature where magnetic fluctuation starts building. We have explicitly evaluated the temperature dependencies of orbital occupancies of all Fe-d-orbitals. Occupation probabilities of all the Fe-d-orbitals exhibit temperature dependence indicating their possible contribution in orbital fluctuation. This need to be contrasted with the usual definition of nematic order parameter ($n_{d_{xz}} - n_{d_{yz}}$). Orbital ordering becomes strongly spin dependent in presence of magnetic interaction. Spin-polarised orbital ordering revealed from this work would be experimentally observable.

Content of this chapter is published in J. of Alloys and Compounds, **675** (2016) 416.

Chapter 6: Fermiology and dimensional cross-over in Fe-based superconductors.

Fermiology is believed to play a significant role in magnetism and superconductivity of hight temperature superconductors including Fe-based SCs. In this chapter Fermiology of various doped 122 systems are studied through first principles simulation. Simulated Fermi surfaces (FSs) of parent compounds of 122 Fe-based SCs are topologically very similar. Presence of quasi-two-dimensional hole and electron-like FSs enhances the possibility of nesting. A dimensional cross-over, in theoretically computed FS topologies of various members of "122" family are presented with various kinds of doping. These results are consistent with experimental observations and its possible significance to magnetism and superconductivity are presented. In case of electron and hole doping, sizes of the electron and hole Fermi pockets evolve oppositely with increasing doping concentration. Isovalent Ru substitution up to certain doping concentration makes no visible modifications in the electron and hole-like FSs providing no clue regarding the nature of charge carrier doping. However, in case of 32% P doping there are substantial changes in the hole FSs. 100% Ru substitution in Fe site modifies hole FSs significantly. From all these calculated FSs it is very clear that dimensionality of FS (linked with FS nesting) plays an important role in 122 Fe-based superconductors.

Contents of this chapter is published in Physics Letters A, **379** (2015) 843.

Chapter 7: Electronic topological transitions in Fe based superconductors.

Our findings of chapter 6 that in case of electron and hole doping, sizes of the electron and hole Fermi pockets evolve oppositely with increasing doping concentration remains valid only in absence of topological transition. Doping and temperature dependent electronic topological transitions (ETT)/ Lifshitz transitions (LT) in 122 family of Fe-based superconductors are presented in this chapter. It has been shown that only a few percentage of Sn doping at the Ba site on $BaFe_2As_2$, can cause electronic topological transition, namely, the Lifshitz transition. A hole like d_{xy} band of Fe undergoes electron like transition due to 4% Sn doping. Lifshitz transition is found in $BaFe_2As_2$ system around all the high symmetry points. Detailed first principles simulation predicts absence of any Lifshitz transition in other 122 family compounds like $SrFe_2As_2$, $CaFe_2As_2$ up to 5% Sn doping. This work bears practical significance due to the facts that a few percentage of Sn impurity is in-built in tin-flux grown single crystals method of synthesizing 122 materials and inter-relationship among the Lifshitz transition, magnetism and superconductivity.

It has been systematically shown in a variety of high T_c Fe-based superconductors that superconductivity occurs at the verge of LT/ETT where magnetism disappears. This is achieved through detailed evaluation of FSs through first principles simulations with experimental structural parameters as a function of doping (temperature) as inputs and detailed demonstrations of LT/ETT. This definitely indicates the intriguing heed to the inter-relationship between superconductivity and LT in Fe-based SCs. LT/ETT occurs in the electron Fermi surfaces for hole doping, whereas in hole Fermi surfaces for electron doping as well as iso-electronic doping.

Contents of this chapter can be found in J. of Alloys and Compounds, **677** (2016) 245.

Chapter 8: Summary and conclusions

This chapter summarizes the work carried out in the thesis and discusses the scope for further extension of the work reported here. In chapter 1, we provide a brief introduction of Fe-based superconductors in terms of their crystal structure, physical properties *etc.* In this thesis, we have utilized two methodologies : (i) Model studies (described in chapters 2, 3 in details) and (ii) First principles studies to address some of the unsolved issues of Fe-based SCs discussed in chapter 1. Through model studies an important conclusion is reached that anomalous BCS ratio, thermal behaviour of specific heat jump with superconducting transition temperatures can only be understood if there is substantial intra as well as inter band pairing. In chapters 4, 5, we have discussed the origin of structural and magnetic transition as well as correlation between the orbital order and nematic order from density functional electronic structure calculations. Structural transition is found to be electronic in origin. ‘Orbital order’ obtained from density functional studies with experimental structural parameters as inputs for a number of 122 materials, show that the structural transition characterized by orthorhombicity parameter is directly related to the orbital order. When normalized, both the orbital order as well as the orthorhombicity parameter quantitatively matches with each other as far as their temperature and doping dependencies are concerned. A relationship between orbital order and nematic order parameter is discussed. Fermiology and electronic topological transitions in Fe-based SCs from first principles studies are presented in chapters 6 and 7. Electronic topological transitions are found to occur due to impurity, doping as well as temperature in a number of Fe-based superconductors. Doping dependent Lifshitz transitions are found to occur at doping concentrations where superconductivity attains maximum T_c.

References

[1] Shimoyama Jun-ichi, Supercond. Sci. Technol. **27**, 044002 (2014).

[2] G. R. Stewart, Rev. Mod. Phys. **83**, 1589 (2011).

[3] D. V. Evtushinsky *et al.*, New J. Phys. **11**, 055069 (2009).

[4] Chang Liu *et al.*, Phys. Rev. B **84**, 020509(R) (2011).

[5] N. Xu *et al.*, Phys. Rev. B **88**, 220508(R) (2013).

[6] Yong Liu and Thomas A. Lograsso, Phys. Rev. B **90**, 224508 (2014).

[7] T. Li, J. Phys.: Condens. Matter **20**, 425203 (2008).

[8] S. Raghu *et al.*, Phys. Rev. B, **77**, 220503(R) (2008).

[9] H. Ghosh and H. Purwar, Europhys. Lett. **98**, 57012 (2012).

[10] H. Ghosh, S. Sen, H. Purwar, AIP Conf. Proc. **1591**, 1621 (2014).

[11] M. Sunagawa *et al.*, Sci. Rep. **4**, 4381 (2014).

[12] P. Hohenberg and W. Kohn, Phys. Rev. B, **136**, 864 (1964).

[13] O. V. Dolgov *et al.* Phys. Rev. B **79**, 060502(R) (2009).

[14] S. L. Budko *et al.*, Phys. Rev. B **79**, 220516 (2009).

[15] J. S. Kim *et al.*, J. Phys.: Condens. Matter **23**, 222201 (2011).

[16] R.S. Dhaka *et al.*, Phys. Rev. Lett. **110**, 067002 (2013).

List of Figures

Chapter 1

Introduction

1.1 The road to high temperature superconductivity

Superconductivity is undoubtedly one of the most revolutionary and profound scientific triumph of 20th century, achieved in April 1911 by Kamerlingh Onnes at the University of Leiden. To his utter surprise Onnes perceived that the d.c. resistance below a certain critical temperature (called superconducting transition temperature) at around 4K of mercury showed a discontinuous decrease to zero [1]. Later on in 1933 Walther Meissner and Robert Ochsenfeld discovered the complete expulsion of magnetic field lines from a superconductor during its transition to the superconducting state by measuring the magnetic field down to the critical temperature in lead and tin samples [2]. This remarkable phenomenon guided to a new definition of superconductor (SC), *i.e.,* all superconductors below the critical temperature are perfect diamagnets. Several decades after this discovery, spotlight of research was to discover new superconducting materials with higher T_c values and develop a proper understanding about the mechanism of superconductivity. First major success accomplished in the year of 1950 with the advent of phenomenological Ginzberg-Landau theory [4]. The complete microscopic theory of superconductivity was eventually proposed in 1957 by Bardeen, Cooper, and Schrieffer [5] and is popularly

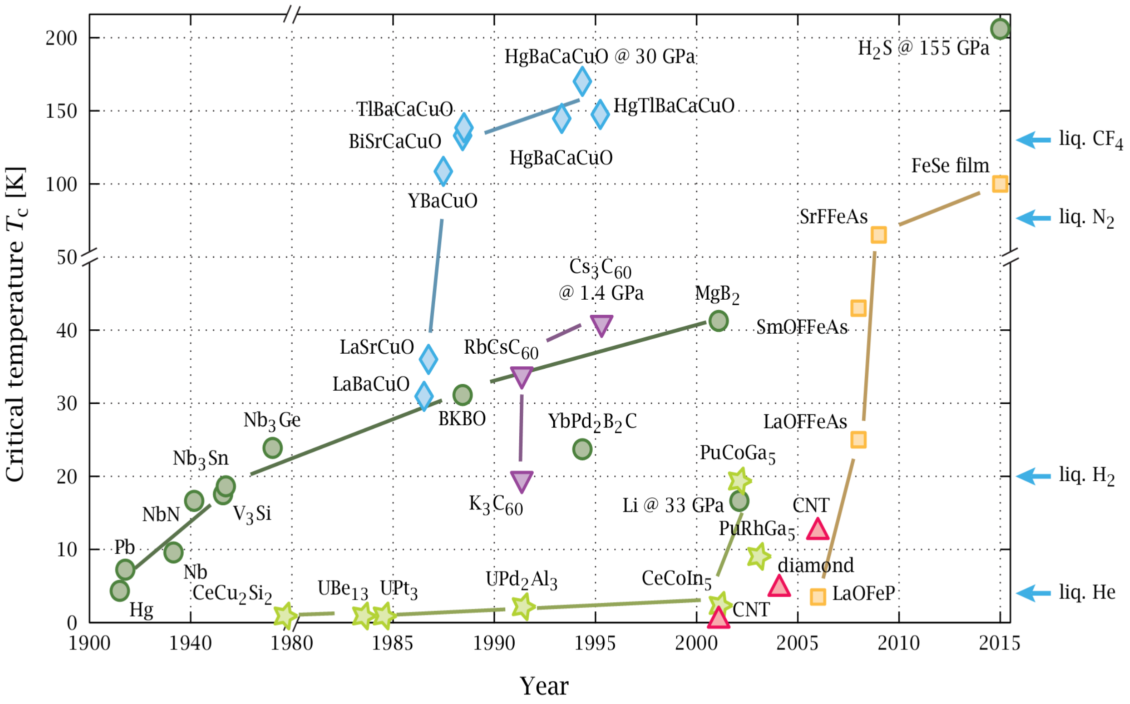

Figure 1.1: Chronology of the discoveries of various superconductors including Fe-based high T_c superconductors and its critical temperatures (taken from [3]).

known as BCS theory. This theory is the only theory which gave a microscopic explanation of the superconductivity so far and almost all of the conventional superconductors can be explained with the help of BCS theory. Now in 1978 with the invention of heavy fermion superconductors, unconventional superconductivity entered into the field of superconductivity but the real surprise came in 1986, when Bednorz and Müller discovered superconductivity at 35K in "LBCO" (a mixed oxide of lanthanum, barium, and copper) with radically higher transition temperature [6] and a new era began. The discovery was a revelation not simply because of the large increase in T_c, but also because it revealed that the oxides formed an unsuspected new classes of superconducting materials with great potential. Highest T_c achieved in $HgBa_2CaCu_2O_{6+x}$ compound at ambient pressure is 133K [7] (with pressure, one can achieve T_c as high as 150K [8]). Many years after its discovery, there exists no microscopic theory of unconventional superconductivity till to date. In 2008, Kamihara and his group discovered a new classes of superconductors in iron-pnictide (Fe-Pn) [9] systems created much stir in the community as it creates a drastic change in the belief that Fe is deleterious to superconductivity. This remarkable invention ended the monopoly of cuprates as the only high-T_c SC and opened a new prospect for the high-T_c SCs. In Fig.1.1, we provide a glimpse of time line of superconductors.

1.2 Iron based superconductors: An Overview

Iron-based superconductors are chemical compounds containing iron with superconducting properties. Till its discovery, high temperature superconductivity in cuprates, created a prejudice that Cu-oxides are the indispensable building blocks for a high temperature superconducting material. This new type of superconductors (iron-based) is based on conducting layers of iron and a pnictide/chalcogenide (typically arsenic/selenium) and seems to show a great promise as the next generation of high temperature superconductors. Fe-based SCs shared a number of common features with high T_c cuprates like proximity of superconductivity and magnetism, quasi 2-D structure and phonons unlikely to play any dominant role in their superconductivity *etc.* On the other hand, Fe-based SCs also possess a number of properties that are distinct from that of the high T_c cuprates like parent compounds of iron-based superconductors are semi-metallic (cuprates are antiferromagnetic (AF) Mott insulators), multi-band, superconducting pairing symmetry still to be decided (cuprates SCs have d-wave paring) *etc.* These iron pnictide and chalcogenide (FePn/Ch) superconductors have Fe-d orbitals at the Fermi surface together with an unusual Fermi surface topology that can change rapidly with doping. This may lead to very different normal and superconducting state properties compared to those of the standard electron-phonon coupled “conventional” superconductors. Phase diagram of Fe based SCs bears the signature of several exotic phases like spin density wave, orbital density wave, nematic phase *etc.,* apart from its exciting superconducting phase in the close propinquity of magnetism. There are a large number of evidences showing that superconductivity, magnetism, orbital fluctuations are intimately related and coexist in these materials although the mechanism of superconductivity in these compounds is still far from being settled and in the spotlight of main stream research. The capability of manufacturing a large variety of novel iron-pnictide based superconductors through chemical substitutions has empower the possibility to optimize of superconducting transition temperature and led to a number of families of Fe-based SCs with tuning the Fe-Pn layers and crystal structures. Due to its multi-band nature of the Fermi level and the presence of various exotic phases, it is very difficult to construct a simplified starting model Hamiltonian for these classes of superconducting materials. Although some of these materials are believed to be weakly correlated, presence of strong magnetic fluctuation imposes a great challenge to apply density functional theory to these compounds.

1.3 Family of Fe based superconductors

Fe-based superconductors are broadly classified into six families namely 1111, 111, 11, 122, 21311 and 122* and the nomenclature is based on their ratios of the constituent elements. So for example the ’111’ family features three element types in equal proportion. On the other hand ’122’ family ascribes three element types with one of the elements being half as abundant as the other two. In Fig.1.2, we depict the crystal structure of five Fe based families with their T_c values. These structures, as shown in Fig.1.2, all share a common layered structure based upon a planar layer of iron atoms joined by tetrahedrally coordinated pnictogen (P, As) or chalcogen (S, Se, Te) anions arranged in a stacked sequence separated by alkali, alkaline earth or rare earth and oxygen/fluorine "blocking layers." The common feature in all these families of Fe-based materials are the Fe-As/Se layers, which are believed to play a key role in the superconductivity. First invented Fe-based SC belongs to group of oxypnictides (LaFeAsO) *i.e.,* 1111 family. The second but the most important family is the so called ’122’, the parent compound with general notation AFe_2As_2 (A=Ba, Sr, Ca, Eu). Among all the families, 122 family is the most studied family, both experimentally as well as theoretically. The main reason for that is the availability of high quality large single crystals for 122 systems. It should also

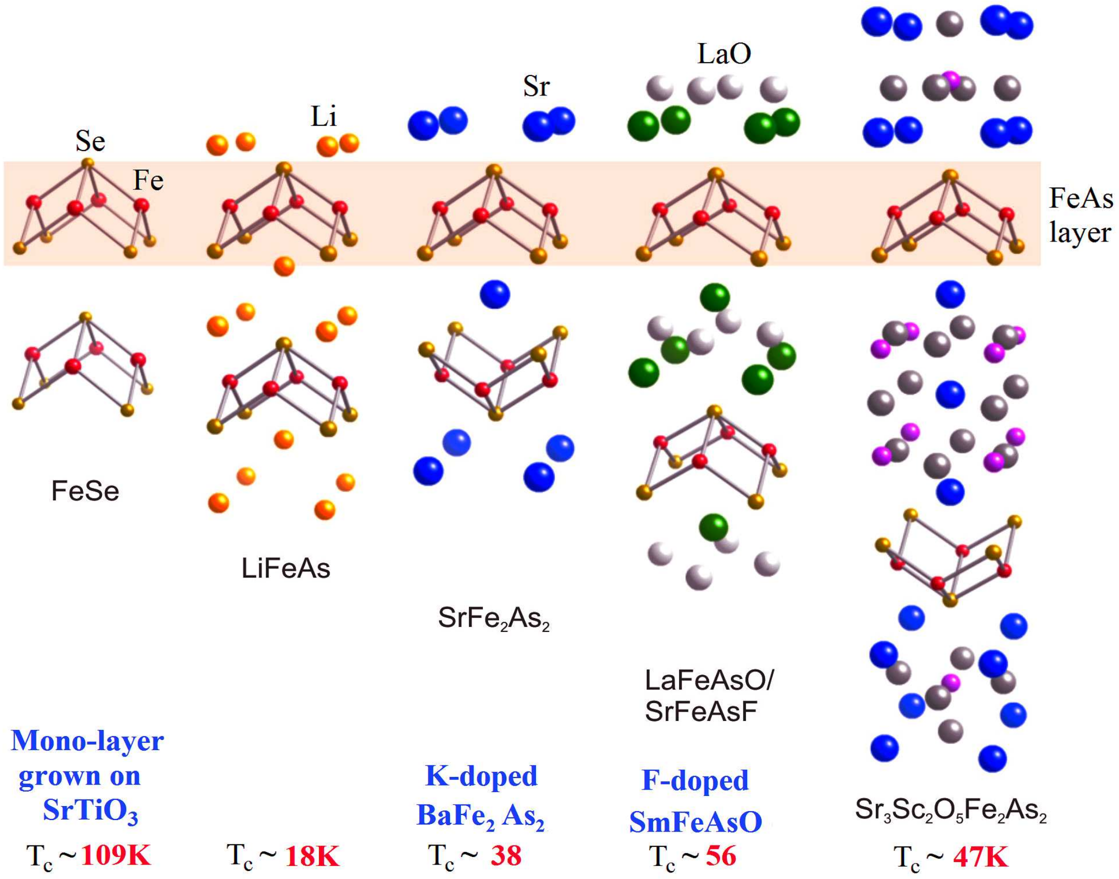

Figure 1.2: Crystal structures of various families of Fe based SC with their maximum T_cs.

be noted that the parent compounds of 122 family like $BaFe_2As_2$ is not superconducting at ambient pressure but it shows magnetic order in the form of spin density wave (SDW). Superconductivity appears in this system when SDW order is suppressed and that can be accomplished either by applying hydrostatic pressure [10–12] or chemical pressure *i.e.*, by doping [13–15]. In these compounds long range SDW order is suppressed before the onset of superconductivity. Initially it was envisaged to be a purely charge-doping effect, where extra electrons or holes are added to the 'blocking' layers leading to an optimal charge density for superconductivity but recent work has revealed that even iso-electronic substitution can introduce superconductivity [16, 17]. 11 family is the simplest among all of them, just consists of FeSe layers and 21311 and 122* are the two complex families of Fe-based SCs. It is now interesting to see the integrity and diversity of all these families in terms of their crystal structures.

1.4 Structural aspects of Fe based superconductors

1.4.1 Crystal structure

Like high T_c cuprates, crystal structure plays an important role in the physical properties of Fe-based SCs. Now we discuss the room temperature crystal structures of various Fe-based families. 1111 family have the tetragonal, tP8 (8 atoms per unit cell) ZrCuSiAs (prototypical compound) structure with 2D layers of FeAs. They belong to space group with space group number 129 (tetragonal) [9]. These materials undergo tetragonal to orthorhombic structural transition. The most studied and probably the largest numbers of superconductors are in the 122 family which are made up of combinations of metallic alkaline earth (Ba, K, Sr, Ca,...)-transition metal (Fe, Co, Ni,...)-pnictogen (As,P). More than 450 compounds are possible within these combinations. Similar to the 1111 compounds they are also in tetragonal structure with tI10 (10 atom unit cell) with axes a and b being of same length and c labelling the longer axis of the unit cell [18]. Our main focus will also be the 122 compounds, that show a rich variety of phases. The unit cell of $BaFe_2As_2$ consists of two Ba atoms, four Fe and four As atoms in one formula unit (f.u.). Ba atom is situated at the centre of the unit cell as well as in all eight corners of the unit cell, while the Fe atoms form two parallel, planar square in the a-b plane, separated by Ba layers. Fe atoms is located at the centre of a distorted $FeAs_4$ tetrahedron, with the As atoms being displaced evenly in the positive as well as negative c axis out of the Fe layer. This distance between As atom from the Fe plane is known as "Anion height" which plays a crucial role in determining various physical properties of Fe-based SCs. These 122 system undergoes simultaneous structural (from low temperature orthorhombic to high temperature tetragonal phase) as well as magnetic transition (from low temperature spin density wave order to paramagnetic order at high temperature) [19]. Lattice parameters of $BaFe_2As_2$ at 175 K, are $a = b = 3.95702$Å, $c = 12.9685$Å, space group I4/mmm (No. 139) and at 5 K, $a = 5.61587$Å, $b = 5.57125$Å, $c = 12.9428$Å, space group Fmmm

(No. 69) as revealed by the neutron diffraction measurement [19]. In Fig.1.3 we depict the crystal structure of $BaFe_2As_2$ system in the room temperature tetragonal phase. The 111-type iron-based superconductors crystallize into tetragonal tP6 Cu_2Sb structure with symmetry P4nmm. In the layered structure, iron pnictide and a Li or Na layer are stacked alternately. Fe atoms are in a four-fold coordination, forming a tetrahedron $FeAs_4$. Members of 11 family have tetragonal tP4 PbO structure. The crystal structure of the so called 21322 or sometimes called the 42622 family can be visualize as layers of 122 $SrFe_2P_2$ alternating with perovskite $Sr_3Sc_2O_6$ layers. Purpose of intercalation of the perovskite layers of atoms sandwiched between the FeAs layers is to increase T_c. Our main focus will be the 122 compound, that shows a rich variety of phases.

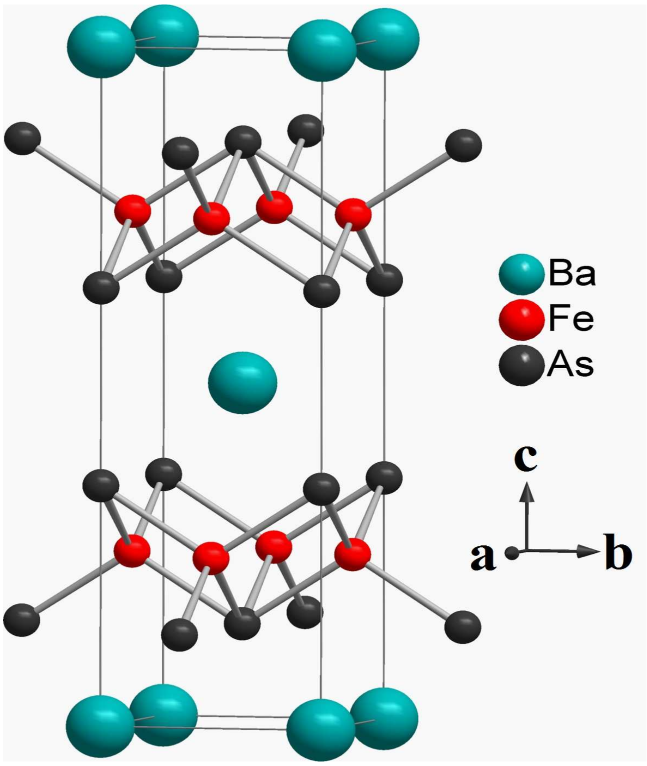

Figure 1.3: Crystal structure of $BaFe_2As_2$ (tetragonal), one of the parent compounds of 122 family

1.4.2 Structural correlation to T$_c$

Correlation of superconducting transition temperature and other physical properties with structural parameters is well established [20–24]. Fe-As (pnictides) or Fe-Se (chalcogenides) planes are back bone structures of these Fe-based superconductors where As atoms are placed above and below the Fe plane. Height of this As atom from Fe plane is defined as 'anion height' which is closely related to z_{As} *i.e.,* the fractional co-ordinate of As atom. In Fig.1.4 the critical temperature T$_c$ as a function of the anion height for various types of Fe based superconductors are depicted. It was observed that critical temperatures follow a unique curve at ambient as well as high pressure with anion height sharply peaked around 1.38Å. The onset of zero-resistivity temperatures at ambient pressure are indicated by small light blue circles. Filled diamonds indicate the data at ambient

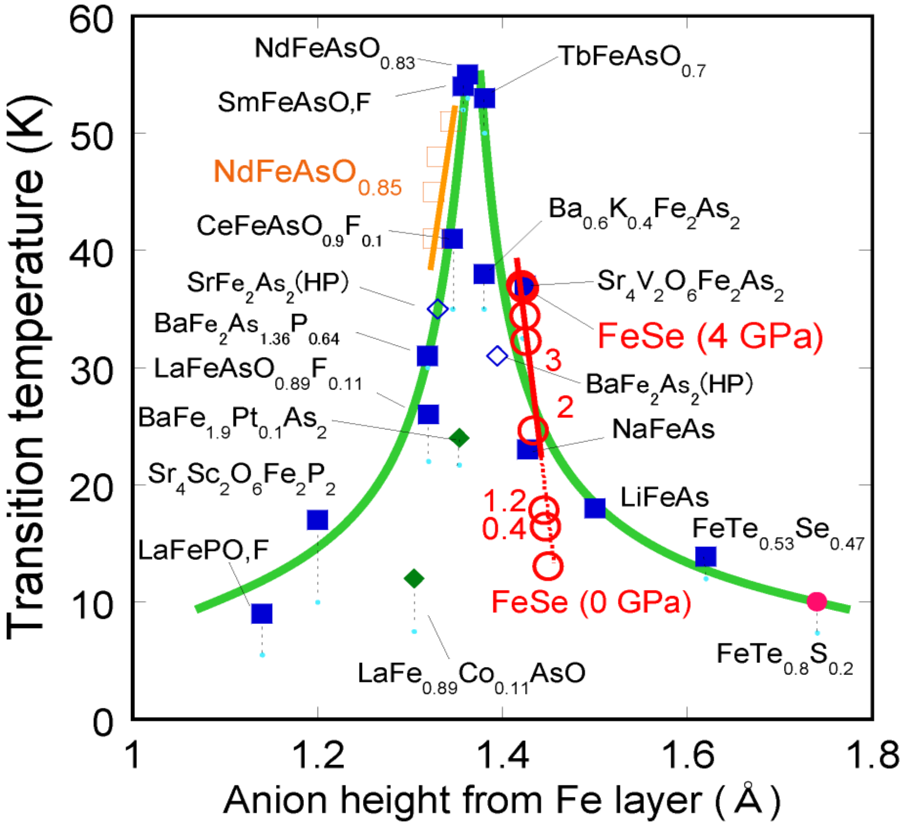

Figure 1.4: Anion height vs T$_c$ plot for various Fe-based SCs. Large symbols indicate the onset temperature. The zero-resistivity temperatures at ambient pressure are indicated by small light-blue circles. Filled (open) symbols indicate the data at ambient (high) pressure (taken from [20]).

pressure. Unfilled symbols indicate the superconducting transition temperatures at high pressure. Further correlations between superconducting T_cs and structural parameters can also be found in the existing literature like the influence of the distortion of the FeAs4 tetrahedrons on the transition temperature T_c. It was found that a distortion of the FeAs4 tetrahedron away from a ideal tetrahedron with bond angles of 109.47° is actually unfavourable to superconductivity for a wide range of FeAs compounds like (La,Nd)FeAsO [25] and $CeFeAsO_{1-x}F_x$ [26]. It is also evident from literature that, as far as veracity of calculation of electronic structure is concerned, the role of various structural [27] parameters specially z_{As} is instrumental [28–30]. It is worth mentioning here that density functional theory within local density approximation (LDA) as well as generalized gradient approximation (GGA) was unable to achieve the experimental value of z_{As} (fractional co-ordinate of As) fairly accurately [29–34]. In fact, the optimized value of z_{As} is about 0.1 Å smaller than that of the experimental z_{As}. The reason behind this discrepancy is the presence of strong magnetic fluctuation, emerging due to the existence of Fe atoms in these materials [35]. We discuss this issue in chapter 4-7 with respect to our results.

1.5 Physical properties

Physical properties of the Fe-based superconductors are fundamentally different both from those of a conventional electron-phonon coupled superconductor and from those of the unconventional high T_c cuprates. Some of the paramount physical properties which we investigated in this thesis, are briefly discussed in this section.

1.5.1 Superconducting gap and pairing symmetry

Superconducting state has a strong link with the band structure close to the FL. The superconducting order parameter (OP) Δ_{SC}, or ‘gap function’ *i.e.* superconducting gap, is a complex function that characterizes the macroscopic quantum state of Cooper pairs.

Amplitude of this pairing state can in general depend on direction of momentum and can change sign through its phase component, but simplest case (conventional superconductor) is isotropic s-wave (constant value for all momenta). In general pairing potential involves a variation of amplitude as a function of momentum k, or even a variation in phase that results in a change in the sign of Δ_{SC}. Simple s-wave pairing in Fe-based SCs is ruled out by experimental evidence as it is unable to explain many observed physical properties. Magnetic (anti-ferromagnetic spin) fluctuation in high T_c cuprates provide pairing in $d_{x^2-y^2}$ channel [36] whereas in Fe-based superconductors it is believed to provide $s^{\pm}$ pairing symmetry [31]. But s^{++} pairing mediated by orbital fluctuation [37] and/or coexistence of $s^{\pm}$, s^{++} pairing states [38] are also proposed. Though the issue is still not settled. Next, we discuss one of the most interesting parameters $2\Delta/K_BT_c$ which dictates superconducting properties of any superconductor and more importantly transpire the information about superconducting gap. From BCS theory it can be shown that the numerical value of $2\Delta/K_BT_c$ is approximately equal to 3.5, known as BCS characteristics ratio and it turns out that for most of the conventional superconductors, experimentally estimated $2\Delta/K_BT_c$ fall in the range from 3.0 to 4.5 with mostly clustered around the BCS value of 3.5. $2\Delta/K_BT_c$ ratio represents the fundamental coupling strength of superconductivity. Neutron scattering experiments yield convincing stipulation about sign changing SC energy gap on different parts of the FS in a number of iron based superconductors. Moreover, it is also revealed from experiments that there are two nearly isotropic superconducting gaps both vanish at same superconducting transition temperature with characteristics ratios $2\Delta/K_BT_c = 2.5 \pm 1.5$ (for small gap on the outer C-barrel) and 7 ± 2 (on the inner C-barrel and the propeller-like structure around the X point, for large gap). In Fig.1.5 taken from reference [39] values of $2\Delta/K_BT_c$ for various Fe-pnictides are depicted as revealed by different experimental techniques (refer to Fig.1.5 for expansion of the abbreviations). In the figure, the points corresponding to the data taken on 122 systems are denoted by stars, points corresponding to 1111 systems are denoted by squares and points corresponding to 11 are denoted by spindle-like symbols. Studies on the 122 single

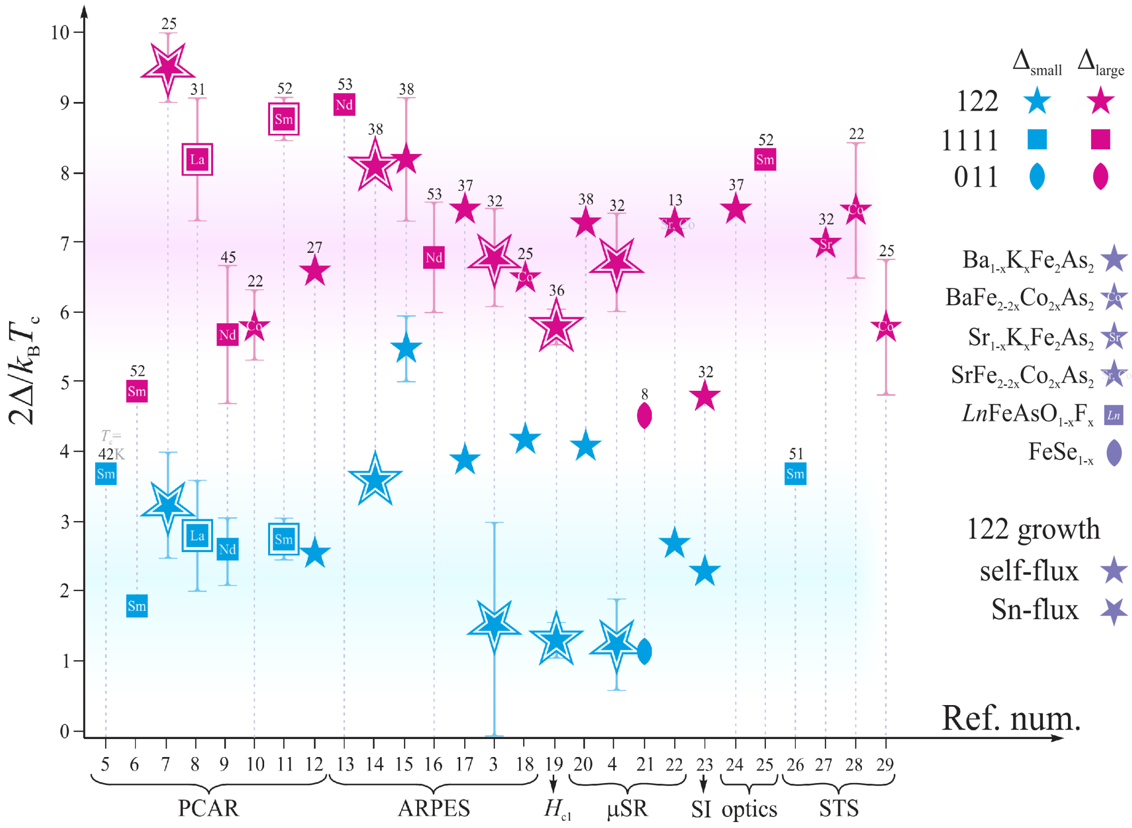

Figure 1.5: Characteristics ratio $2\Delta/K_B T_c$, of Fe-based SCs, as revealed by different experimental techniques (taken from [39]).

crystals grown by the Sn-flux method are shown as overturned stars. Data points denoting the most comprehensive and quality studies are marked by an extra frame. There are clearly two superconducting gaps (red and blue) in these systems the ‘small’ one and the ‘large’ one, although some studies overlook one of the gaps. In chapter 1 we exclusively showed that combined intra-inter band pairing symmetry is an essential requirement to have this kind of characteristics ratio/coupling constant ($2\Delta/K_B T_c$).

1.5.2 Electronic specific heat

Experimentally measured specific heat data of FePn/Ch SCs reveals the higher temperature transitions, like structural (T_S) and (T_{SDW}) SDW transition. If enough magnetic field can be applied to conquer appreciably, C/T extrapolated to T=0 from normal state data gives Sommerfeld constant γ_n, which is proportional to the renormalized bare electron density of states at the Fermi energy N(0); i.e. γ_n $(1 + \lambda)N(0)$ (where λ can be combination of electron-phonon and electron-electron interactions). It is a very useful parameter given by specific heat as it can be related to band structure calculations of N(0) and de Haas van Alphen measurement of effective masses of various Fermi surface orbits. Because of large phononic contribution at higher temperature, the specific heat jump is not clear in some cases. If the phonon contribution to the specific heat below T$_c$ can be accurately estimated, e.g. via a neighbouring composition (replacing Fe by Co doping as they have almost same molar mass) which is not superconducting, one can extrapolate the electronic specific heat below T$_c$ using the second order nature of the superconducting transition and matching entropies. Then one can easily get the electronic part of the specific heat in the superconducting state. Another important correlation between specific heat jump and T$_c$ is proposed by Bud'ko, Ni and Canfield [40] popularly known as BNC plot shown in Fig.1.6a (taken from [40]). They proposed that in the basis of measurement of 14 samples of various 122 systems, $\Delta C/T_c = aT_c^2$ with a $0.056 mJ/moleK^4$. A extended and modified BNC plot has been put forwarded by Kim *et al.,* to include all other families of Fe-based SCs along with other different classes of SCs like conventional metals, A-15 compounds, Heavy Fermions. This revised BNC plot, with $\Delta C/T_c$ $0.083T_c^{1.89}$ is shown in Fig.1.6b taken from reference [41]. Both the conventional superconductor and heavy fermion superconductors have shown different behaviour than the FePn/Ch superconductor. This unconventional behaviour of FePn/Ch superconductors provide a link between superconductivity and related parameter like which may provide a theoretical understanding of mechanism of superconductivity. To explain this behaviour Kogan *et al.,* considered that FePn/Ch superconductors are weak coupled Fermi liquids and specific heat jump of iron-pnictides are interpreted as caused by strong pair-breaking [42, 43]. On the other hand, Zaneen proposed that $\Delta C/T_c$ T_c^2 scaling standing against the Fermi liquid picture rather superconductivity arises due to non Fermi liquid quantum criticality [44]. Moreover, Vavilov et al. stated that below optimal doping this behaviour is due to coexistence of SDW magnetism and superconductivity with s$^{\pm}$ pairing [45]. We through our proposed two band model (construction of model is discussed in chapter 2), showed that considering intra-inter band pairing in equal footing, one can reproduce this BNC scaling of specific heat jump. We further showed that our work is consistent with the $s^{\pm}$ pairing which is the most promising pairing mechanism proposed till now.

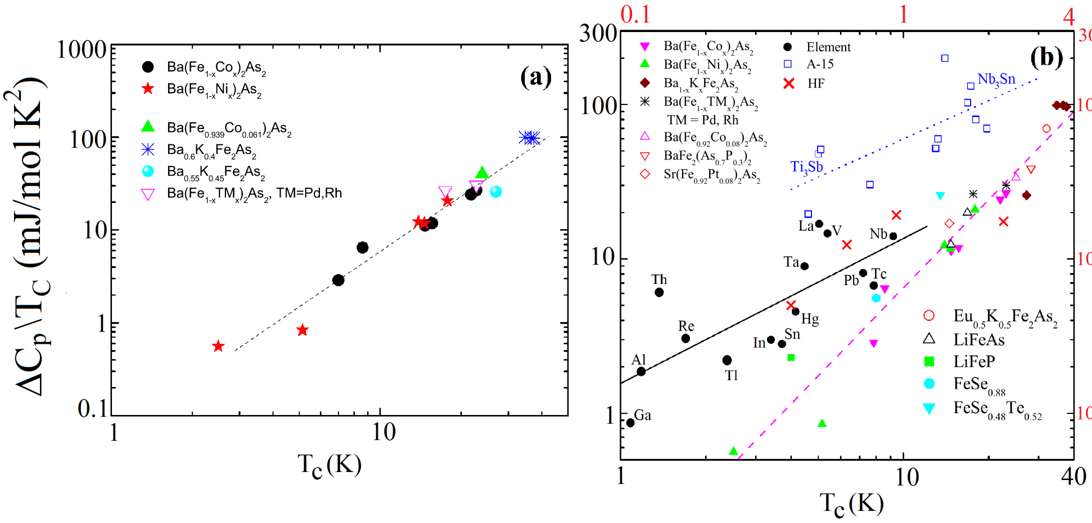

Figure 1.6: (a) Log-log plot of $\Delta C_p/T_c$ vs T_c for various doped 122 Fe-based SCs (taken from [40]). Dashed line has a slope n=2 and is just guide to the eyes. (b) Log-log plot of $\Delta C_p/T_c$ vs T_c for various Fe-based SCs along with various other SCs like conventional SCs (elements in black solid circles and A-15 compounds in blue open squares), heavy fermion SCs (red Xs). Fig.1.6b is taken from [41]

1.5.3 Fermiology

Fermiology of FePn/Ch superconductors reveals the information about pairing mechanism, symmetry and structure of the energy gap. Theoretically computed Fermi surfaces (from first principles study) of undoped LaFeAsO have two electron cylinders around the tetragonal M point, two hole cylinders and a hole pocket around the Γ point [32]. But there are also evidences of existence of only one kind of Fermi surface [46]. A schematic of a typical FS is shown in Fig.1.7. Fermi surface of undoped FePn/Ch with the hole pocket (full circle) at the centre (Γ point) at (0, 0) with energy gap +Δ and the electron pockets (quarter circles) at (π, π) [the corner (M or X) points] with energy gap −Δ is presented in Fig. 1.7. The spin density wave momentum wave vector Q spanning the two nested pockets are also indicated in the figure. This schematic Brillouin zone (BZ) follows the two Fe atoms/unit cell "folded" BZ (FBZ) notation [47, 48]. Inelastic neutron scattering experiments in polycrystalline K doped $BaFe_2As_2$ samples [49] reveals a magnetic resonance below T_c, for a sign change in on different parts of the Fermi surface which is consistent with theory [47, 48]. Same other experiments on single crystals of $BaFe_{1.84}Co_{0.16}As_2$ done by Lumsden et al., found 2D nature like cuprates and magnetic fluctuations associated resonance [50]. Mazin et al. have shown that in electron doped $LaFeAsO_{1-x}F_x$ one can get simplified Fermi surface with the hole pocket filled and they also proposed that pairing is due to spin fluctuations (opposing triplet pairing) [31, 51]. ARPES measurements of Ding et al. revealed that two superconducting gaps with different values: a large gap (12 meV) on the two small hole-like and electron-like Fermi surface (FS) sheets, and a small gap (6 meV) on the large hole-like Fermi surface. Both gaps, terminating simultaneously at the bulk transition temperature (T_c), are node less and nearly isotropic around their respective Fermi surface sheets [52]. In Fig.1.8, we depict some of the experimentally measured (FeSe at 20K, $(Tl_{0.58}Rb_{0.42})Fe_{1.72}Se_2$ at 32K, $Ba_{1.6}K_{0.4}Fe_2As_2$) as well as theoretically computed FSs (FeSe system). These FS structures are extremely sensitive to temperature, doping as well as pressure. Added to that, electronic topological transition/Lifshitz transition is also experimentally observed

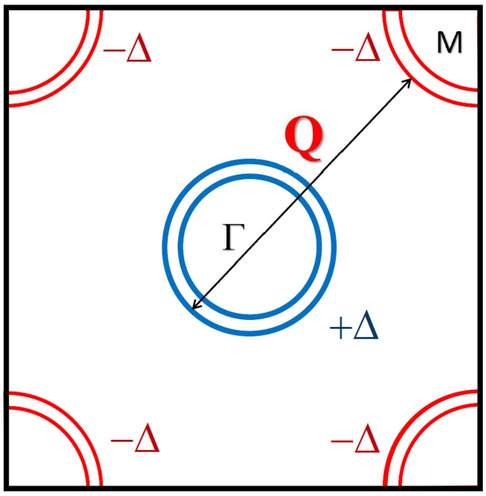

Figure 1.7: A schematic of a typical FS of Fe-based SC.

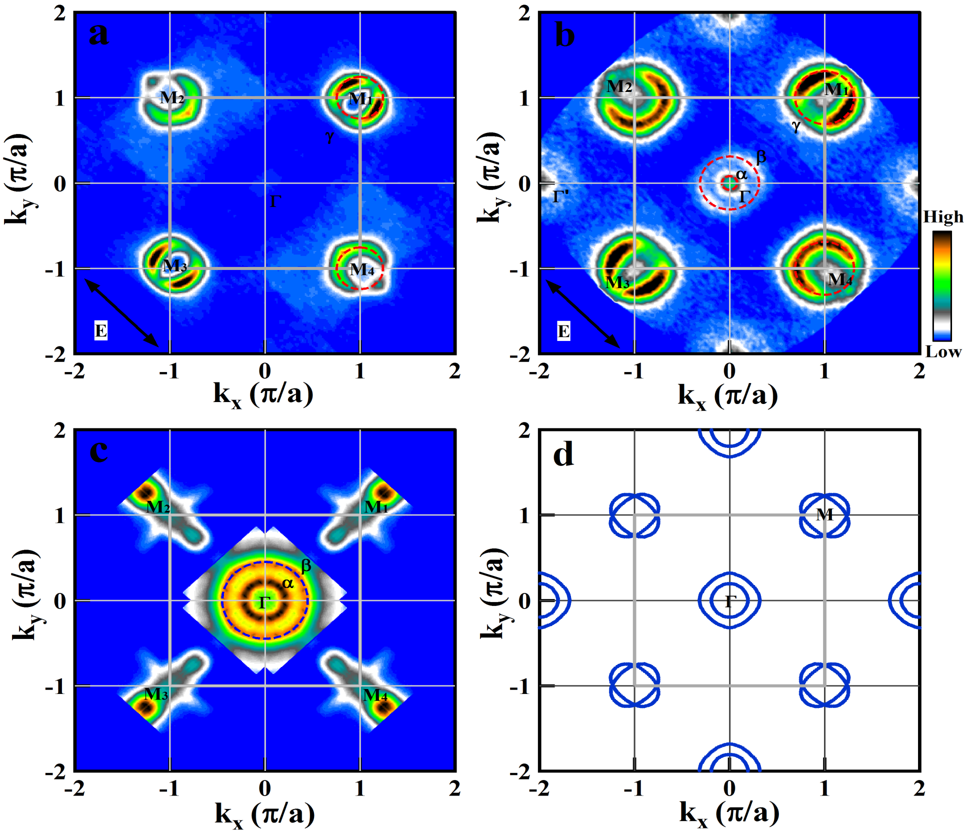

Figure 1.8: (a) Fermi surface mapping of single layer FeSe measured at 20K which consists only electron-like Fermi surfaces. (b) Fermi surface mapping of $(Tl_{0.58}Rb_{0.42})Fe_{1.72}Se_2$ superconductor (T_c=32K) which consists both electron-like as well as hole-like Fermi surfaces. (c) Experimental FSs of $Ba_{1.6}K_{0.4}Fe_2As_2$. (d) theoretically computed Fermi surfaces of β FeSe (taken from [46]).

in some of the Fe-based systems. In chapter 6 and 7 we address those issues related to Fermi surface of 122 Fe-based SCs.

1.5.4 Phase diagram

Phase diagrams play a supreme role in the understanding of physical properties of any material. For Fe-based SC, the correct interpretation of their phase diagrams is very important because of the close interplay between lattice, orbital and spin degrees of freedom and the possible coexistence of magnetism and superconductivity. Some problems for understanding the phase diagrams are: 1) the origin of the structural transition and its relationship with magnetism; 2)Nematic phase and its link to magnetism and superconductivity; (3) Role of electronic topological transition on superconductivity and magnetism *etc.* In Fig.1.9a, we present the phase diagram of some 122 Fe based SCs (K, Co

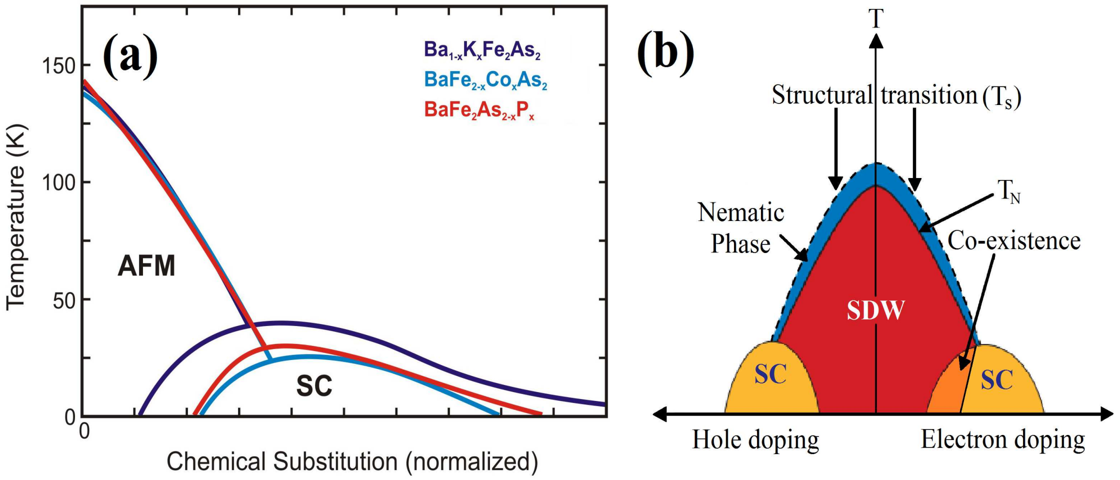

Figure 1.9: (a) Phase diagrams of some 122 Fe based SCs (taken from [53]). (b) A schematic phase diagram of Fe based SC indicating different phases and their coexistence.

and p doped BaFe$_2$As$_2$ system) and in Fig.1.9b, we depict a schematic phase diagram of Fe-based SC. These materials have well established coexistence magnetism and superconductivity. The magnetism is caused by spin density wave (SDW) type transition seen in resistivity, spin susceptibility and neutron scattering measurements. Strongly anisotropic in-plane transport properties (measured experimentally) like resistivity *etc.* which is also viewed as “preferential transport” in the 122 systems [54] in the orthorhombic phase or in tetragonal phase in presence strain field, created a lot of attention leading to a new phase called ‘nematic phase’ in the phase diagram of these materials. A nematic phase of matter is one in which the order parameter for a transition breaks rotational symmetry but time-reversal symmetry is preserved similar to the order parameter in the nematic phase of liquid crystals. In a crystalline lattice, a nematic phase corresponds to the breaking of discrete rotational symmetry, and in the context of the Fe based SC, this order parameter is non-zero in the orthorhombic phase where the C$_4$ symmetry is broken at the structural transition, T$_S$. As mentioned earlier, in certain systems, the structural and the magnetic transition are identical (T$_S$=T$_N$), and since the magnetic order (stripe SDW) by itself breaks C$_4$ symmetry, the primary order parameter for nematicity appears to be magnetic one. In the nematic phase actually all the three parameters (a) structural distortion (phonon driven), (b) charge/orbital order (n$_{d_{xz}}$, n$_{d_{yz}}$ being different), (c) spin order (static spin susceptibility along q$_x$ and q$_y$ being different) are non-zero, no mater what drives the nematic instability. A bilinear combinations of these order parameters (a, b, c) that break tetragonal symmetry are invariant under symmetry transformations and forms essential part of Landau Free energy. As a result, from principle of minimization one order parameter induces the other. And that is precisely the experimental challenge as how to determine the primary order parameter responsible for nematic transition. Consequently, the issue of nematicity is more crucially posed for those systems where the structural transition precedes the magnetic one (T$_S$ T$_N$), leaving a finite temperature interval where C4 symmetry is broken but the material remains paramagnetic [55–58]. The most notable example being FeSe where only a structural transition [59, 60] is detected (the difference between the T$_s$ and T$_N$ being the largest) and the system remains paramagnetic till its SC phase [61], indicating that nematic degrees of freedom are not necessarily magnetic ones but probably orbital one. The microscopic origin of the nematic order is debatable with a few competitive probable scenarios. One scenario is that the structural transition is an anharmonic lattice potential driven instability, so the lattice orthorhombicity would be the primary order parameter. A second scenario is that the C4 symmetry is broken primarily by electronic interactions so that lattice degrees of freedom are secondary order parameters that passively follow the symmetry breaking induced by the electronic interactions hence the primary order parameter is electronic in origin. One such scenario is the spin-nematic transition whereby the spins of the two Fe sublattices phase-lock, this breaks C4 symmetry, without developing any spontaneous magnetization, *i.e.*, without breaking time reversal symmetry [62–70]. Another possible candidate in this scenario is ferro-orbital ordering [70–75], where below nematic transition either the occupations or the hopping matrix elements (or both) of the d$_{xz}$ and the d$_{yz}$ orbitals of Fe become inequivalent. Apart from the above two electronic scenarios, other possibilities include a d-wave Pomeranchuk instability [76], in which the Fermi surfaces undergo symmetry-breaking distortions due to interaction effects. From above discussions it turns out that the primary step would be to show beyond doubt as to whether the structural transition is electronic in origin or lattice driven. In chapter 4 and 5, we address these issues and providing a correlation between experimental evidence and theory.

Chapter 2

Theoretical methods

The main purpose of this thesis is to study some of the important theoretical aspects of normal and superconducting state properties of Fe-based SCs. In the previous chapter, we introduce many interesting and distinctive superconducting as well as normal state physical properties of Fe-based SCs along with its crystal structures. Experimental and theoretical studies of Fe-based SCs reveals that phase diagram of these SCs possess several exotic phases along with its novel superconducting features. A large part of the phase diagram of Fe based SCs are still to be explored with many unsolved issues; better understanding about those phases is required. In this thesis, we addressed some of these unresolved issues as discussed in the previous chapter. In this thesis, we opt two approaches; (i) study of Fe-based materials through minimal model Hamiltonian and (ii) first principles studies using density functional theory. In this particular chapter, we briefly discussed the basic principles of these two methodologies. Theoretically, disorder has been treated within virtual crystal approximation (VCA) as well as super-cell methods. A brief description of these two methods along with its applicability to various doped Fe-based SCs are also included in this chapter.

2.1 Models of Fe based superconductors

High critical superconducting transition temperatures and the nature of electronic structures near the Fermi level suggest that the pairing interaction of the Fe-pnictide superconductors is of electronic origin [77]. First principles band structure calculations indicate that the superconductivity in these materials is associated with the Fe-pnictide layer, and that the density of states near the Fermi level gets its maximum contribution from the all five Fe-3d orbitals namely $3d_{xz}$, $3d_{yz}$, $3d_{xy}$, $3d_{z^2}$ and $3d_{x^2-y^2}$ while the As-4p orbitals contribute more to the bands well below the Fermi level [31, 78–81]. Unfolded Brillouin zone of these Fe-based SCs reveals that the Fermi surface consists of electron pockets at the X and Y points, two hole pockets in Γ and a hole pocket at M points, with reasonably good agreement with de Haas van Alphen experiments in the non-magnetic state [82, 83]. Angle resolved photo-emission spectroscopy (ARPES) measurements also provide the evidence of Fermi pockets at these symmetry points with very similar FS topology [33, 52]. In this regard, the role of FS nesting over superconductivity and magnetism is instrumental. It seems to appear that these multiple pieces of Fermi surfaces play an essential role in determining the momentum dependence of the spin and orbital fluctuations which would mediate an entirely different electronic pairing mechanism in Fe-based SCs than that of the other high T_c SCs. Therefore, it is essential to implement multi-orbital models to investigate these Fe-based superconductors, including two-, three- or five-orbital models that include various many body electronic correlations, exchange-interactions, Hunds coupling *etc.*

An appropriate and reasonable tight-binding model is the fundamental building block of any theoretical treatment in a lattice of these SCs. Several tight binding models have been proposed to explain the electronic structure and physical properties of Fe-based SCs. Cao *et al.* used 16 localized Wannier functions to construct a tight binding effective Hamiltonian [78], whereas Kuroki *et al.* have used 5 orbital tight binding model to fit the band structure of these Fe based SCs near the Fermi energy [84]. The five-orbital

Hamiltonian [85] consists of two terms,

$$H = H_{TB} + H_{int}$$

where H_{TB} is the kinetic part arising from the tight-binding fit to the density functional theory (DFT) band structures.

$$H_{TB} = \sum_{ij,\mu\nu,\sigma} t_{ij}^{\mu\nu} c_{i\mu\sigma}^{\dagger} c_{j\nu\sigma} - \mu_0 \sum_{i\mu\sigma} n_{i\mu\sigma}$$

The operator $c_{i\mu\sigma}^{\dagger}(c_{j\nu\sigma})$ creates (annihilates) an electron at site i (site index) in orbital state μ (orbital index) with spin σ (spin index) and μ_0 is the chemical potential fixed such that the doping $\delta = \langle n \rangle - 6.0$ is zero. The indices μ and ν denote the five iron orbitals d$_{xz}$, d$_{yz}$, d$_{xy}$, d$_{z^2}$ and d$_{x^2-y^2}$. The second term H_{int} describes the Coulomb interactions.

$$H_{int} = U \sum_{i,\mu} n_{i\mu\uparrow} n_{i\mu\downarrow} + (U' - J/2) \sum_{i,\mu<\nu,\sigma\sigma'} n_{i\mu\sigma} n_{i\nu\sigma'}$$
$$-2J \sum_{i,\mu<\nu} \mathbf{S}_{i\mu}.\mathbf{S}_{i\nu} + J' \sum_{i,\mu<\nu,\sigma} c_{i\mu\sigma}^{\dagger} c_{i\mu\bar{\sigma}}^{\dagger} c_{i\nu\bar{\sigma}} c_{i\nu\sigma}$$

First term of the interaction Hamiltonian denotes the intra-orbital interaction with interaction strength U and the second term denotes the inter-orbital interaction with U′ being the interaction strength. The relation $U' = U - 2J$ between the Kanamori parameters has been used where J is the Hund's coupling. Third term of the interaction Hamiltonian is Hund's coupling that favours the ferromagnetic (FM) alignment of the spins in different orbitals at the same lattice site. Last term of the Hamiltonian is pair hopping energy (J′). In principle one can solve this Hamiltonian using mean field approximation. But the presence of so many interaction terms along with five orbital degrees of freedom in the Hamiltonian, it is quite complicated, time consuming, tedious and numerically expensive job to find a solution to this five orbital model Hamiltonian of Fe-based superconductors.

Various electronic structure calculations reveals that the major contribution to the density

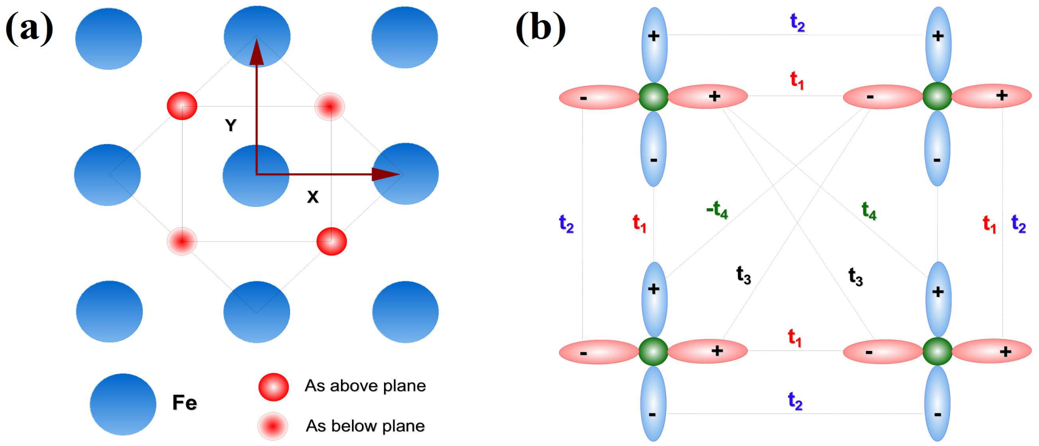

Figure 2.1: (a) The Fe atoms form a square lattice and the crystallographic unit cell contains two Fe and two As atoms. The As atoms are located above and below the Fe plane. (b) A schematic representation of the hopping parameters in a two-orbital model d$_{xz}$-d$_{yz}$ on a square lattice. The projections of the d$_{xz}$ (d$_{yz}$) orbitals onto the xy plane are depicted in red (blue). Here t_1 is a first nearest neighbour hopping between σ orbitals, t_2 is a near neighbour hopping between π orbitals, t_3 is the second neighbour hopping between similar orbitals and t_4 is the second neighbour hopping between different orbitals.

of states within several eV of the Fermi surface arises from the Fe 3d orbitals which has very weak dispersion along the z-direction. However, the band structure near the Fermi level is relatively simple in the unfolded 1Fe/cell BZ where it primarily involves three Fe orbitals: d$_{xz}$, d$_{yz}$, d$_{xy}$ (or d$_{x^2-y^2}$) [31]. Based on these result we construct a two-dimensional square lattice with two degenerate d$_{xz}$, d$_{yz}$ orbitals per site. The effect of third orbital d$_{xy}$ (or d$_{x^2-y^2}$) come into the picture in a approximated way where a next near neighbour hybridization between d$_{xz}$, d$_{yz}$ are considered which control the relative sizes and eccentricities of the electron and hole pockets. We found that a two-orbital model can lead to a very similar Fermi surface topology which resembles with that obtained from the band structure calculations. The Fe atoms form a square lattice which is interlaced with another square lattice of As atoms. These As atoms are situated above and below the plane that contains Fe atoms and distributed in the centre of each square plaque formed by the Fe lattices as indicated in the fig.2.1. This leads to two distinct Fe sites and a crystallographic unit cell which accommodate two Fe and two As atoms. This model has two orbitals (d_{yz},

d_{zx}) per site on a two dimensional square lattice of iron. The tight-binding parameters of the 2-orbital model illustrated in fig.2.1

The tight binding part of the Hamiltonian for two orbital per site model can be written as,

$$H_0 = \sum_{k\sigma} c^{\dagger}_{k\sigma}\{[\epsilon_+ (k) - \mu]\, I_{\,2\times 2} + \epsilon_{-k}(k)\tau_3 + \epsilon_{xy}(k)\tau_1\}c_{k\sigma}$$

Where the wavefunction $c_{k\sigma}$ is given by

$$c_{k\sigma} = \begin{pmatrix} c_{d_{yz}k\sigma} \\ c_{d_{xz}k\sigma} \end{pmatrix}$$

$c_{k\sigma}$ is the annihilation operator for spin σ electrons in the two orbitals and similarly $c^{\dagger}_{k\sigma}$ is the creation operator for spin σ electrons in the two orbitals. And

$$\epsilon_+(k) = -(t_1 + t_2)\left(\cos k_x + \cos k_y\right) - 4t_3 \cos k_x \cos k_y$$

$$\epsilon_-(k) = (t_1 - t_2)\left(\cos k_x - \cos k_y\right)$$

$$\epsilon_{xy}(k) = -4t_4 \sin k_x \sin k_y$$

$I_{\,2\times 2}$ is 2×2 identity matrix, $\tau_3$and $\tau_1$are the standard Pauli's matrices given by:

$$\tau_3 = \begin{pmatrix} 0 & 1 \\ 1 & 0 \end{pmatrix} \quad and \quad \tau_1 = \begin{pmatrix} 1 & 0 \\ 0 & -1 \end{pmatrix}$$

So the Hamiltonian can be rewritten as,

$$H_0 = \sum_{k\sigma} \begin{pmatrix} c^{\dagger}_{d_{yz}k\sigma} & c^{\dagger}_{d_{xz}k\sigma} \end{pmatrix} \left\{ \begin{pmatrix} \epsilon_+ (k) - \mu & 0 \\ 0 & \epsilon_+ (k) - \mu \end{pmatrix} + \begin{pmatrix} \epsilon_- (k) & 0 \\ 0 & -\epsilon_- (k) \end{pmatrix} + \begin{pmatrix} 0 & \epsilon_{xy}(k) \\ \epsilon_{xy}(k) & 0 \end{pmatrix} \right\} \begin{pmatrix} c_{d_{yz}k\sigma} \\ c_{d_{xz}k\sigma} \end{pmatrix}$$

Now if we put all the terms $\epsilon_+(k)$, $\epsilon_-(k)$, $\epsilon_{xy}(k)$ in this Hamiltonian and a bit algebra will give us:

$$H_0 = \sum_{k\sigma} [\{-t_1(e^{ik_x} + e^{-ik_x}) - t_2(e^{ik_y} + e^{-ik_y}) - t_3(e^{ik_x} + e^{-ik_x})(e^{ik_y} + e^{-ik_y})\}c^{\dagger}_{d_{yz}k\sigma}c_{d_{yz}k\sigma} +$$

$$\{-t_1\left(e^{ik_y} + e^{-ik_y}\right) - t_2\left(e^{ik_x} + e^{-ik_x}\right) - t_3(e^{ik_x} + e^{-ik_x})(e^{ik_y} + e^{-ik_y})\}\, c^{\dagger}_{d_{yz}k\sigma}c_{d_{yz}k\sigma} + \ldots]$$

From this we can understand various hopping terms.

Using Bogoliubov transformation we have,

$$\begin{pmatrix} c_{d_{yz}k\sigma} \\ c_{d_{xz}k\sigma} \end{pmatrix} = \begin{pmatrix} u_k & -\sigma v_k \\ \sigma v_k & u_k \end{pmatrix} \begin{pmatrix} \alpha_{k\sigma} \\ \beta_{k\sigma} \end{pmatrix}$$

Putting this in the above Hamiltonian and it reduced to

$$H_0 = \sum_{k\sigma} [\{\epsilon_+(k) + \epsilon_-(k) - \mu\}u_k^2 + \{\epsilon_+(k) - \epsilon_-(k) - \mu\}\, v_k^2 + 2\sigma\epsilon_{xy}(k)u_k v_k]\alpha^{\dagger}_{k\sigma}\alpha_{k\sigma}$$

$$+ \sum_{k\sigma} [\{\epsilon_+(k) + \epsilon_-(k) - \mu\}v_k^2 + \{\epsilon_+(k) - \epsilon_-(k) - \mu\}\, u_k^2 - 2\sigma\epsilon_{xy}(k)u_k v_k]\alpha^{\dagger}_{k\sigma}\alpha_{k\sigma}$$

$$+ \sum_{k\sigma} \{-2\sigma\epsilon_-(k)u_k v_k + \epsilon_{xy}(k)(u_k^2 - v_k^2)\}(\alpha^{\dagger}_{k\sigma}\beta_{k\sigma} + \beta^{\dagger}_{k\sigma}\alpha_{k\sigma})$$

Now we demand the coefficient of the off-diagonal terms (last term) equal to zero to get,

$$2\sigma\epsilon_-(k)\, u_k v_k = \epsilon_{xy}(k)(u_k^2 - v_k^2)$$

And from the normalization condition we already have,

$$u_k^2 + v_k^2 = 1$$

Solving this equation we get:

$$|u_k|^2 = \frac{1}{2}\left\{1 \pm \frac{\epsilon_-(k)}{\sqrt{\epsilon_-{}^2(k) + \epsilon_{xy}{}^2(k)}}\right\}$$

$$|v_k|^2 = \frac{1}{2}\left\{1 \mp \frac{\epsilon_-(k)}{\sqrt{\epsilon_-{}^2(k) + \epsilon_{xy}{}^2(k)}}\right\}$$

And

$$u_k v_k = \frac{1}{2}\left\{\frac{\epsilon_{xy}(k)}{\sqrt{\epsilon_-{}^2(k) + \epsilon_{xy}{}^2(k)}}\right\}$$

Substituting these values back into the Hamiltonian we get a diagonalized Hamiltonian of the form:

$$H_0 = \sum_{k\sigma} (\epsilon_k^+ \alpha_{k\sigma}^\dagger \alpha_{k\sigma} + \epsilon_k^- \beta_{k\sigma}^\dagger \beta_{k\sigma})$$

Where

$$\epsilon_k^\pm = \epsilon_+(k) \pm \sqrt{\epsilon_-{}^2(k) + \epsilon_{xy}{}^2(k)} - \mu$$

This result can also be interpreted in a slightly different manner; we can label the two energy eigenvalues or dispersion relations as electron and hole dispersions. We select ϵ_k^+ and label it as ϵ_k^e and similarly ϵ_k^- as ϵ_k^h.

Fermi surfaces are constant energy surfaces. For two dimensions these can br regarded as constant energy contours or plots. In fig.2.2 the FSs are plotted using the dispersions for the normal state derived as,

$$\varepsilon_k^e = \varepsilon_k^+ = \epsilon_+(k) + \sqrt{\epsilon_-^2(k) + \epsilon_{xy}^2(k)} \approx 0 \text{ \{Red dots\}}$$

$$\varepsilon_k^h = \varepsilon_k^- = \epsilon_+(k) - \sqrt{\epsilon_-^2(k) + \epsilon_{xy}^2(k)} \approx 0 \text{ \{Blue dots\}}$$

taking the constant energy close to zero (may also be called zero energy plots) with chemical potential $\mu = 1.42$ and other tight binding parameters $t_1 = -1.0$ eV, $t_2 = 1.3$ eV and $t_3 = t_4 = -0.85$ eV. Blue coloured lines (dots) correspond to the hole pockets and red corresponds to electron pockets.

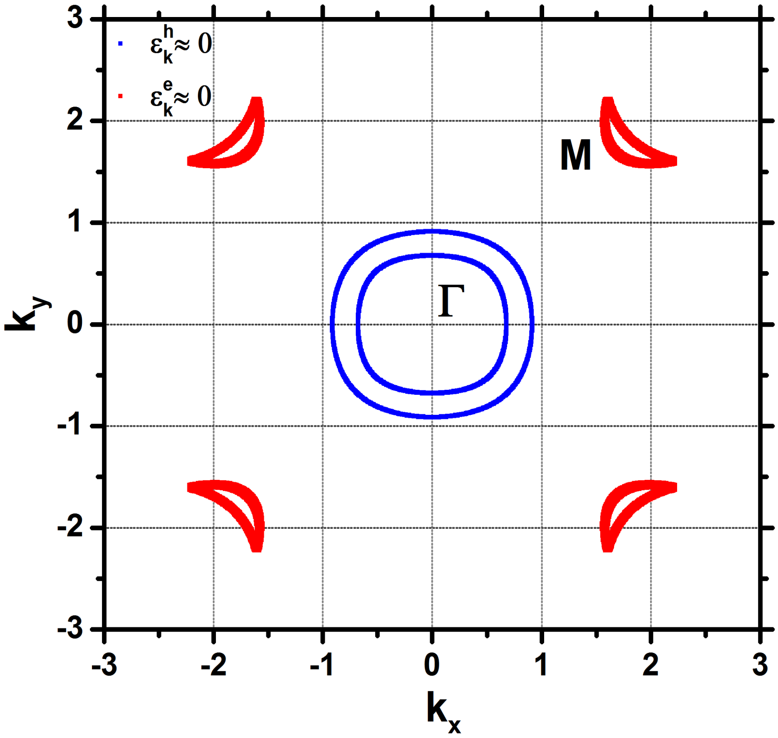

Figure 2.2: Fermi Surface (or zero energy contour) in the reduced + rotated brillouin zone for μ = 1.42 evaluated within two band model.

The FSs that obtained from this two band model possess a very similar topology as that of the experimental as well as theoretically simulated FSs as revealed by DFT band structure calculations. Therefore, a minimal two band model can be used to explain many important physical properties of Fe-based SCs. It has been shown that in the normal state, the susceptibilities in orbital and spin channel display a strong peak around the nesting wave vector Q =(0, π) or (π, 0) which indicate the possibility of orbital density wave and/or spin density wave instabilities [86, 87]. Therefore, to construct any model Hamiltonian of Fe-based SCs one must consider those SDW and ODW type interaction along with superconductivity. Using this simplistic two band model Hamiltonian we explain some of the physical properties of Fe-based SCs. More details can be found in Chapter 3. Although this approximated two band model can unfold many important physical properties with desirable accuracy, it is unable to explain many fundamental features of Fe-based SCs. For example, this two band model is unable to predict the structural transition in Fe-based SCs and overlook the important role of anion height over different physical properties including superconductivity. Therefore, three or five band model Hamiltonian have the edge over two band model Hamiltonian as the former can produce more accurate result than the later. On the other hand, first principles density functional theory also can deliver a more realistic picture (all five bands are considered) about the electronic structures of Fe-based SCs. Using first principles density functional theory methods we elucidate many unresolved issues of Fe-based SCs and presented in chapter 4, 5, 6 and 7 respectively. In the next section we discuss the basic principles of density functional theory and the relevant components that has been utilized in this thesis.

2.2 First principles studies using density functional theory (DFT)

A number of physical and chemical properties of materials are governed by electrons which glue the atoms together to form molecules and solids. Therefore, electronic structure play a key role in understanding many physical and chemical properties of solids. According to quantum theory of solids, the ground state properties of many-particle systems containing electrons and nuclei, can be described by the time-independent Schrödinger equation. The time-independent Schrödinger equation for the system having many electrons moving under the nuclear potentials is as given by:

$$\hat{\mathbf{H}}\Psi(r_1, r_2, ...r_N, R_1, R_2, ...R_{N_I}) = E\Psi(r_1, r_2, ...r_N, R_1, R_2, ...R_{N_I}) \tag{2.1}$$

where $\hat{\mathbf{H}}$ is the Hamiltonian and E is the total energy of the system. Ψ is the many-body wave-function. r and R denotes the spatial co-ordinate of electrons and nuclei respectively. We will use atomic units, i.e,

$$m_e = e = \hbar = \frac{1}{4\pi\epsilon_0} = 1$$

and all energies are given in Hartree ($1 Hatree = 27.211 eV$). The Hamiltonian operator for a many body system is given as (in the atomic units):

$$\hat{\mathbf{H}} = -\frac{1}{2}\sum_{i=1}^{N} \nabla_i^2 - \frac{1}{2}\sum_{I=1}^{N_I} \frac{\nabla_I^2}{M_I} + \sum_{i<j=1}^{N} \frac{1}{|\mathbf{r_i} - \mathbf{r_j}|} + \sum_{I<J=1}^{N_I} \frac{Z_I Z_J}{|\mathbf{R_I} - \mathbf{R_J}|} - \sum_{i=1}^{N}\sum_{I=1}^{N_I} \frac{Z_I}{|\mathbf{r_i} - \mathbf{R_I}|} \tag{2.2}$$

where the First term corresponds to the kinetic energy of electrons (T^e). Second term corresponds to the kinetic energy of the nucleus (T^n) and **R** represents the nuclear coordinate, M_I is the ratio of the mass of the nucleus I to the mass of an electron and N_I is number of nuclei. Third term corresponds to electron-electron interaction (V^{ee}); N is number of electrons and **r** represents electronic coordinate. Fourth term corresponds to nuclear interaction (V^{nn}). Fifth term corresponds to nucleus-electron attractive interaction (V^{ne}) and Z represents nuclear charge.

Due to the presence of complicated electron-electron interaction term the above Hamiltonian, it can not be solved. Therefore, solving the Schrödinger equation corresponding to the many body Hamiltonian given by equation 2.2 is a formidable problem as one has to deal with 3(N_n +N_n) degrees of freedom. Added to that the motion of electrons and nuclei are also coupled. We have to introduce some approximation method to solve the many body Hamiltonian. However, we can decouple the nuclear and electronic degrees of freedom through the so called the Born-Oppenheimer approximation and solely focus on the electronic part.

2.2.1 Born-Oppenheimer Approximation

Nuclei are much heavier than electrons (e.g, $\frac{M_H}{m_e} = 1840$). Therefore they react significantly slower to external perturbations than the electrons. As a first approximation electrons will react instantaneously to the nuclear motions and we can decouple the electronic and nuclear motion. Then we can treat the nuclei as clamped and solve only the electronic problem. If the nuclei were fixed in space, V^{ne} in equation 2.2 become an external potential and the problem becomes purely electronic:

$$H^e\Phi^e = [T^e + V^{ee} + V^{ne}]\Phi^e$$

This approximation enables us to separate the motion of electrons and nuclei. Additionally, in this approximation, nuclear motion is not accompanied by the changes in the electronic state of the system. Further, the nuclear-nuclear interaction term is independent of the coordinates of electrons. So this term is considered constant for a fixed set of nuclei. Further, the nuclei are stationary at different positions (nuclear position coordinates) although they are considered to be at rest with respect to the electrons. Thus, the wave function Ψ can be decomposed into electronic and nuclear wave-function and can be written as

$$\Psi(r_1, r_2, ...r_N, R_1, R_2, ...R_{N_I}) = \psi(r_1, r_2, ...r_N)\phi_n(R_1, R_2, ...R_{N_I})$$

So, as a result of this approximation, we are left with the following terms in the many-body Hamiltonian:

1. Kinetic energy of electrons
2. Electron-electron interaction
3. Interaction between electrons and nuclei

So the above Hamiltonian reduces to the electronic Hamiltonian which is given by:

$$\hat{H}_e = -\frac{1}{2}\sum_{i=1}^{N}\nabla_i^2 + \sum_{i<j=1}^{N}\frac{1}{|\mathbf{r_i} - \mathbf{r_j}|} - \sum_{i=1}^{N}\sum_{I=1}^{N_I}\frac{Z_I}{|\mathbf{r_i} - \mathbf{R_I}|} \qquad (2.3)$$

As we can see from the expression of the Hamiltonian that it still contains the electron-electron interaction term which hinders us to solve the many-electron Schrödinger equation exactly. Hence, in order to solve the many-electron Schrödinger equation, to obtain the wave-function and the energy of the system, there are various approximate methods. Density Functional theory is one of the most popular method for obtaining the ground state of a many-body problem in terms of single particle Schrödinger equations. DFT uses the electron density as the basic variable.

In quantum mechanics, *the electronic density determines the measure of the probability of an electron occupying an infinitesimal element of space* dr_1 *surrounding any given point* r_1. It is given as:

$$\rho(r_1) = N\sum_{s_1}.....\sum_{s_N}\int dr_2....\int dr_N|\psi(r_1, s_1, r_2, s_2, ...r_N, s_N)|^2 \tag{2.4}$$

where $s_1, s_2, ...s_N$ are the spins corresponding to the electrons.

Hamiltonian of the many electron system can be defined uniquely, if we know the total number of electrons N, position of the nuclei **R** and the charge of the nuclei Z_I. This information is respectively provided by the characteristics of the density given below

1. $\int \rho(r)dr = N$ which determines the total number of electrons of the many electron system.
2. $\rho(r)$ shows a maximum with a finite value at the position of any atom; cusp at the coordinate of the nucleus.
3. The charge of the nucleus is given by the cusp condition [88]

$$\lim_{r\to R_I}\left[\frac{\partial}{\partial r} + 2Z_I\right]\rho_{av}(r) = 0 \tag{2.5}$$

where $\rho_{av}(r)$ is the average (over angles) electron density and is given by [89]:

$$\rho_{av}(r) = \frac{1}{4\pi}\int d\theta d\phi \sin\theta\rho(r, \theta, \phi) \tag{2.6}$$

2.2.2 Hohenberg-Kohn theorem:

A landmark theory for electronic structure calculations based on density was given by Hohenberg and Kohn in 1964. It primarily consists of two theorems [90].

Hohenberg-Kohn First theorem:

Hohenberg-Kohn uses the density of electrons as the basic variable to describe the ground state properties of a system. The theorem states that[91]

"There is a one to one correspondence between the ground state density $\rho(r)$ and the external potential (the potential due to coulomb interaction between electron and nucleus) for any interacting system under an external potential $v_{ext}(r)$. An immediate consequence is that the expectation value of any observable is a unique functional of the exact ground state electron density."

Since knowing $\rho(r)$ determines uniquely the external potential and consequently the Hamiltonian and in principle the wave-function of a given system, thus as a consequence of first Hohenberg-Kohn theorem, it is clear that it should be possible to write the electronic energy as a functional of density.

$$E_v[\rho(r)] = T[\rho(r)] + E_{ne}[\rho(r)] + E_{ee}[\rho(r)] = F_{HK}[\rho(r)] + \int \rho(r)v_{ext}(r)dr \tag{2.7}$$

where

$$F_{HK}[\rho(r)] = T[\rho(r)] + E_{ee}[\rho(r)] \tag{2.8}$$

and it is called **Hohenberg Kohn energy functional** which is a **universal functional** of the ground state density in the sense that it does not depend on the external potential of the system. $E_v[\rho(r)]$ is the total energy functional under the external potential v_{ext}. $E_{ne}[\rho(r)]$ is the energy corresponding to the attractive potential between the electrons and the nucleus and is the energy corresponding to the external potential. $E_{ee}[\rho(r)]$ is the energy due to the repulsive potential between electrons. From Hohenberg-Kohn first theorem, it can be concluded that if we have the exact ground state density of a given system then in principle we can obtain many of the physical properties of interest. But the problem is that if we are given some density $\rho(r)$, how do we ensure that it is the correct ground state density? This information is provided by the second Hohenberg-Kohn theorem.

Hohenberg-Kohn Second Theorem:

This theorem states that [92]
"For a given trial density $\tilde{\rho}(r)$*, such that* $\tilde{\rho}(r) \geq 0$ *and* $\int \tilde{\rho}(r)dr = N$ *,*

$$E_o \leq E_v[\tilde{\rho}] \tag{2.9}$$

where $E_v[\tilde{\rho}]$ *is the energy functional of equation (2.7)"*

In other words, if $E_v[\tilde{\rho}]$ for a given external potential (v_{ext}) is evaluated for some density that is not the ground state density of the system under that potential, one can never find the energy that is below the true ground state energy. Since from the Hohenberg-Kohn first theorem, any trial density $\tilde{\rho}$ corresponds to some external potential $\tilde{v}(r)$, as well as the Hamiltonian and the wave function $\tilde{\psi}$, then this wave function can be used as the trial wave function for the problem of interest having the external potential $v(r)$. Thus, we have

$$\left\langle \tilde{\psi}|H|\tilde{\psi} \right\rangle = \int \tilde{\rho}(r)v(r)dr + F_{HK}[\tilde{\rho}] \tag{2.10}$$

$$\left\langle \tilde{\psi}|H|\tilde{\psi} \right\rangle = E_v[\tilde{\rho}] \geqslant E_v[\rho] \tag{2.11}$$

As it is clear from above eq (2.8) that the universal functional $F_{HK}[\rho(r)]$ contains the kinetic energy term as well as the electron-electron interaction term. Let us focus on the second term of $F_{HK}[\rho(r)]$ which is expressed as follows:

$$E_{ee}[\rho(r)] = J[\rho(r)] + \text{non-classical term}$$

$J[\rho(r)]$ represents the classical term which is the electrostatic repulsion energy between the electronic charge distribution of electrons and it contains the self interaction. In Hatree-Fock, self interaction is exactly cancelled but with the Local density approximation, self interaction is not cancelled. The expression for the $J[\rho(r)]$ is given by:

$$J[\rho(r)] = \frac{1}{2}\int\int \frac{\rho(r_1)\rho(r_2)}{r_{12}} dr_1 dr_2 \tag{2.12}$$

The non classical term contains all the contributions of quantum mechanical correlation effects and the correction for the self-interaction. So the universal functional $F_{HK}[\rho(r)]$ becomes, $F_{HK}[\rho(r)] = T[\rho(r)] + J[\rho(r)]$ + a non-classical term, in which the functional form of $T[\rho(r)]$ and the non-classical term is not known. Knowing their forms is a major challenge in DFT. If we knew the exact form of these functionals, then the self interaction would be cancelled. We emphasis here that, the Hohenberg-Kohn theorems are mathematical foundations to DFT. This gives an exact picture about how to know the ground state properties for any given system. But this theory does not give the functional form of $F_{HK}[\rho]$. However, the key step towards such problem, taken by Kohn and Sham, in 1965 and came to the rescue.

2.2.3 Kohn-Sham ansatz:

The Kohn-Sham approach maps a given N-particle interacting system, which is of our interest, having the real potential onto a non-interacting (fictitious) system under some potential, provided that **both the systems have the same density**. The advantage of this approach is that it helps to evaluate or determine the major part of the kinetic energy (which corresponds to N non-interacting particles) and the residual (small) amount of kinetic energy (corresponding to the interaction of the actual interacting system of N electrons) can be calculated using some approximations.

Consider a non-interacting particle system with Hamiltonian $\hat{H}_s$ under an external potential v_s having ground state density ρ_s with N number of electrons in the system. The ground state wave function is a Slater determinant of single-particle orbitals ϕ_i [92, 93]

$$\psi_s = \frac{1}{\sqrt{N!}} \det[\phi_1 \phi_2 ......\phi_N] \tag{2.13}$$

where ϕ_is satisfy the equations:

$$[-\frac{1}{2}\nabla^2 + v_s]\phi_i(r) = \epsilon_i \phi_i(r) \tag{2.14}$$

And the ground state density for the non- interacting system is given by:

$$\rho_s(r) = \sum_i^N |\phi_i(r)|^2 \tag{2.15}$$

Applying the Hohenberg-Kohn theorem to this non-interacting system we can get at most one external potential which generates the density ρ_s. Therefore, knowing ρ_s, all the properties of the system are determined like the kinetic energy and the total energy which are given as:

$$T_s[\rho_s] = \left\langle \psi_s | \sum_i^N (-\frac{1}{2}\nabla_i^2) | \psi_s \right\rangle \tag{2.16}$$

$$= \sum_i^N \left\langle \phi_i | (-\frac{1}{2}\nabla_i^2) | \phi_i \right\rangle \tag{2.17}$$

and

$$E_{v_s}[\rho_s] = T_s[\rho_s] + \int \rho_s(r) v_s(r) dr \tag{2.18}$$

The functional $T_s[\rho_s]$ is the Kohn-Sham kinetic energy and $\phi_i(r)'s$ are the Kohn-Sham orbitals. The minimization of energy gives the ground state density of the system. The constraint is $\int \rho_s(r)dr = N$. So we have:

$$\frac{\delta}{\delta\rho}[E_{v_s}[\rho_s] - \mu_s \int \rho_s(r)dr] = 0 \tag{2.19}$$

$$\mu_s = \frac{\delta T_s[\rho_s]}{\delta\rho_s(r)} + v_s(r) \tag{2.20}$$

where the Lagrange multiplier μ_s is used to take care of the constraint. Now we consider our real interacting system with an external potential $v_{ext}(r)$ which has an electronic density $\rho(r)$ (which is equal to $\rho_s(r)$). The energy for this system is given by:

$$E_v[\rho] = T_s[\rho] + J[\rho] + E_{ext}[\rho] + E_{xc}[\rho] \tag{2.21}$$

where

$$E_{xc}[\rho] = T[\rho] - T_s[\rho] + E_{ee}[\rho] - J[\rho] \tag{2.22}$$

is the exchange-correlation energy. $E_{xc}[\rho]$ is functional of density by virtue of the HK theorem for interacting system and $T_s[\rho]$ is functional of density by virtue of the HK theorem for the non-interacting system. The density dependence of $E_{ext}[\rho]$ and $J[\rho]$ are known. It is clear from above that, through the introduction of orbitals, the major part of the kinetic energy, which is the kinetic energy for the non-interacting system, $T_s[\rho]$, is determined by equation 2.12. But the form of the $E_{xc}[\rho]$ is not known. So various approximations to $E_{xc}[\rho]$ are made in the literature so that the exact density and the energy of the given interacting N-electron system can be obtained.

Corresponding to the Kohn-Sham scheme for any ground state density $\rho(r)$ of an interacting system there exists a non-interacting system with the same ground state density. Hence, the equation (2.21) can be written as:

$$E[\rho] = \sum_i \int \phi_i^*(r)(\frac{-1}{2}\nabla^2)\phi_i(r)dr + J[\rho] + E_{xc}[\rho] + \int v_{ext}\rho(r)dr \tag{2.23}$$

Using the fact that the equations for the interacting and the non-interacting systems are solved for the same density, we have $\rho(r) = \sum_i |\phi_i(r)|^2$. So the energy is expressed in terms of orbitals.

Also, from the orthogonality condition, we have $\int \phi_i{}^*(r)\phi_j(r)dr = \delta_{ij}$. Let us now define a functional of N orbitals:

$$\Omega[\{\phi_i\}] = E[\rho] - \sum_{i=1}^{N} \epsilon_{ij} \int \phi_i{}^*(r)\phi_j(r)dr \tag{2.24}$$

where ϵ_{ij} is the Lagrange's multiplier. Minimization of $E[\rho]$ requires $\delta\Omega[\{\phi_i\}] = 0$. Minimization of the functional $\Omega[\{\phi_i\}]$ gives us the famous Kohn-Sham equations as:

$$[-\frac{1}{2}\nabla^2 + v_s(r)]\phi_i(r) = \sum_j \epsilon_{ij}\phi_j(r) \tag{2.25}$$

where

$$v_s(r) = v_{ext}(r) + \int \frac{\rho(r')}{|r - r'|}dr' + v_{xc}([\rho], r) = v_{ext}(r) + v_H(r) + v_{xc}([\rho], r) \tag{2.26}$$

where $v_{xc}(r) = \frac{\delta E_{xc}[\rho]}{\delta\rho}$.

Now making the unitary transformation $U\phi_i = \Phi_i$ where U is the unitary transformation matrix, we get

$$[-\frac{1}{2}\nabla^2 + v_s(r)]\Phi_i(r) = \epsilon_i\Phi_i(r) \tag{2.27}$$

Thus the ground state density of the interacting system can be found by solving the Kohn-Sham equations 2.25. And

$$E = \sum_i \epsilon_i - \frac{1}{2}\int\int \frac{\rho(r)\rho(r')}{|r - r'|}drdr' - \int v_{xc}\rho(r)dr + E_{xc}[\rho]$$

It is clear from the above energy expression that the problem of finding good approximations to the functional F_{HK} is reduced to the problem of finding good approximations for the quantity E_{xc}.

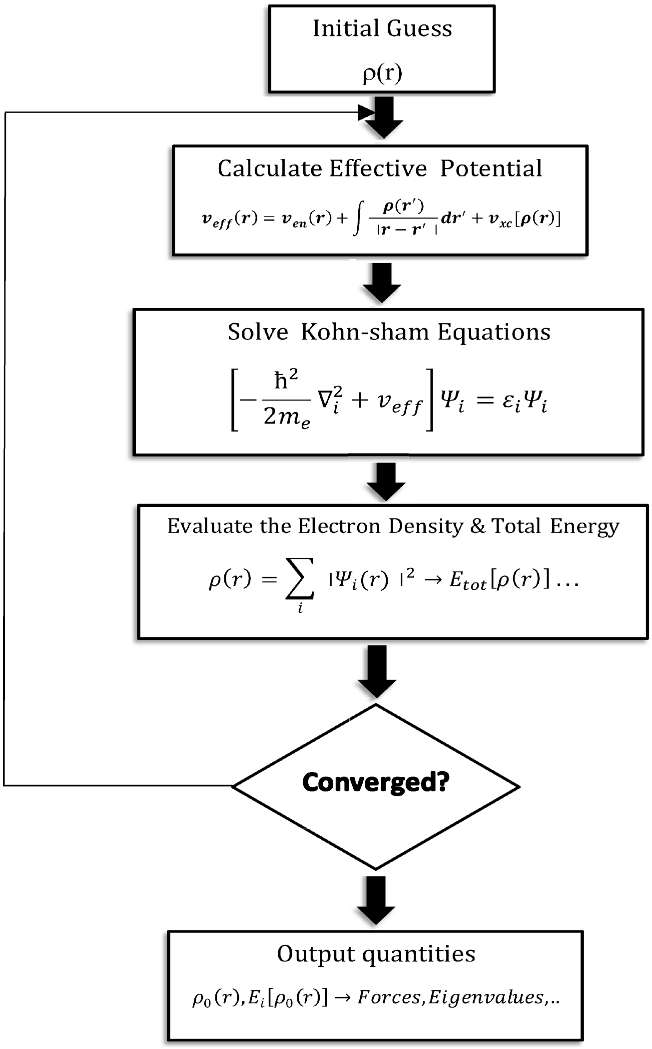

Figure 2.3: A flow chart representation of the self-consistent loop for solution of Kohn-Sham equation.

The equation (2.27) can be written as:

$$\hat{H}_{SP}\Phi_i(r) = \epsilon_i \Phi_i(r) \tag{2.28}$$

where $\hat{H}_{SP}$ is the single particle Hamiltonian and Φ_i is the i^{th} single particle orbitals. The above equations can be solved by expanding the single particle orbitals in terms of basis vectors $\varphi_\mu(r)$ [91] i.e.

$$\Phi_i(r) = \sum_{\mu=1}^{M} c_\mu^i \varphi_\mu(r) \tag{2.29}$$

Ideally M is infinite because Φ_i is a member of the function space which has infinite dimensionality. But, in practice, M is finite.

Once we choose the basis, we substitute Φ_i in the equation (2.28). So, we get

$$\hat{H}_{SP}\sum_{\mu=1}^{M} c_{\mu}^{i}\varphi_{\mu}(r) = \epsilon_i \sum_{\mu=1}^{M} c_{\mu}^{i}\varphi_{\mu}(r) \tag{2.30}$$

Now, multiplying on the left by $\varphi_{\nu}^{*}(r)$ and integrating, we get,

$$\sum_{\mu=1}^{M} c_{\mu}^{i} \int dr\varphi_{\nu}^{*}(r)\hat{H}_{SP}\varphi_{\mu}(r) = \epsilon_i \sum_{\mu=1}^{M} c_{\mu}^{i} \int dr\varphi_{\nu}^{*}(r)\varphi_{\mu}(r) \tag{2.31}$$

Now, let us define the overlap matrix S which is a M x M matrix as:

$$S_{\nu\mu} = \int dr\varphi_{\nu}^{*}(r)\varphi_{\mu}(r) = \left\langle \varphi_{\nu}|\varphi_{\mu}\right\rangle \tag{2.32}$$

The basis functions, are in general, not orthogonal. So, the above matrix contains off diagonal terms too. If the basis functions are orthonormal, then the matrix $S_{\nu\mu}$ is an identity matrix. Also, we can define another matrix $H_{\nu\mu}$ as:

$$H_{\nu\mu} = \int dr\varphi_{\nu}^{*}(r)\hat{H}_{SP}\varphi_{\mu}(r) = \left\langle \varphi_{\nu}|\hat{H}_{SP}|\varphi_{\mu}\right\rangle \tag{2.33}$$

which is also a M x M matrix.

So, we see that the problem of finding Φ_i (single particle orbital) reduces to finding the coefficients of the basis functions.

The Kohn-Sham single-particle equations are exact and are easy to solve. However, *the unknown exchange-correlation energy must be approximated.* Some of the approximations of exchange-correlation energy will be described in the next section. The schematic of Kohn-Sham approach is shown in fig.2.3.

2.2.4 Various Exchange-Correlation Functionals

Local Density Approximation:

Although the Kohn-Sham equations let the major part of the energy functional $F_{HK}[\rho]$ to be known, still the exchange- correlation functional $E_{xc}[\rho]$ is an unknown quantity whose explicit form is needed to specify the KS equations. Finding this quantity continues to be the greatest challenge in DFT. In this section, we will describe the simplest approximations called the Local Density Approximation (LDA). In LDA, "the exchange correlation energy of the inhomogeneous system with electron density $\rho(r)$ is locally approximated by exchange correlation-energy density of a uniform electron gas (UEG)".

As per the assumption made by this model, we can write the exchange-correlation functional in the following way:

$$E_{xc}^{LDA}[\rho] = \int \rho(r)\epsilon_{xc}(\rho)dr \tag{2.34}$$

where $\epsilon_{xc}(\rho)$ is the exchange -correlation energy per particle of uniform electron gas of density $\rho(r)$. $\epsilon_{xc}[\rho]$ for the homogeneous electron gas is numerically known. This form of the exchange-correlation functional is reasonable: it means that the exchange-correlation energy due to a particular density could be found by dividing the material in infinitesimally small volumes which has been assumed to have a constant density. Each such volume contributes to the total exchange-correlation energy by an amount equal to the exchange-correlation energy of an identical volume filled with a homogeneous electron gas, that has the same overall density as the original material has in this volume. By construction, LDA is expected to perform well for systems with a slowly varying density. Now the term $\epsilon_{xc}[\rho]$ is split into two parts given as:

$$\epsilon_{xc}(\rho) = \epsilon_{x}(\rho) + \epsilon_{c}(\rho) \tag{2.35}$$

The exchange energy term is approximated by Dirac [92] as:

$$E_x[\rho] = -\frac{3}{4}\left(\frac{3}{\pi}\right)^{\frac{1}{3}} \int \rho(r)^{\frac{4}{3}} dr \tag{2.36}$$

The correlation term does not have simple dependence on density as is the case for exchange term. Exact analytic expressions for ϵ_c for homogeneous electron gas are known only in the extreme limits and using these two limits the functional form of the correlation term is obtained. The high density limit ($r_s \to 0$) is given by[92]:

$$\epsilon_c(\rho) = 0.311 \ln r_s - 0.048 + r_s (A \ln r_s + C) \tag{2.37}$$

and the low density limit ($r_s \to \infty$) is given by[92]:

$$\epsilon_c(\rho) = \frac{1}{2}\left(\frac{g_o}{r_s} + \frac{g_1}{r_s^{\frac{3}{2}}} + \frac{g_2}{r_s^2} + ...\right) \tag{2.38}$$

where A, g_o, g_1, g_2 are constants and $r_s = (\frac{3}{4\pi\rho})^{\frac{1}{3}}$ is the radius in (atomic unit) of a sphere which encloses the unit of electron charge. LDA is exact for uniform densities and nearly-exact for slowly varying density. It is to be noted that $E_x < 0$ and $E_c < 0$ in LDA.

The local density approximation can also be extended to the spin polarized case:

$$E_{xc}^{LSDA}[\rho^{\uparrow}, \rho^{\downarrow}] = \int \rho(\mathbf{r})\epsilon_{xc}\Big(\rho^{\uparrow}(\mathbf{r}), \rho^{\downarrow}(\mathbf{r})\Big)d\mathbf{r}$$

If we write in terms of spin polarization $\eta(\mathbf{r}) = \frac{\rho^{\uparrow}(\mathbf{r}) - \rho^{\downarrow}(\mathbf{r})}{\rho(\mathbf{r})}$ we get

$$E_{xc}^{LSDA}[\rho, \eta] = \int \rho(\mathbf{r})\epsilon_{xc}\Big(\rho(\mathbf{r}), \eta(\mathbf{r})\Big)d\mathbf{r}$$

By construction local spin density approximation (LSDA) is exact and can produce desirably accurate results for the homogeneous electron gas. Therefore, LSDA is expected to perform well for systems with slowly varying density for *e.g.*, simple metallic systems.

Generalised Gradient Approximation:

LDA does not take into account the gradient of density. So it is essential to add information about the gradient of the charge density, in order to take into consideration the inhomogeneity of the true electron density. So, the approximation which takes into account the spatial variation of density, and the functionals which include the gradient of the electronic charge density (use both the density and its gradient at each point) are called Generalised Gradient Approximation. The exchange energy functional form is given as:

$$E_{xc}^{GGA}[\rho] = \int f(\rho(r), \nabla\rho(r))dr \tag{2.39}$$

As in LDA, the exchange correlation functional is split into exchange and correlation terms

$$E_{xc}^{GGA}[\rho] = E_{x}^{GGA}[\rho] + E_{c}^{GGA}[\rho] \tag{2.40}$$

and they are approximated individually. In the GGA framework, the exchange energy can be written as:

$$E_{x}^{GGA}[\rho] = \int \rho(r)\epsilon_{x}^{LDA}(\rho)F_{x}(s)dr \tag{2.41}$$

where $F_x(s)$ is the exchange enhancement factor due to density gradients and is dependent on the reduced density gradient, s as

$$s = \frac{|\nabla\rho(r)|}{2(3\pi^2)^{\frac{1}{3}}\rho(r)^{\frac{4}{3}}} \tag{2.42}$$

But, unlike LDA, there is no single universal form. Popular GGAs include PBE which is described as follows.

Perdew, Burke, and Ernzerhof (PBE)-GGA:

It is the most popular generalised gradient approximation. This functional comes under non-empirical functional. It exploits only the basic rules of quantum mechanics and special limiting conditions to determine the parameters in a general form. Also satisfies as many exact conditions as possible. The exchange enhancement factor for PBE-GGA [94] is given as:

$$F_x^{PBE} = 1 + \kappa\left(1 - \frac{1}{1 + \frac{\mu s^2}{\kappa}}\right) \tag{2.43}$$

The parameters, $\mu = 0.2195$ and $\kappa = 0.804$.

We can see that if there is very slow variation in density or no variation, then s goes to zero and PBE boils down to LDA .

The PBE correlation energy [95] is given by

$$E_c^{PBE} = \int \rho(r)[\epsilon_c^{LDA}(r_s, \zeta) + H(r_s, \zeta, t)]dr \tag{2.44}$$

where ϵ_c^{LDA} is the correlation energy density for the LDA (*i.e.,* for the uniform electron gas). $H(r_s, \zeta, t)$ takes care of the gradient contribution to the correlation energy. $\zeta = (\rho_{\uparrow}(r) - \rho_{\downarrow}(r))/\rho(r)$ where $\rho_{\uparrow}(r)$ and $\rho_{\downarrow}(r)$ are the spin-up and spin-down number densities.

2.2.5 CASTEP

The Cambridge Serial Total Energy Package, CASTEP is a commercial software package which utilizes density functional theory with a plane wave basis set for performing *ab-initio* calculations of solids, liquids, gases, surfaces, *etc.* at the atomic level [96]. One can obtain electronic structure, geometric structure (atomic positions as well as lattice parameters), phonon dispersion and vibrational density of states, finite temperature Molecular dynamic results, electric field perturbations, *etc.* LDA, many GGA functionals (such as PBE, PW91 *etc.*) and some non-local exchange-correlation functionals (such as

B3LYP, HSE03 *etc.*) are implemented in CASTEP. The CASTEP program renders a robust and productive implementation of DFT. CASTEP uses plane-wave pseudopotential approach and fast Fourier transform (FFT) for the evaluation of the Hamiltonian terms. The concept of a pseudopotential is a tricky one for plane-wave basis set since the alternative all electron potential decays too slowly to be accurately represented by a desirably small number of Fourier components. CASTEP offers a variety of choice for electronic relaxation. The default method is based on density mixing (Kresse and Furthmuller, 1996) and one of the most effective methods. In this scheme, sum of all the eigenvalues is minimized in the fixed potential instead of the self-consistent minimization of the total energy. The new modified charge density at the end of the minimization is then added with the initial guess charge density in proper weightage and the process is repeated until the desired convergence is obtained. CASTEP also offers efficient approaches like virtual crystal approximation along with the versatile super-cell method for implementation of disorder in a periodic system.

2.2.6 LDA+U method

DFT can produce the ground state properties of a system, if the exact form of the exchange-correlation potential were known. For electronic excitations to be modelled within Kohn-Sham approach must be substituted by the Dyson equation, where instead of the unknown exchange-correlation potential the energy dependent self energy operator is implemented. This operator often can be represented by the local and energy-independent exchange-correlation potential. However, this approach is not appropriate for a large class of compounds, so-called strongly correlated electron systems. These systems require a combination of the Hubbard model and DFT. One of the simplest models that have been formulated to rationalize the physics of correlated materials, is the Hubbard model. In its simplest, one-band incarnation, the Hubbard Hamiltonian can be written as follows:

$$H_{Hub} = t \sum_{<ij>,\sigma} (c^{\dagger}_{i,\sigma} c_{j,\sigma} + h.c.) + U \sum_{i} n_{i,\uparrow} n_{i,\downarrow}$$

where $< ij >$ denotes nearest-neighbour interaction, $c^{\dagger}_{i,\sigma}$, $c_{j,\sigma}$ are the electronic creation and annihilation operators for electron of spin σ on site i. $n_{i,\sigma}$ is the number operator for electron of spin σ on site i. Therefore, for a system where electrons are strongly localized, their motion is dictate by a "hopping" process from one atomic site to its neighbours (first term of the above Hamiltonian) with an amplitude t, which is proportional to the dispersion of the valence electronic states and represents the single-particle term of the total energy. In virtue of the strong localization, the Coulomb repulsion is only accounted for between electrons on the same atom through a term proportional to the product of the occupation numbers of atomic states on the same site, whose strength is U(the "Hubbard U"). One of the most popular implementation is known as the LDA+U method as introduced by Anisimov and co-workers (1991) [97].

The CASTEP implementation of LDA+U (it means "+U" correction applied to a generic approximate DFT functionals, not necessarily LDA)) opts a simplified, rotationally invariant outlook (Cococcioni and de Gironcoli, 2005, Dudarev et al., 1998)[98, 99]. The one only external parameter required for this approach is the effective value of the on-site Coulomb parameter, U, for the affected orbitals. This parameter can be computed theoretically (Cococcioni and de Gironcoli, 2005). However, tuning the U value one can produce accurate results depending on the property of interest. In CASTEP, the appropriate value of U for a given material is not evaluated rather it is being used as an input parameter to find the desired effect.

2.3 Virtual crystal approximation and super-cell methods for doping

As mentioned earlier in $BaFe_2As_2$ system that one can dope at any of the three sites to make it superconducting. Phase diagrams of Fe-based superconductors play a crucial role in the understanding of various physical properties, which are very sensitive to doping and temperature. A generic phase diagram of 122 family of Fe-based superconductors consists of various phases like superconductivity, SDW order, C_2 and C_4 structural transition, nematic phase *etc.* [55, 100–105]. All these phases are intimately dependant on doping concentration. There exists a large diversity in the phase diagrams of various doped $BaFe_2As_2$ systems. For electron doped Fe-based superconductors, superconducting and other exotic phases exist in the system upto 15-20% doping concentration which is less compared to other 122 systems [55, 103, 104]. However, superconductivity appears in Ru doped 122 systems at a very high doping concentration. We shall demonstrate in this work that the nature of the calculated electronic structures (specially in large doping region, in some cases) are very different depending on the method of calculation, VCA or SC being used. Therefore, in the context of Fe-based material our study become extremely relevant.

Study of disordered systems employing first principles electronic structure methods requires some amount of approximation to implement disorder or doping theoretically. To treat such disordered or doped systems there exist two very popular methods as mentioned earlier: super-cell (SC) method and virtual crystal approximation (VCA). It is very important to mention the advantages and shortcomings of both the approaches before we discuss the theoretical background of those methods. The super-cell method can give more accurate results than the other one but certainly needs much more computational resources as well as CPU time compared to the VCA formalism. Accuracy of calculation is associated to the fact that the SC method can portray the local interaction between two 'real' atoms whereas the VCA method is unable to recount on that. One of the most important drawbacks for SC method is that it artificially imposes periodicity which sometime may not mimic the real physical situation of randomly doped system. This approach certainly demand for a critical look at the finite size effect as well as the imposed artificial periodicity. On the other hand, a more lucid and computationally inexpensive approach for treating doped systems is to introduce the virtual crystal approximation [106], in which a doped crystal with the original periodicity, but composed of fictitious 'virtual atoms' is created to mimic the actual doped system. For example, one can construct a compound atom like lattice of $A_{1-x}B_x$, where x is the doping concentration. To apply VCA method in order to study the case of doping, one must concern about certain important issues: firstly, the accuracy of calculation, secondly, the efficiency for treating the heterovalent systems and lastly the electronic property that one is trying to calculate. There exists a different formalism called "computational alchemy" [107, 108] to go beyond VCA. But this method is much more intricate than standard VCA formalism, demanding the utilization of density-functional linear-response methods.

Now we discuss the development of SC and VCA formalisms and some of their theoretical aspects. The super-cell method defines a new unit cell with relatively large number of atoms where doping has been implemented, and then repeats that cell throughout all space using periodic (or toroidal) boundary conditions [109]. For constructing our super-cells we follow three steps. At first we replicate the crystal unit cell in all 3 directions to get a larger new unit cell with relatively large number of atoms. Then we introduce doping by substituting atoms with the dopant atoms. At the last step, we check the convergence of electronic properties with gradually increasing the size of the super-cell. In this thesis, in order to implement doping in various sites of Ba122 system, we use different kinds of super-cells. In case of K doping at Ba site we use $2 \times 2 \times 2$ super-cell which contain 16 Ba atoms (total 80 atoms) and $2 \times 2 \times 1$ super-cells which contain 16 Fe atoms (total 40 atoms) are used in case of Ni and Ru substitution in place of Fe. On the other hand, for handling the case of small percentage of Co doping, we take $2 \times 2 \times 2$ super-cells consists of 32 Fe atoms (total 80 atoms). Also for the purpose of comparing the calculated band structures a few VCA calculations are carried out in the same cell. On the other hand, the base of the VCA formalism is simple mixing of pseudopotentials [110]. The supremacy of VCA method is in its simplicity but in some cases it is not sufficiently accurate. The reason of in-correctness lies in the fact that only mixing of pseudopotential is considered. Ramer and Rappe [110] developed a more perfect VCA approach by considering averages at the atomic level, such as the averages of eigenvalues of valence orbitals, charge densities of core electrons, nuclear potentials, wavefunctions *etc*. Major disadvantages of this method is that it is incapable of treating heterovalent atoms. In this thesis, we use the VCA method, developed by Bellaiche and Vanderbilt [111] based on weighted averaging of pseudopotentials. Below we describe the method briefly. Total energy of N valence electrons in terms of one-particle wave functions ϕ_i can be written in atomic units as:

$$\begin{aligned} E_T[\{\phi_i\},\{\mathbf{R_l}\}] &= \sum_i <\phi_i \mid -\frac{1}{2}\nabla^2 + V_{ext} \mid \phi_i> \\ &+\frac{1}{2}\int\int d\mathbf{r}d\mathbf{r}'\frac{\mathbf{n(r)n(r')}}{\mid \mathbf{r}-\mathbf{r}' \mid} + E_{XC}[n] + U(\{\mathbf{R_l}\}) \end{aligned} \tag{2.45}$$

where

$$V_{ext}(\mathbf{r},\mathbf{r}') = \sum_l V^l_{ps}(\mathbf{r}-\mathbf{R_l},\mathbf{r}'-\mathbf{R_l}) \tag{2.46}$$

$\mathbf{R}_l$ is the location of the site 'l', and V^l_{ps} are the pseudopotentials. n($\mathbf{r}$) is the electron density at $\mathbf{r}$, E_{XC} is the exchange correlation energy and $U(\{\mathbf{R_l}\})$ is the ion-ion interaction energy. In case of local as well as non local pseudopotential, 'VCA' operator equation can be derived by averaging the pseudopotential of the doped element on site 'l' as,

$$V^l_{ps}(\mathbf{r},\mathbf{r}') = (1-x)V^A_{ps}(\mathbf{r},\mathbf{r}') + xV^B_{ps}(\mathbf{r},\mathbf{r}'); \tag{2.47}$$

where, A=Ba and B=K for example in $Ba_{1-x}K_xFe_2As_2$. For other undoped sites C (Fe or

As site), pseudopotential can be written as,

$$V^{l}_{ps}(\mathbf{r},\mathbf{r}') = V^{C}_{ps}(\mathbf{r},\mathbf{r}') \tag{2.48}$$

Now V_{ext} takes the form,

$$V_{ext}(\mathbf{r},\mathbf{r}') = \sum_{l}\sum_{S} w^{l}_{S} V^{S}_{ps}(\mathbf{r}-\mathbf{R_{lS}},\mathbf{r}'-\mathbf{R_{lS}}) \tag{2.49}$$

where V^{S}_{ps} and w^{l}_{S} are the pseudopotential and 'weight' (statistical composition) of an atom of type S respectively.

It is quite evident from the phase diagram of Fe-based superconductors that superconductivity and magnetism are very sensitive to doping. Therefore, it is essential to find out a computer time-cost effective and computationally easier method of doping in order to study the evolution of magnetism and superconductivity with desirable accuracy. VCA with spin polarized calculation can also produce electronic structure in the magnetic phase but one essentially needs to consider larger unit cell for studying electronic structures with spin stripe phase or spin density wave spin arrangements. Moreover, Pulikkotil et al., has already shown that within CPA, density of states of K doped Sr122, for magnetic and non-magnetic calculations lead to essentially same result [112]. Super-cell (SC) approach is a superior method of doping than VCA/CPA. We provide a bridge between the two, it shows how and when VCA calculations are nearly comparable or same as SC one. This become extremely useful, as demonstrated in this thesis, in determining the FS topology of a doped superconducting material which can be comfortably obtained by VCA. FS topology is necessary to determine the degree of nesting of FS which is extremely important in itinerant magnetism. On the other hand, superconductivity is spread over a wide part of the phase diagram in the tetragonal phase as well of Fe-based superconductors. Hence our study focused mainly in the tetragonal phase where magnetism is (usually) absent, is sufficient to provide base for the 'proof of concept'.

Implementing doping effect via VCA and SC methods, we have presented a detail comparative study of electronic structures of various doped $BaFe_2As_2$ systems through first principles simulation. We have investigated the density of states (including partial density of states), band structures and Fermi surfaces of electron doped, hole doped as well as isovalently doped $BaFe_2As_2$ systems using VCA and SC approaches. Both the methods produce similar electronic structures in case of doping at the passive site (*e.g*, replacing K in place of Ba), but in case of doping at the active sites (Fe/As site) electronic structure obtained from VCA method deviates from that of the SC method, specially in the higher doping regime. We here found that in case of homovalent doping using VCA method is also unable to produce the accurate electronic structures. This is against the conventional belief. In case of hole doping, both the methods produce very similar electronic structures as far as electronic DOS and BS calculations are concerned. In case of isovalent P substitution at As site, there is some difference in the calculated PDOS for VCA and SC approaches resulting from some modification in Fe-As hybridization. In case of electron doped (Co/Ni) $BaFe_2As_2$ systems VCA and SC methods provide very similar electronic structures for both the cases for low doping concentrations. But in case of higher doping concentration, we find that the calculated electronic structures are remarkably different for these two methods as clearly evident from the BS and PDOS calculation of 50% Ni doped $BaFe_2As_2$ systems. On the other hand, in case of iso-electronic substitution in Fe site (Ru substitution in place of Fe), calculated electronic structure is very much dissimilar for different methods. An extra shift in the chemical potential is observed in the electronic structures of Ru doped $BaFe_2As_2$ systems, when VCA method is employed for low doping concentration. But for larger Ru doping concentration the electronic structures are quite different for these two different methods. We also explicitly show that by considering this chemical shift in a proper way, one can simulate FSs accurately by VCA formalism in case of low Ru doping concentration. This work give a clear idea about the application of VCA and SC methods for calculating the electronic structure of various doped 122 systems of Fe-based superconductors.

Chapter 3

Model studies of Fe-based superconductors

3.1 Introduction

As discussed in the introduction chapter, dominance of Fe electrons at the Fermi surface (FS) and unusual Fermiology, that can be modulated by doping, makes normal and SC state properties of iron-based superconductors quite unique compared to those of conventional electron-phonon interaction induced superconductors [113]. These Cu (sometimes also O) free new compounds are different from the high T_c cuprates and may lead to a non-BCS (Bardeen, Cooper and Schrieffer Theory) type superconductivity with a better theoretical and experimental understandings on the mechanism of unconventional high-T_c superconductivity. Importance of mutual influences of electronic spin degrees of freedom (magnetism), orbital degrees of freedom (orbital order) and pairing symmetry of superconducting state can not be overemphasised, all these play a special role in Fe-based materials [104, 114]. Pairing mechanism and information about the pairing symmetry of the cooper pair wave-functions are the key ingredients for developing a theory of these iron-based superconductors. The total electronic wave function of the cooper pairs must be antisymmetric under their exchanges. Therefore, for spin singlet state ($S = 0$) which is antisymmetric, its orbital wave function would be symmetric, leading to s-wave, d-wave, g-wave type orbital natures. In contrast, for spin triplet state ($S = 1$), its spin wave function being symmetric, its orbital wave function would be anti-symmetric (p-wave, f wave etc.). In the conventional low T_c superconductors (*e.g.*, Pb, Al, Hg, Nb, Nb_3Sn etc.), the phonon mediated electron-electron interaction leads to spin singlet pairing with s-wave symmetry. On the other hand, the pairing symmetry of cooper pairs in the high T_c cuprate superconductors is dominantly $d_{x^2-y^2}$ kind and it corresponds to l=2 orbital angular momentum [115–117]. With significantly improved sophisticated experimental and theoretical tools, the question of pairing symmetry in Fe-based superconductors is thoroughly studied and there are enough experimental evidences for some version of the so-called $s^{\pm}$ state [31, 118, 119], although predictions of other pairing states like s^{++} state mediated by orbital fluctuations are also available in the literature [37, 120]. However, order parameter (OP) symmetry and the pairing mechanism are far from being settled. Neutron scattering experiments provide convincing indication for a sign changing SC energy gap $\Delta(k)$ on different parts of the FS in a number of iron based superconductors [49]. Experimental studies on the SC gap in iron-based superconductors reveal that there are two nearly isotropic gaps with characteristics ratios $2\Delta_{SC}(\mathrm{k})/\mathrm{k}_B\mathrm{T}_c = 2.5 \pm 1.5$ (for small gap on the outer Γ-barrel) and 7±2 (on the inner Γ-barrel and the propeller-like structure around the X point, for large gap) which is considerably different from the conventional BCS characteristic ratio 3.5 [39]. The behaviour of specific heat of these iron-based superconductors is also distinctly different. For conventional BCS superconductors, the electronic specific heat (C_e) decreases exponentially with decrease of temperature below T_c. But in case of iron-based superconductors the electronic specific heat decreases with decreasing temperature below T_c obeying power law. In general, specific heat data not only reveals the SC transition at lower temperatures but also about the higher temperature transitions, like structural and magnetic [for example, spin density wave (SDW), orbital density wave (ODW) *etc.*] transitions. If enough magnetic field is applied to conquer

T_c appreciably, C/T extrapolated to $T = 0$ from normal state data provides Sommerfeld constant $\gamma_n \equiv \lim_{T\to 0} C_{normal}/T$, which is proportional to the renormalized bare electron density of states at the Fermi energy N(0); *i.e.*, $\gamma_n \sim (1 + \lambda)$N(0), (where λ can be a combination of electron-phonon and electron-electron interactions). It is a very useful parameter exploitable from specific heat data, as it is related to band structure calculations, resulting density of state N(0). Furthermore, the same is also related to the de Haas van Alphen measurement of effective masses of various FS orbits ($\gamma_n \propto m^*$). Because of large phononic contribution at higher temperatures, the specific heat jump (ΔC) is not clear in some cases. If the phonon contribution to the specific heat below T_c can be accurately estimated, e.g., via substitution of a neighbouring composition (replacing Fe by Co doping as they have almost same molar mass) that is not superconducting, one can extrapolate the electronic specific heat (C_e) below T_c and calculate γ_n. Another important parameter that correlates ΔC and T_c is $\Delta C/T_c$, and dependence of $\Delta C/T_c$ with T_c for iron-based superconductors is again quite different from all other classes of superconductors including electron-phonon coupled conventional superconductors. Bud'ko, Ni and Canfield (BNC) plotted $\Delta C/T_c$ as a function of T_c^2 for 14 different samples of various doped $BaFe_2As_2$ superconductors which indicate $\Delta C/T_c = aT_c^2$ with $a \sim 0.056$ mJ/mole-K^4 [40]. Later on J. S. Kim *et al.*, modified BNC plot to include all other FePn/Ch superconductors and showed $\Delta C/T_c = aT_c^{1.9}$ with $a \sim 0.083$ mJ/mole-K^4 [41] whereas the electron-phonon coupled conventional superconductors show significantly different temperature dependence (e.g., $\Delta C/T_c \propto T_c$). In this respect also Fe-based materials are unique, in the sense that none of the so far known earlier classes (like conventional BCS, A-15, heavy fermion, high T_c cuprates etc.) of superconductors follow $\Delta C/T_c \propto T_c^2$. In this chapter our main aim is to provide a simple model study to begin with attempting to understand several experimental observations. As mentioned in the previous chapter, a realistic model for Fe-based materials would involve five band model of Fe. In this chapter we shall show even the minimal two band model is sufficiently physical enough to grasp a number of physical properties. We use the minimal two band model (d_{xz}, d_{yz}) of superconductivity in three different scenarios: (i) intra band pairing (ii) inter band pairing and (iii) combined intra-inter band pairing on equal footing to study Fe-based superconductors. In case of intra band pairing two distinctly different T_cs are obtained which does not meet the experimental finding of single T_c from angle resolved photo emission studies (ARPES). Therefore, only intra band pairing is not sufficient to describe Fe-based materials and hence excluded from our calculations. In the inter-band only pairing potential, single T_c is obtained. In this picture, we present our analytical results of integral gap equations involving all the orders like SDW, ODW and superconducting (SC) gaps around electron, hole Fermi surfaces. We show that in the limiting case of vanishing SDW, ODW orders, the SC gap equations reproduce similar form as published in [121]. Therefore, our work is more generalization of the work [121] including SDW and ODW orders. We show that only inter-band pairing interaction of superconductivity can not produce specific heat jump such that $\Delta C/T_c \propto T_c^2$. Thus, as suggested in [121] we consider both intra-band and inter-band pairing on an equal footing which reproduces some of the experimental features like the ratio of large gap/small gap at T= 0K (that inter-band picture fails to produce). We show that the behaviour of $\Delta C/T_c$ with T_c and the estimated values of $2\Delta_{SC}/k_BT_c$ are consistent with the experimental observations on 122 family of FePn in the combined intra-inter band pairing picture. From our theoretically calculated data we found two jumps in the thermal variations of electronic specific heat, one at low temperature (SC transition) and another at higher temperature (SDW and ODW transition). We also calculate the value of $2\Delta_{SC}/k_BT_c$ within two band model of Fe-based superconductors (both electron and hole doped situation), for all possible allowed pairing symmetries from the temperature dependent superconducting order parameters (SCOP). We further studied in detail, the behaviour of specific heat as a function of temperature for all possible allowed pairing symmetries like isotropic s-wave, d+s, s_{xy} etc. In each case, we have calculated the value of $\Delta C/T_c$ as a function of T_c which matches nicely with experimental behaviour. Based on these model calculations we argue that, both inter as well as intra band pairing (irrespective of pairing mechanism) is required to explain some of the observed data. Rest of the chapter is organized as follows. In the next section we describe our theoretical model describing its essential ingredients leading to the detailed calculations of the various OPs which are then used to calculate specific heat. In the results and discussions section we discuss our detailed results and finally conclude in the conclusion section.

3.2 Theoretical Model

As discussed in the previous chapter, first principles electronic structure calculation disclose that FL of Fe-based SCs have dominantly Fe-3d character and all the five Fe-d orbitals are significantly contributed to the electronic structure near FL. Therefore, five band model is an ideal and obvious choice for studying the physical properties of Fe-based SCs. But due to the presence of several interaction terms as well as additional orbital degrees of freedom, makes it very difficult and numerically expensive to solve the five band model Hamiltonian as introduced in the previous chapter. We also have shown that minimal two band model can produce topologically similar FS as observed in the experiments. We use orbital (d$_{yz}$, d$_{xz}$) per site on a two dimensional square lattice of iron. We take the mean field model Hamiltonian within the two band picture as [87],

$$\begin{aligned} H \;=\; & \sum_{k,\sigma}^{FBZ} \varepsilon_k^e C^\dagger_{k,\sigma} C_{k,\sigma} + \sum_{k,\sigma}^{FBZ} \varepsilon_k^h f^\dagger_{k,\sigma} f_{k,\sigma} + \sum_{k,\sigma}^{FBZ} \Delta_S (C^\dagger_{k,\sigma} \sigma^z_{\sigma,\sigma'} f_{k+Q,\sigma'} + h.c.) \\ & -i \sum_{k,\sigma}^{FBZ} \Delta_O (C^\dagger_{k,\sigma} f_{k+Q,\sigma} - f^\dagger_{k+Q,\sigma} C_{k,\sigma}) + \sum_{k}^{FBZ} \Delta_{SC}(k) (C_{-k,\downarrow} C_{k,\uparrow} + f_{-k,\downarrow} f_{k,\uparrow} + h.c.) \end{aligned} \tag{3.1}$$

The first two terms of the above Hamiltonian represent kinetic (band) energies in the electronic ($C_{k,\sigma}$ being the annihilation operator of an electron with spin σ) and hole ($f_{k,\sigma}$ being the annihilation operator of a hole) bands around the four corners M and Γ points respectively (see Fig.2.2). The OPs Δ_S, Δ_O represent respectively the spin density wave

(SDW) and orbital density wave (ODW) that involves ordering between the electron and hole like bands (that are nested by the nesting vector Q = $(0, \pi)$ or $(\pi,0)$. This ingredient in our model that the electron-like FS nests with the hole-like one and vice versa, is justified as it is consistent with recent experimental finding [122]. In ref [122] weak z-direction dispersion among the Γ barrel and electron FSs are found resulting quasi-2d nested nature [123]. For further details see below. The fifth term represent the terms involving superconductivity (SC) where $\Delta_{SC}(k) = (\Delta^{e}_{SC}(k) - \Delta^{h}_{SC}(k))$; $\Delta^{e/h}_{SC}$ being SCOP around the electronic and hole FSs respectively. Our model consideration of 3d$_{yz}$,3d$_{xz}$ orbitals for superconductivity is also consistent with very recent finding of electron pairing at Fe-3d$_{yz,xz}$ orbitals [124]. The most general form of on-site interaction Hamiltonian for two band model may be obtained as, $H_{on-site} = \frac{1}{2}\sum_{i,\sigma,\sigma'}\sum_{\alpha,\beta,\gamma,\delta=c,f} U^{\alpha,\beta}_{\gamma,\delta}\Psi^{\dagger}_{i,\alpha,\sigma}\Psi^{\dagger}_{i,\beta,\sigma}\Psi_{i,\delta,\sigma'}\Psi_{i,\gamma,\sigma'}$ where, $\Psi^{\dagger}_{i,c,\sigma} = C^{\dagger}_{i,\sigma}$ and $\Psi^{\dagger}_{i,d,\sigma} = f^{\dagger}_{i,\sigma}$ as used in the Hamiltonian (1) in momentum representation. Several intra and inter pocket electron-electron repulsion terms exists and according to the formulation [125], the mean field theory of SDW and ODW is obtained considering the mean field OPs as, $\Delta_S = -U_{inter}\sum^{FBZ}_{k,\sigma} < C^{\dagger}_{k,\sigma}f_{k+Q,\sigma} + h.c. >$ and $\Delta_O = -iV_O\sum^{FBZ}_{k,\sigma} < C^{\dagger}_{k,\sigma}f_{k+Q,\sigma} - f^{\dagger}_{k+Q,\sigma}C_{k,\sigma} >$ where both the U_{inter} and V_O are related to U^{dd}_{cc} (see for details [125]). Typical terms corresponding to superconductivity are given as follows, $H_{SC} = \sum^{FBZ}_{k,k'}(V^{e}_{k,k'}C^{\dagger}_{k\uparrow}C^{\dagger}_{-k\downarrow}C_{-k'\downarrow}C_{k'\uparrow} + V^{h}_{k,k'}f^{\dagger}_{k\uparrow}f^{\dagger}_{-k\downarrow}f_{-k'\downarrow}f_{k'\uparrow} + V^{e-h}_{k,k'}C^{\dagger}_{k\uparrow}C^{\dagger}_{-k\downarrow}f_{-k'\downarrow}f_{k'\uparrow} + h.c.)$. The first two terms correspond to intra-band pairing and the pairing interaction $V_{k,k'}$ is defined either around the electron like or hole like Fermi Surface; whereas the third term corresponds to inter-band type pairing interaction. All these terms are considered to arrive at the mean field Hamiltonian (3.1). As mention earlier we will solve this Hamiltonian (3.1) in three different scenarios. Before that we will see how the Hamiltonian look like for various sign changing and non sign changing OPs.

3.2.1 Hamiltonian for sign changing and non sign changing order parameters

First we take the case of pure s-wave pairing where OPs do not change its sign that means

$$\Delta_{SC}^{e/h}(k) = \Delta_{SC}^{e/h}(0)\,\eta_k$$

where $\eta_k = 1.0$

Hamiltonian for this case can be written as,

$$H = \sum_{k,\sigma}\Big\{\Big(\varepsilon_k^e C_{k,\sigma}^\dagger C_{k,\sigma} + \varepsilon_k^h f_{k,\sigma}^\dagger f_{k,\sigma}\Big) - \Big(\varepsilon_k^h C_{k+Q,\sigma}^\dagger C_{k+Q,\sigma} + \varepsilon_k^e f_{k+Q,\sigma}^\dagger f_{k+Q,\sigma}\Big)$$

$$+\Delta_S\left(C_{k,\sigma}^\dagger \sigma_{\sigma,\sigma'}^z f_{k+Q,\sigma'} + C_{k+Q,\sigma}^\dagger \sigma_{\sigma,\sigma'}^z f_{k,\sigma'}\right) + \Delta_S\left(f_{k+Q,\sigma'}^\dagger \sigma_{\sigma,\sigma'}^z C_{k,\sigma} + f_{k,\sigma'}^\dagger \sigma_{\sigma,\sigma'}^z C_{k+Q,\sigma}\right)$$

$$-i\Delta_O\left(C_{k,\sigma}^\dagger f_{k+Q,\sigma} - f_{k,\sigma}^\dagger C_{k+Q,\sigma}\right) + i\Delta_O^*\left(f_{k+Q,\sigma}^\dagger C_{k,\sigma} - C_{k+Q,\sigma}^\dagger f_{k,\sigma}\right)\Big\}$$

$$+\sum_k\Big\{\Delta_{SC}^e(0)\left(C_{-k\downarrow}C_{k\uparrow} - f_{-k-Q\downarrow}f_{k+Q\uparrow}\right) + \Delta_{SC}^e(0)\left(C_{k\uparrow}^\dagger C_{-k\downarrow}^\dagger - f_{k+Q\uparrow}^\dagger f_{-k-Q\downarrow}^\dagger\right)$$

$$-\Delta_{SC}^h(0)\left(f_{-k\downarrow}f_{k\uparrow} - C_{-k-Q\downarrow}C_{k+Q\uparrow}\right) - \Delta_{SC}^h(0)\left(f_{k\uparrow}^\dagger f_{-k\downarrow}^\dagger - C_{k+Q\uparrow}^\dagger C_{-k-Q\downarrow}^\dagger\right)\Big\}$$

Expressing the above Hamiltonian in matrix form we have,

$$H = \Psi^\dagger H_k \Psi$$

with Ψ being,

$$\Psi = \begin{pmatrix} C_{k\uparrow} \\ C^{\dagger}_{-k\downarrow} \\ f_{k+Q\uparrow} \\ f^{\dagger}_{-k-Q\downarrow} \\ f_{k\uparrow} \\ f^{\dagger}_{-k\downarrow} \\ C_{k+Q\uparrow} \\ C^{\dagger}_{-k-Q\downarrow} \end{pmatrix}$$

and H_k being,

$$H_k = \begin{pmatrix} \varepsilon^e_k & \Delta^e_{SC}(0) & \Delta_S - i\Delta_O & 0 & 0 & 0 & 0 & 0 \\ \Delta^e_{SC}(0) & -\varepsilon^e_k & 0 & \Delta_S - i\Delta^{\star}_O & 0 & 0 & 0 & 0 \\ \Delta_S + i\Delta^{\star}_O & 0 & -\varepsilon^e_k & -\Delta^e_{SC}(0) & 0 & 0 & 0 & 0 \\ 0 & \Delta_S + i\Delta_O & -\Delta^e_{SC}(0) & \varepsilon^e_k & 0 & 0 & 0 & 0 \\ 0 & 0 & 0 & 0 & \varepsilon^h_k & -\Delta^h_{SC}(0) & \Delta_S + i\Delta_O & 0 \\ 0 & 0 & 0 & 0 & -\Delta^h_{SC}(0) & -\varepsilon^h_k & 0 & \Delta_S + i\Delta^{\star}_O \\ 0 & 0 & 0 & 0 & \Delta_S - i\Delta^{\star}_O & 0 & -\varepsilon^h_k & \Delta^h_{SC}(0) \\ 0 & 0 & 0 & 0 & 0 & \Delta_S - i\Delta_O & \Delta^h_{SC}(0) & \varepsilon^h_k \end{pmatrix}$$

Now we see the case of sign changing OPs. For example we take S_{xy} pairing. For this case,

$$\Delta^{e/h}_{SC}(k) = \Delta^{e/h}_{SC}(0)\,\eta_k = \Delta^{e/h}_{SC}(0)\cos k_x \cos k_y$$

and

$$\eta_{k+Q} = -\eta_k$$

Hamiltonian for this case can be written as,

$$H=\sum_{k,\sigma}\Big\{\left(\varepsilon_k^e C_{k,\sigma}^{\dagger}C_{k,\sigma}+\varepsilon_k^h f_{k,\sigma}^{\dagger}f_{k,\sigma}\right)-\left(\varepsilon_k^h C_{k+Q,\sigma}^{\dagger}C_{k+Q,\sigma}+\varepsilon_k^e f_{k+Q,\sigma}^{\dagger}f_{k+Q,\sigma}\right)$$

$$+\Delta_S\left(C_{k,\sigma}^{\dagger}\sigma_{\sigma,\sigma'}^{z}f_{k+Q,\sigma'}+C_{k+Q,\sigma}^{\dagger}\sigma_{\sigma,\sigma'}^{z}f_{k,\sigma'}\right)+\Delta_S\left(f_{k+Q,\sigma'}^{\dagger}\sigma_{\sigma,\sigma'}^{z}C_{k,\sigma}+f_{k,\sigma'}^{\dagger}\sigma_{\sigma,\sigma'}^{z}C_{k+Q,\sigma}\right)$$

$$-i\Delta_O\left(C_{k,\sigma}^{\dagger}f_{k+Q,\sigma}-f_{k,\sigma}^{\dagger}C_{k+Q,\sigma}\right)+i\Delta_O^{\star}\left(f_{k+Q,\sigma}^{\dagger}C_{k,\sigma}-C_{k+Q,\sigma}^{\dagger}f_{k,\sigma}\right)\Big\}$$

$$+\sum_{k}\Big\{\Delta_{SC}^{e}(0)\,\eta_k\left(C_{-k\downarrow}C_{k\uparrow}+f_{-k-Q\downarrow}f_{k+Q\uparrow}\right)+\Delta_{SC}^{e}(0)\,\eta_k\left(C_{k\uparrow}^{\dagger}C_{-k\downarrow}^{\dagger}+f_{k+Q\uparrow}^{\dagger}f_{-k-Q\downarrow}^{\dagger}\right)$$

$$-\Delta_{SC}^{h}(0)\,\eta_k\left(f_{-k\downarrow}f_{k\uparrow}+C_{-k-Q\downarrow}C_{k+Q\uparrow}\right)-\Delta_{SC}^{h}(0)\,\eta_k\left(f_{k\uparrow}^{\dagger}f_{-k\downarrow}^{\dagger}+C_{k+Q\uparrow}^{\dagger}C_{-k-Q\downarrow}^{\dagger}\right)\Big\}$$

Again expressing the Hamiltonian in the matrix form with same Ψ as mentioned above we have,

$$H_k=\begin{pmatrix}
\varepsilon_k^e & \Delta_{SC}^e(k) & \Delta_S-i\Delta_O & 0 & 0 & 0 & 0 & 0\\
\Delta_{SC}^e(k) & -\varepsilon_k^e & 0 & \Delta_S-i\Delta_O^{\star} & 0 & 0 & 0 & 0\\
\Delta_S+i\Delta_O^{\star} & 0 & -\varepsilon_k^e & \Delta_{SC}^e(k) & 0 & 0 & 0 & 0\\
0 & \Delta_S+i\Delta_O & \Delta_{SC}^e(k) & \varepsilon_k^e & 0 & 0 & 0 & 0\\
0 & 0 & 0 & 0 & \varepsilon_k^h & -\Delta_{SC}^h(k) & \Delta_S+i\Delta_O & 0\\
0 & 0 & 0 & 0 & -\Delta_{SC}^h(k) & -\varepsilon_k^h & 0 & \Delta_S+i\Delta_O^{\star}\\
0 & 0 & 0 & 0 & \Delta_S-i\Delta_O^{\star} & 0 & -\varepsilon_k^h & -\Delta_{SC}^h(k)\\
0 & 0 & 0 & 0 & 0 & \Delta_S-i\Delta_O & -\Delta_{SC}^h(k) & \varepsilon_k^h
\end{pmatrix}$$

Next we solve these Hamiltonians for sign changing and non sign changing cases for three scenarios as discussed earlier.

3.2.2 Intra-band superconducting pairing

When only intra-band pairing terms are considered in the Hamiltonian (3.1), we obtained the gap equations:

$$\begin{aligned}\Delta_S &= U_S \sum_k \frac{\Delta_{SC}^{e^-}}{E_k^{e^-}} \tanh\left(\frac{\beta E_k^{e^-}}{2}\right) + \frac{\Delta_{SC}^{e^+}}{E_k^{e^+}} \tanh\left(\frac{\beta E_k^{e^+}}{2}\right) \\ &\quad + \frac{\Delta_{SC}^{h^-}}{E_k^{h^-}} \tanh\left(\frac{\beta E_k^{h^-}}{2}\right) + \frac{\Delta_{SC}^{h^+}}{E_k^{h^+}} \tanh\left(\frac{\beta E_k^{h^+}}{2}\right) \end{aligned} \tag{3.2}$$

$$\begin{aligned}\Delta_O &= V_O \sum_k \frac{\Delta_O}{E_k^{e^-}} \tanh\left(\frac{\beta E_k^{e^-}}{2}\right) + \frac{\Delta_O}{E_k^{e^+}} \tanh\left(\frac{\beta E_k^{e^+}}{2}\right) \\ &\quad + \frac{\Delta_O}{E_k^{h^-}} \tanh\left(\frac{\beta E_k^{h^-}}{2}\right) + \frac{\Delta_O}{E_k^{h^+}} \tanh\left(\frac{\beta E_k^{h^+}}{2}\right) \end{aligned} \tag{3.3}$$

$$\Delta_{SC}^{e} = \sum_{k'} V_{kk'}^{e} \left\{ \frac{\Delta_{SC}^{e-}}{E_{k'}^{e^-}} \tanh \frac{\beta E_{k'}^{e^-}}{2} - \frac{\Delta_{SC}^{e+}}{E_{k'}^{e^+}} \tanh \frac{\beta E_{k'}^{e^+}}{2} \right\} \tag{3.4}$$

$$\Delta_{SC}^{h} = \sum_{k'} V_{kk'}^{h} \left\{ \frac{\Delta_{SC}^{h-}}{E_{k'}^{h^-}} \tanh \frac{\beta E_{k'}^{h^-}}{2} - \frac{\Delta_{SC}^{h+}}{E_{k'}^{h^+}} \tanh \frac{\beta E_{k'}^{h^+}}{2} \right\} \tag{3.5}$$

where the quasi particle energies in equations (3.2,3.3,3.4,3.5) are obtained as,

$$\begin{aligned} E_k^{e^\pm} &= \pm\sqrt{\left(\varepsilon_k^e\right)^2 + \left(\sqrt{\Delta_S^2 + \Delta_O^2} \pm \Delta_{SC}^e\right)^2} \\ &= \pm\sqrt{\left(\varepsilon_k^e\right)^2 + \left(\Delta_{SC}^{e^\pm}\right)^2} \\ E_k^{h^\pm} &= \pm\sqrt{\left(\varepsilon_k^h\right)^2 + \left(\sqrt{\Delta_S^2 + \Delta_O^2} \pm \Delta_{SC}^h\right)^2} \\ &= \pm\sqrt{\left(\varepsilon_k^h\right)^2 + \left(\Delta_{SC}^{h^\pm}\right)^2} \end{aligned} \tag{3.6}$$

An effective gap around the electron Fermi Surface ($\Delta_{SC}^{e^{\pm}}$) appears in the electronic band (ε_k^e) where as the same around the hole Fermi Surface ($\Delta_{SC}^{h^{\pm}}$) appears in the hole band (ε_k^h). In presence of SDW and ODW orders the two SC orders $\Delta_{SC}^{e/h}(k)$ (given by equation (4,5)) are still coupled through the equations (2,3) appearing in the quasi-particle energies (6). To note that the SDW, ODW orders are inter-band in nature and thus even in intra-band pairing picture both the $\Delta_{SC}^{e/h}(k)$ orders have inter-band effect. In the intra-band picture however, the self-consistent solutions of the gap equations results in two SC gaps which vanish at two distinctly different T$_c$s [126]. Such a picture would result in two specific heat jumps below T_c. These features do not support the well known ARPES data [52], and hence excluded from rest of our calculations. In the limiting case of vanishing Δ_S, Δ_O, the SC gap equations take usual BCS form,

$$\Delta_{SC}^e = \sum_{k'} V_{kk'}^e \frac{2\Delta_{SC}^e}{E_{k'}^e} \tanh\left(\frac{\beta E_{k'}^e}{2}\right) \tag{3.7}$$

$$\Delta_{SC}^h = \sum_{k'} V_{kk'}^h \frac{2\Delta_{SC}^h}{E_{k'}^h} \tanh\left(\frac{\beta E_{k'}^h}{2}\right) \tag{3.8}$$

Where the quasi particle energies are given as,

$$\begin{aligned} E_k^e &= \pm\sqrt{\left(\varepsilon_k^e\right)^2 + \left(\Delta_{SC}^e\right)^2} \\ E_k^h &= \pm\sqrt{\left(\varepsilon_k^h\right)^2 + \left(\Delta_{SC}^h\right)^2} \end{aligned} \tag{3.9}$$

3.2.3 Inter-band superconducting pairing

We also obtain the gap equations in the inter-band pairing only, such gap equations take very similar form as that of in ref [121]; temperature dependence of those results in a single T$_c$.

$$\begin{aligned}\Delta_S &= U_S \sum_k \frac{\Delta_{SC}^{e^-}}{E_k^{e^-}} \tanh\left(\frac{\beta E_k^{e^-}}{2}\right) + \frac{\Delta_{SC}^{e^+}}{E_k^{e^+}} \tanh\left(\frac{\beta E_k^{e^+}}{2}\right) \\ &\quad + \frac{\Delta_{SC}^{h^-}}{E_k^{h^-}} \tanh\left(\frac{\beta E_k^{h^-}}{2}\right) + \frac{\Delta_{SC}^{h^+}}{E_k^{h^+}} \tanh\left(\frac{\beta E_k^{h^+}}{2}\right) \end{aligned} \tag{3.10}$$

$$\begin{aligned}\Delta_O &= V_O \sum_k \frac{\Delta_O}{E_k^{e^-}} \tanh\left(\frac{\beta E_k^{e^-}}{2}\right) + \frac{\Delta_O}{E_k^{e^+}} \tanh\left(\frac{\beta E_k^{e^+}}{2}\right) \\ &\quad + \frac{\Delta_O}{E_k^{h^-}} \tanh\left(\frac{\beta E_k^{h^-}}{2}\right) + \quad \frac{\Delta_O}{E_k^{h^+}} \tanh\left(\frac{\beta E_k^{h^+}}{2}\right) \end{aligned} \tag{3.11}$$

$$\Delta_{SC}^{e} = \sum_{k'} V_{kk'}^{e} \left\{ \frac{\Delta_{SC}^{h-}}{E_{k'}^{e^-}} \tanh \frac{\beta E_{k'}^{e^-}}{2} - \frac{\Delta_{SC}^{h+}}{E_{k'}^{e^+}} \tanh \frac{\beta E_{k'}^{e^+}}{2} \right\} \tag{3.12}$$

$$\Delta_{SC}^{h} = \sum_{k'} V_{kk'}^{h} \left\{ \frac{\Delta_{SC}^{e-}}{E_{k'}^{h^-}} \tanh \frac{\beta E_{k'}^{h^-}}{2} - \frac{\Delta_{SC}^{e+}}{E_{k'}^{h^+}} \tanh \frac{\beta E_{k'}^{h^+}}{2} \right\} \tag{3.13}$$

where the quasi particle energies are calculated as,

$$\begin{aligned} E_k^{e^\pm} &= \pm\sqrt{\left(\varepsilon_k^e\right)^2 + \left(\sqrt{\Delta_S^2 + \Delta_O^2} \pm \Delta_{SC}^h\right)^2} \\ &= \pm\sqrt{\left(\varepsilon_k^e\right)^2 + \left(\Delta_{SC}^{h^\pm}\right)^2} \\ E_k^{h^\pm} &= \pm\sqrt{\left(\varepsilon_k^h\right)^2 + \left(\sqrt{\Delta_S^2 + \Delta_O^2} \pm \Delta_{SC}^e\right)^2} \\ &= \pm\sqrt{\left(\varepsilon_k^h\right)^2 + \left(\Delta_{SC}^{e^\pm}\right)^2} \end{aligned} \tag{3.14}$$

Equation(3.14) may be contrasted with that of the (3.6). Unlike the previous case of intra-band pairing, in the inter-band picture the effective gap ($\Delta_{SC}^{h^\pm}$) which involves SC gap around the hole FS, appears in the electronic band (ε_k^e). On the other hand, the effective gap ($\Delta_{SC}^{e\pm}$) appears in the hole band (ε_k^h) involves Δ_{SC}^e, the SC gap around the electronic FS. Such nature of quasi-particles lead to several unusual properties like large BCS Characteristic ratio, identical transition temperatures to multi-gaps, their thermal behaviours in general, does not follow weak-coupling behaviours. In the limiting case of vanishing Δ_S, Δ_O the SC gap equations take forms as,

$$\Delta_{SC}^e = \sum_{k'} V_{kk'}^e \frac{2\Delta_{SC}^h}{E_{k'}^e} \tanh \frac{\beta E_{k'}^e}{2} \tag{3.15}$$

$$\Delta_{SC}^h = \sum_{k'} V_{kk'}^h \frac{2\Delta_{SC}^e}{E_{k'}^h} \tanh \frac{\beta E_{k'}^h}{2}. \tag{3.16}$$

Where the quasi particle energies are given as,

$$\begin{aligned} E_k^e &= \pm\sqrt{\left(\varepsilon_k^e\right)^2 + \left(\Delta_{SC}^h\right)^2} \\ E_k^h &= \pm\sqrt{\left(\varepsilon_k^h\right)^2 + \left(\Delta_{SC}^e\right)^2}. \end{aligned} \tag{3.17}$$

The gap equations (3.15, 3.16) may be contrasted with that of the reference [121]. In ref[121] the gap equations have slightly different form than that of equations (3.15, 3.16) in our work. The difference appears in the form of quasi-particle energies, $E_k^{(1,2)} = \sqrt{(\varepsilon_k^{(1,2)} - \mu)^2 + \Delta_{1,2}^2}$ in ref[121], in contrast to $E_k^{e/h}$ [given in equations (3.17)]. The reason for this difference is that no nesting between ϵ_k^1 and ϵ_k^2 are considered in work [121]. Also there is no considerations on influence of sign-changing superconducting order parameter. Given the fact that Fe-based superconductors do show evidence of nesting, sign changing of SC-order parameter these considerations are essential. This has caused difference between our equations (3.15,3.16) and that of ref[121]. In our work, the results in the equations (3.15,3.16) include consideration of inter-band nesting and sign changing effect of the SCOP ($\varepsilon_{k+Q}^e = -\varepsilon_k^h$, $\varepsilon_{k+Q}^h = -\varepsilon_k^e$ and $\Delta_{SC}^e(k+Q) = -\Delta_{SC}^h$, $\Delta_{SC}^h(K+Q) = -\Delta_{SC}^e$) from electron like FS to the hole like FS and vice versa. By construction of the gap equations in this subsection, vanishing or finite magnitude of any of the SC-gaps $\Delta_{sc}^{e/h}$ ensures the same for the other gap $\Delta_{sc}^{h/e}$. This is precisely the reason for a single T_c in the inter-band picture and such pairing interaction is an essential feature of Fe-based materials.

However, in a multi-band system like Fe-based materials intra band pairing cannot be neglected. Moreover, the thermal variation of the specific heat jump when computed based on purely inter-band pairing does not follow the $\Delta C/T_c \propto T_c^2$ form. In the combined intra-inter band pairing mechanism the BCS characteristic ratio, specific heat results resemble with experimentally observed one. Our findings of large values of BCS characteristic ratio is a consequence of the strong inter band pairing. These findings not only further asserts some of the findings of the earlier work that the BCS theory for such superconductors is not the weak-coupling limit of the Eliashberg theory [121], but also the fact that the present work is a more generalization of the same including magnetic, orbital orders as applicable to Fe based systems.

3.2.4 Intra-Inter superconducting band pairing

More appropriate picture that describes Fe-based superconductors, may be intra-inter band pairing. In that case all the terms of the (3.1) are to be considered. Together with the intra and inter band nature of SC-pairing interaction, the above Hamiltonian (3.1) also have the ability to handle sign changing as well as no-sign-changing SCOPs. In the two cases the Hamiltonian takes two different forms which when solved leads to two different set of eigenvalues namely, for sign-changing OPs,

$$\begin{aligned} E_k^{e^{\pm}} &= \pm\sqrt{\left(\varepsilon_k^e\right)^2 + \left(\sqrt{\Delta_S^2 + \Delta_O^2} \pm \Delta_{SC}(k)\right)^2} \\ &= \pm\sqrt{\left(\varepsilon_k^e\right)^2 + \left(\Delta_{SC}^{\pm}(k)\right)^2} \end{aligned}$$

$$
\begin{aligned}
E_k^{h^\pm} &= \pm\sqrt{\left(\varepsilon_k^h\right)^2 + \left(\sqrt{\Delta_S^2+\Delta_O^2} \pm \Delta_{SC}(k)\right)^2} \\
&= \pm\sqrt{\left(\varepsilon_k^h\right)^2 + \left(\Delta_{SC}^{\pm}(k)\right)^2}, \qquad (3.18)
\end{aligned}
$$

and for no-sign-changing OPs,

$$
\begin{aligned}
E_k^e &= \pm\sqrt{\left(\varepsilon_k^e\right)^2 + \Delta_S^2 + \Delta_O^2 + (\Delta_{SC}(k))^2} \\
E_k^h &= \pm\sqrt{\left(\varepsilon_k^h\right)^2 + \Delta_S^2 + \Delta_O^2 + (\Delta_{SC}(k))^2} \qquad (3.19)
\end{aligned}
$$

when intra and inter-band pairing are treated on an equal footing.

We also obtain and solve the gap equations involving various orders to calculate specific heat. The gap equations in the sign-changing OP scenario are given as below.

$$
\begin{aligned}
\Delta_S &= U_S \sum_k \frac{\Delta_{SC}^-}{E_k^{e^-}} \tanh\left(\frac{\beta E_k^{e^-}}{2}\right) + \frac{\Delta_{SC}^+}{E_k^{e^+}} \tanh\left(\frac{\beta E_k^{e^+}}{2}\right) \\
&\quad + \frac{\Delta_{SC}^-}{E_k^{h^-}} \tanh\left(\frac{\beta E_k^{h^-}}{2}\right) + \frac{\Delta_{SC}^+}{E_k^{h^+}} \tanh\left(\frac{\beta E_k^{h^+}}{2}\right) \qquad (3.20)
\end{aligned}
$$

$$
\begin{aligned}
\Delta_O &= U_O \sum_k \frac{\Delta_O}{E_k^{e^-}} \tanh\left(\frac{\beta E_k^{e^-}}{2}\right) + \frac{\Delta_O}{E_k^{e^+}} \tanh\left(\frac{\beta E_k^{e^+}}{2}\right) \\
&\quad + \frac{\Delta_O}{E_k^{h^-}} \tanh\left(\frac{\beta E_k^{h^-}}{2}\right) + \frac{\Delta_O}{E_k^{h^+}} \tanh\left(\frac{\beta E_k^{h^+}}{2}\right) \qquad (3.21)
\end{aligned}
$$

$$
\Delta_{SC}^e(k) = \sum_{k'} V_{kk'}^e \left\{ \frac{\Delta_{SC}^-}{E_{k'}^{e^-}} \tanh\frac{\beta E_{k'}^{e^-}}{2} - \frac{\Delta_{SC}^+}{E_{k'}^{e^+}} \tanh\frac{\beta E_{k'}^{e^+}}{2} \right\} \qquad (3.22)
$$

$$
\Delta_{SC}^h(k) = \sum_{k'} V_{kk'}^h \left\{ \frac{\Delta_{SC}^-}{E_{k'}^{h^-}} \tanh\frac{\beta E_{k'}^{h^-}}{2} - \frac{\Delta_{SC}^+}{E_{k'}^{h^+}} \tanh\frac{\beta E_{k'}^{h^+}}{2} \right\} \qquad (3.23)
$$

For no-sign-changing OP symmetries we have obtained,

$$\frac{\Delta_S}{2U_S} = \sum_k \left\{ \frac{\tilde{\Delta}}{E_k^e} \tanh \frac{\beta E_k^e}{2} + \frac{\tilde{\Delta}}{E_e^h} \tanh \frac{\beta E_k^h}{2} \right\} \tag{3.24}$$

$$\frac{\Delta_O}{2U_O} = \sum_k \left\{ \frac{\Delta_O}{E_k^e} \tanh \frac{\beta E_k^e}{2} + \frac{\Delta_O}{E_k^h} \tanh \frac{\beta E_k^h}{2} \right\} \tag{3.25}$$

$$\Delta_{SC}^e = \sum_{k'} V_{kk'}^e \frac{2\Delta_{SC}}{E_{k'}^e} \tanh \left(\frac{\beta E_{k'}^e}{2} \right) \tag{3.26}$$

$$\Delta_{SC}^h = \sum_{k'} V_{kk'}^h \frac{2\Delta_{SC}}{E_{k'}^h} \tanh \left(\frac{\beta E_{k'}^h}{2} \right) \tag{3.27}$$

For the set of gap equations (3.20, 3.21, 3.22, 3.23) the quasi-particle energies involved are given by (3.18) whereas for the set of gap equations (3.24, 3.25, 3.26, 3.27) the quasi-particle energies involved are given by (3.19).

Therefore, we solve these four gap equations numerically following the procedure as in [87] for different allowed pairing symmetries like d$_{x^2-y^2}$+s$_{x^2+y^2}$ / s$^{\pm}$, s$_{xy}$ that changes sign between the electron and hole like Fermi Surface and isotropic s-wave for no sign changing OP, in the combined intra-inter band pairing mechanism. Variation of SCOPs (energy gap) with temperature, as obtained from the four coupled equations, can be used to calculate $2\Delta_{SC}/k_B T_c$ as well as specific heat as a function of temperature. Specific heat can be obtained from the electronic entropy which is defined as:

$$S_{es} = -2k_B \sum_k [(1 - f_k) \ln(1 - f_k) + f_k ln f_k] \tag{3.28}$$

where $f_k = (1 + e^{\beta E_k})^{-1}$ is the Fermi function and $\beta = 1/k_B T$. Electronic specific heat can be found using the relation C= -$\beta\frac{dS_{es}}{d\beta}$

Different pairing symmetries are imposed on SCOPs which significantly modifies the temperature variation of all the OPs as they are coupled with each other (see for details in the next section). Doping (electron or hole) is controlled by chemical potential μ. Behaviour of the electronic specific heat particularly the jump in specific heat are also modified depending on the pairing symmetry.

3.3 Result and discussion

BCS characteristics ratio, is defined as $2\Delta_{SC}/k_BT_c$, where Δ_{SC} is the SC gap at T=0K. Weak coupling BCS theory predicts characteristics ratio of conventional superconductors as 3.5. We have solved all the four coupled gap equations numerically for three cases (i) intra-band (ii) inter-band and (iii) intra-inter band pairing on an equal footing to get different OPs (SDW, ODW, SC around electron and hole FS) as a function of temperature. In case of intra-band pairing we got two different T_cs for two SCOPs (electron and hole band) as reported earlier [126]. As this behaviour is not consistent with the experiments, other two possibilities (inter-band and intra-inter band pairing) are examined thoroughly. Temperature dependence of various order parameters (SDW, ODW, SC around electron and hole FS) for inter-band and intra-inter band pairing are shown in Fig.3.1(a) and Fig.3.1(b) respectively for d+s pairing symmetry (all other conditions remain identical for both the cases).

3.3.1 Calculation of BCS Characteristic ratio

A closer look to the SC gap equations [sec IIB, equations(3.12,3.13)] in the purely inter-band picture indicates the following. If at a given temperature and doping Δ^e_{sc} becomes zero (or finite) then it simultaneously make Δ^h_{sc} also zero (or finite). That is both the

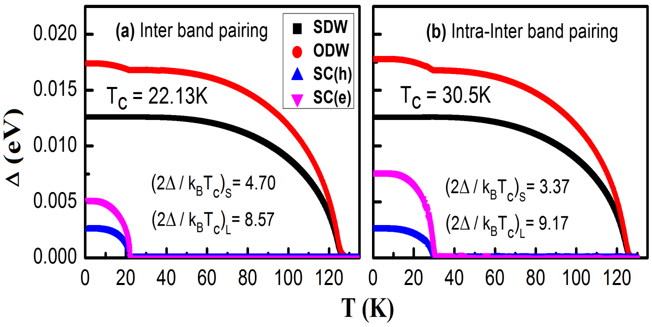

Figure 3.1: Temperature variation of various OPs like SDW (in black), ODW (in red) and superconductivity (electron FS violet, Hole FS blue) in only inter-band **(left)** and intra-inter **(right)** band pairing for hole doped (μ = 1.42) system having d+s pairing symmetry. Characteristics ratios and SC T_cs are indicted in the figure.

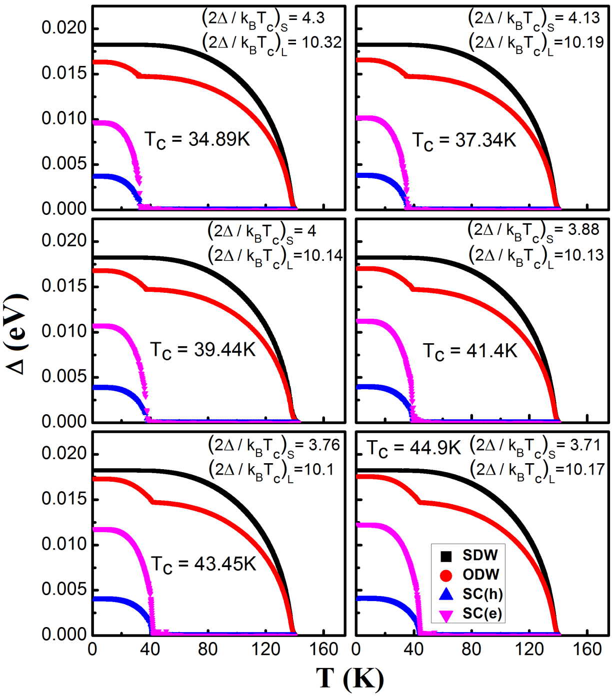

Figure 3.2: Temperature variation of various OPs like SDW (in black), ODW (in red) and superconductivity (electron FS violet, Hole FS blue) for different 122 FePn having different T$_c$s for electron doped (μ = 1.53) system having d+s pairing symmetry. Variation of BCS characteristic ratio with different T$_c$s are indicated.

SCOPs either exist or does not exist, ensuring simultaneous opening up of both the gaps. Since respective gaps are opened to their partner's band density of states, there is a competition between them. So the growth of both of the gaps are competitive leading to large $2\Delta_{SC}/k_BT_c$ ratio. In the combined intra-inter band picture however; the pairing strength

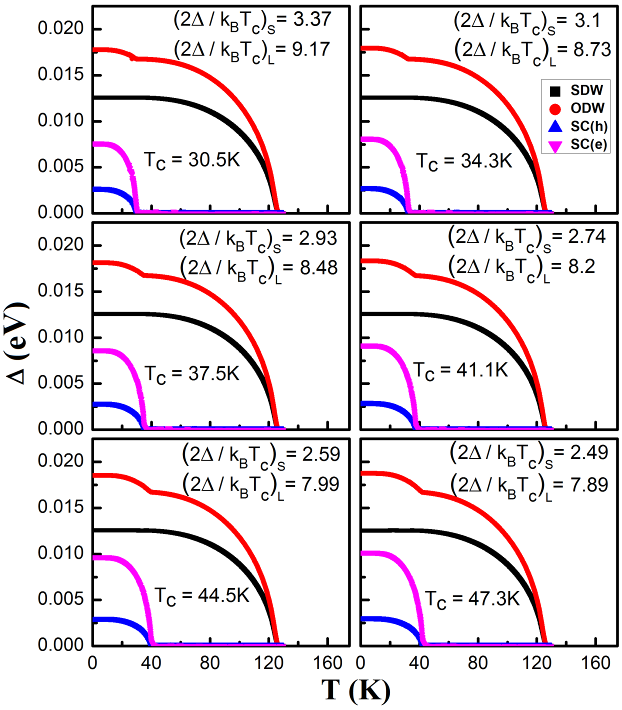

Figure 3.3: Temperature variation of various OPs like SDW (in black), ODW (in red) and superconductivity (electron FS violet, Hole FS blue) for different 122 FePn having different T$_c$s for hole doped (μ = 1.42) system having d+s pairing symmetry. Variation of BCS characteristic ratio with different T$_c$s are indicated

contribution from intra-band one leads to opening up of any of the gaps slightly higher in temperature leading to higher T_c. This also leads to larger growth of the gaps at the lower temperatures leading $\Delta^{large}(0)/\Delta^{small}(0)$ towards 3. This is also the reason for moderate $2\Delta_{SC}/k_BT_c$ ratio in this picture. Temperature dependencies are very similar in both the cases, but superconductivity is more favoured in the combined intra-inter band case and T_c is smaller in inter-band only pairing compared to that of intra-inter band picture. The zero temperature gap ratio (large to small) in the inter-band only pairing is slightly less than 2 whereas that in the intra-inter band picture is greater than 2 ($\sim$ 2.5 – 3) [124]. The later scenario matches with the experimental scenario much better. Fig.3.2, Fig.3.3, Fig.3.4, Fig.3.5 shows the temperature variation of SDW, ODW and SCOPs for various OP symmetries of the SC state like d+s, s_{xy} and isotropic s-wave considering combined intra and inter band pairing on an equal footing. In all those figures (Fig 2-6) SDW OP, ODW OP and SCOP for electron and hole like Fermi surfaces are represented through

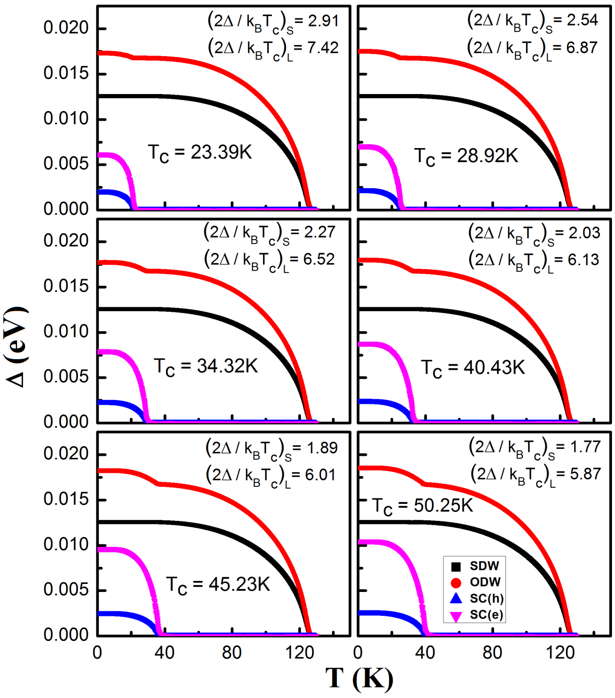

Figure 3.4: Temperature variation of various OPs like SDW (in black), ODW (in red) and superconductivity (electron FS violet, Hole FS blue) for different 122 FePn having different T$_c$s for hole doped (μ = 1.42) system having s$_{xy}$ pairing symmetry. Variation of BCS characteristic ratio with different T$_c$s are indicated

black, red, violet and blue respectively. These thermal variations of various OPs are used to establish the influence of OP symmetries in specific heat calculations. At T=0K the SC gap (both around electron and hole FS) is maximum, we take it as Δ_{sc} (T=0). As there are two energy gaps (around electron and hole like FS) we got two characteristics ratios one is large for Δ^e_{sc} and other one is small for Δ^h_{sc}. The momentum averaged $\Delta^{small}_{sc}(k)$ is obtained by taking average of Δ^h_{sc} over the outer Γ Fermi line of Fig.2.2 whereas the momentum averaged $\Delta^{large}_{sc}(k)$ is obtained by taking average of Δ^e_{sc} over the inner Γ Fermi line. In doing so, momentum dependence of the SCOPs for various pairing symmetries are considered. In each of the four cases (electron and hole doped d+s wave, electron doped isotropic s-wave and hole doped s_{xy} pairing symmetry) we have found the value of large and small $2\Delta_{SC}/k_BT_c$ for different transition temperatures and their values are presented inside the figures for each set. Since in this work we are predicting properties like $2\Delta_{SC}/k_BT_c$, $\Delta C/T_c$ etc. as a function of T_c, we need to vary T_c and calculate these

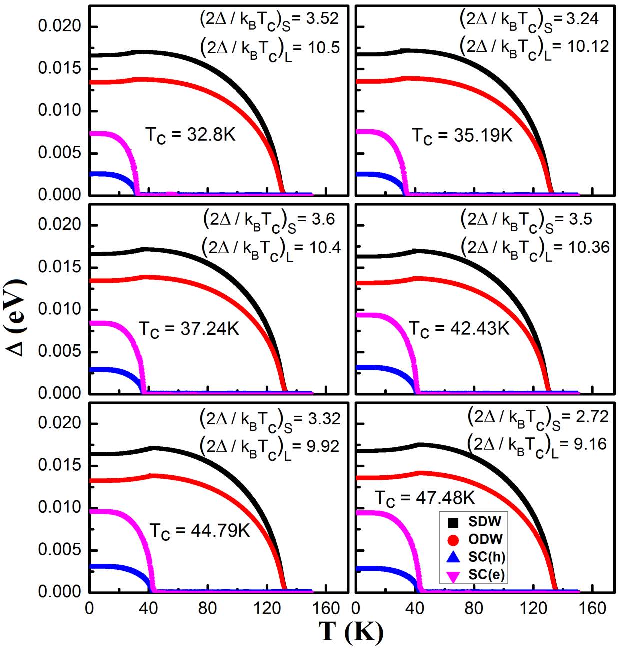

Figure 3.5: Temperature variation of various OPs like SDW (in black), ODW (in red) and superconductivity (electron FS violet, Hole FS blue) for different 122 FePn having different T$_c$s for electron doped system having isotropic s-wave pairing symmetry. Variation of BCS characteristic ratio with different T$_c$s are indicated

properties. The SC transition temperatures can be varied either by changing chemical potential μ (for hole and electron doped cases) or by modifying the effective attractive electron-electron interaction strength $V_0^{e/h}$ (where $V_{kk'}^{e/h}$ are factorized as $V_0^{e/h}\eta_k\eta_{k'}$, the momentum dependencies of η_k determines the symmetry of the SCOP). While the values of chemical potentials are presented in each figures 3–5, variations in T_cs are obtained as explained above and its values are presented in each figure. Specific heats for a particular pairing symmetry are calculated using the temperature dependencies of various order parameters in corresponding pairing symmetries. In only inter-band scenario the value of $2\Delta_{SC}^{small}/k_BT_c$ is larger compared to that from the experimental observation of $\sim 2.5 \pm 1.5$. From our calculation we have got (in d+s pairing symmetry) small and large $2\Delta_{SC}/k_BT_c$ values around 4 and 10 for electron doped system and 3 and 9 for hole doped system respectively. Both small and large $2\Delta_{SC}/k_BT_c$ values are smaller in the hole doped case (around 3 and 9) which is also consistent with experimental results [39].

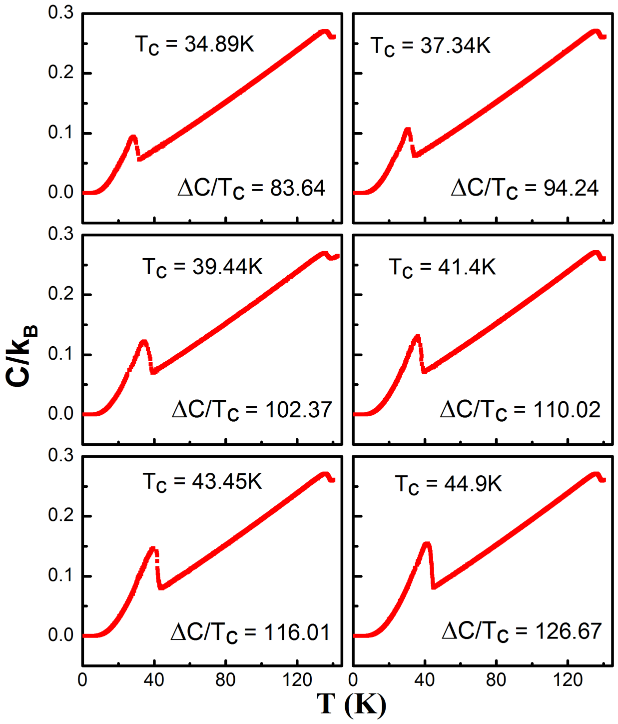

Figure 3.6: Variation of electronic specific heat as a function of temperature at different T_c for electron doped 122 FePn systems having d+s pairing symmetry and corresponding $\Delta C/T_c$ values indicated in the graph in mJ/moleK^2.

3.3.2 Thermal variation of electronic specific heat

Temperature dependent specific heat is calculated using the relation mentioned above in the theoretical model section. In this subsection we present the behaviour of specific heat as a function of temperature for inter-band only and combined intra-inter band scenarios. The SC gap (in the inter-band picture only) around the hole FS uses the density of states near the electron FS and vice versa. As a result, for example, when V_h^0 is raised (which increases the Cooper pair binding around the hole FS but uses the states around electron FS for pairing) to increase the SC T_c, the increment is only nominal compared to that in the intra-inter band picture. This also causes a distinct difference in the temperature dependencies of specific heat. This in turn causes difference in $\Delta C/T_c$ vs T_c^2 dependence. Fig.3.10c shows the variation of specific heat as a function of temperature for both only inter-band and intra-inter band cases. From Fig.3.10c it is very clear that the specific heat jump is smaller in only inter band picture. In intra-inter band case all

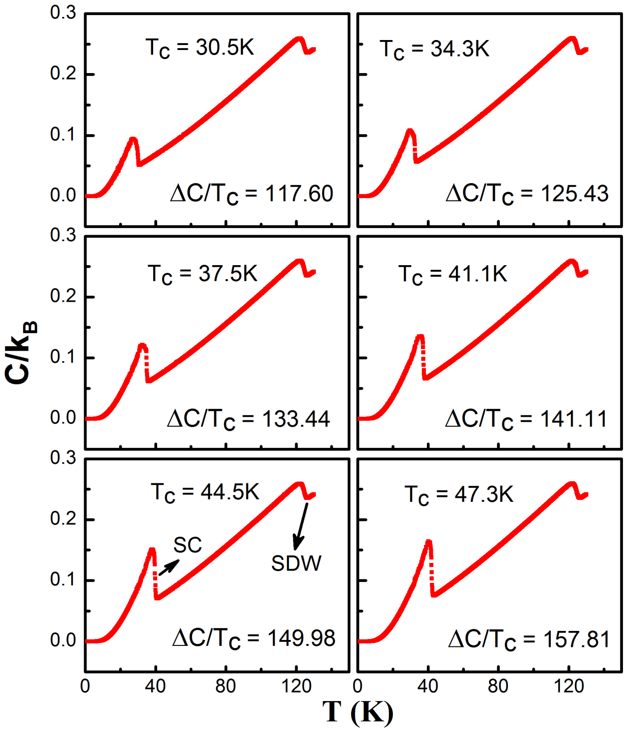

Figure 3.7: Variation of electronic specific heat as a function of temperature at different T_c for hole doped 122 FePn systems having d+s pairing symmetry and corresponding $\Delta C/T_c$ values indicated in the graph in mJ/moleK^2. SC and SDW/ODW jumps are indicated in one of the figures.

the four allowed pairing symmetries are considered as indicated earlier. Fig.3.6, Fig.3.7, Fig.3.8 and Fig.3.9 shows the variation of specific heat with temperature for d+s (electron and hole doped), s_{xy}(hole doped) and isotropic s-wave pairing (electron doped) symmetry respectively. In each case, we have calculated the specific heat jump ΔC at different T_cs and plotted $\Delta C/T_c$ as a function of T_c^2. Our calculated value of specific heat is in the unit of eV per 2 atoms. Most of the experimental results *i.e.*, the value of specific heat are in the unit of mJ/moleK. Scaling between mole and atom needs to be considered in order to compare theoretical results with that of the experiment. For example, in 122 system that contains 5 atoms, then without concern to whether all the atoms has greater or lesser contribution to the Fermi level (in case of 122 system, a mole of 122 is not considered to be consists of only two Fe atoms even though the contribution of density of states at Fermi level mostly comes from the Fe orbitals for these material) one has to multiply the

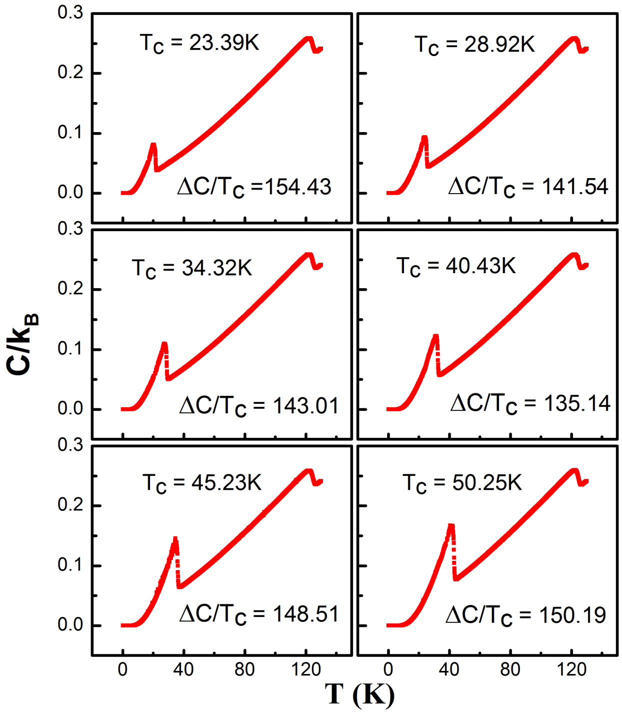

Figure 3.8: Variation of electronic specific heat as a function of temperature at different T_c for hole doped systems having s_{xy} pairing symmetry and corresponding $\Delta C/T_c$ values indicated in the graph in mJ/moleK^2.

value of specific heat by a factor n (n = 5 for 122 case) [113]. From these figures we clearly see that there are two jumps in the specific heat value, one at low temperature for SC transition (T_c) and other one at higher transition temperature for SDW and ODW.

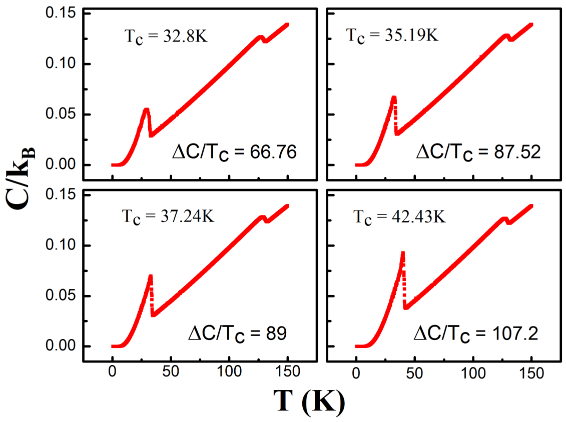

Figure 3.9: Variation of electronic specific heat as a function of temperature at different T_c for electron doped systems having isotropic s-wave pairing symmetry and corresponding $\Delta C/T_c$ values indicated in the graph in mJ/moleK^2.

Calculated values of $\Delta C/T_c$ with a fixed T_c, for electron and hole doped systems with d+s pairing symmetry matches well with the experimental results [53, 127]. The estimated value of $\Delta C/T_c$ for other pairing symmetries like s_{xy}, isotropic s-wave are not very consistent with the experimental observation. $\Delta C/T_c$ is nearly constant with T_c for s_{xy} pairing symmetry (see Fig.3.8). Fig.3.10a and Fig.3.10b shows that $\Delta C/T_c$ is proportional to T_c^2 [in those figure of $\Delta C/T_c$ vs T_c^2, theoretical data points are compared with linear curve (solid red line)] for both electron and hole doped system with d+s pairing symmetry which is consistent with the experimental findings [41, 53]. For other paring symmetry the behaviour of $\Delta C/T_c$ vs T_c^2 is not very clear as far as our calculation is concerned but certainly it is not proportional to T_c^2.

3.4 Conclusions

We present within two-band model of superconductivity a detailed study of BCS characteristic ratio and electronic specific heat. To calculate the above properties we present detailed study on the temperature dependencies of various OPs, like SDW, ODW and superconductivity in the electron and hole bands. Our entire work in the present chapter may be summarized as follows. Three scenarios of SC pairings are considered. (i) intra-band pairing (ii) inter-band pairing and (iii) intra-inter band pairing. Superconductivity within all the above scenarios are studied in presence of inter-orbital SDW and ODW order together with different allowed pairing symmetries. The intra-band pairing leads to two distinct T_cs and characteristic ratios similar to the weak coupling BCS theory and hence found not suitable for Fe-based superconductors , as it does not have much experimental evidence. In the solely inter-band pairing picture, single global T_c is achieved and larger $2\Delta_{SC}/k_BT_c$ consistent with experimental findings are seen. This picture still suffers from drawbacks in the following (a) $\Delta^{large}/\Delta^{small} \leqslant 2$, (b) $2\Delta_{SC}^{small}/k_BT_c$ exceeds experimental findings, (c) $\Delta C/T_c \propto T_c^2$ with proportionality constant which is negative. In the third scenario with combined intra-inter band pairing all the above mentioned shortcomings are

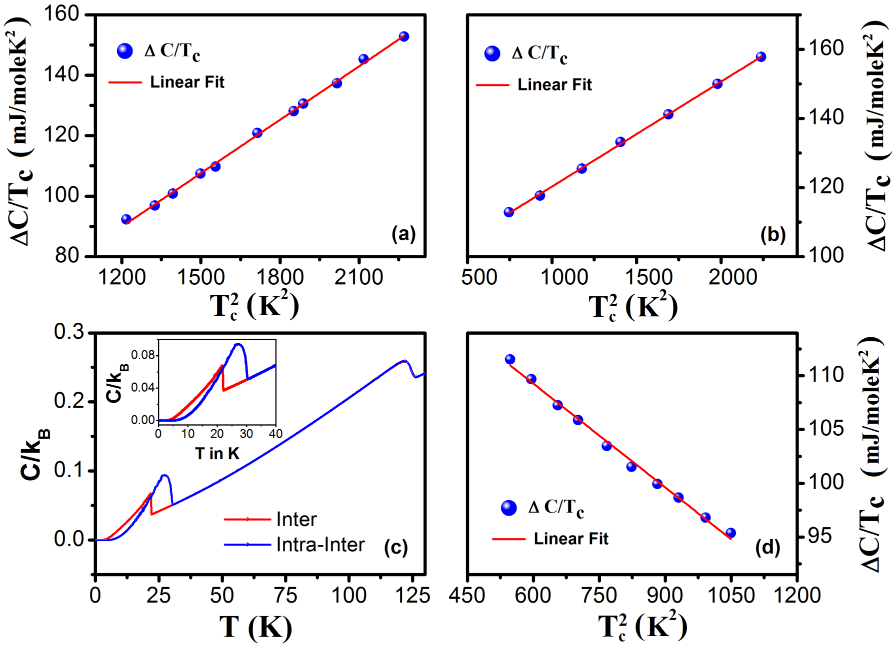

Figure 3.10: Variation of ΔC/T$_c$ as a function of T$_c^2$ for (a) electron and (b) hole doped 122 FePn systems having d+s pairing symmetry. (c) Specific heat as a function of temperature in only inter-band vs combined intra-inter band pairing. (d) Variation of ΔC/T$_c$ as a function of T$_c^2$ for only inter-band pairing.

overcome. In all the above pictures coupled gap equations involving SDW, ODW and SC-gaps are presented. Nature of quasi-particles in the above three pictures are also pointed out. Specially, in the inter-band only picture nature of gap equations (in absence of magnetic and orbital orders) reproduces that of the ref.[121]. The larger value of $2\Delta_{SC}/k_BT_c$ is found to be primarily due to the presence of inter-band pairing (this includes also the conclusion of ref.[121]). Within combined intra-inter band pairing for sign changing OPs we find that the temperature dependence of specific heat jump is very different from other classes of superconductors like conventional electron-phonon mediated BCS superconductors, A15 compounds, high T_c cuprates. We have shown that the characteristics ratios and $\Delta C/T_c$ variation with T_c matches very well with experimental findings [39] in case of d+s pairing symmetry (for both electron and hole doped). Therefore, combined intra and inter band pairing reproduces important features from experiment.

Finally, sign-changing $d_{x^2-y^2} + s_{x^2+y^2}$ pairing symmetry reproduces the desired $\Delta C/T_c$ as function of T_c^2 behaviour than other pairing symmetries in the combined intra-inter band pairing. Such paring symmetry is very much consistent with the recent trends of experimental and theoretical research in the field [63, 128–132]. The d+s pairing symmetry are consistent with the nematic phase observed in the phase diagram of Fe-based systems; according to this scenario the electronic ground state preserves the translational symmetry of the crystal but not the rotational symmetry [133]. Furthermore, we have argued elsewhere [117] that the d+s pairing symmetry is equivalent to $s^{\pm}$ symmetry in our model. We demonstrate that independent of pairing mechanism any theoretical model for Fe-based superconductors should contain contribution from both the intra and inter band pairing channels.

Chapter 4

Origin of magneto-structural transition in 122 family of Fe-based superconductors

4.1 Introduction

In the previous chapter we demonstrated that using a very simple two band model, one can explain various interesting physical properties of Fe-based SCs but it is not adequate to explain some of the important features which are integral parts of Fe-based SCs. For example, the role of anion height (closely related to z_{As}) in governing the various phases of Fe-based SCs including superconductivity, is instrumental but the realization of influence of anion height is beyond the scope of the minimal two band model (essentially a two dimensional model). There are plenty of instances where two band model is insufficient to produce quantitatively correct explanation of observed physical properties of Fe based SCs. Therefore, it is prerequisite to consider all five d-orbitals that dominate at the Fermi level of Fe-based SCs. We opt for first principles density functional theory which is in principle an exact theory. Within this approach we will show in the subsequent chapters that one can explore and resolve various important features of Fe-based SCs. We use T=0 density theory formalism but we use temperature dependent experimental data as the input of our first principles calculation to predict the temperature dependent electronic structures [134, 135]. The main effect on the electronic structure from finite temperature is the underlying crystal structure, and the average crystal structure at finite T can usually be reliably determined from the diffraction experiment at a given temperature T. Main purpose of this chapter is to study the origin of magneto-structural transition; in this endeavour we show that the structural transition is electronic in origin. The discovery of the iron-based superconductors modified the notion of uniqueness of high temperature superconductivity in cuprates and is interesting even after eight years of its discovery not only because they have the ability to exhibit superconductivity at very high transition temperatures, but also because it provides a rich prototype interplay of various degrees freedom, the lattice and the electronic charge, spin, and orbital degrees of freedom all have intriguing roles. The 122 family of Fe based superconductors are multi-band in nature and multi-orbital metals at all doping values, this should be contrasted with high T_c cuprates which are Mott-insulators. The undoped and doped compounds undergo a structural transition from a high-temperature tetragonal to a low-temperature orthorhombic phase which is followed in close proximity in temperature by a magnetic transition, below which the system is believed to be antiferromagnetic like spin density wave (SDW) metal. These transitions are suppressed with electron or hole doping (pressure) and beyond a certain doping superconductivity (SC) with high transition temperature appears along with coexistence between both SDW and SC. Initial investigations focused mainly on the interplay between a stripe-like antiferromagnetism (where the magnetic ordering wave-vector is $(\pi, 0)$ or $(0, \pi)$ in the 1Fe/cell notation) and superconductivity. It is popularly believed that the fluctuations associated with the stripe antiferromagnetism give rise to a $s^{\pm}$ superconducting pairing symmetry [31, 84, 136] in most, but possibly not all [137], Fe SC families.

Structurally, building block of all families of Fe-based materials is Fe-pnictogen/chalcogen layers in which the pnictogens/chalcogens are slightly above or below the Fe-plane. There exists a definite correlation among structural lattice parameters like z_{As} (anion height), bond lengths (Fe-Fe and Fe-As), As-Fe-As bond angles and superconducting transition temperature T_c in all families of Fe-based superconductors [20, 22–24]. In particular, superconducting transition temperature (T_c) is very closely related to anion height from Fe layer (directly related to z_{As}). For most of the Fe-based families like 1111, 122, 111 and 11 the anion height as a function of T_c follows a universal trend in ambient pressure as well as under high pressure [20]. Relation among Fe-Fe and Fe-As bond distances with T_c is also available in the literature [23]. The bond angle of As-Fe-As is also related to T_c as the distortion of $FeAs_4$ tetrahedron reduces T_c and maximum T_c is obtained when the $FeAs_4$ tetrahedron is perfectly regular [22, 24]. All these structural parameters mentioned above are very sensitive functions of temperature, doping etc. Any microscopic understanding on origin of various temperature dependent experimental observations (*e.g*, temperature dependent angle resolved photo emission (ARPES) studies etc. [135]) calls for temperature dependent first principles studies. However, first principles studies which evolve from solution of many body Schrödinger equation cannot account for such temperature dependencies. On the other hand, density functional theory has failed to produce optimized structures reproducing experimental values of z_{As}, which is found to be extremely crucial in reproducing other experimentally observed structural parameters and associated physical properties [28, 29, 32, 34, 123]. Therefore, hybridization of experimental inputs of temperature/doping/pressure dependent basic lattice parameters along with z_{As} in density functional theory would be a state-of-the-art first principles approach for understanding experimental observations on Fe-based materials. The main aim of this chapter is to find out the origin of magneto-structural transition in Fe-based SCS and point out some universal correlation between structural parameters and electronic structures through first principles simulation.

4.2 Computational details

Temperature dependent Rietveld quality data specially on z_{As} of any of the Ba122 system is important. Recently, such high quality Rietveld data established relationship among various structural lattice parameters like z_{As}, bond lengths (Fe-Fe and Fe-As), to the structural transition temperature in 5% Ru doped $BaFe_2As_2$ [29] material. Using temperature dependent and doping dependent experimental lattice parameters a (T,x), b (T,x), c (T,x) and z_{As}(T,x) [29] as inputs in our first principles simulations we obtain electronic band structure, density of states, Fermi surfaces as a function of temperature to explain the observed anomalies microscopically. Our first principles *ab-initio* simulations of electronic structure calculations are performed employing Material Studio 7.0, CASTEP package [96] which exploits the plane-wave pseudopotential method based on density functional theory (DFT). In all of our calculations the electronic exchange correlation is treated within the generalized gradient approximation (GGA) using Perdew-Burke-Enzerhof (PBE) functional [95]. Tackling small fraction of Ru substitution in place of Fe is accomplished by considering virtual crystal approximation (VCA) based on the Mixture Atom Editor of CASTEP program in Material Studio 7.0, CASTEP by forming $Fe_{2-x}Ru_x$ compound atom as well as super-cell approach. The composition of Fe and Ru at the given site is modified so as to be consistent with Ru fractional substitutions like x =0.1, 0.2, 0.3 etc. Spin polarized constrained optimization and single point energy calculations are performed using anti-ferromagnetic spin-stripe configuration [138] for the low temperature orthorhombic phase with space group symmetry Fmmm (No.69) using ultrasoft pseudopotentials and plane wave basis set with energy cut off 500 eV and self consistent field (SCF) tolerance 10^{-6} eV/atom. Brillouin zone is sampled in the k space within Monkhorst-Pack scheme and grid size for SCF calculation is $16\times16\times7$. Non-spin polarized and spin polarized calculations are performed for high temperature tetragonal phase with space group symmetry I4/mmm (No.139). For Fermi surface calculations grid size for SCF calculation is chosen as $25\times25\times33$.

4.3 Results and Discussions

4.3.1 Origin of magneto-structural transition in $BaFe_{2-x}Ru_xAs_2$

In this section, using temperature and doping dependent lattice parameters $a(x,T)$, $b(x,T)$, $c(x,T)$ and $z_{As}(x,T)$ obtained from Synchrotron radiation X-ray diffraction studies on Ru doped $BaFe_2As_2$ as inputs, we show that the results of first principles simulations reproduce experimentally observed ARPES data which so far remained unexplained. We show that the observed structural transition in this compound is electronic in origin whereas the suppression of the concurrent magnetic transition is due to loss of temperature dependent nesting of Fermi surface. In particular, we demonstrate through first principles simulations, that the temperature dependent pnictide height ($z_{As}(T)$) plays a very crucial role in structural and magnetic transition. Temperature dependencies of the electronic structure closely follow that of the $z_{As}(T)$ for x= 0.1 for $BaFe_{2-x}Ru_xAs_2$ and is essential in explaining the temperature dependent band shifts observed in ARPES studies. We further show, both experimentally as well as theoretically, that below the structural transition there exists two distinct Fe - Fe bond distances which modify the Fe-d_{xy} orbital largely due to its planar spatial extension leading to Lifshitz transition [139], (a more detailed discussion about Lifshitz transition in 122 Fe based SCs can be found in chapter 7) whereas the Fe-d_{xz} and d_{yz} orbitals become non-degenerate, which were degenerate above the structural transition giving rise to orbital order. We establish that the orbital order follows the temperature dependence of the experimentally determined orthorhombicity indicating electronic nature of the structural transition (see Fig.4.1). On the other hand, the two distinct Fe - Fe bond distances (which would correspond to two different exchange couplings [140, 141]), is a consequence of complex orbital order and also marks the appearance of the magnetic ground state as evidenced through the temperature dependence of the net difference in the up and down spin electronic density of states at the Fermi level – resulting in a simultaneous electronic magneto-structural transition.

The hole Fermi surface shrinks with temperature but the electron Fermi surface expands comparatively slowly. Therefore, the observed structural transition in this compound is electronic in origin and the suppression of the concurrent magnetic transition is due to loss of temperature dependent nesting of Fermi surface. We show that by employing temperature and doping dependent basic lattice parameters a satisfactory explanation to the observed ARPES data by Dhaka *et al.*, can be obtained using observed lattice parameters.

In Fig.4.1 there are three columns, in the first column experimentally observed structural parameters are presented (except the fourth and fifth rows). In the second and third columns theoretically computed results are presented. While it is clear from Fig.4.1(a) and (b) that both the z_{As}(T) and Fe-As (T) follow nearly the same temperature variation; structural transition is marked by the evolution of the orthorhombicity parameter δ, which occurs exactly at the same temperature where both z_{As}(T) and Fe-As (T) show an anomalously peaked value. Values of z_{As} or Fe-As bond lengths are nearly same at very low and high temperatures but show a very rapid temperature variations in between 80 to 125 K indicating the structural change. Almost same temperature dependencies are seen in Fig.4.1(d), (g), (h) and (i) which represent respectively the sum total of electronic density of states of up and down spins at the Fermi level, partial DOS of Fe up spins, partial DOS of Fe down spins, and the total ground state energy of the 5 % Ru doped $BaFe_2As_2$ system obtained through DFT simulations. (The same temperature dependence is also followed by the As-p orbitals, shown in Fig.4.1 **(l)**.) It is also the same temperature where z_{As} or Fe-As show anomaly, below which there exists two distinct Fe-Fe distances [29] (see Fig.4.1 (c), (f) and (j)). In Fig.4.1(e), difference in the DOS of up and down spins (scaled as 10^4) as a function of temperature is presented. This observation correspond to AFM transition because just above the AFM transition $N_{\uparrow}(E_F) - N_{\downarrow}(E_F) \neq$ zero whereas it is zero inside the AFM phase clearly indicates the onset of AF magnetic transition. The same behaviour in the temperature dependence of the calculated net magnetic moment of the unit cell is also found (not shown here). In figure 1 (f) we show that there

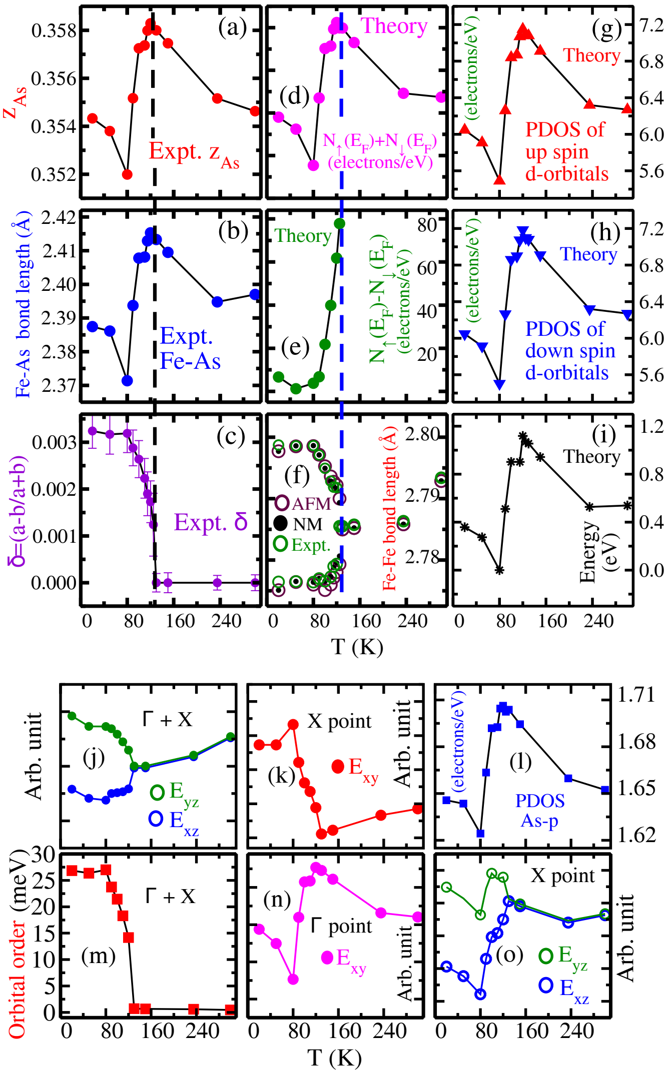

Figure 4.1: Experimental temperature variation of **(a)** z$_{As}$ **(b)** Fe-As bond distance **(c)** orthorhombicity δ of BaFe$_{1.9}$Ru$_{0.1}$As$_2$ from ref [29]. The orthorhombic distortion occurs rapidly after the high temperature tetragonal phase transforms into low temperature orthorhombic phase around 125 K. Theoretically simulated thermal variations of **(d)** total density of state at the Fermi level, **(e)** difference of up and down electron density of states at the Fermi level and **(f)** magnetic moment in the second column. Thermal variations of density of states of Fe **(g)** up **(h)** down electrons. **(i)** The total converged energy as a function of temperature also follows to that of the z$_{As}$, Fe-As and justify the behaviour of DOS. **(j)** Sum of the energies of the d$_{xz}$ at Γ and X points and the same for d$_{yz}$ as a function of temperature is the cause of two Fe-Fe-bond distances. **(m)** The orbital order as a function of temperature (see text for details). **(k)** Energies of the d$_{xy}$ band as a function of temperature at X and **(n)** Γ points. **(l)** Partial density of states of As as a function of temperature. **(o)** Energies of d$_{xz}$ and d$_{yz}$ of Fe as a function of temperature at the X-point

exists two distinct Fe-Fe bond distances exactly below the magnetic and structural transition — the two distinct Fe-Fe distances are quite robust and is observable even in case

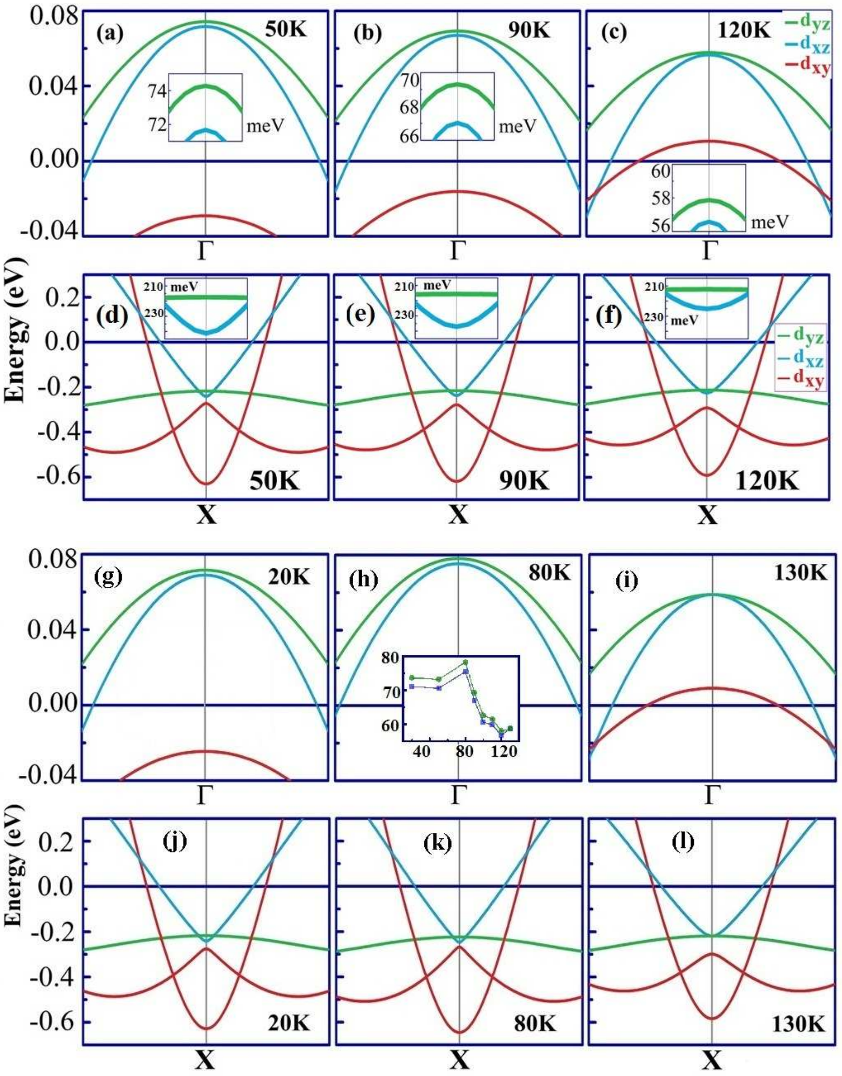

Figure 4.2: Band structure around Γ (first and third row) and X-points (second and forth row) respectively at different temperatures. Lifshitz transition is observed as the d_{xy} orbital moves down the Fermi level [see figures **(a)**,**(b)**,**(g)**, **(h)**]. Splits between the d_{xz} and d_{yz} orbitals are presented by insets in the figures (**a, b, c, d, e, f**), corresponding energies at the Γ point is shown in the inset **(h)** (see also the same at X point in the lowest row of Fig.4.1).

of non-magnetic calculations. Two distinct Fe-Fe bond distances would correspond to two distinct exchange coupling constants, a scenario observed earlier by Yildirim [140]. Furthermore, an important noticeable feature in all the temperature dependent structural parameters (see figures 1 (a), (b), (c), (i)) is that below T ∼ 80 K all the parameters increase with lowering in temperature to reach values closer to that of the room temperature one, the exactly same behaviour is also seen in the thermal behaviours of the density of states. Therefore, since it is the modifications in the temperature dependent electronic density of states that correlates with all the structural lattice parameters, the associated structural transition is likely to be electronic in origin. We discuss further on the same below. Figures of the lowest two rows of Fig.4.1 are obtained from detailed temperature dependent electronic band structure calculations, a glimpse of which are shown in Fig.4.2. In Fig.4.2, electronic band structures around Γ (1st/3rd row) and X (2nd/4th row) points are presented for different temperatures. One of the most important observations from the band structures around Γ point is that the Fe-d_{xy} orbital width increases with temperature so much (which will cause modifications in its occupation) that at 120 K it crosses the Fermi level. The observation that the Fe-d_{xy} level going below the Fermi level at T= 90 K, 50 K gives rise to Lifshitz transition [139]. Such temperature dependent modifications in the electronic bands crossing the Fermi level, enhancement in the widths, are possible source of orbital fluctuations. The tip of the d_{xy} band around Γ and X-points are shown in Fig.4.1 **(k)**, **(n)** respectively which actually follows the temperature dependencies of As-Fe-As angles. The tip of the d_{xz}, d_{yz} bands at the Γ/X point is degenerate at T = 125 K becomes non-degenerate in the orthorhombic phase, causing an orbital ordering between the orbitals (d_{xz}, d_{yz}) and two Fe-Fe distances (see Fig.4.1 **(j)** and follow below). Such non-degenerate d_{xz}, d_{yz} bands are observed experimentally recently [122]. We define orbital order as, $< O >= \sum_{i=\Gamma,X} E_{d_{xz}}(i) - E_{d_{yz}}(i)$ which are presented as a function of temperature in the first two figures of the bottom row of Fig.4.1 **(m)**. Needless to say that the temperature dependence of the orbital order $< O >$ reproduces that of the experimentally determined orthorhombicity (δ, compare figures **(c)** and **(m)**) indicating orbital ordering is the principal origin of the structural transition. The temperature dependence of the tip of the d_{xz} and d_{yz} (shown in Fig.4.2) bands at X-point given by E_{xz} and E_{yz} respectively which follow the similar temperature dependence as that of the z_{As} (cf. 4.1 **(o)**). Sum of the energies at X and Γ points of d_{xz} and d_{yz} bands respectively are presented in Fig.4.1 **(j)** showing its temperature dependence similar to as that of the two distinct Fe-Fe distances in Fig.4.1 **(f)**. These remarkable results clearly show that the structural transition dictated

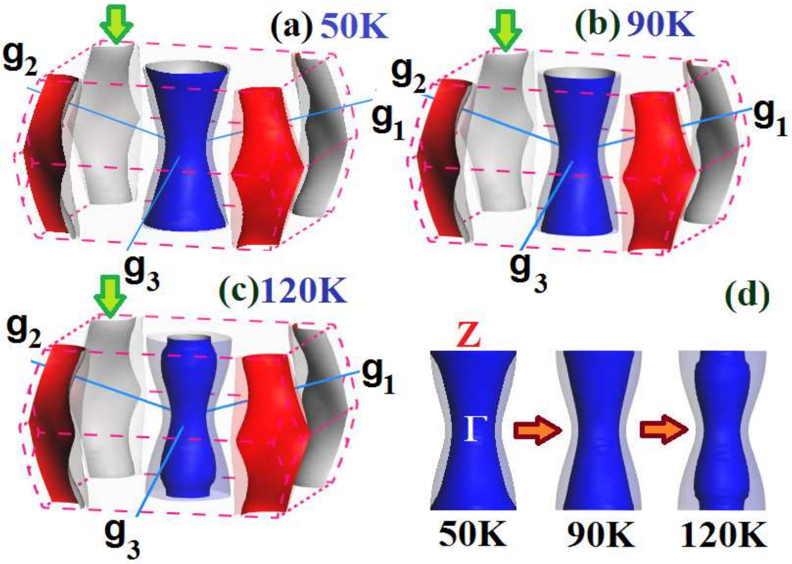

Figure 4.3: Theoretically calculated three dimensional Fermi surfaces at different temperatures **(a - d)**. Shrinking of hole like FS towards higher temperatures as well as surging of electron like FS leading to loss of nesting of FS is appreciable.

by δ, two Fe-Fe distances, anion height z_{As}, are orbital driven. Experimentally observed temperature dependencies of z_{As}, Fe-As bond distance, orthorhombicity parameter δ are consequences of the temperature dependent modifications in the electronic structure and vice versa. On the other hand, the feature that the tip of the d_{xz}, d_{yz} bands approach the Fermi level and that there is about 25 meV shift of the $d_{xz}(\Gamma)$, $d_{yz}(\Gamma)$ bands downwards to the Fermi energy from 20 K to 125 K which are consistent with ARPES studies of Dhaka *et al*.,. It should further be noted that such temperature dependence was not achievable when only thermal expansion of lattice parameters were considered in their DFT simulations. Furthermore, widths of the d_{xz}, d_{yz} bands around Γ point (evaluated along X–Γ–X path) decreases with temperature whereas the same around X-point (evaluated along Γ–X–Γ path) increases (comparatively) slowly. This causes the d_{xz}, d_{yz} bands cutting the Fermi level at a shorter $\Delta k = k_2 - k_1$ (where k_1 and k_2 are the two points in the k space at which the band cuts the FS) around Γ point whereas at a somewhat larger Δk around the X -point. This makes the hole Fermi surface around the Γ point shrink whereas that around X-point expand a bit with temperature (see Fig.4.3) causing temperature dependent loss of Fermi surface nesting. This is the reason behind the decrease in hole Fermi surface radius around the Z-point (also Γ point) with temperature. This naturally explains the momentum distribution curves obtained in ARPES studies [135]. Therefore, the orbital order that causes structural transition also causes damage to the FS nesting, suppressing SDW and thus both are inter coupled [87].

4.3.2 Universal direct correlations of orbital order to orthorhombicity in 122 family of Fe-based SCs

In this section we consider several other Fe-based superconducting materials from 122 family to show a direct quantitative correlations between the orbital order and orthorhombicity. The orbital order is calculated from electronic band structures through first principles simulations using doping and temperature dependent structural parameters. The orthorhombicity parameter is taken from already established experimental studies [100, 142, 143] as a function of various doping concentrations. When such variations are normalized, be it thermal variation or doping dependent, both the above quantities (orbital order and orthorhombicity) quantitatively corresponds to each other in terms of their doping as well as temperature variations. This is shown universally for hole doped, electron doped or iso-electronic substituted materials. The orbital order being (the difference in band energies $E_{d_{xz}}$, $E_{d_{yz}}$ at high symmetry k-points) derived from electronic band structure, its complete matching with orthorhombicity proves that the structural transition in Fe-based materials is electronic in nature. This is thus a direct proof that orthorhombic distortion is *not* due to lattice but an electronic one. A first step to reject one of the order parameters that may lead to nematicity. That leaves orbital fluctuation or spin order as primary order for nematic phase. An universal correlations among various structural parameters and electronic structure is also obtained in this section of the chapter so that electronic origin of structural and magnetic transitions are convincing. Most remarkable among them is the mapping of two Fe-Fe distances in the low temperature orthorhombic phase, with the band energies $E_{d_{xz}}$, $E_{d_{yz}}$ of Fe at the high symmetry points of the Brillouin zone. This correspondence of band energies with two Fe-Fe distances is true for its variation either with doping or temperature. Furthermore, the fractional co-ordinate z_{As} of As which essentially determines anion height is inversely (directly) proportional to Fe-As bond distances (with exceptions of K doped $BaFe_2As_2$) for hole (electron) doped materials as a function of doping. On the other hand, Fe-As bond-distance is found to be inversely (directly) proportional to the density of states at the Fermi level for hole (electron) doped systems. Chemical effect in terms of size of doping elements and nature of substitution, in-plane or out of plane is employed to understand various doping dependent electronic structure.

First we calculate the band structures of various doped $BaFe_2As_2$ (Ba122) systems as a function of doping concentrations using experimental lattice parameters (a, b, c and z_{As}) in the orthorhombic as well as tetragonal phases. We present the band structures around high symmetry k points (Γ, X and Y) of K and Na doped (hole doped) Ba122 systems in Fig.4.4 and Fig.4.5 respectively for various doping concentrations as indicated in figures. Different colours are used to designate various orbital projected bands near the Fermi level (FL). It is also an well established fact that electronic structure near the FL of these Fe-based SCs are mainly dominated by Fe-d orbitals. It is quite evident from the two figures (Fig.4.4 and Fig.4.5) that as a consequence of hole doping, hole like bands around Γ points (mainly d_{xz} and d_{yz} bands near FL) move away from the FL with increasing hole doping concentration. On the other hand, electron like bands (mainly d_{xy} bands near FL) around X, Y points move towards the FL. This whole scenario is consistent with the hole doping picture where hole like Fermi surfaces expand and electron like Fermi surfaces shrink with increasing hole doping concentration. We also depict the calculated band structures around high symmetry points (Γ, X and Y) of P doped (iso-electronic) Ba122 system in the orthorhombic and tetragonal phases in Fig.4.6 for various doping concentrations. Fig.4.6 reveals that there is no significant modifications in the position of the bands near FL due to P doping at As sites in Ba122 system. However there is some visible moderation in the d_{xy} band near FL around Γ point with the variation of P doping

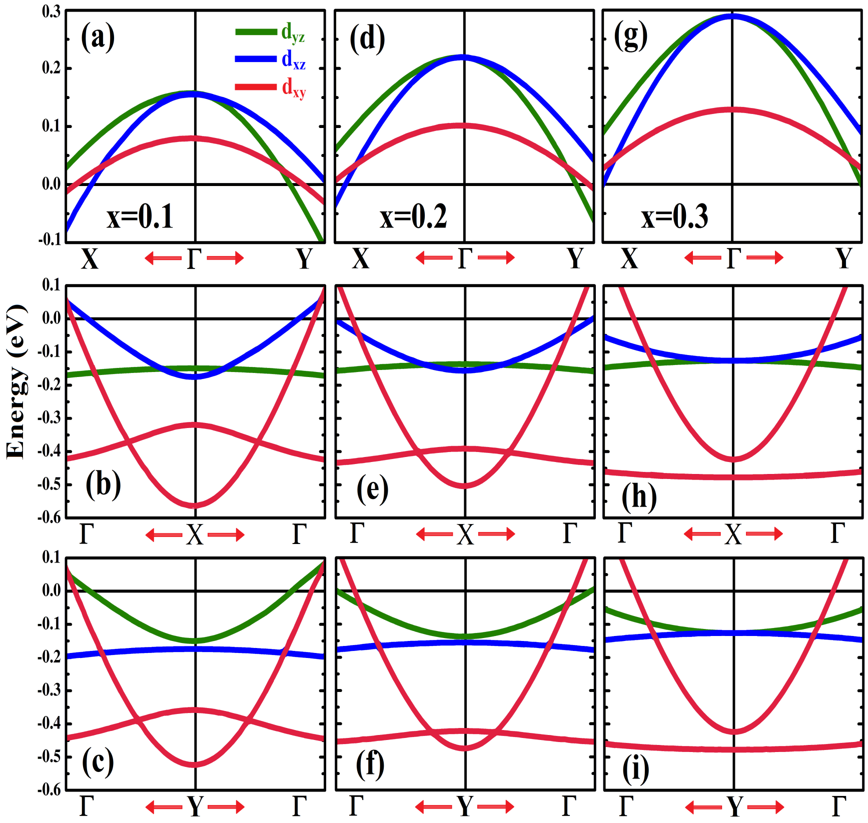

Figure 4.4: Calculated band structures of $Ba_{1-x}K_xFe_2As_2$ within VCA method in the low temperature phase around Γ (1st row), X (2nd row) and Y (3rd row) points for (a, b, c) $x = 0.1$ (d, e, f) $x = 0.2$ and (g, h, i) $x = 0.3$. Fermi level is denoted by horizontal black line at zero energy. Orbital orders around all these high symmetry points are calculated.

concentration. Iso-electronic P doping at As site is like in-plane substitution (substitution in the Fe-As layer) contrasting with K or Na substitution at Ba site which is out of plane substitution (in between two Fe-As layer). Therefore, P doping at As site affects the d_{xy} bands more drastically than the other bands (mainly d_{yz} and d_{xz} bands) near FL. As a result d_{xy} band (being planer in nature) gets modified remarkably with increasing doping concentration. However, in case of K and Na doping at Ba site (hole doping) which is by nature an out of plane substitution, d_{xy} band near FL is least affected and there are notable moderation in the d_{yz} as well as d_{xz} bands near FL due to hole doping. From Figs.4.4, 4.5, 4.6, we calculate the band energies of d_{xz} and d_{yz} bands around all high symmetry k points: X, Y, Γ for K, Na and P doped Ba122 systems. In Fig.4.7, sum of the band energies *i.e.*, $E_{d_{xz}}$ and $E_{d_{yz}}$ around X, Y, Γ points as a function of doping concentration for various

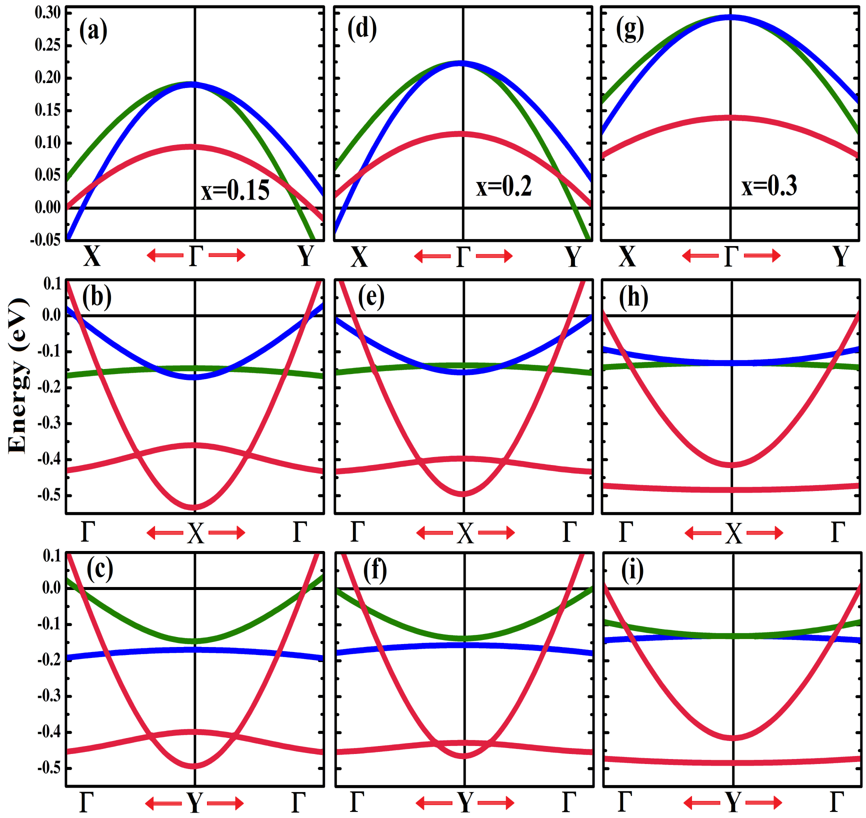

Figure 4.5: Calculated band structures of $Ba_{1-x}Na_xFe_2As_2$ within VCA method in the low temperature phase around Γ (1st row), X (2nd row) and Y (3rd row) points for (a, b, c) $x = 0.15$ (d, e, f) $x = 0.2$ and (g, h, i) $x = 0.3$. Fermi level is denoted by horizontal black line at zero energy. Orbital orders around all these high symmetry points are calculated.

doped Ba122 systems are presented. It has been explicitly shown that these band energies ($E_{d_{xz}}$ and $E_{d_{yz}}$) follow the same behaviour as that of the two Fe-Fe bond lengths (in the orthorhombic phase of these Ba122 systems, there are two different Fe-Fe bond lengths) as a function of doping concentration for K, Na as well as P doped Ba122 systems. In Fig.4.7 (1st column), we also display the experimental values of Fe-Fe bond lengths as a function of doping concentration for various doped Ba122 systems taken from references [100, 142, 143]. We also estimate the differences of those band energies around Γ, X, Y points which is defined as orbital order (orbital order = $\sum_i E^i_{d_{xz}}$-$E^i_{d_{yz}}$, where $i = \Gamma, X, Y$) for a number of 122 systems for each doping concentration (see Fig.4.8b, 4.8e, 4.8h). In Fig.4.8, we show the experimentally measured variation of orthorhombicity parameter [defined as $\delta = (a-b)/(a+b)$)] of Ba122 systems with K, Na as well as P doping concen-

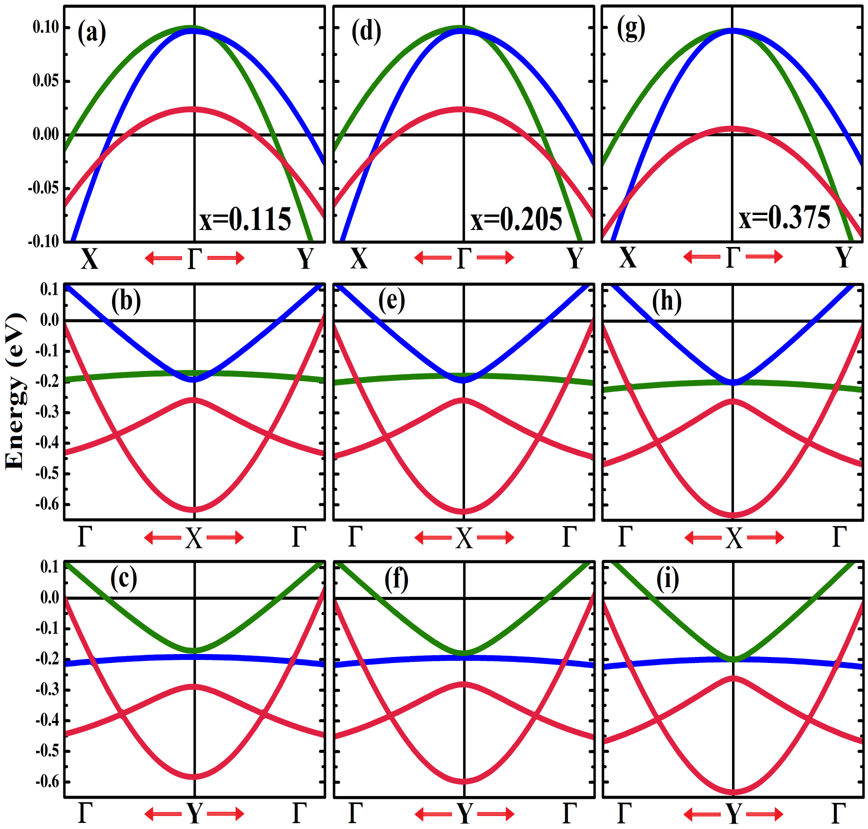

Figure 4.6: Calculated band structures of $BaFe_2(As_{1-x}P_x)_2$ within VCA method in the low temperature phase around Γ (1st row), X (2nd row) and Y (3rd row) points for (a, b, c) $x = 0.115$ (d, e, f) $x = 0.205$ and (g, h, i) $x = 0.375$. Fermi level is denoted by horizontal black line at zero energy. Orbital orders around all these high symmetry points are calculated.

tration (1st row). Estimated orbital order as a function of doping concentration around X, Y and Γ points for the same three systems are also presented in Fig.4.8b, 4.8e, 4.8h. We also plot the normalized orthorhombicity parameter as well as orbital order for the same three systems as a function of doping concentration in Fig.4.8c, 4.8f, 4.8i to visualize the universal mapping of structural transition to the orbital ordering. One can easily see from those figures (Fig.4.8c, 4.8f, 4.8i) that orbital order and orthorhombicity parameter quantitatively follow identical behaviour with doping concentration for all the studied 122 systems (K, Na and P doped Ba122). We further extend our studies in case of temperature dependent structural transitions for undoped as well as K-doped Ba122 systems to prove the universal mapping of orbital order to orthorhombicity parameter. We calculate the band structures of undoped as well as K-doped Ba122 systems (10%

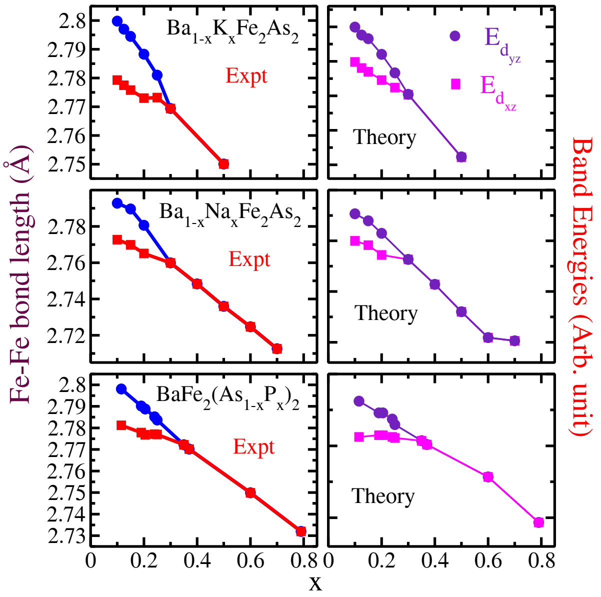

Figure 4.7: Experimental two Fe-Fe bond lengths (1st column) and sum of the calculated band energies of d_{yz} and d_{xz} bands around high symmetry points (2nd column) as a function of doping for K (1st row), Na (2nd row) and P (3rd row) doped $BaFe_2As_2$ systems

and 20% K doping) using temperature and doping dependent experimentally determined structural parameters [$a(x,T), b(x,T), c(x,T)$ and z_{As}]. Calculated band structures around X, Y, Γ points at various temperatures for undoped and 20% K doped Ba122 systems are presented in Fig.4.9 and Fig.4.10 respectively. Unlike doping dependent band structures, there is not significant variation in the band structures near the FL with temperature. But a more closer look in the band structures for various temperatures, reveals some important informations about structural transition and its link to electronic structures. Here also we calculate the sum of band energies $E_{d_{xz}}$ and $E_{d_{yz}}$ around X, Y, Γ points at each temperature and compare these values with temperature dependent experimentally measured Fe-Fe bond lengths. In Fig.4.11, experimentally measured temperature dependent Fe-Fe bond lengths taken from ref [142] are presented in column one for undoped as well as 10% and 20% K doped Ba122 systems. In the second column of Fig.4.11, temperature variation of band energies ($E_{d_{xz}}$ and $E_{d_{yz}}$) are presented for the same three systems. Temperature dependence of band energies quantitatively follow, experimentally observed thermal behaviour of two Fe-Fe distances. This should also be contrasted with Fig.4.7 where doping

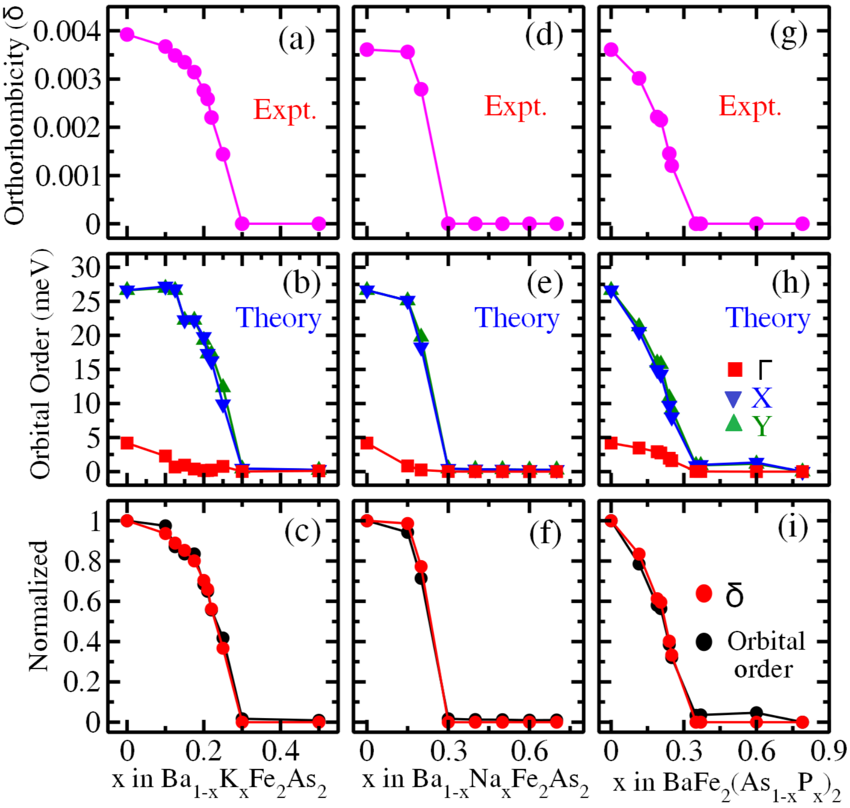

Figure 4.8: Experimental orthorhombicity parameter (1st row), theoretically calculated orbital orders around Γ, X, Y points (2nd row) and normalized orthorhombicity parameter as well as orbital order (3rd row) as a function of doping for (a, b, c) K doped (d, e, f) Na doped (g, h, i) P doped $BaFe_2As_2$ respectively.

dependent Fe-Fe distances are also followed by the band energies. This is an example of universal correlation of experimental structural parameters with electronic structure. We also calculate the orbital orders around X, Y, Γ points as a function of temperature for these systems and present in Fig.4.12b, 4.12e and 4.12h. Experimentally observed orthorhombicity parameter as a function of temperature is also depicted in Fig.4.12a, 4.12d, 4.12g for these systems. We also show in Fig.4.12c, 4.12f, 4.12i, that the normalized orbital order maps with that of the orthorhombicity parameter as a function of temperature. Thus it is very clear that the structural transition in 122 Fe-based SC is due to the orbital ordering between d_{xz}, d_{yz} bands and thus electronic in origin. This also suggest that electronic structure is highly sensitive to structural parameters and there are universal correlation between structural parameters to the electronic structure in these types of su-

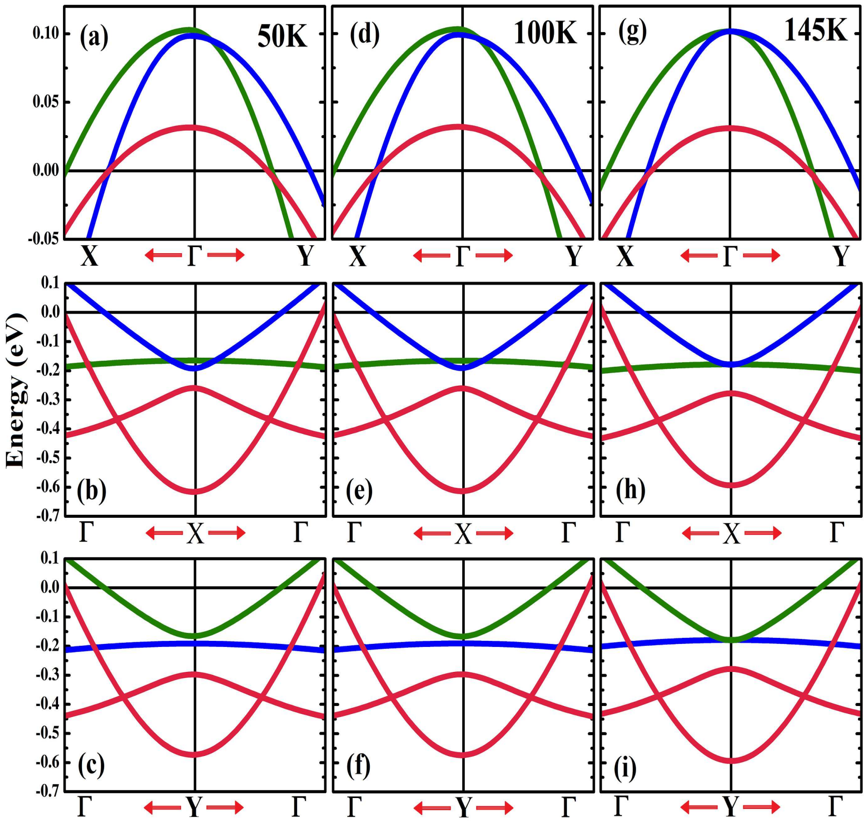

Figure 4.9: Calculated band structures of undoped $BaFe_2As_2$ around Γ (1st row), X (2nd row) and Y (3rd row) points for (a, b, c) T=50K (d, e, f)T=100K and (g, h, i) T=145K. Fermi level is denoted by horizontal black line at zero energy. Orbital orders around all these high symmetry points are calculated.

perconductors as evident from the fact that the two band energies ($E_{d_{xz}}$ and $E_{d_{yz}}$) follow the same temperature as well as doping dependencies as that of the two Fe-Fe bond lengths.

4.3.3 Correlation among structural parameters and electronic structure

In order to find some universal correlation among the structural parameters and electronic structures, we further investigate various doped Ba122 compounds in the orthorhombic and tetragonal phases. First we calculate the density of states for different doping concentrations for undoped and various doped Ba122 systems like $Ba_{1-x}K_xFe_2As_2$, $Ba_{1-x}Na_xFe_2As_2$, $BaFe_{2-x}Co_xAs_2$, $BaFe_{2-x}Ru_xAs_2$ and $BaFe_2(As_{1-x}P_x)_2$. In Fig.4.13, we

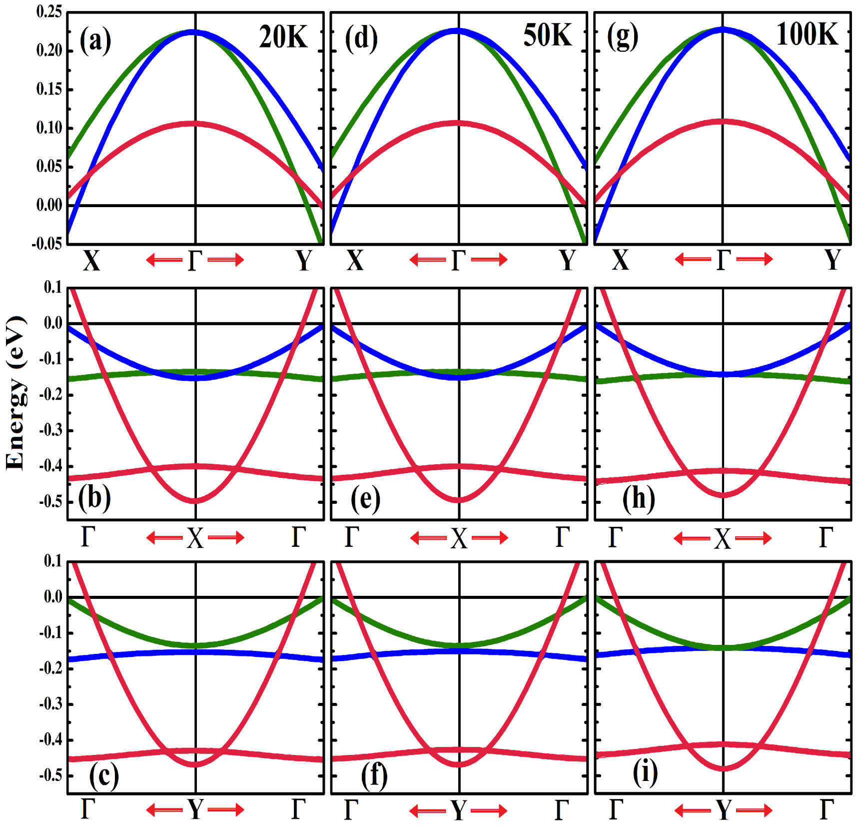

Figure 4.10: Calculated band structures of $Ba_{0.8}K_{0.2}Fe_2As_2$ within VCA method around Γ (1st row), X (2nd row) and Y (3rd row) points for (a, b, c) T=20K (d, e, f)T=50K and (g, h, i) T=100K. Fermi level is denoted by horizontal black line at zero energy. Orbital orders around all these high symmetry points are calculated.

depict the calculated density of states of undoped, 10% Co doped, 50% K doped and 32% P doped Ba122 systems near the FL. In Fig.4.13b, 4.13c, 4.13d, we also exhibit the density of states of the undoped system with the doped one for comparison. We precisely choose to present the density of states of the doped Ba122 compounds with optimal doping concentrations at which these materials have the highest T_c. It is evident from Fig.4.13, that the chemical potential (Fermi level) shifts in the opposite directions in case of hole and electron doping as expected. From this figure it also turns out that the case of iso-electronic P doping is very similar to the case of electron doping. Up to 25% doping although it is not very clear whether Ru doping correspond to hole or electronic doping, at higher doping (not shown here) it behaves like hole doping. Main purpose of this figure is to provide guidelines to the readers regarding the possible behaviour of the

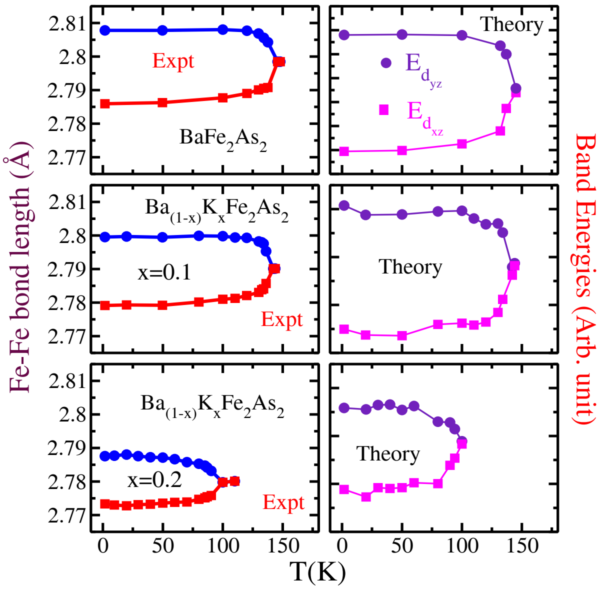

Figure 4.11: Experimental Fe-Fe bond lengths (1st column) and sum of the calculated band energies of d_{yz} and d_{xz} bands around high symmetry points (2nd column) as a function of temperature for undoped BaFe$_2$As$_2$ (1st row), 10% (2nd row) and 20% (3rd row) K doped BaFe$_2$As$_2$ systems

DOS presented in the third rows of the figures4.14 and 4.15. In Fig.4.14 and Fig.4.15, we display the experimentally measured various structural parameters (taken from ref [13, 29, 55, 100, 142, 143]) and theoretically computed electronic structures as a function of doping for a number of doped Ba122 systems in the orthorhombic and tetragonal phases. In the first and second rows of Fig.4.14, we exhibit the experimental variation of z_{As} as well as Fe-As bond lengths with doping concentration respectively for K, Na, P doped Ba122 systems. In Fig.4.14c, g, k (3rd row), calculated density of states at the FL for these systems are presented as a function of doping concentration. In the last row, we exhibit the experimentally estimated in-plane and out of plane As-As distances as a function of doping concentration for these three systems. Although in all these three systems doping is in the passive sites, there are significant variation of structural parameters with doping concentration. Now we move to the case of active site doping *i.e.,* Co and Ru doping in Fe site. In Fig.4.15, we present the variation of experimental z_{As} as well as experimental Fe-As bond length with doping concentration for Co, Ru doped Ba122 in 1st and 2nd rows respectively. Calculated density of states at the FL (N(E_F)) for these two

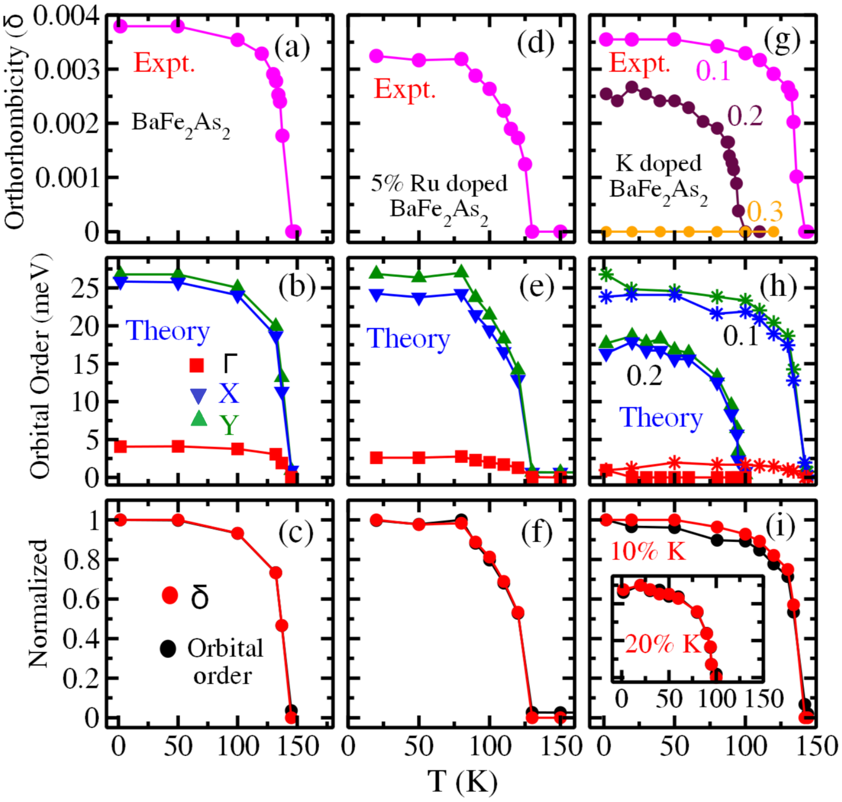

Figure 4.12: (a, b, c) Experimental orthorhombicity parameter, calculated orbital orders around Γ, X, Y points and normalized orthorhombicity parameter as well as orbital order (as defined in the text) as a function of temperature for undoped BaFe$_2$As$_2$ respectively. (d, e, f) Experimental orthorhombicity parameter, calculated orbital orders around Γ, X, Y points and normalized orthorhombicity parameter as well as orbital order (as defined in the text) as a function of temperature for 5% Ru doped BaFe$_2$As$_2$ respectively. (g, h, i) Experimental orthorhombicity parameter (including 30% K doped BaFe$_2$As$_2$), calculated orbital orders around Γ, X, Y points and normalized orthorhombicity parameter as well as orbital order (as defined in the text) as a function of temperature for 10%, 20% K doped BaFe$_2$As$_2$ respectively.

systems as a function of doping concentration are exhibited in the 3rd row of Fig.4.15. In the last row of Fig.4.15, we depict the variation of in plane and out of plane As-As distances with doping concentration for Co and Ru doped Ba122 systems. From Fig.4.14 and Fig.4.15, we observe that, there are diversities in the behaviour of structural parameters as well as electronic structure with doping concentration. But there exists universality in the behaviour of structural parameters and electronic structure. In case of hole doping (K and Na doped Ba122 systems), density of states at the FL inversely follow the variation of Fe-As bond length with doping. On the contrary, density of states at the FL follow

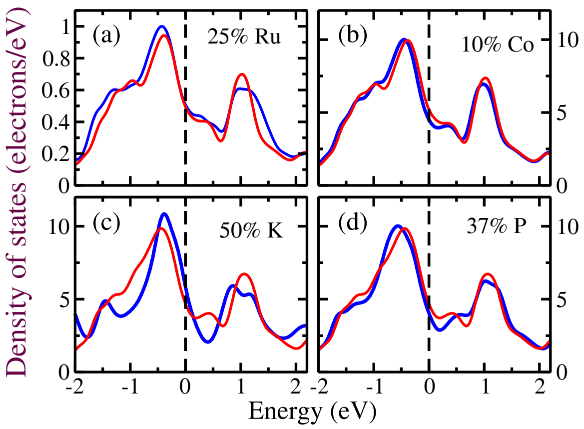

Figure 4.13: Calculated density of states of (a) 25 % Ru doped (iso-electronic doping) (b) 10% Co doped (electron doping), (c) 50% K doped (hole doping) and (d) 37% P doped (iso-electronic doping) $BaFe_2As_2$ respectively. To compare the shift of chemical potential μ due to doping, density of states of the undoped 122 is also depicted with a solid red line. Vertical dashed line at 0 eV indicate the Fermi level.

the same behaviour as that of the Fe-As bond length with doping for the case of electron doped (Co doped) Ba122 system. Moreover, the case of iso-electronic P doping in As site is very similar to the case of electron doping as evident from the doping dependent behaviour of experimental z_{As}, Fe-As bond length as well as calculated density of states at the FL. Although the case of iso-electronic Ru doping at Fe site is similar to the hole doping scenario where density of states at the FL follow the same doping variation as that of the Fe-As bond length; there is in general a universal link between the variation of density of states at the FL with that of the experimental z_{As} with doping and it turns out that z_{As} is inversely (directly) proportional to Fe-As bond distances (with exceptions of K doped $BaFe_2As_2$) for hole (electron) doped materials as a function of doping.

Now we shed more light into the universality and diversities in the behaviour of electronic structure and structural parameters in 122 Fe based materials. In plane and out of plane As-As distances also play a very important and crucial role in controlling the electronic structures. First, we study the case of out of plane substitution *i.e.,* K and Na doping at Ba site. Size of the Ba atom (2.22Å) [atomic radius in metalic bonding] is larger than Na atom (1.86Å) but smaller than K atom (2.27Å). Because of this reason, with the

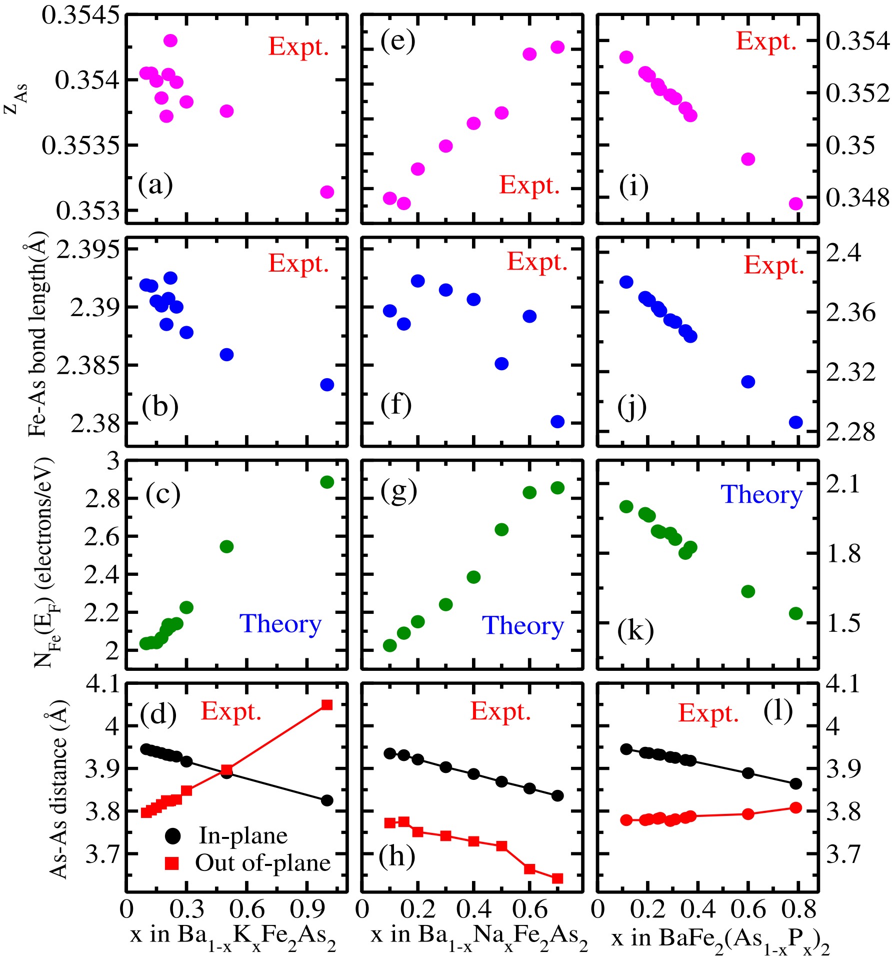

Figure 4.14: Experimental z_{As} (1st row), Experimental Fe-As bond length (2nd row), Calculated DOS of Fe atoms at Fermi level (3rd row) and experimental in-plane as well as out of plane As-As distance (4th row) as a function of doping concentration for (a-d) K (e-h) Na and (i-l) P doped $BaFe_2As_2$ systems.

substitution of K atom in place of Ba atom, out of plane As-As distance increases and exactly opposite behaviour of out of plane As-As distance is observed in the case of Na substitution in Ba site. It should also be noted that the c-axis increases with increasing doping concentration for both Na and K doping (in case of Na doped Ba122 system c-axis increases with doping upto certain doping concentration and after that it decreases). This qualitatively explains the observed behaviour of z_{As} with doping for K and Na doped Ba122 systems. On the other hand, in both the hole doped cases, in plane As-As distance decreases with increasing doping concentration following the doping variation of Fe-As bond length. Next we investigate the case of in plane substitutions (Co/Ru substitution at

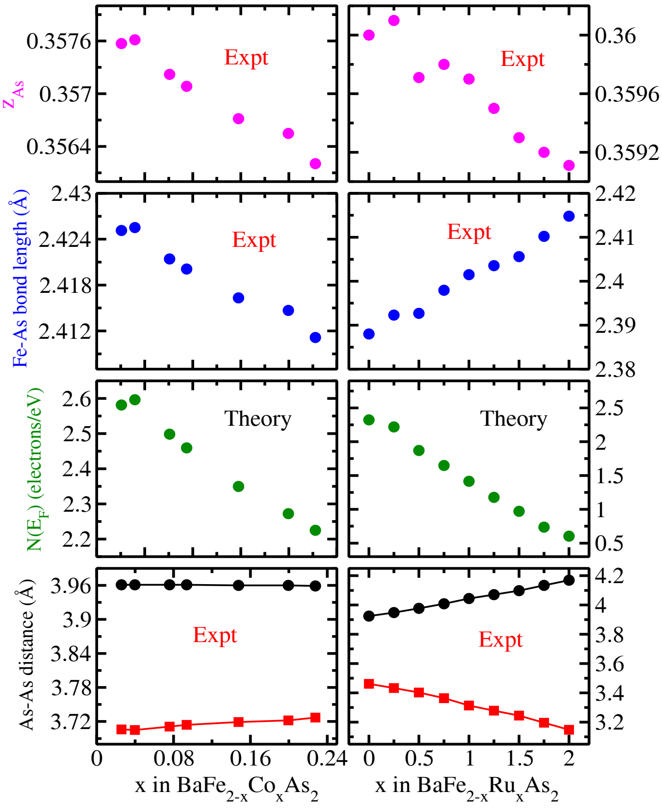

Figure 4.15: Experimental z_{As} (1st row), Experimental Fe-As bond length (2nd row), Calculated DOS of Fe atoms at Fermi level (3rd row) and experimental in-plane as well as out of plane As-As distance (4th row) as a function of doping concentration for Co (1st column) and Ru (2nd column) doped $BaFe_2As_2$ systems.

Fe site and P substitution at As site). Size of Fe atom (1.26Å) is smaller than Ru atom (1.34Å) but larger than Co atom (1.25Å). Therefore, Fe-As bond length decreases with doping in case of Co substitution but increases with doping in case of Ru substitution in place of Fe. This is consistent with the behaviour of in-plane as well as out of plane As-As distances as a function of doping. Since size of P atom (1Å) is smaller than As atom (1.15Å), Fe-As bond length decreases with increasing doping concentration just like the case of Co doped (electron doped) system. These are also consistent with the doping dependent variation of out of plane As-As distance (in all the cases of in plane substitution c-axis decreases with increasing doping concentration). Moreover, in plane As-As distance in all these cases (in plane substitution) follow the same doping dependencies as that of the Fe-As bond length. Thus all these structural parameters are crucially controlling the electronic structures near the FL of the Ba122 compounds and follow universal characteristics features.

4.4 Conclusions

We provide a microscopic origin of structural transition in 122 family of Fe-based SC. First, we take the case of $BaFe_{2-x}Ru_xAs_2$ and then we consider a number of other family members of 122 system. Using temperature and doping dependent lattice parameters on Ru doped $BaFe_2As_2$ we show through detailed first principles simulations that the electronic structure carries the 'finger prints' of the structural parameters like z_{As}, Fe-As bond distance and reproduces the experimentally observed angle resolved photo emission spectroscopy data that so far was unexplained. Below structural transition an orbital order develops between d_{xz} and d_{yz} orbitals of Fe. On the other hand, temperature dependent modifications of d_{xz}, d_{yz} bands cause loss of nesting causing suppression of spin density wave transition. Total band energies at high symmetric Γ & X-points of d_{xz}, d_{yz} bands become non-degenerate at structural transition whose temperature dependence is very similar to that of the observed two Fe-Fe distances (or a (T) and b (T)); whereas the difference of band energies at Γ & X-points of the said bands give rise to orbital order that follows the temperature dependence of the orthorhombicity parameter. Therefore, orbital fluctuations play a dominant role in the magneto-structural transition in Ru doped $BaFe_2As_2$ systems. The hole like Fermi surface shrinks with temperature but the electron Fermi surface expands but comparatively slowly. This explains the momentum distribution curves observed in ARPES and temperature dependent loss of Fermi surface nesting. Finally, we demonstrated that the thermal variations of z_{As} obtained from experiments, when used as inputs in first principles simulation studies, produce realistic theoretical results with respect to the electronic structure that is observed experimentally and perhaps should be used in all families of Fe-based materials in order to provide better insight.

An extended detailed first principles electronic structure calculation on a number of other doped 122 family of Fe-based SCs are also presented. Experimental structural parameters like lattice parameters (a, b, c) together with z_{As} as a function of doping as well as temperature are used as fixed inputs in our calculations. Various kinds of doping like; electron doping, hole doping, iso-electronic doping are considered (within VCA) in this study. It has been shown very rigorously and quantitatively for a number of Fe-based SCs that the orbital ordering between the d_{xz}, d_{yz} orbitals is the origin of structural transition. The calculated orbital ordering from electronic structure calculations when normalized its variation with temperature as well as doping identically follows (quantitatively) with that of the experimental orthorhombicity parameter. This conclusively proves that the structural transition in 122 family of Fe-based SCs is not lattice driven but electronic one. Therefore, our work supports the electronic origin of the nematic phase observed in 122 family of Fe-based materials. An universal correlation among the structural parameters and the electronic structure is described in this chapter.

In the next chapter we will see whether orbital order, magnetic order and nematic order are coupled or not.

Chapter 5

Nematicity and ferro-spin-orbital ordering in 122 Fe-based superconductors

5.1 Introduction

Seven years after the discovery of Fe-based SCs, while a clear consensus on the mechanism of superconductivity has not yet been reached, understanding on the structural, magnetic transitions and their mutual influences on superconductivity remain central issue of frontier research [129, 144, 145]. A large number of undoped Fe-based materials show spin density wave (SDW) magnetic state whose transition temperature coincides with that of the structural transition (which gets separated through doping as well as pressure). If both the transitions would be second order in nature, there can have a conflict with Landau theory of phase transition unless there would be a precursor transition at higher temperatures. Neutron diffraction measurement on single crystal of $BaFe_2As_2$ reveal that both the magnetic and structural transition occur simultaneously at 138 K and both are second order phase transition [146]. According to Landau theory, occurrence of two simultaneous transitions may be purely coincidental, mutually independent, or one of the transitions be first order type or there must be a precursor to one of the transitions at a higher temperature. What is that precursor ?

In last chapter we explicitly show that origin of the structural transition in 122 Fe based SCs is not lattice driven but an electronic one; the orbital ordering of Fe d_{yz} and d_{xz} orbitals [30, 133] is the primary reason for structural transition. Among some of the normal state properties of these compounds, transport in "preferred" direction has been observed unambiguously in many experiments – inelastic neutron scattering (INS) [23], scanning tunnelling microscope, impurity [147], resistivity [54], optical conductivity [148], angle resolved photo electron spectroscopy [133] and so on. Overall, origin of such phenomena is related to the breaking of four-fold rotational (C_4) symmetry of the tetragonal phase known as nematicity — the precursor. Whether the origin of nematic phase is spin driven or orbital driven is far from being settled. The nematic phase is observed in FeSe materials, that has structural transition at 90 K but no trace of long-range magnetic order [149] indicating nematicity is orbital fluctuation driven [150]. However, observation of an additional C_4 phase deep inside the orthorhombic (C_2) phase in $Ba_{1-x}Na_xFe_2As_2$ close to the suppression of magnetic spin density wave (SDW) order favours magnetically driven nematic order [151]. Role of nematic phase as regards to the mechanism of superconductivity or symmetry of Cooper pair wave function is not straight forward [152] but the fact that spin fluctuation leads to s^{+-} superconductivity [31] whereas the orbital fluctuation leads to s^{++} superconductivity in Fe-pnictides [37] are established and magnetism competes with superconductivity [87, 153]. There are also evidences of 'nematic order' in the pseudogap phase of the other class of high temperature cuprates superconductors which are known to be strongly correlated materials [154–157]. On the other hand, 122 family of Fe-based superconductors are generally considered as weakly correlated systems. Therefore, study of nematicity in Fe-based superconductors is of fundamental importance. Possible origins of nematic phase are well described in [66] as (a) structural distortion, (b) charge/orbital order, (c) spin order. Whatever be the nematic order parameter it must couple linearly to the orthorhombic distortion [158] and as shown in the previous chapter, orthorhombic distortion is electronic in origin. Nematicity on the other hand, introduces electronic anisotropy leading to two different nesting vectors which in turn leads to two competing spin density wave (SDW) instabilities ($Z_2 \times O(3)$ symmetry breaking) [153]. Coupling of the orbital order to SDW and vice versa has been used as inputs in Ginzburg-Landau formalism which provides qualitative understanding of nematic phase. A clear first principles understanding on whether there is any direct coupling between the magnetic (SDW) and orbital order in Fe-pnictides is absent till to date — is the main aim of this chapter.

Various modern X-ray diffraction techniques (*e.g.,* using Synchrotron radiation source *etc.,*) that determines crystallographic information at different external perturbations are essentially result of diffraction from various atomic charge densities (Bragg's diffraction). Using such experimentally determined structural parameters as a function of temperature for $BaRu_xFe_{2-x}As$ as inputs in first principles studies are expected to provide very accurate results, we provide results of such first principles simulations. We show through electronic structure calculation that the electronic orbital ordering locally breaks the in-plane symmetry and generate two non-equivalent a, b directions. In particular, we show that below structural transition (orthorhombic phase) there is a strong orbital anisotropy along the $\Gamma - X$ and $\Gamma - Y$ polarizations; the band at X is dominantly Fe-d_{yz} derived whereas that at Y, Fe-d_{xz} derived respectively. This feature reproduces correctly experimental angle resolved photo electron spectroscopy (ARPES) observation [133]. This is the root cause of orbital ordering in $BaFe_{2-x}Ru_xAs_2$ — we show that the temperature dependence of the orbital ordering at X(Y) point reproduces exactly that of orthorhombicity parameter (hence structural transition). Thus structural transition is primarily electronic in origin and phonons can not be a primary order parameter for nematicity. Whereas the temperature dependence of the same at Γ point is very weak (nearly independent of temperature) as observed experimentally [159]. Interestingly, Zhang et al., [159] observed that the orbital splitting (ordering) at Γ point (in case of FeSe) persists beyond structural transition temperature and argued that as against ferro-orbital ordering. In order to have a complementary first principles understanding over the experimental and other studies [23, 129, 133, 150, 151, 159] we introduce magnetic interaction through tuning integrated spin density defined as, I_s=$\int$($n_\uparrow$ (r) -$n_\downarrow$ (r))d^3r. In presence of finite integrated spin density I_s, spin selective orbital ordering are observed. Due to electronic orbital anisotropy (see Fig. 5.3) the SDW state may be viewed as a superposition of two SDW states. This is because of two reasons, (i) nesting wave vector that connects nested parts of Fermi arcs along the $\Gamma - X$ and $\Gamma - Y$ directions are different; (ii) overlap of Fe-d_{xy} band with d_{xz} and d_{yz} band is different (below structural transition) causing anisotropic charge and spin density fluctuations. Tuning I_s causes further perturbation to the underlying SDW as well as splits the spin degeneracy of energy bands. This magnetic interaction couple with orbital (charge) fluctuations causing further orbital anisotropy. Remarkably, this latter effect is observable only in the orthorhombic phase and *not* in the tetragonal phase. This would be experimentally verifiable by ARPES in presence of weak Zeeman field. In presence of I_s, we evaluate thermal variations of orbital ordering at different high symmetry points. We show that the magnetic interaction couples to the zone centre orbital ordering very strongly where as it has a substantial effect on the corner zone orbital fluctuation. We show that even if the energy orderings between d_{xz}/d_{yz} orbital is vanishingly small at the structural transition, the nematic order parameter, which is usually defined in literature as, ($n_{d_{xz}}$-$n_{d_{yz}}$) (that also reproduces thermal variations of orthorhombicity) remains finite above structural transition and has nearly no temperature dependence. These observations support the claim by Zhang [159], Fernandes [129] of magnetic origin of nematic phase. Finally, we show that the orbital occupancies of all the five d-orbitals of Fe show temperature dependencies below structural transition. This indicates to the fact that nematic order parameter may not simply be defined as ($n_{d_{xz}}$-$n_{d_{yz}}$) but charge fluctuations from other orbitals also need to be considered, for example, the thermal variation of ($n_{d_{xz}}$-$n_{d_{yz}}$)+($n_{d_{x^2-y^2}}$-$n_{d_{xy}}$) also follows that of orthorhombicity (see inset Fig. 5.5c). This will put constraints on many theoretical and experimental works so far.

5.2 Computational details

First principles density functional theories (see also chapter 2) can produce reasonably accurate solutions of the many electron Schrödinger equation if exact electronic density is being used as input. Various modern X-ray diffraction techniques *e.g.*, Synchrotrons radiation source *etc.* that determines crystallographic information at different external perturbations are essentially the result of diffraction from various atomic charge densities (Bragg's diffraction). Considering experimentally determined structural parameters at different temperatures as input thus in turn provides temperature dependent densities in our first principles calculation. These input structural parameters are kept fixed through out the calculation for a fixed temperature. This is how we use a T=0 DFT formalism to bring out temperature dependent observables with the help of experimental input. The main effect on the electronic structure from finite temperature is the underlying crystal structure, and the average crystal structure at finite T can usually be reliably determined from the diffraction experiment at a given temperature T. This method is somewhat superior to other similar methodology, like molecular dynamics (MD) simulation as follows. Through MD simulation one finds temperature dependent lattice parameters and then use standard T=0 DFT method using GGA exchange potential to calculate electronic structures [134, 135]. However, experimentally determined temperature dependent lattice parameters can be obtained with accuracy better than 0.001Å which may not be possible in MD. Using temperature and doping dependent experimental lattice parameters a(T,x), b(T,x), c(T,x) and z_{As}(T,x) [29], we obtain electronic structure as a function of temperature as well as doping, to explain the experimentally observed anomalies microscopically. We simulate electronic structures for both the phases, low temperature orthorhombic phase with anti-ferromagnetic (AFM) as well as spin density wave (SDW) ordering and high temperature paramagnetic tetragonal phase. In low temperature orthorhombic phase, along with non magnetic structures various spin configurations have been employed among which the lowest energy configuration is considered for electronic structure calculation [160]. Our first principles electronic structure calculations are carried out implementing plane-wave pseudopotential method within the framework of density functional theory [96]. In all of our temperature and doping dependent calculations the electronic exchange correlation energy is treated under the generalized gradient approximation (GGA) using Perdew-Burke-Enzerhof (PBE) functional [95]. Tackling small fraction of Ru substitution in place of Fe is accomplished by considering both, the virtual crystal approximation (VCA) as well as super-cell method for convenience. Super-cell method is a computationally expensive method adopted to mimic finite percentage of doping at a particular site. Let's say, for 5% doping at the Fe site one needs to build a super-cell (bigger unit cell) that contains 20 Fe atoms; then 1 of the Fe atoms are replaced by Ru atom (say). In the present case however, a super-cell containing 16 Fe atoms (total 40 atoms) are taken out of which one is replaced by a Ru (shown in FIG.5.1). This corresponds to $\sim$ 6% Ru doping which is close to the experimental situation. Note the size of the unit cell in the given symmetry is such that it does not allow exactly a super-cell with 20 Fe atoms. Spin polarized single point energy calculations are performed using

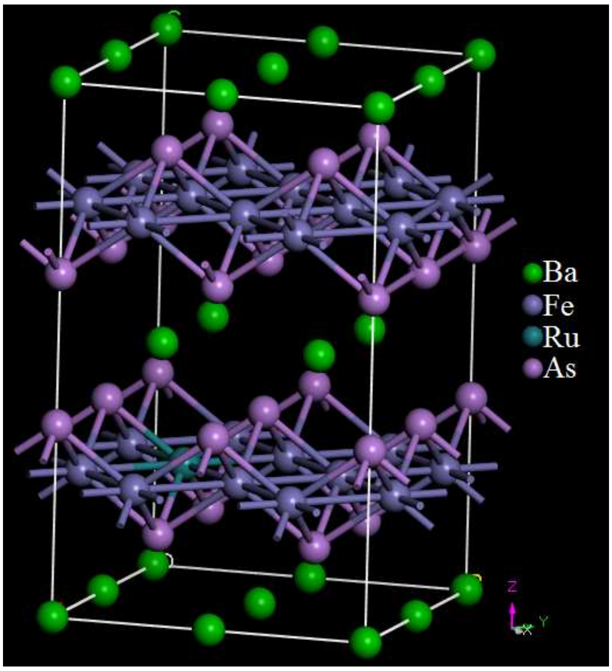

Figure 5.1: Structure of a 40 atoms super-cell of $BaFe_2As_2$, which contains 16 Fe atoms and one Ru atom. Different colours are used to indicate different atoms.

AFM and SDW configuration [161] (see inset Fig.5.5) for the low temperature orthorhombic phase with space group symmetry Fmmm (No.69) using ultrasoft pseudopotentials. Plane wave basis set with energy cut off 500 eV and self consistent field (SCF) tolerance 10^{-6} eV/atom has been opted for all calculations. Brillouin zone is sampled in the k space within Monkhorst-Pack scheme and grid size for SCF calculation is $12 \times 12 \times 12$ for electronic density of state calculation in primitive cell for orthorhombic phase. Band structure calculations are performed along various k-paths (X, Γ and Y) with k point separation 10^{-3} Å. Standard rotationally invariant approach due to Matteo Cococcioni and Stefano de Gironcoli [98] and V. I. Anisimov [97] is used to treat the Hubbard on site repulsion effect by post-DFT LSDA+U method which calculates and uses the total spin-projected occupation of the localized manifold, as this is essential to treat the Hubbard term. Therefore, the method of calculation of occupation probabilities of U effected orbitals remains same as that of the reference [97, 98] above which remains valid even in the limit U tending to zero.

5.3 Results and discussions

5.3.1 Orbital anisotropy in $BaFe_2As_2$

To probe orbital anisotropy, we have calculated band structures of $BaFe_2As_2$ system for anti-ferromagnetic (AFM) spin configuration (total spin zero) using experimental lattice parameters at 20K as well as 300K along some specified k-path. Our calculated band structures of $BaFe_2As_2$ along the k path $\Gamma-X-\Gamma-Y-\Gamma$ at two different temperatures corresponding to orthorhombic and tetragonal (20K and 300K) phases respectively are shown in Fig. 5.2. Circular envelopes are drawn around X,Y points which are then shown in Fig.5.3 where splitting of d_{xz}/d_{yz} at Γ point has also been highlighted. It is very clear from Fig.5.3(a) that at 20K (orthorhombic phase), band dispersion along $\Gamma - X$ direction is quite different compared to that in the $\Gamma - Y$ direction. In Fig. 5.3 the splitting of d_{xz}/d_{yz}

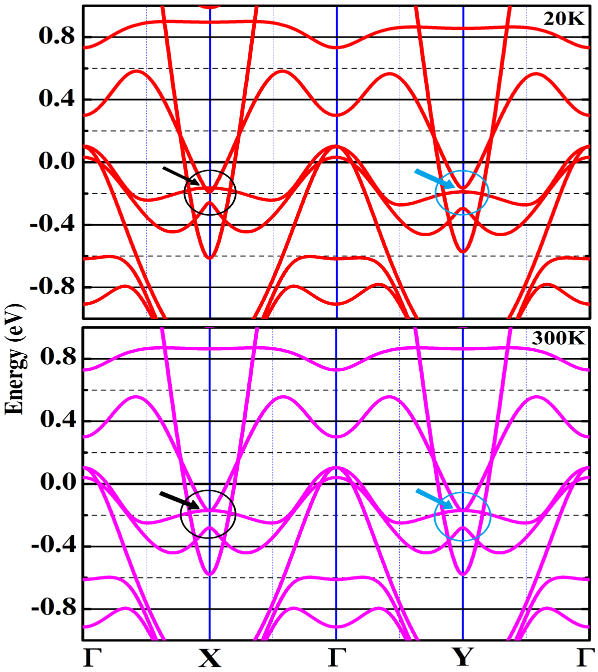

Figure 5.2: Calculated band structure of $BaFe_2As_2$ along $\Gamma-X-\Gamma-Y-\Gamma$ direction at 20K (red) in orthorhombic phase and 300K (magenta) in tetragonal phase. Orbital anisotropy along $\Gamma-X$ and $\Gamma-Y$ direction in the orthorhombic phase is worth noticing.

at Γ point has also been highlighted in the inset. The same for the room temperature is then compared with. Fig.5.3 demonstrate that the orbital ordering locally breaks the in plane symmetry and generates two non-equivalent a, b directions ⊥ to c. This results in two different nesting wave vectors along $Q_x = (\pi, 0)$ and $Q_y = (0, \pi)$ directions - that is spins are parallel to each other along X-direction and anti-parallel along Y-direction (O_3). We would also like to mention that at lower temperatures there exists two Fe-Fe distances (Z_2) [29, 162] and this makes the system anisotropic both magnetically as well as in terms of band motion. This situation resembles to that of the nematic phase where the bilinear combination of the order parameter ($O_3 \times Z_2$) breaks the tetragonal symmetry and is invariant under symmetry transformation. Because of the anisotropy of the bands along X and Y directions, in general, (overlap of the d_{xy} band with d_{xz} and d_{yz} bands are specially different) causes inter-band charge and spin fluctuations, which may cause for example, coupling between them resulting in different amplitudes of the SDW along Q_x and Q_y directions. Energy orderings of the non-degenerate d_{xz}/d_{yz} bands sets in orbital

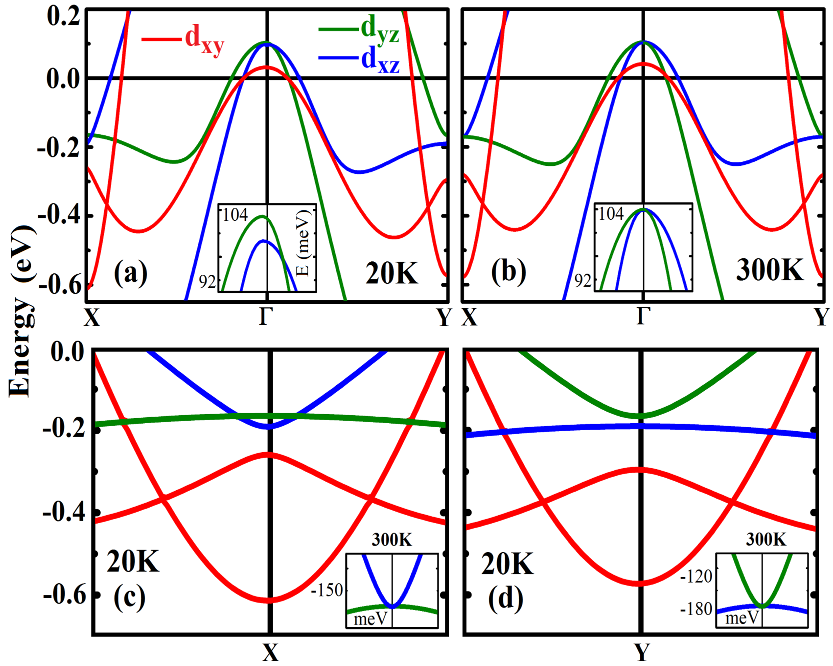

Figure 5.3: Calculated band structure of BaFe$_2$As$_2$ along $\Gamma - X - \Gamma - Y - \Gamma$ direction at 20K (upper) and 300K (lower) indicating various d orbital (d$_{yz}$, d$_{xz}$ and d$_{xy}$) using different colours. Orbital ordering in the orthorhombic phase is shown in the inset figure. Electronic orbital anisotropy at the X and Y points in the orthorhombic phase is the root cause of orbital order leading to structural transition.

ordering [162, 163], temperature dependence of which defines structural transition. This

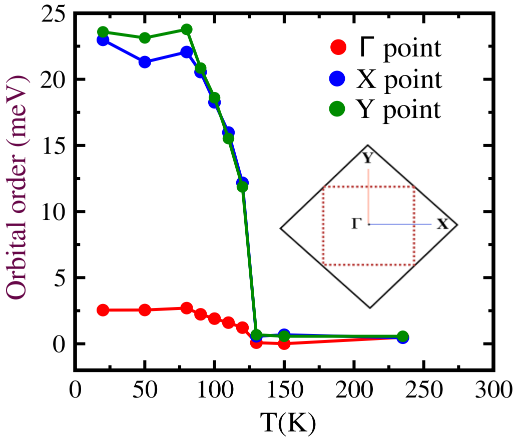

Figure 5.4: Calculated orbital order (meV) around X (blue), Y (green) and Γ (red) points as a function of temperature for 5% Ru doped BaFe$_2$As$_2$. Brillouin zone of orthorhombic BaFe$_2$As$_2$ has been shown in the inset of the figure indicating various k points (X, Y and Γ). The temperature dependence of orbital order is same as that of orthorhombicity (δ) [29].

is depicted in Fig.5.4. It should be clearly noted that the structural distortion is predominantly determined by the orbital ordering at X(Y) point; it is very weakly influenced by the orbital ordering at Γ point which has very weak temperature dependence. This clearly shows that the orbital ordering is very anisotropic. Now, question is why is that the orbital ordering at the (zone centre) Γ point is so weak but finite and independent of temperature? This is also observed experimentally by Zhang et al., [159] and modelled as bond-order. We argue below, this as manifestations of orbital anisotropy in presence of zone folding due to magnetic order in 122 systems. It is easy to envisage from the band structure in Fig.5.3 that because of inter-band nesting $\mathrm{E}_{d_{xz}}(k + Q_x) = -E_{d_{xz}}(k)$, but $\mathrm{E}_{d_{yz}}(k + Q_x) = -E_{d_{xz}}(k)$ and $\mathrm{E}_{d_{xz}}(k + Q_y) = -E_{d_{yz}}(k)$, but $\mathrm{E}_{d_{yz}}(k + Q_y) = -E_{d_{yz}}(k)$. These would make the nematic order parameter ($\mathrm{n}_{d_{xz}}$-$\mathrm{n}_{d_{yz}}$) null if the nesting wave vectors Q_x, Q_y were equivalent, but as it is not, it results in some small but finite quantity which is nearly independent of temperature. This feature is indicative of the fact that the orbital ordering would form a density wave and this along with the SDW state is inter-band in nature [87].

5.3.2 Relationship between nematic and orbital order

By now through above discussions it is nearly evident as to what is the source of temperature dependence of the orbital order parameter and may relate to the same of the nematic order parameter. The Fe band energies presented in Figs. 5.3 may be written as, $\mathrm{E(k)}=\sum_i \epsilon_i(k)n_i(k); i = d_{xz}, d_{yz}, d_{xy}, d_{x^2-y^2}, d_{(3z^2-r^2)}$ and the corresponding eigenstates involving orbitals are $\Psi = \sum_i c_i\phi_i$. $\epsilon_i(k)$ and n_i(k)s are the band energies and occupation probabilities of 'i'th orbital ϕ_i respectively. The ϵ_i(r)s being the Kohn-Sham orbit energies and the corresponding Fourier transformed ϵ_i(k)s are independent of temperature (and magnetic interaction introduced later through I_s), whereas the orbital occupancies (or densities) n_i(k) are function of temperature. Therefore, lifting of degeneracy of the d_{xz}, d_{yz} bands at the Γ and X points, as the temperature is lowered below structural transition temperature is a consequence of the fact that their occupation probabilities become different (*i.e*, partial densities become unequal). Note, the energy difference between the d_{xz},

d_{yz} bands at the Γ and X points is a function of temperature (see Fig. 5.4). The temperature difference essentially originates from the temperature dependencies of $n_{d_{xz}}$, $n_{d_{yz}}$ and is proportional to $n_{d_{xz}}$-$n_{d_{yz}}$ (see Fig. 5.5c). Therefore, it is desirable to calculate the temperature dependencies of the occupation probabilities of all the five d-orbitals of Fe from first principles calculation. Such a rare calculation is presented in Fig. 5.5. This quantity ($n_{d_{xz}}$-$n_{d_{yz}}$) represents inter orbital charge fluctuation or orbital fluctuation in short, one of the important contenders for nematic phase and is also called nematic order parameter. Using super-cell of orthorhombic $BaFe_2As_2$ structure corresponding to 5 % Ru doping and two types of spin arrangements AFM and SDW (shown in the inset of Fig. 5.5) first principles simulations of orbital occupancies are presented. Why dope $BaFe_2As_2$ with Ru? Like hole doped 122 systems iso-electronic Ru doped 122 system also have inseparably same structural as well as magnetic transitions and the nematic phase in this system remain unexplored. This is unlike other iso-electronic P doping in place of As. It is particularly an interesting case, it is not clear as to where does the charge carrier go in case of Ru dop-

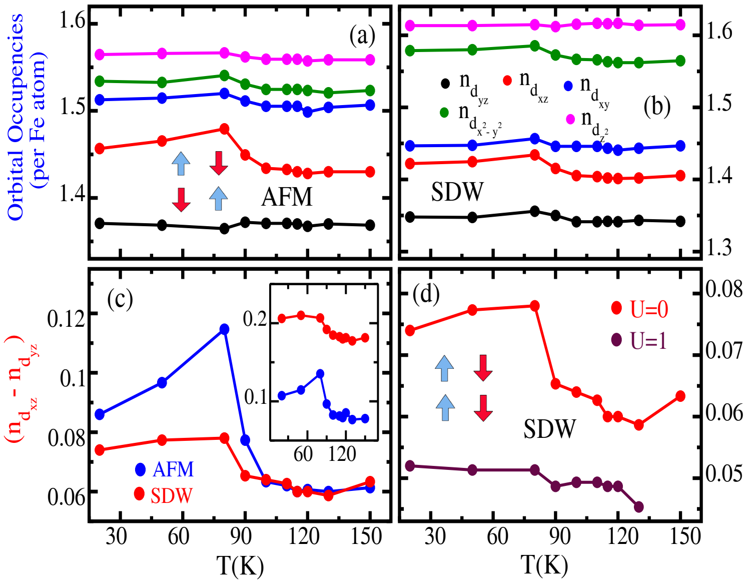

Figure 5.5: Total orbital occupancies per Fe atom (in real space) of various d orbitals of all Fe-atoms in the super-cell as a function of temperature for (a) AFM and (b) SDW spin configuration indicated in the inset. (c) ($n_{d_{xz}}$-$n_{d_{yz}}$) and ($n_{d_{xz}}$-$n_{d_{yz}}$)+($n_{d_{x^2-y^2}}$-$n_{d_{xy}}$) (inset) as a function of temperature for AFM (blue) and SDW (red) spin structures. (d) Thermal variation of ($n_{d_{xz}}$-$n_{d_{yz}}$) for SDW spin configuration considering correlation (U=1) using GGA+U formalism and with out correlation (U=0).

ing in place of Fe. Both the hole and electron Fermi pockets either remain unaltered or expands at an equal rate [123, 135]). Furthermore, both the structural and magnetic transitions are 2nd order in nature in case of underdoped Ru-122 system. Therefore, study of temperature dependence of orbital fluctuation from first principles is of genuine interest. In Fig.5.5 orbital occupancies of d$_{xz}$ orbital (n$_{d_{xz}}$) modifies significantly with temperature compared to the other d orbitals specially d$_{yz}$ and d$_{xy}$ (but they also do show substantial temperature dependence). We have also calculated the difference in the occupancies of d$_{xz}$ and d$_{yz}$ orbitals *i.e*, n$_{d_{xz}}$-n$_{d_{yz}}$ (nematicity) as a function of temperature for both AFM and SDW spin configuration (see Fig. 5.5c). Since, above structural transition there is no splitting between the d$_{xz}$ and d$_{yz}$ bands (*i.e,* $\epsilon_{xz} = \epsilon_{yz}$) temperature dependence of the nematic order parameter n$_{d_{xz}}$-n$_{d_{yz}}$ is proportional to that of the orbital order. In other words, the nematic order essentially grow as orbital order which is responsible for orthorhombic transition. Therefore, this result may be interpreted as the first principles evidence of the fact that if orbital fluctuation is the primary order responsible for nematicity, then it is proportional to the orthorhombicity parameter [129]. This is one of the inputs of all the theories involving Ginzburg Landau formalism. As already mentioned towards the end of computational details section: the method of calculation of occupation probabilities of U effected orbitals remains same as that of the ref. [97, 98] which is also valid even in the limit U tending to zero. Therefore, occupation probabilities are obtained for a very small U= 0.01eV (not exactly equal to zero) which makes up/down spin states different even in the tetragonal phase. As a result n$_{d_{xz}}$-n$_{d_{yz}}$ become very small but non-zero and has no temperature dependence. The difference in the nematic order parameter for SDW and AFM clearly indicates that it is also a spin nematicity. Furthermore, in the inset of Fig. 5.5c, we depict the thermal variation of (n$_{d_{xz}}$-n$_{d_{yz}}$)+(n$_{d_{x^2-y^2}}$-n$_{d_{xy}}$) which also reproduces thermal behaviour of orthorhombicity corresponding to orbital fluctuation involving all four d-orbitals. Thus, in contrast to the usual belief in literature, nematic order parameter which is defined as n$_{d_{xz}}$-n$_{d_{yz}}$, perhaps involve all other *d*-orbitals as well.

5.3.3 Magnetic interaction and orbital anisotropy

The nematic order parameters show substantial modifications near the temperature where magnetic order is very strong (see Fig.5.6). This provides a distinct evidence to the fact that probably magnetic order is behind the nematicity (we discuss this issue below). Also it should be noted that the orbital occupancies of d$_{xz}$ orbital is always greater than that of the d$_{yz}$ orbital *i.e.,* n$_{d_{xz}}$>n$_{d_{yz}}$. This propounds ferro-orbital ordering. Partial densities n$_{xz}$, n$_{yz}$ being unequal would correspond to different bonding along x and y directions, a mark of nematicity due to orbital anisotropy. Unlike cuprates it is experimentally well established that 122 family of Fe-based SCs are weakly correlated. In Fig. 5.5(d) temperature dependence of n$_{d_{xz}}$-n$_{d_{yz}}$ has been shown with small on site correlation (U=1) and with out correlation. It is clear that correlation reduces orbital order and so the magnetic order (see Fig. 5.6b). Magnetism plays an important role in these family of Fe-based SCs. By calculating Stoner factor one can predict the magnetic interaction in any system. Stoner factor of this compound can be defined as $I^{Fe} \times [N^{Fe}(E_F)]^2 + I^{Ru} \times [N^{Ru}(E_F)]^2$, where $N^{Fe}(E_F)$ and $N^{Ru}(E_F)$ are the density of states at the Fermi level from Fe and Ru atoms respectively [164, 165]. The value of Stoner parameters I^{Fe} and I^{Ru} are taken from ref [164, 166]. We have calculated the Stoner factor as a function of temperature and displayed in Fig.5.6a. As temperature changes, partial density of states of Fe and Ru at the Fermi level (E$_F$) get modified due to substantial moderation of Fe-As hybridization. This is the root cause of temperature dependence of Stoner factor. This observation is very much consistent with recent experimental findings [167]. In Fig. 5.6b thermal variation of Stoner factor has been depicted with different values of U (strength of electron correlation). It is clear that with increasing electron repulsion (system would prefer stable antiferromagnetic configuration) magnetic interaction is actually decreasing (so is the nematic order) which suggests that magnetism orbital fluctuation and nematic phase are intertwined.

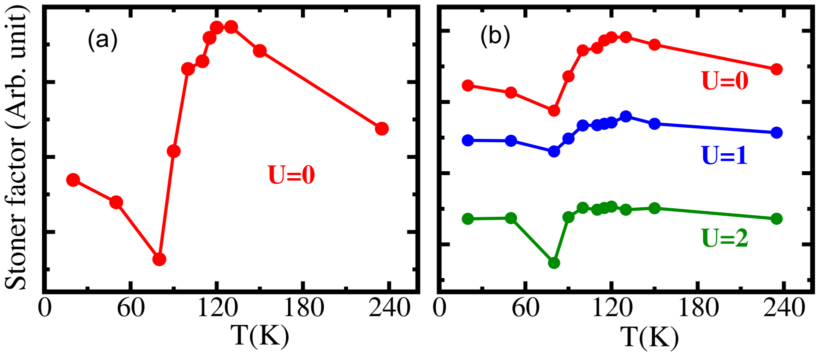

Figure 5.6: (a) Calculated Stoner factor ($I^{Fe} \times [N^{Fe}(E_F)]^2 + I^{Ru} \times [N^{Ru}(E_F)]^2$) as a function of temperature for 5% Ru doped $BaFe_2As_2$ and (b) thermal variation of Stoner factor for different U values as indicated in the figure.

For this purpose, we tune magnetic interaction manually by introducing integrated spin density parameter as introduced above and see its influence on electronic structure. While keeping initial AFM spin structure we provide constraint through the integrated spin density parameter for spin polarized calculations which induces some magnetic moment in the system. This method is a simple extension of standard LSDA formalism where total energy as a function of moment can be obtained. After complete spin polarized calculation being performed, the main idea is to perform a single point energy calculation keeping the total moment constrained to some fixed small but finite non zero values. This is equivalent to generating a weak Zeeman field (see also the form of the integrated spin density parameter). In this way by keeping the AFM spin configuration, magnetic interaction can be introduced to the system by simply fixing the total (difference in up and down spin) magnetic moment of the system through integrated spin density parameter. Actually, from electronic structure calculation we calculate orbital ordering again in presence of magnetic interaction (see below) and see that orbital anisotropy is enhanced, and hence the nematicity. In presence of finite integrated spin density, the bands of up spin electrons and bands of down spin electrons split. We observed that for I_s = 1 and 2, one of the bands (up spin) goes deep below the Fermi level. So only one of the spin electronic bands are contributing significantly at the Fermi level. In Fig. 5.7 we have shown the band structures of 5% Ru doped $BaFe_2As_2$ systems at 20 K, I_s = 1 for down spin (left) and up spin

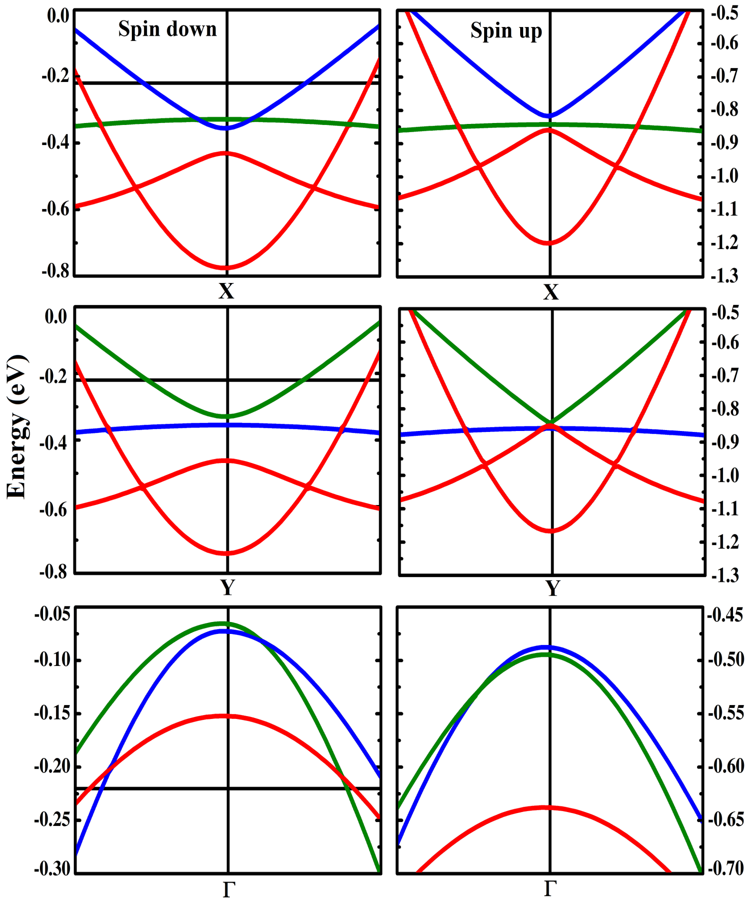

Figure 5.7: Calculated band structure of 5% Ru doped $BaFe_2As_2$ at 20 K with $I_s = 1$ for down spin (left) and up spin (right) electrons around X, Y and Γ points. We assign red green and blue colours to d_{xy}, d_{yz} and d_{xz} orbitals respectively.

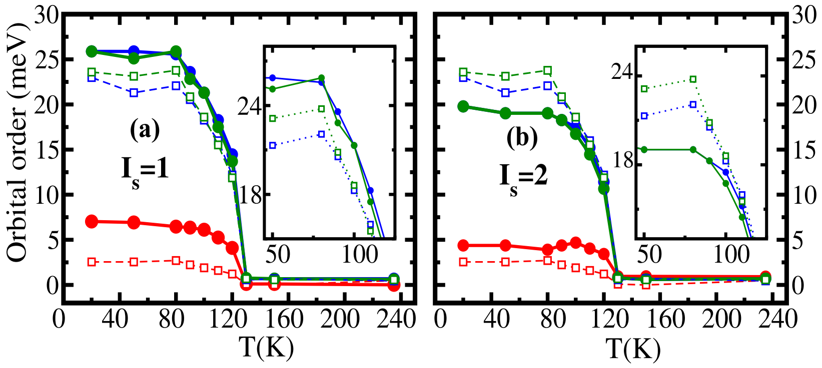

Figure 5.8: Calculated orbital order (meV) around X (blue), Y (green) and Γ (red) points as a function of temperature for (a) $I_s = 1$ and (b) $I_s = 2$ for 5% Ru doped $BaFe_2As_2$ systems. Hollow symbols represent data from Fig. 5.4.

(right) electrons around different k points (X, Y and Γ points). Notably, around X, Y and Γ points all the orbitals are ordered differently. Around X as well as around Γ point the energy ordering of d_{xz} and d_{yz} orbitals are exactly opposite to each other for up spin and down spin bands. This leads to spin-polarized orbital orderings (possibly orbital density wave). We do all the same exercises (in all the figures above) for K doped as well as P doped 122 systems and found that the orbital ordering is a common phenomena (there are differences in details). In Fig. 5.8 we have presented temperature variation of orbital order around X, Y and Γ points for $I_s = 1$ (Fig. 5.8a) and $I_s = 2$ respectively (Fig. 5.8b) after extracting the required information from Fig. 5.7. In case of $I_s = 1$ the orbital order around Γ increases to about 3 fold compared to the case where we optimized the total spin of the system (represented by hollow symbols). However, the orbital ordering around the zone corners X(Y) are less affected. When the integrated spin density is increased to 1 from 0, it stabilizes the underlying SDW, but when I_s is further increased to 2, the underlying SDW ordering will be strongly suppressed due to ferromagnetic nature of the I_s. Hence, orbital ordering is coupling of magnetic degrees of freedom to the underlying magnetic degrees of freedom. We consider this as an evidence of magnetic origin of nematic phase and our study thus is complementary to recent studies [129, 133, 159, 168, 169] on nematic phase.

5.4 Conclusions

We establish the microscopic relationship between the orbital order, structural transition and nematic order in 122 family of Fe-based superconductors. While electronic orbital anisotropy gives rise to orbital order, temperature dependence of the orbital order is found to be exactly same as that of the orthorhobicity, indicating orbital ordering is responsible for structural transition as discussed in quite details in the previous chapter. Temperature dependence of the orbital order is proportional to the temperature dependence of the nematic order ($n_{d_{xz}}$-$n_{d_{yz}}$). This indicates that the nematic order grows as orbital order in the orthorhombic phase. We have explicitly evaluated the temperature dependencies of orbital occupancies of all Fe-d-orbitals. Almost all the d-orbitals show substantial charge fluctuations in the orthorhombic phase, indicating that the actual definition of nematic order parameter may be more complicated. The nematic order parameter is found to show temperature dependence close to the onset of magnetic instability, obtained rigorously through evaluation of Stoner factor. When Stoner factor is enhanced, the orbital fluctuations are also enhanced and vice versa establishing their couplings. Spin-polarised orbital ordering revealed from this work would be experimentally observable. Finally, our work supports coupling of magnetic degrees of freedom to nematicity in 122 family of Fe-based superconductors.

Chapter 6

Fermiology and dimensional cross-over in Fe-based superconductors

6.1 Introduction

Iron based superconductors (SCs) possess very unusual Fermi surface topology or in short Fermiology, which is extremely sensitive to various external parameters like doping, pressure as well as temperature. Close proximity of superconductivity to structural and magnetic transitions, glue for the superconducting pairing, etc. are concomitant to electronic structure near Fermi energy or more precisely Fermiology which is believed to play a key role in magnetism and superconductivity of high T$_c$ superconductors including Fe-based SCs. The Fermi surface is simply the surface in momentum space where, all the Fermionic states with (crystal) momentum $|k| < |k_F|$ are occupied, and all the higher momentum states are empty. Fermi surface (FS) of Fe-based SCs mainly comprises of Fe d-orbital. Angle-resolved photo-emission spectroscopy (ARPES) is one of the proficient experimental techniques by which FSs can be mapped. With the purpose of elucidating the relevance of Fermiology to the superconducting pairing mechanism from an experimental standpoint, several ARPES measurements have been performed on iron-based superconductors [170–172]. The role of FS in the development of understandings in superconductivity cannot be overemphasized [31, 37, 47, 113, 136, 173]. Electronic states of Fe-based superconductors and superconducting (SC) pairing mechanism are very much different from that of the high-T_c cuprates [173, 174]. FS measurement is one of the probing ingredients to understand the nature of pairing of electrons in Fe-based SCs. Shape of the Fermi surface is very crucial as it determines the degree of nesting in Fe based SCs which in turn give rise to magnetic and orbital ordering [87]. Unlike spin fluctuation mediated superconductivity in cuprates and heavy fermions, orbital fluctuation has also been proposed as one of the possible pairing mechanism of superconductivity in these materials [31, 84, 175]. Such fluctuations are supposed to be resulting from the quasi nesting between hole and electron like Fermi surfaces (FSs). Angle-resolved photo emission spectroscopy (ARPES) measurements, have been conducted on iron-based superconductors, especially for 122 family to reveal the Fermiology of Fe-based superconductors because of availability of large numbers of high quality single crystals in this series. Theoretically calculated FS of 122 family is also available in literature [165, 174, 176–178]

The 122 family like $BaFe_2As_2$, $CaFe_2As_2$, $SrFe_2As_2$ *etc.* comprises the heart of Fe-based superconductors where best quality single crystals are available. All these materials (undoped) exhibit spin density wave (SDW) order below a transition temperature (T_{SDW}) and incidentally at the same transition temperature where the structural transition from tetragonal to orthorhombic (low temperature) phase occurs. Although these parent compounds of 122 family are not superconducting and superconductivity can emerge either by applying external pressure or by chemical doping. In fact doping can be performed in any of the three sites (Ba, Fe and As). When Ba is replaced by K or Fe is replaced by Co, incorporate hole [18] and electron doping [13] respectively. The introduction of extra hole or electron shifts the chemical potential in $Ba_{1-x}K_xFe_2As_2$ [18] and $BaFe_{2-x}Co_xAs_2$ [13] in such a way that the size of the electron and hole like FSs evolve oppositely which diminishes the nesting between them, resulting suppression of spin density wave (SDW), orbital density wave (ODW) orders and SC emerges. What change in FS is then expected for isovalent substitutions? (like Ru substitution at Fe site or P substitution at As site) The observation of suppression of SDW order with isovalent substitution in $BaFe_2(As_{1-x}P_x)_2$ and $BaFe_{2-x}Ru_xAs_2$ systems is therefore, still not understood properly [103, 179–182]. We show that there are no significant changes either in electron or hole like FSs upon substantial Ru substitution and this observation is consistent with the observations of Dhaka *et al.,*[179]. But at about 50% doping there is significant change in the hole like FSs which is also consistent with the experimental findings of N. Xu *et al.,*[183]. We study on the nature of FSs when doped in any of the three sites mentioned above through first principles simulations. From our calculations we explicitly show that in case of hole doping the charge carriers go to hole FSs resulting expansion of hole FSs and shrinking of electron FSs and a reverse situation occurs in case of electron doping. This however, is not the case when FS undergoes topological modification (see chapter 7 for details). In case of isovalent P substitution in place of As, causes substantial z-direction dispersion in the hole bands, making shape of some of the hole FSs more like three dimensional which is consistent with experiments [105, 184] and is believed to be responsible for nodal superconductivity. On the other hand, two dimensional FSs which are more favourable to nesting are believed to be responsible for high T_c superconductivity in Fe-based materials [122]. Theoretically computed FSs of various doped “122” systems like $BaFe_2As_2$, $SrFe_2As_2$, $Ba_{1-x}K_xFe_2As_2$, $BaFe_{2-x}Ru_xAs_2$, $BaFe_{2-x}Co_xAs_2$, $BaFe_2As_{2-x}P_x$ are presented in this chapter. Similarities and dissimilarities are compared among them, and compared with available experimental data.

6.2 Computational details

As discussed in the second chapter of the thesis (Theoretical methods), one of the shortcomings of the density functional theory (DFT) under the generalized gradient approximation (GGA) is that it fails to reproduce experimental z_{As} which governs many other physical properties crucially [29–32]. Experimental doping dependent lattice parameters $a(x)$, $b(x)$, $c(x)$ and $z_{As}(x)$ are used as inputs in our first principles simulations. Our first-principles ab initio simulations of Fermi surfaces are performed using CASTEP module of Material studio 7.0 [96], which exploits the plane-wave pseudopotential method based on density functional theory (DFT). In our simulations the electronic exchange correlation is treated under the generalized gradient approximation (GGA) using Perdew-Burke-Enzerhof (PBE) functional [95]. Geometry optimization has been carried out for two parent compounds of 122 system in which we fixed z_{As}. Tackling small fraction of doping (Co/Ru/K/P) in place of Fe/Ba/As is implemented by considering virtual crystal approximation (VCA) based on the Mixture Atom Editor of CASTEP in Material Studio 7.0. Non-spin polarized and spin polarized single point energy calculations are performed for tetragonal phase with space group symmetry I4/mmm (No.139) using ultrasoft pseudopotentials and plane wave basis set with energy cut off 500 eV and self-consistent field (SCF) tolerance as 10^{-6} eV/atom. Brillouin zone is sampled in the k space within Monkhorst-Pack scheme and grid size for SCF calculation is $25 \times 25 \times 33$. All these calculations have been carried out using primitive unit cell.

6.3 Results and discussion

6.3.1 Geometry optimized Fermi surfaces of 122 systems

FSs have been calculated for two 122 parent compounds $BaFe_2As_2$ and $SrFe_2As_2$ using experimental structural parameters in tetragonal phase as well as geometry optimized structures. Fig.6.1 depicts the simulated FSs of $BaFe_2As_2$ and $SrFe_2As_2$ where three hole like FSs appear at the centre of the brillouin zone around Γ point and two electron like FSs appear at the four corners of the brillouin zone (X point). Calculated FS topology for both parent compounds are very similar. There are experimental evidence of SDW ordering in both the parent compounds at low temperature. This SDW ordering is the result of inter band nesting between electron and hole like FSs [87]. Two dimensional nature of the FSs in both the systems enhance nesting and results SDW ordering. Whereas FSs generated

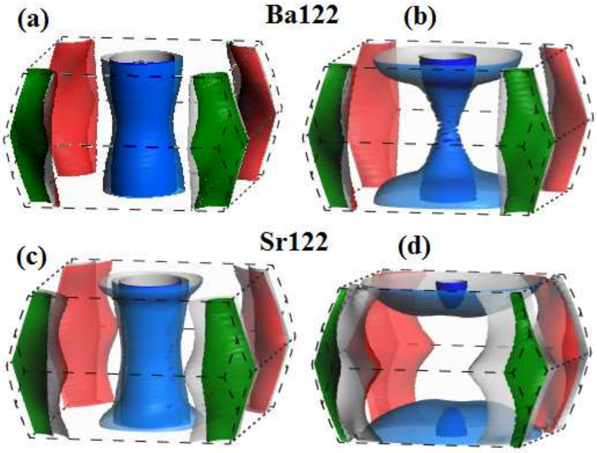

Figure 6.1: Calculated FSs of undoped 122 Fe-based SCs for (a) $BaFe_2As_2$ (b) optimized structure of $BaFe_2As_2$ (c) $SrFe_2As_2$ and (d) optimized structure of $SrFe_2As_2$. In each figure FSs at the center are hole like FSs, shaded blue and FSs at the corners are electron like FSs, shaded red and green.

from optimized structure is more like three dimensional which works against nesting and reduces the chance of SDW ordering. So FSs calculated using experimental lattice parameters provide more realistic FSs that resembles with the experimentally observed one [52, 185].

6.3.2 Fermi surface of doped 122 systems

We have also studied various doped “122” systems using VCA approach. Fe d-orbitals mainly constitute the FSs of Fe based SCs. We found that at larger doping at the Fe site VCA fails and deviates from the actual FS topology. So for some of the calculations we adopt super cell method for example 50 % Ru doping. Fig.6.2 and Fig.6.3 illustrate simulated FSs of K-doped (hole doping) systems at various K doping concentrations. It is very clear from Figure6.2 and Figure6.3 that K doping exerts extra holes to the system which expand the hole like FSs at the centre whereas electron like FSs shrink at the corners. Exactly the reverse scenario occurs for Co doping (see Fig.6.4a and 6.5a) is observed. A more closer look on Fig.6.2 and Fig.6.3 reveals that there is significant changes in electron

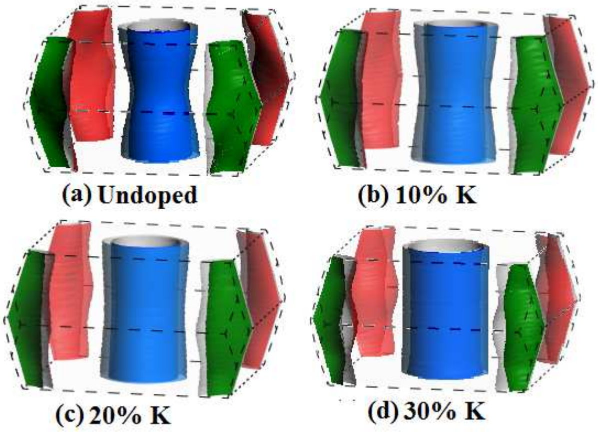

Figure 6.2: Simulated FSs of K doped $BaFe_2As_2$ system for various K doping concentration

and hole like FSs upon K doping. With increasing K concentration the k_z dispersion of one of the hole FS (outer one) becomes more and more weak whereas around 30 % doping all the hole FSs take the shape of a perfect cylinder. Electron FSs also evolve significantly with doping and shows weaker k_z dispersion with increasing doping concentration. Thus a transition in FS structure from quasi -3d to quasi -2d structure with doping is observed. As the hole and electron FSs evolve oppositely with K doping, the overall nesting condition degrades due to size mismatch of the FSs resulting in suppression of SDW order but at the same time two dimensionality of the FSs in these systems favours very large density of states, at the Fermi level, enhancing the electron pairing possibilities. So a competing order of superconductivity and magnetism are likely to co-exist.

Using two band model it was shown that apart from inter band pairing superconductivity can also arise from intra band pairing and combined intra-inter band pairing results in higher T_c compared to only inter band scenario [162]. The effect of inter band scattering also depends on the topology of FS. These facts probably explain the reason of significantly higher T_c in K-doped system compared to other 122 systems. In case of Co doping with increasing doping concentration the electron FSs expand and hole FSs shrink whereas the k_z dispersion is stronger. It is presented in Figs 6.4, Fig.6.5a and is found consistent with earlier theoretical and experimental results [174]. This suppresses magnetic

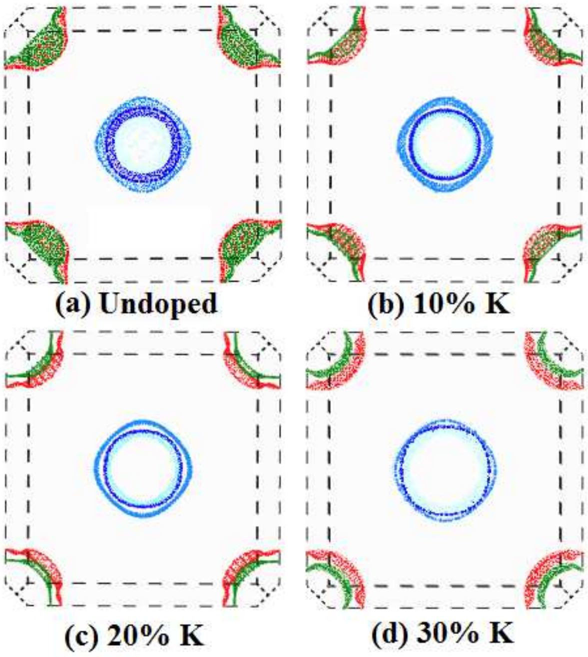

Figure 6.3: Top view of the calculated FSs of K doped $BaFe_2As_2$ for various K doping concentration (in k_x-k_y plane) along k_z direction.

ordering and superconductivity emerges into these systems. On the other hand, substantial P doping in place of As, (like 32%) modifies hole FSs considerably as shown in Fig.6.4b and Fig.6.5b. Contrast to K doping, in P-doping (in place of As, a clear dimensional cross-over from two to three dimensions is observed in the FS structure modifications consistent with the result of reference [186]. However, no significant changes in both the electron and hole FSs occur upon Ru substitution up to 35%, as was also found in experiments [179]. At about 50% Ru doping there is significant modifications in the hole like FSs; more precisely, a dimensional crossover from two to three dimension occurs which is also consistent with recent experiments[183]. But calculated FS of $BaRu_2As_2$ indicates complete loss of two dimensionality of hole FSs which in turn causes degradation of nesting. This explains the absence of magnetic order (SDW) in $BaRu_2As_2$. In Fig.6.4c, 6.4d and 6.4f, evolution of FSs with Ru doping has been depicted. In Fig.6.5 “top view" of all the FSs of Fig.6.4 are represented to illustrate the changes in the sizes of the Fermi pockets. A closer look at all the Fermi pockets (Fig.6.5) reveal that there are three hole like FSs in most the cases, one symbolized by light blue ring (outer) and other one by deep blue ring

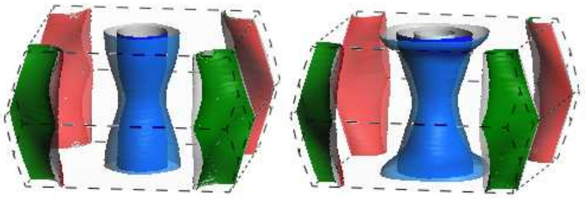

(a) 10% Co (b) 32% P

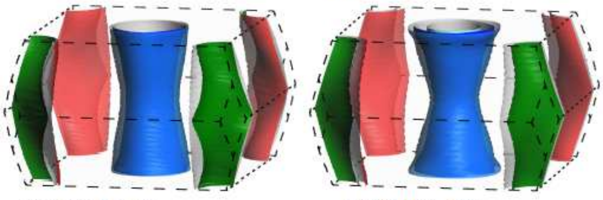

(c) 10% Ru (d) 50% Ru

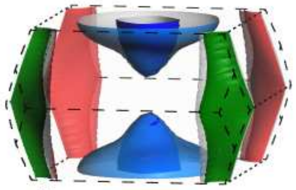

(e) 100% Ru

Figure 6.4: Fermi Surface of various doped 122 system: (a) 10% Co doped (b) 32% P doped (c) 10% Ru doped (d) 50% Ru doped $BaFe_2As_2$. (e) Calculated FS of $BaRu_2As_2$

(inner). The inner and outer radii of any of the “Fermi rings" denote the radii of the FSs around Γ and Z points respectively (k_z dispersion). These are experimentally measurable through ARPES studies and are found to be consistent with some of the observed momentum distribution curves [179]. Momentum distribution curves in general, are useful to estimate both components of the electronic self energy (real and imaginary parts) which is a powerful aspect of ARPES study. The momentum distribution curves of Fe-based materials are directly related to the Fermi surface radii because, it is a measure of electronic band structure dispersion width of a given band — how close or far (thus proportional to Δk) the electronic band intersects two Fermi points. In case of Co, P doping, changes in the sizes of the FSs and dimensionality cross-over (3D) reduce nesting and thus suppress magnetic order, e.g., $BaRu_2As_2$. All these results indicate a possible competition between superconductivity and magnetic order (SDW). SDW order (or orbital order) is controlled by inter band nesting of FSs which in turn is related to the dimensionality of the FSs. Emergence of superconductivity in these Fe-based systems seem to be originated from

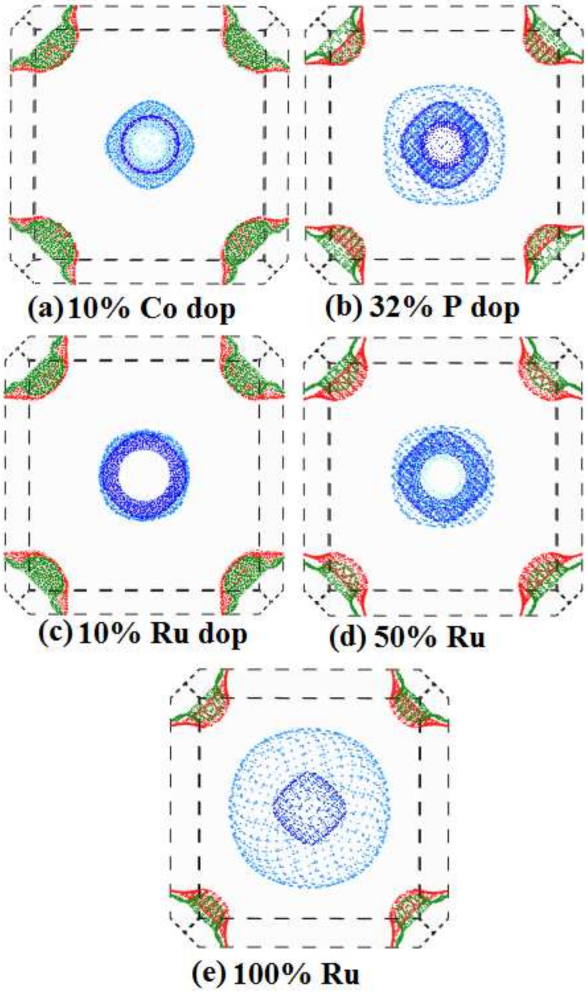

Figure 6.5: Top view of the FSs of various doped "122" system (in k_x-k_y plane) along k_z direction.

spin fluctuation or orbital fluctuation which may be enhanced by quasi nesting of two dimensional electron and hole FSs as suggested by M. Sunagawa *et al.,*[122]. Since the FS are Fe-d orbital derived, Co-doping (which has a lesser d-electron) clearly causes disturbance and makes modification to the electronic and hole FSs. On the other hand, P doping in place of As does not cause change in the d-orbital occupancy of Fe directly, but it causes change in the pnictide height causing a z-direction dispersion. Similarly, Ru having larger atomic dimension than Fe, when replaced, the in-plane lattice parameter *a* increases whereas the out of plane lattice parameter *c* decreases after certain doping, affecting z-dispersion in band structures. Both the above two does not occur in case of K doping in place of Ba that effectively. These are the possible origins for different nature of dimensional cross-over in the FS structure with substitutions in various 122 systems.

6.4 Conclusions

Calculated FSs of the parent compounds of 122 systems are very similar in topology. Presence of quasi two dimensional hole and electron like FSs enhances the chance of nesting. This is the reason why these parent compounds display magnetic and orbital ordering [122, 187]. A dimensional cross-over, in theoretically computed FS topologies of various Fe-based materials of “122" family are presented with various kinds of doping. Our results are consistent with experimental observations and its possible significance to magnetism and SC are presented. In case of electron and hole doping, sizes of the electron and hole Fermi pockets evolve oppositely with increasing doping concentration. Isovalent Ru substitution up to certain doping makes no visible modifications in the electron and hole like FSs but in case of 32% P doping there are substantial changes in the hole FSs. 100% Ru substitution modifies hole FSs remarkably. From all these calculated FSs it is very clear that dimensionality of FS (linked with inter band FS nesting) plays an important role in 122 Fe-based SCs. While we stop discussing FS-topology of 122 materials in this chapter, a great deal of it are revisited in chapter 7 in the context of topological transitions in Fe-based SCs. Behaviour of FS topology is very different than seen in this chapter in presence of electronic topological transition.

Chapter 7

Electronic topological transitions in 122 family of Fe-based superconductors

7.1 Introduction

In the previous chapter, we investigated the evolution of Fermiology of various doped 122 Fe-based SCs with increasing doping concentration which remains valid only in the absence of electronic topological transition. Electronic topological transition of the Fermi surface with no broken symmetries, also known as Lifshitz transition plays significant role in numerous branches of condensed mater physics. For example, the collapse of the normal state pseudogap at a Lifshitz transition in $Bi_2Sr_2CaCu_2O_{8+\delta}$ cuprate superconductor [188], Lifshitz transition in underdoped cuprates [189], Dirac Semi metal [190], relativistic insulator $NaOsO_3$ [191], discontinuous Lifshitz transition in Na_xCoO_2 [192], Zeeman driven Lifshitz transition in $YbRh_2Si_2$ [193], in two-dimensional Hubbard model [194], bilayer graphene [195], Quantum Hall Liquids [196], to mention a few. The Lifshitz transition which is recently considered as a quantum phase transition in strongly correlated electron systems also plays a remarkable role in Fe-based high T_c superconductors owing to its special 'Fermiology' and multi-band nature [197, 198]. The phase diagrams of

Fe-based superconductors (SCs) consists of a number of exhilarating features apart from its novel superconducting phase [103–105, 142, 199]. Various phases are very much sensitive to external parameters like impurity, doping, temperature and pressure. If we only consider the most studied 122 family of Fe-based SCs, the emergence of superconductivity as well as other exotic phases (like spin density wave, orbital order, nematic and structural phases etc.,) are not very well understood. On the other hand, Lifshitz transitions are experimentally observed with respect to some of the above mentioned external parameters [200–202]. Therefore, the possible influence of the Lifshitz transition on various phases of Fe-based superconductors and on various physical properties cannot be underestimated.

A lot of theoretical and experimental investigations are carried out to procure understanding of all the phases that are present in the 122 Fe based superconducting family [37, 70, 87, 113, 129, 136, 142, 203]. But still there remains a large number of unanswered questions to be addressed. For example, the mechanism of superconductivity or the pairing symmetry [31, 37, 75, 162, 204], the primary order for the nematic phase, its influence on superconductivity and other phases [70, 129, 168, 169], as well as the role of Lifshitz topological transition to superconductivity etc. The electronic structure of these 122 Fe-based superconducting system is quite complicated as replicated from its unusual Fermi surface (FS) topology. It is also well established that the electronic structure, superconducting T_c, Stoner factor *etc.* are highly sensitive to various structural parameters like anion height (z_{As}, fractional z co-ordinate of As atom), Fe-As bond length, as well as As-Fe-As bond angles [20, 24, 28–30]. This makes comparison of theoretically predicted electronic structures (Fermi surface, band structure, density of states) with the experimentally measured one a delicate issue. Lifshitz transition (LT) or electronic topological transition (ETT), where FSs/electronic bands alter topology, have been usually investigated as zero temperature phenomena arising due to impurity, doping or pressure etc. However, temperature dependent LT/ETT is observed recently in WTe_2 [205]. In order to examine the influence of LT/ETT to superconductivity as well as on other phases, a comprehensive thorough study of LT/ETT on a large number of 122 family compounds is required. This is the primary aim of this work.

The consequences of these LT/ETT are innumerable. It can lead to anomalies or singularities in the density of states near Fermi level (FL), anomalies in the kinematics, dynamics and thermodynamics of electrons *etc*, which in turn results in anomalies in various physical properties [139]. LT/ETT is also observed in Fe-based SCs mainly induced by pressure, impurity and doping as far as current literature is concerned [198, 200, 206–208]. In this chapter, we mainly discuss the impurity, doping as well as temperature induced Lifshitz transitions in 122 family of Fe-based SCs. In particular, for Ba122 system, LT is predicted theoretically due to small but unintentional Sn impurity in contrast to other 122 systems like Sr122 and Ca122 [207]. In hole doped Ba122 system LT is also found in the heavily doped regime as evident from the theoretical work of Khan et. al., [198]. On the other hand, experimental observation of LT in electron doped Ba122 system is also available in the literature [205]. But temperature induced LT not only in Fe based SCs but in general is rare. In this chapter we present detailed investigations of ETT/LT in 122 family of Fe-based SCs. In this context, the possible correlation between LT/ETT and superconductivity is achieved and discussed in fare details. We have also predicted the manifestations of temperature dependent LT in Ru doped Ba122 system. The crucial role of structural parameters obtained from experiments, in these ETT/LT are also presented in this chapter.

7.2 Computational details

Our first principles electronic structure calculations are performed by using CASTEP which is a plane wave psudopotential method based on density functional theory [96], where the electronic exchange correlation is treated under the generalized gradient approximation (GGA) using Perdew-Burke-Ernzerhof (PBE) functional [95]. Experimentally measured orthorhombic (20 K) as well as tetragonal (300 K) structural parameters *i.e., a*, *b*, *c* and z_{As} (fractional z co-ordinate of As atom)[18, 209–211] are used as inputs of our first principles electronic structure calculations like density of states (DOS), band structures and Fermi surface. Implementation of Sn impurity in $BaFe_2As_2$, $CaFe_2As_2$ and $SrFe_2As_2$ systems as well as implementation of doping has been treated within virtual crystal approximation. This VCA methods forge us to use the same atomic co-ordinates for Ba and Sn atoms which is not the actual condition, where Sn atoms are situated at slightly different co-ordinates (0, 0, 0.093) close to Ba (0, 0, 0) atom. This displacement of Sn atom is accounted for the stereo-chemical active lone pair of the formal divalent Sn atom which results in a change of the coordination sphere which is a Sn^{2+}−typical square pyramidal coordination by four As atoms [209]. In this case, we use the virtual crystal approximation (VCA) method, developed by Bellaiche and Vanderbilt [111] based on weighted averaging of pseudopotentials (discussed in chapter 2). In VCA, a doped crystal with original periodicity but composed of fictitious ‘virtual atoms’ is created to mimic the actual doped system. For example, one can construct a virtual atom like $A_{1-x}B_x$ for a single lattice site, where x is the doping concentration and thus overlooks any possible short range order. One uses ultra-soft pseudopotentials which are prone to generating ghost states in the VCA framework, while none of the individual potentials has a ghost state. There is a standard way of testing the VCA approach for ghost states, one should always examine the value of the derivative of the total energy w.r.t. E_{cut} (E_{cut} defines the size of plane wave basis set) during the finite basis set correction calculation. It should be of the same order as the derivatives for the end-member structures [212]. We have checked this value for all these three systems up to 5% Sn doping in order to inspect the applicability of VCA method in these cases. Both spin-polarized (for orthorhombic phase with space group symmetry Fmmm [No. 69]) as well as non-spin-polarized single point energy calculations are carried out (for tetragonal phase with space group symmetry I4/mmm [No.

139]) using ultrasoft pseudo-potentials and plane-wave basis set with energy cut off 600 eV and self-consistent field (SCF) tolerance 10^{-6} eV/atom. Brillouin zone is sampled in the k space within Monkhorst–Pack scheme and grid size for SCF calculation is chosen as $26 \times 26 \times 26$.

7.3 Results and discussion

7.3.1 Impurity induced Lifshitz transition

Single crystals of $BaFe_2As_2$ (Ba122), $SrFe_2As_2$ (Sr122) and $CaFe_2As_2$ (Ca122), synthesized from tin-flux method contain a few percentage (1%-5%) of Sn incorporated into the crystal structure. As a result of Sn impurity, the crystallographic structure of 122 systems get modified [18, 209, 213]. It was found that 95% of the 2a site (0,0,0) is occupied by Ba atoms and the rest are found to be replaced by Sn atoms at the site 4e (0,0,z with z=0.093) [209]. It is obvious from current literature that electronic structures of 122 systems are highly influenced by certain moderation of structural parameters [28, 29, 123]. This incorporation of Sn impurity leads to certain changes in the physical properties of Ba122 system. The presence of a small fraction of Sn impurity in $BaFe_2As_2$ (Ba122) system curtails down the structural as well as SDW transitions from 138K to 85K and also give rise to a notable difference in the thermal behaviour of electrical resistivity and magnetic susceptibility [208, 213–215]. On the other hand, no significant modifications in the physical properties of Sr122 and Ca122 systems are observed due to the presence of Sn impurity. Since these structural and magnetic transitions are intimately related to the electronic structures, it calls for the study of detailed electronic structure through density of states (DOS), band structures and Fermi surfaces of $BaFe_2As_2$ in presence of Sn impurity. Such a study is absent from current literature. In this section, we present our detail calculated DOS, band structures and FSs of Ba122, Sr122 and Ca122 systems with inbuilt Sn impurity. Our main aim is to examine effect of Sn impurity in the electronic

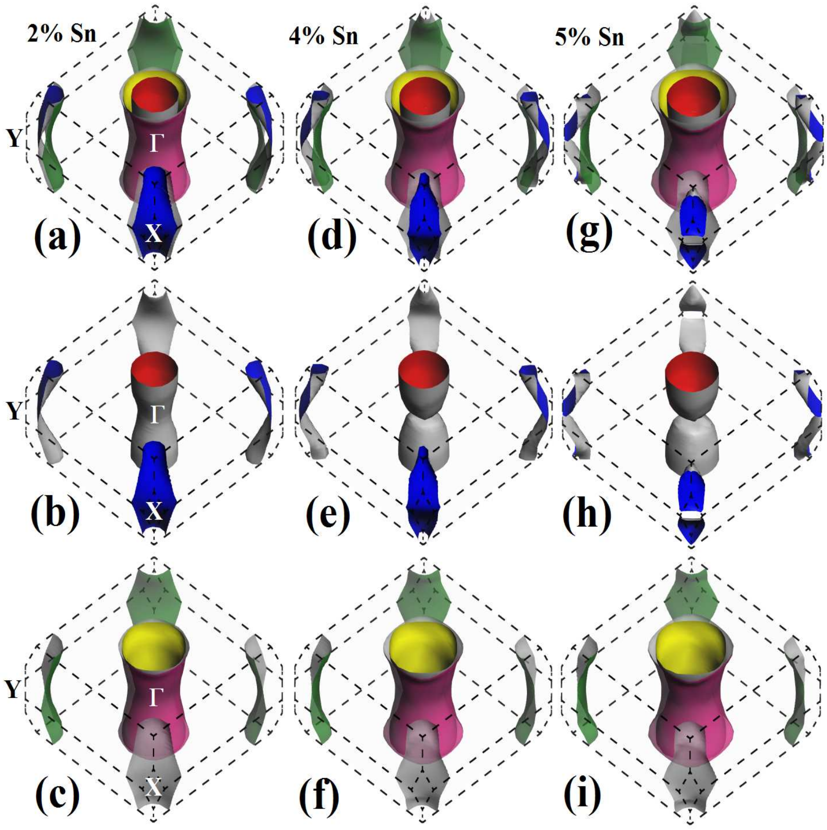

Figure 7.1: Calculated Fermi surfaces in orthorhombic phase within VCA method for (a, b, c) $Ba_{0.98}Sn_{0.02}Fe_2As_2$, (d, e, f) $Ba_{0.96}Sn_{0.04}Fe_2As_2$ and (g, h, i) $Ba_{0.95}Sn_{0.05}Fe_2As_2$ systems. For clarity individual FSs are shown separately in 2nd and 3rd row. Different colours are used to indicate different FSs. k points in the Brillouin Zone (BZ) are also indicated in (a). Shrinkage of electron like FSs and surging of hole like FSs are worth noticing. This indicates hole doping.

structures of Ba122, Sr122 and Ca122 systems within VCA method. We calculate DOS, band structures and FSs of these three systems (pure and Sn contaminated) using experimental lattice parameters (a, b, c, z_{As}) in the orthorhombic (low temperature) phases. No significant differences in the calculated DOS for pure and Sn contaminated 122 systems are observed. We exhibit our calculated electronic structure in the orthorhombic phase where experimentally measured orthorhombic lattice parameters are used as the input of our first principles calculations. It should be mentioned here that the structural transition in these materials is due to the orbital ordering between d_{yz} and d_{xz} bands around high symmetry k points [30] (see chapter 5). In FIG.7.1 we depict the FSs of $BaFe_2As_2$ systems with various percentages of Sn impurity. There are two electron like FSs around

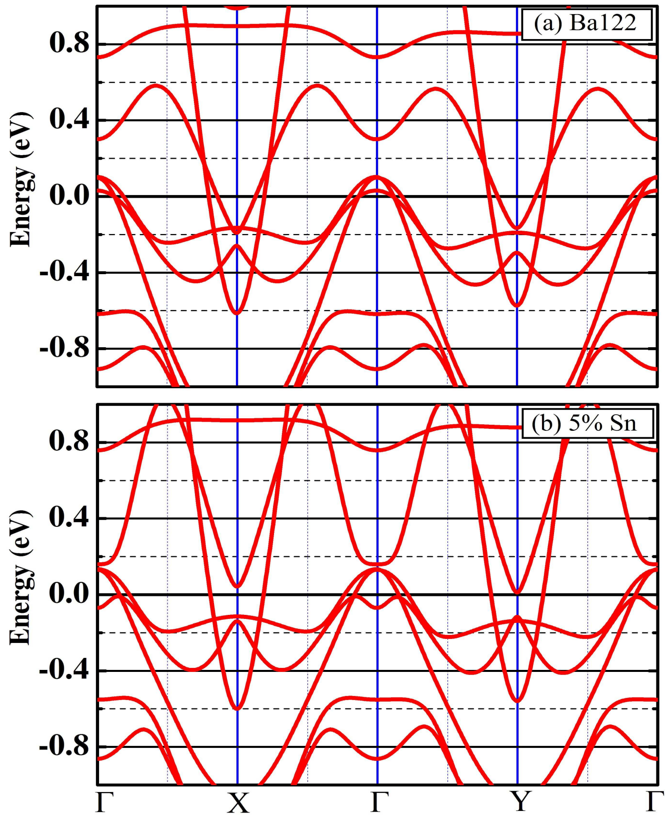

Figure 7.2: Calculated band structures in orthorhombic phase within VCA method for (a) $BaFe_2As_2$ and (b) $Ba_{0.95}Sn_{0.05}Fe_2As_2$ systems along $\Gamma - X - \Gamma - Y - \Gamma$ k-path in the BZ. In comparison to FIG.7.5, 5% Sn doped Ba122 system shows significant modification in band structure as far as electronic topological transitions are concerned.

the four corners and three hole like FSs at the centre of the Brillouin Zone (BZ). In order to provide a clearer view of all the FSs, we present the FSs separately in second and third rows of FIG.7.1. One can see from these FSs that with increasing Sn impurity electron like FSs shrink and hole like FSs expand, which corroborates with the previous experimental picture of hole doping as a consequence of Sn impurity in Ba122 structure [214]. One of our most important observations, is the occurrence of Lifshitz transition upon certain percentage of Sn impurity (see FIG.7.1 and FIG. 7.2). With 4% Sn impurity in Ba122 system, the innermost FS at the centre of the BZ vanishes around Γ point as a direct consequence of Lifshitz transition.

On the whole with increasing Sn percentage, the shapes of FSs become more 3D like, resulting in large degradation of FS nesting. As a result of degradation of nesting mag-

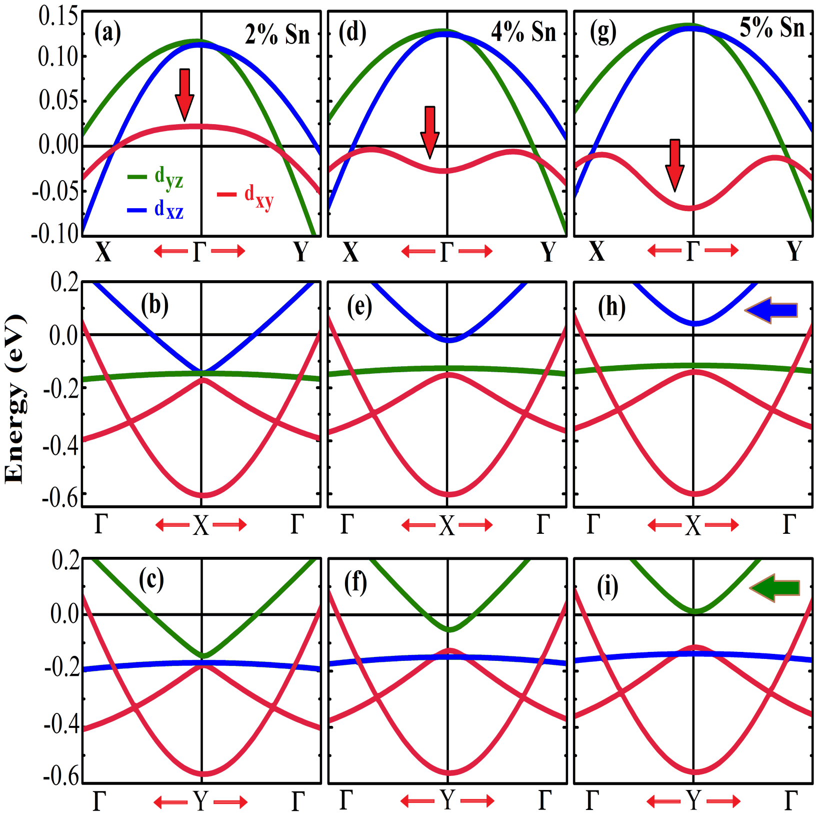

Figure 7.3: Calculated band structures in orthorhombic phase within VCA method for (a, b, c) $Ba_{0.98}Sn_{0.02}Fe_2As_2$, (d, e, f) $Ba_{0.96}Sn_{0.04}Fe_2As_2$ and (g, h, i) $Ba_{0.95}Sn_{0.05}Fe_2As_2$ systems around Γ (1st row), X (2nd row) and Y (3rd row) points. Electronic topological transition (transition of hole like band to electron like band) is indicated using red arrow around Γ point. Movement of the d_{xz} (d_{yz}) band around X (Y) point away from the Fermi level is shown by blue (green) arrow. This figure may be contrasted with FIG.7.6 and FIG.7.9.

netic order becomes weaker which might be the reason of lowering of structural as well as SDW transition temperatures (T_s and T_{SDW}) in Sn contaminated Ba122 systems. To illustrate the observed Lifshitz transition, we exhibit the calculated band structures of Sn contaminated Ba122 system for 2%, 4% and 5% Sn impurity in FIG.7.3. Band structures around Γ, X and Y points are shown in first, second and third rows of FIG.7.3 respectively. It is quite evident from these figures that at around 4% Sn impurity Lifshitz transition occur in Ba122 system. As a signature of this Lifshitz transition, a hole like band (d_{xy} band around Γ point) becomes electron like (see FIG.7.3g). Observation of Lifshitz transition in other high symmetry k points also occur as clearly demonstrated in FIG.7.3. This type of transition can create remarkable topological modification of FSs, which might be the

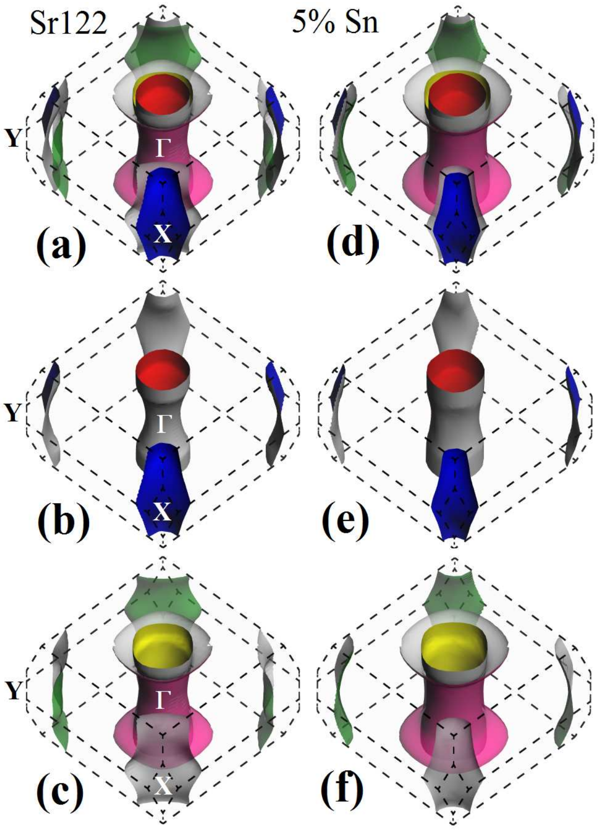

Figure 7.4: Calculated Fermi surfaces in orthorhombic phase within VCA approach for (a, b, c) $SrFe_2As_2$ and (d, e, f) $Sr_{0.95}Sn_{0.05}Fe_2As_2$ systems. For clarity individual FSs are shown separately in 2nd and 3rd row. Shrinkage of electron like FSs and surging of hole like FSs are worth noticing. This indicates hole doping.

reason of alteration of superconducting properties of these Ba122 systems with Sn impurity. Transition of hole like band to electron like band as well as disappearance of electron like band from Fermi level (FL) would not only modify the shape of the FSs but also affect the nesting condition between electron and hole like bands severely. Since nesting of FS is directly related to magnetic SDW transition, lowering of observed magnetic transition in Sn contaminated Ba122 system may be attributed to the electronic topological transition as found from our first principles simulations. Band structures around X and Y points reveal that orbital order also got modified in the presence of slightly higher percentages of Sn impurities (>1%). This according to us is certainly a possible explanation to the reduction of structural transition temperature (T_s). On the other hand, there is no experimental evidence of lowering structural transition temperature (T_s) and SDW tran-

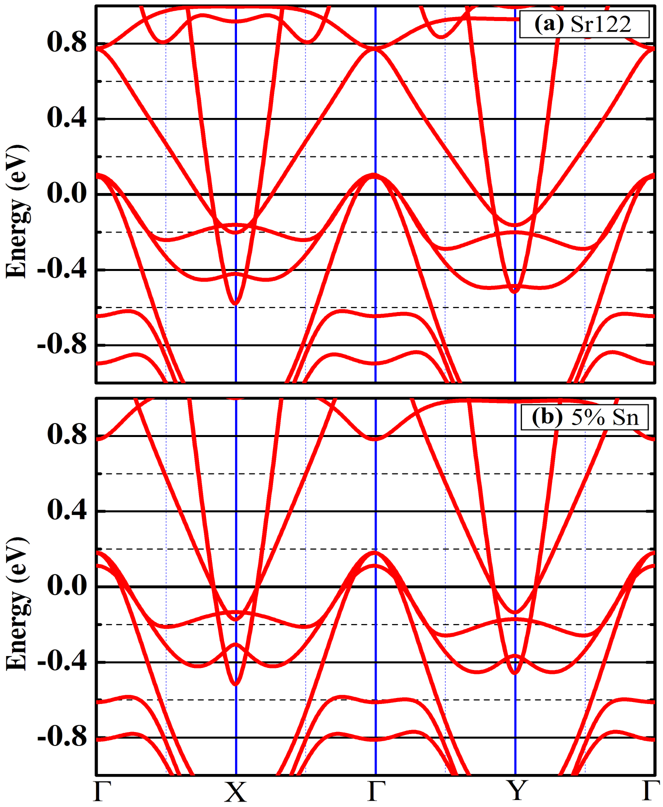

Figure 7.5: Calculated band structures in orthorhombic phase within VCA method for (a) $SrFe_2As_2$ and (b) $Sr_{0.95}Sn_{0.05}Fe_2As_2$ systems along $\Gamma - X - \Gamma - Y - \Gamma$ k-path in the BZ. In comparison to FIG.7.2, 5% Sn doped Sr122 system shows insignificant modification in band structure as far as electronic topological transitions are concerned.

sition temperature (T_{SDW}) in Sr122 and Ca122 compounds, prepared by Sn-flux method (containing Sn impurity). We have also performed electronic structure calculation of Sn contaminated Sr122 and Ca122 systems. In FIG.7.4 we have displayed the FSs of Sr122 system (first column) as well as 5% Sn contaminated Sr122 system (second column). In FIG.7.7 we present the FSs of Ca122 system (first column) as well as 5% Sn contaminated Ca122 system (second column). Calculated FSs of Sr122 and Ca122 system with 5% Sn impurity (FIG.7.4 and FIG.7.7) give a clear indication of hole doping *i.e.,* expansion of hole FSs and shrinkage of electron FSs. However, there is no trace of Lifshitz transition in case of Sn contaminated Sr122 and Ca122 systems contrary to the case of Ba122 system. Besides there is no significant change in the FS topology specially, the change in dimensionality of FSs in presence of 5% Sn impurity. So there is no evidence of degradation of FS nesting in these two systems. This may also stand out as an explanation for the robustness of magnetic, structural and superconducting transition temperatures for Sr122 and Ca122 systems with Sn impurity. We have also simulated the band structure of Sr122

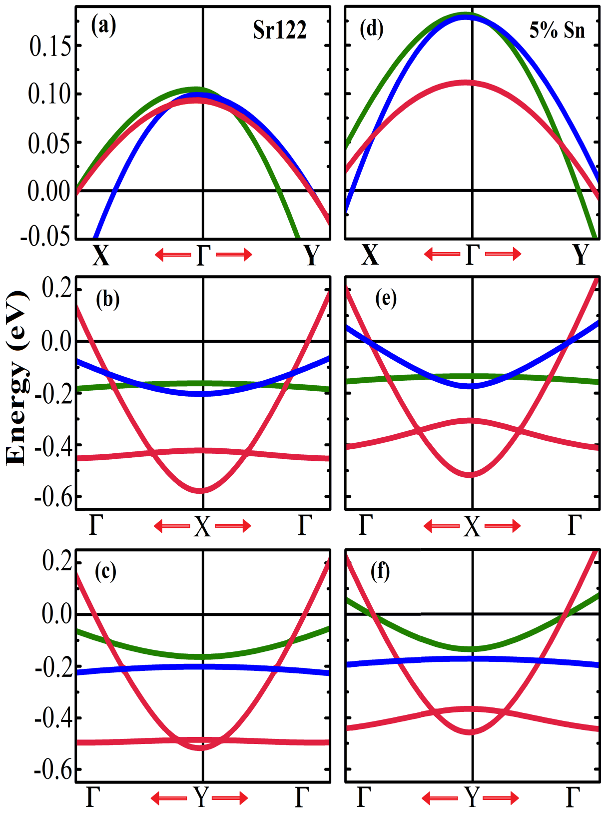

Figure 7.6: Calculated band structures in orthorhombic phase within VCA method for (a, b, c) $SrFe_2As_2$ and (d, e, f) $Sr_{0.95}Sn_{0.05}Fe_2As_2$ systems around Γ (1st row), X (2nd row) and Y (3rd row) points. Modification in the band widths of electron (reduction in band width) and hole (increment in band width) like bands causes apprehendable modifications in the FSs (See FIG.7.4).

and Ca122 systems in order to see the moderation of orbital order if any. In FIG.7.5a, the band structure along the k path $\Gamma - X - \Gamma - Y$ of pure Sr122 system and in FIG.7.5b that for 5% Sn contaminated Sr122 systems are presented. Similarly in FIG.7.8a, the band structure along k path $\Gamma - X - \Gamma - Y$ of pure Ca122 system and in FIG.7.8b that for 5% Sn contaminated Ca122 systems are depicted. Band structures of these pure and impure systems have no qualitative differences. In FIG.7.6 and FIG.7.9 band structure around Γ, X and Y points of pure as well as 5% Sn contaminated Sr122 and Ca122 systems have been shown. There is no sign of Lifshitz transition or any kind of electronic topological transition (ETT) at least up to 5% Sn impurity. And there is almost no change in the nature of orbital ordering between d_{yz} and d_{xz} bands around Γ, X and Y point with the introduction of Sn impurity (5% Sn) in Sr122 and Ca122 systems. Since orbital ordering of d_{yz} and d_{xz} bands around X and Y points are the major contributors to the structural transition from tetragonal (high temperature) to orthorhombic phase (low temperature) in 122 systems [30, 70], no significant moderation of orbital ordering around X and Y points support the experimental observation of the unaffected structural transition temperature in Sn induced Sr122 and Ca122 systems. Lifshitz transition with variation of pressure or doping concentration or even with variation of temperature, plays an important role in 122 Fe-based superconductors and is observed experimentally [198, 200]. Thus one must be sure about the fact whether the observed Lifshitz transitions are artefacts of Sn impurity or not. So by using VCA method for introducing Sn into the Ba122/Sr122/Ca122 structure, we provide a detailed electronic structures for pure and Sn contaminated systems for the first time. We also elucidate the experimentally observed anomalies for these Sn induced 122 systems through our first principles electronic structure calculation which is not available in the current literature. In order to understand the influence of Sn doping on various 122 materials it is essential to identify that the band structures of undoped Ba122, Sr122 and Ca122 systems (in the orthorhombic phase) already have significant differences. For Ba122 system, electronic bands around Γ point is very close to the Fermi level (FL), specially, the flat d_{xy} band nearly touches the FL. The other two bands d_{xz} and d_{yz} are slightly higher in energy compared to that of the d_{xy}. This should be contrasted with that of the Sr122 and Ca122 systems (see FIG.7.2, 7.5, 7.8), where all the d_{xy}, d_{xz} and d_{yz} bands are further away from FL. This is because of the largest size of Ba (253 pm) compared to that of Sr (219 pm) and Ca (194 pm) causing two Fe-As layers furthest in Ba122. It is to be noted that the d_{xy} band is planar (xy) in nature in contrast to the d_{xz}/d_{yz} bands. Sn substitution in the M-atoms (Ba/Sr/Ca) is an out-of-plane substitution. Ba atom being the largest in size among the M-atoms as well as Sn, a few percentage of Sn substitution keeps the effective size of the ‘virtual M atom’ largest in size in case

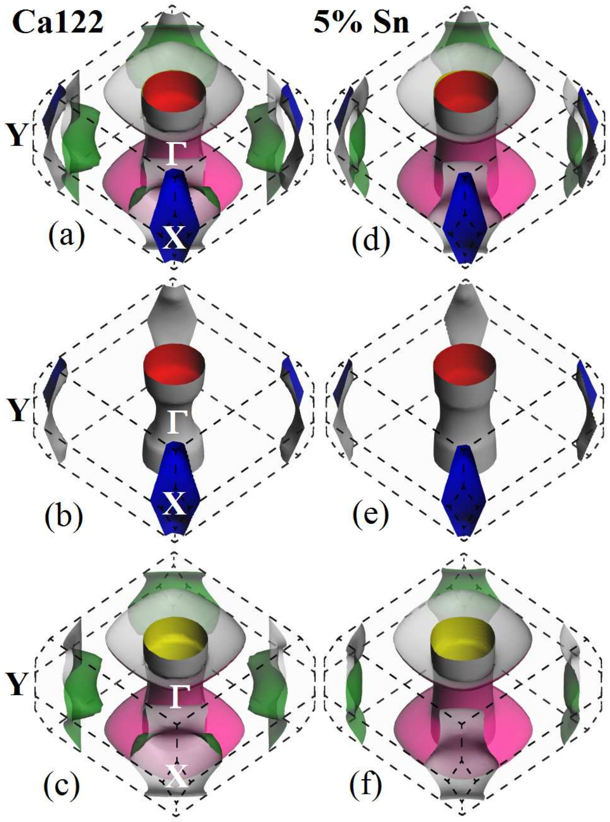

Figure 7.7: Calculated Fermi surfaces in orthorhombic phase within VCA method for (a, b, c) $CaFe_2As_2$ and (d, e, f) $Ca_{0.95}Sn_{0.05}Fe_2As_2$ systems. For clarity individual FSs are shown separately in 2nd and 3rd row. Shrinkage of electron like FSs and surging of hole like FSs are worth noticing. This indicates hole doping.

of Ba, smaller in case of Sr and the smallest in case of Ca. This would cause vertical movement between the Fe-As planes least for Sn-doped Ba-122 but larger for Sn-doped Sr-122 and largest for Sn-doped Ca-122. Therefore, naturally d_{xz}/d_{yz} bands would move furthest in case of Sn-doped Ca-122 whereas least movement to the d_{xy} bands. That also simultaneously explains hole doping effect. Thus, Sn impurity causes splitting between the d_{xy} and the pair of ‘nearly ’degenerate bands d_{xz}/d_{yz}. The modulations of the d_{xz}/d_{yz} bands can also produce modulations in the d_{xy} bands. But the d_{xy} band around the Γ point is much lower in energy compared to that of the d_{xz}/d_{yz} bands and closer to the FL for the undoped Ba122. This is not the case of undoped Sr122, Ca122 where $d_{xy}/d_{xz}/d_{yz}$ are nearly at same but higher in energy. The effect of modulations in the d_{xy} bands due to that of the d_{xz}/d_{yz} bands is thus minimum in case of Sr-122, Ca-122 systems. The d_{xy} band

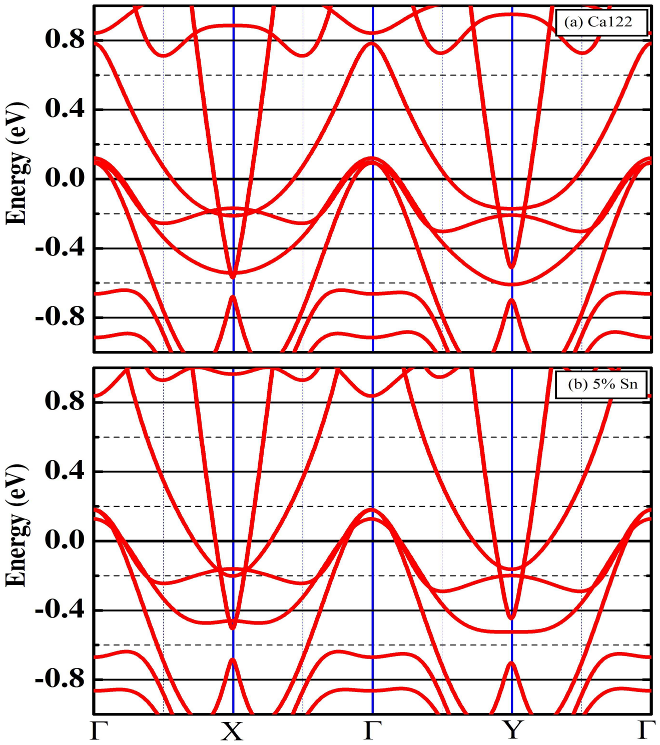

Figure 7.8: Calculated band structures in orthorhombic phase within VCA method for (a) $CaFe_2As_2$ and (b) $Ca_{0.95}Sn_{0.05}Fe_2As_2$ systems along $\Gamma - X - \Gamma - Y - \Gamma$ k-path in the BZ. In comparison to FIG.7.2, 5% Sn doped Ca122 system shows insignificant modification in band structure as far as electronic topological transitions are concerned.

of Ba122 being already very close to the FL in presence of Sn impurity is pushed down below the FL due to such modulation, causing the Lifshitz transition.

7.3.2 Doping induced Lifshitz transition

We consider a variety of doped 122 Fe-based SCs to study the essence of electronic topological transition (ETT) / Lifshitz transition (LT) and its manifold consequences. In this section, we investigate the role of various kinds of doping (electron, hole or iso-electronic) in ETT / LT in 122 Fe-based systems. In Fig.7.10 we depict the FSs of K doped Ba122 compounds for various K doping concentration as indicated in the figure. It is very clear from Fig.7.10a that there are five Fermi pockets, two around X and Y points (electron like) and three around Γ point (hole like). Different colours are used to indi-

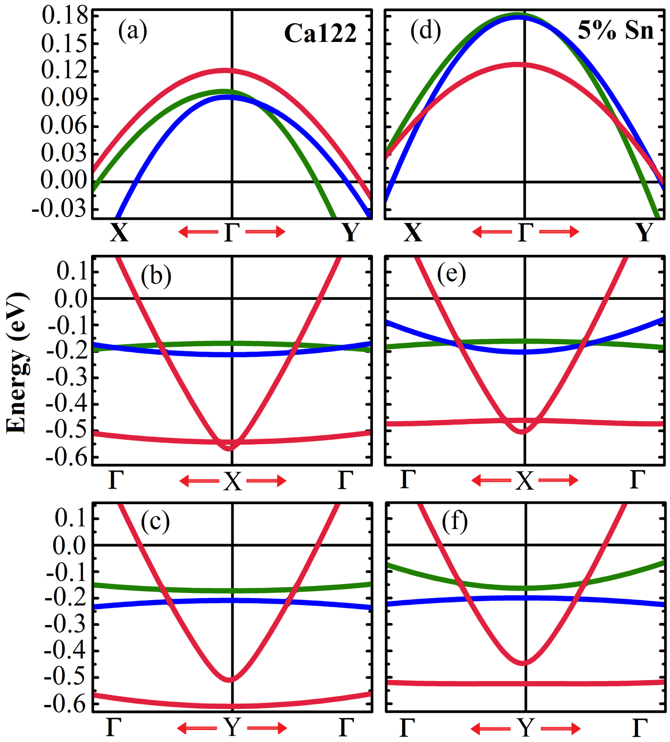

Figure 7.9: Calculated band structures in orthorhombic phase within VCA method for (a, b, c) $CaFe_2As_2$ and (d, e, f) $Ca_{0.95}Sn_{0.05}Fe_2As_2$ systems around Γ (1st row), X (2nd row) and Y (3rd row) points. Modifications in the band widths of electron (reduction in band width) and hole (increment in band width) like bands causes apprehendable modifications in the FSs (See FIG.7.7).

cate different Fermi pockets. As one can see that with increasing K-doping concentration, substantial modifications take place in the topology of various FSs. We point out that one of the electron like FS around X/Y point transform into a different topology. This topological transformation of FS is identified as ETT or LT. In the right column modification of the particular FS which undergoes ETT are presented. An arrow mark is used to indicate portion of FS which is getting modified due to higher percentage of hole doping. A comprehensive electronic band structure study also reveals that there are remarkable changes in the nature of the band dispersion in that particular orbital derived band near the Fermi level (FL). In Fig.7.11 we display the band structures of K-doped Ba122 compound ($Ba_{1-x}K_xFe_2As_2$) along the $\Gamma - X - \Gamma - Y$ k-path for two different doping concentrations ($x = 0.2$ and $x = 0.5$). A circular envelope has been drawn in each figure to point out the modification in the nature of band dispersion around the high symmetry X point due

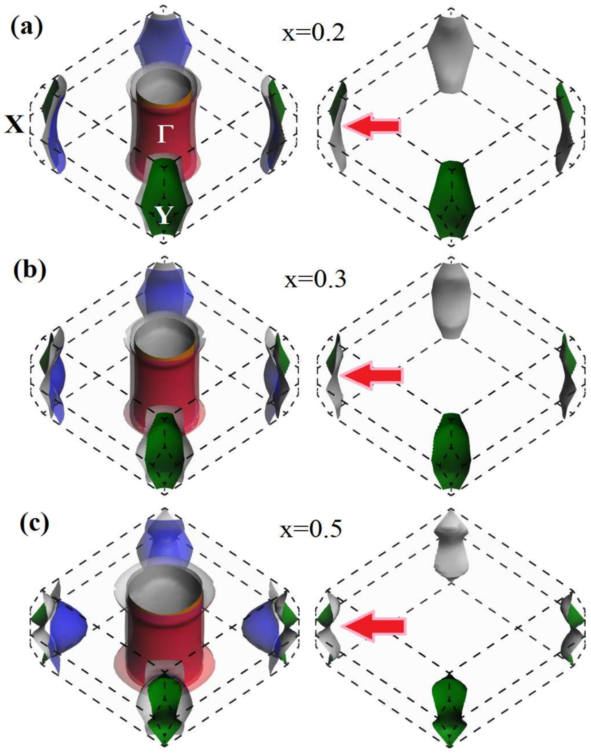

Figure 7.10: Calculated Fermi surfaces (FSs) of $Ba_{1-x}K_xFe_2As_2$ compounds in the low temperature orthorhombic phase for (a) $x = 0.2$, (b) $x = 0.3$ and (c) $x = 0.5$. In the left column all the FSs around Γ (hole like), X and Y (electron like) points are shown using different colours. In the right column topologically modified FS is shown separately for various doping concentrations. Arrows in the figure indicate the portion of the modified FSs.

to K-doping. A very similar kind of modifications in the band dispersion near Y point is also observed in case of $Ba_{1-x}K_xFe_2As_2$ compound with $x = 0.5$. In order to elucidate the nature of band dispersion near X point, we display orbitally resolved band structure of $Ba_{1-x}K_xFe_2As_2$ compound around X point separately in Fig.7.12a and Fig.7.12b for $x = 0.2$ and $x = 0.5$ respectively. Different colours are used to designate different orbital projected bands. The same colour codes are used for all orbital resolved band structures throughout this paper. From Fig.7.11 and Fig.7.12, it is quite clear that the nature of band dispersion of (electron like) d_{xz} band around X and Y points transform into hole like band dispersion as a result of higher percentage of K-doping. On the other hand, with higher K doping concentration one of the hole like d_{xy} band (near -0.45 eV) also getting modified to an electron like band. We also exhibit the FSs of another hole doped Ba122

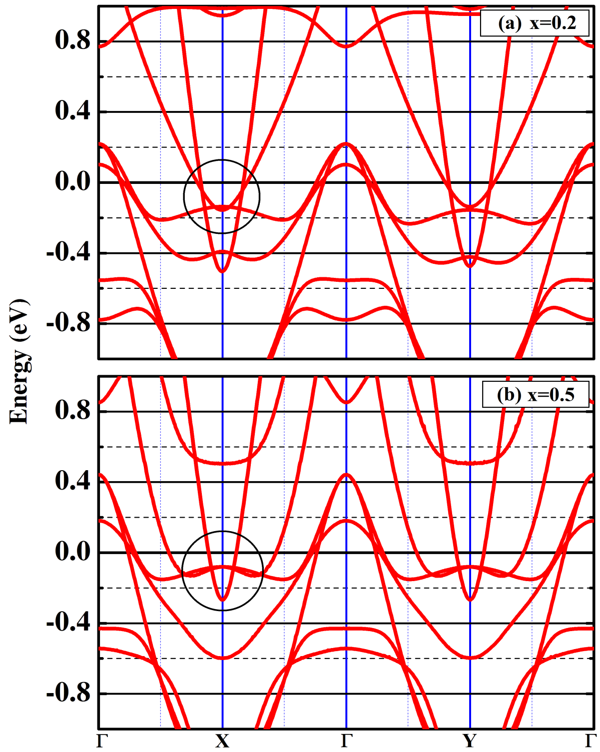

Figure 7.11: Calculated electronic band structures of $Ba_{1-x}K_xFe_2As_2$ compounds in the low temperature orthorhombic phase for (a) $x = 0.2$ and (b) $x = 0.5$ along the $\Gamma - X - \Gamma - Y$ direction. Modifications in the band structure around X point has been highlighted by black circular envelope.

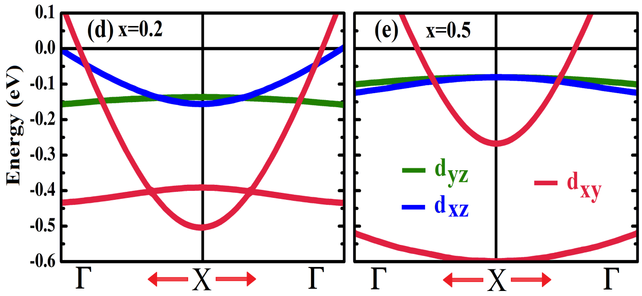

Figure 7.12: Magnified electronic band structure of $Ba_{1-x}K_xFe_2As_2$ from Fig. 7.11 in the low temperature orthorhombic phase for (a) $x = 0.2$ and (b) $x = 0.5$ around X point. Various colours are used to indicate different orbital resolved bands denoted in the figure. Topological transition in the d_{xz} band is observed as electron like d_{xz} band ($x = 0.2$) becomes hole like for higher K doping concentration ($x = 0.5$).

compound *i.e.*, $Ba_{1-x}Na_xFe_2As_2$. In Fig.7.13 we present the FSs of $Ba_{1-x}Na_xFe_2As_2$ compound for various doping concentrations indicated in the figure. Similar to the ETT found in $Ba_{1-x}K_xFe_2As_2$ compounds the same is also found in $Ba_{1-x}Na_xFe_2As_2$ compounds, at around the same doping concentration. Band structures of Na doped Ba122 compounds

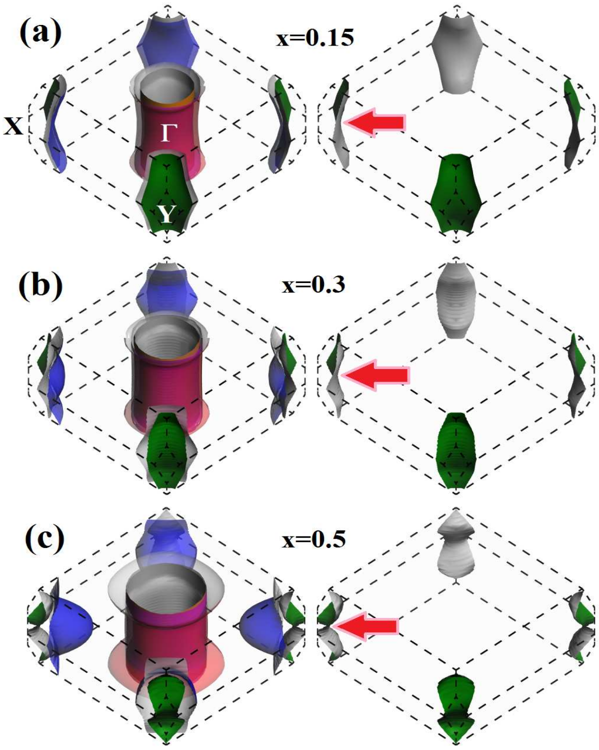

Figure 7.13: Calculated Fermi surfaces of $Ba_{1-x}Na_xFe_2As_2$ compounds in the low temperature orthorhombic phase for (a) $x = 0.15$, (b) $x = 0.3$ and (c) $x = 0.5$. In the left column all the FSs around Γ (hole like), X and Y (electron like) points are shown using different colours. In the right column topologically modified FS is shown separately for various doping concentration. Arrows in the figure indicate the modified portion of the FSs.

presented in Fig.7.14 and Fig.7.15 are qualitatively very similar to that of the K doped Ba122 compound. So we conclude from these two hole doped Ba122 compounds that the ETT is observed in the electron like bands around X and Y points with nearly 50% hole doping. It also turns out from the established phase diagram of hole doped Ba122 SCs that superconducting transition temperature T_c reaches its maximum value at around 50% K doping. Thus one can not underestimate the crucial role of ETT to the advent of superconductivity in these compounds. This will be further evident for electron doped and isovalently doped systems as we proved below. It is worth mentioning that there exists an earlier theoretical prediction (different from the present methodology which uses experimental structural parameters) of ETT/LT in very heavily doped Ba122 compounds [198]. Note the K-122 compounds only have hole FS and therefore LT at very high K-doped

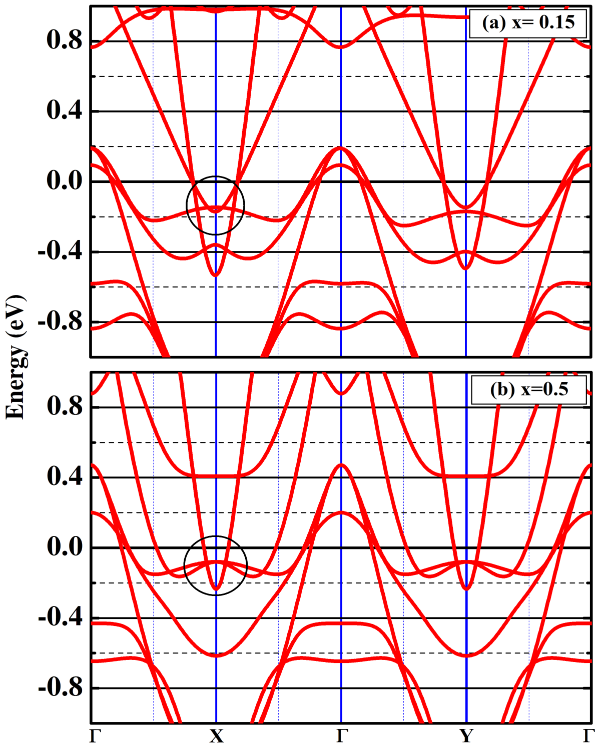

Figure 7.14: Calculated electronic band structures of $Ba_{1-x}Na_xFe_2As_2$ compounds in the low temperature orthorhombic phase for (a) $x = 0.15$ and (b) $x = 0.5$ along the $\Gamma - X - \Gamma - Y$ direction. Modifications in the band structure around X point has been highlighted by black circular envelope.

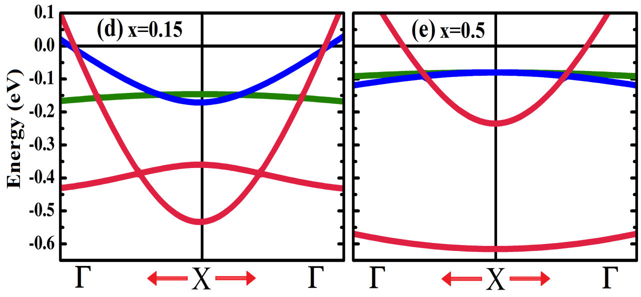

Figure 7.15: Magnified electronic band structure of $Ba_{1-x}Na_xFe_2As_2$ from Fig. 7.14 in the low temperature orthorhombic phase for (a) $x = 0.15$ and (b) $x = 0.5$ around X point. Various colours are used to indicate different orbital resolved bands denoted in the figure. Topological transition in the d_{xz} band is observed as electron like d_{xz} band ($x = 0.15$) becomes hole like for higher Na doping concentration ($x = 0.5$).

Ba-122 compound is likely.

Next we move on to Co doped (electron doped) Ba122 compound to study the ETT/LT

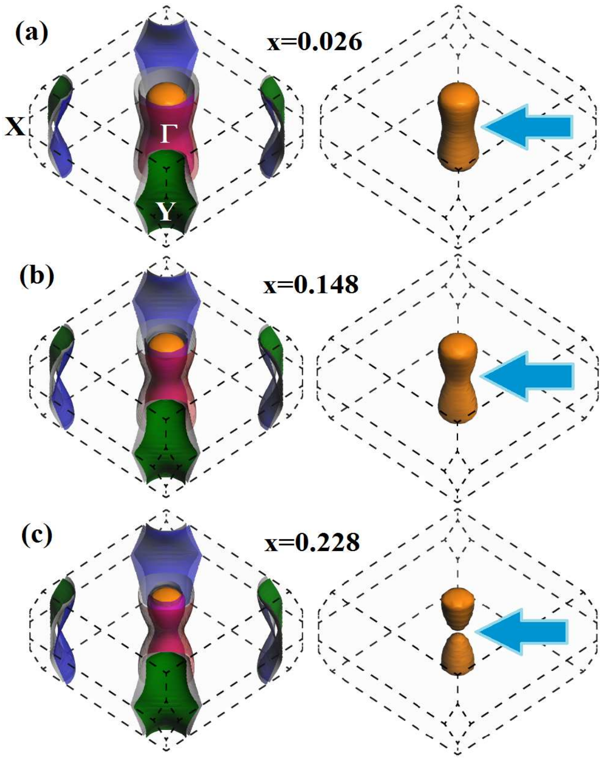

Figure 7.16: Calculated Fermi surfaces of $BaFe_{2-x}Co_xAs_2$ compounds in the high temperature tetragonal phase for (a) $x = 0.026$, (b) $x = 0.148$ and (c) $x = 0.228$. In the left column all the FSs around Γ (hole like), X and Y (electron like) points are shown using different colours. In the right column topologically modified FS is shown separately for various doping concentrations. Arrows in the figure indicate the modified portion of the FSs.

from first principles simulation. There are experimental evidences of Lifshitz topological transition in these electron doped Ba122 compounds. In Fig.7.16, we display the FSs of Co doped Ba122 compound in the tetragonal phase. It is quite clear from the right column of the figure that one of the hole like FSs around Γ points has been modified remarkably as a result of increasing Co doping. In fact for $x = 0.228$ (*i.e*, around 10 % of Co doping) in $BaFe_{2-x}Co_xAs_2$ compound, the FS around Γ point vanishes that corresponds to a topological change in the FS, bears the signature of Lifshitz transition. This observation is quite consistent with experimental observation [200]. In Fig.7.17, we show the electronic band structure of $BaFe_{2-x}Co_xAs_2$ compounds for two different Co doping concentrations. Circular envelope has been drawn to indicate the moderation of band structure around Γ point. This highlighted portion of Fig.7.17 has been separately presented in Fig.7.18 for

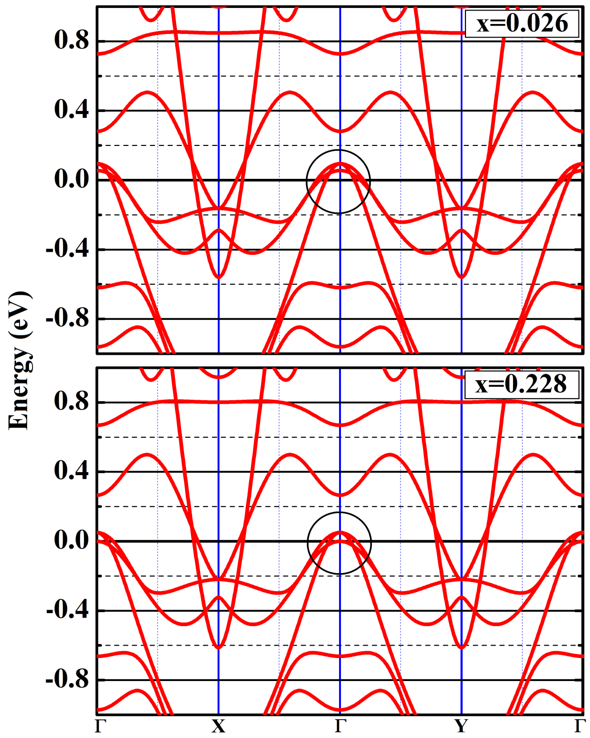

Figure 7.17: Calculated electronic band structure of $BaFe_{2-x}Co_xAs_2$ compounds in the high temperature tetragonal phase for (a) $x = 0.026$ and (b) $x = 0.228$ along the $\Gamma - X - \Gamma - Y$ direction. Modifications in the band structure around X point have been highlighted by black circular envelope (see Fig. 7.18).

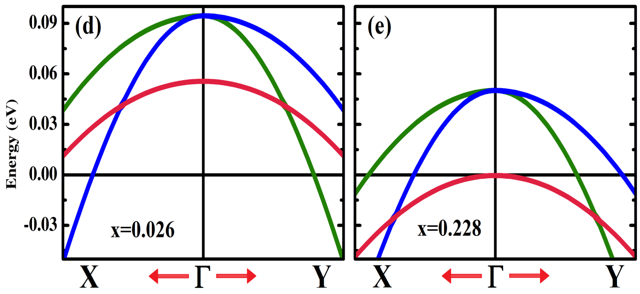

Figure 7.18: Magnified electronic band structure of $BaFe_{2-x}Co_xAs_2$ compounds from Fig. 7.17 in the high temperature tetragonal phase for (a) $x = 0.026$ and (b) $x = 0.228$ around Γ point. Various colours are used to indicate different orbital resolved bands denoted in the figure. Topological transition in the d_{xy} band is observed as this d_{xy} band situated well above the Fermi level ($x = 0.026$) goes below the Fermi level for higher Co doping concentration ($x = 0.228$).

more clarity. One can clearly see from Fig.7.18 that one of the hole like bands (d_{xy}) that lies well above the Fermi level for $x = 0.026$ (Fig. 7.18a) goes below the Fermi level with higher Co doping concentration ($x = 0.228$). This results in topological change in

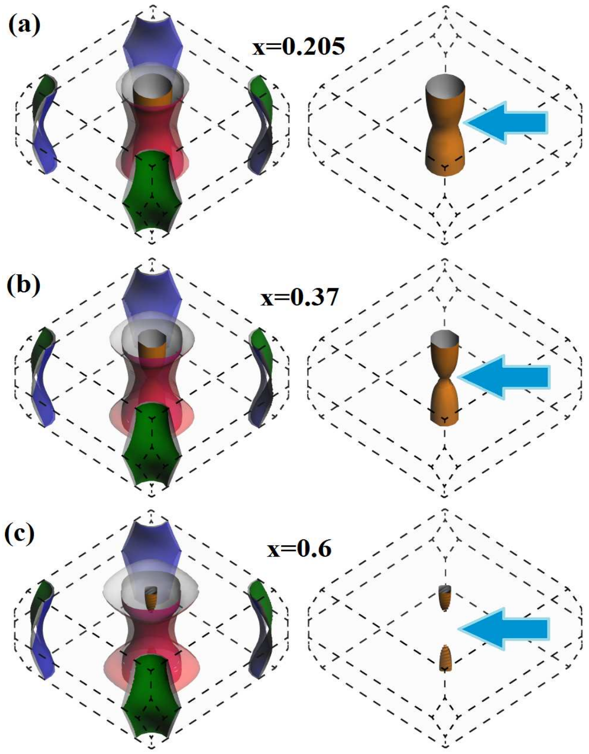

Figure 7.19: Calculated Fermi surfaces of $BaFe_2(As_{1-x}P_x)_2$ compounds in the low temperature orthorhombic phase for (a) $x = 0.205$, (b) $x = 0.37$ and (c) $x = 0.6$. In the left column all the FSs around Γ (hole like), X and Y (electron like) points are shown using different colours. In the right column topologically modified FS is shown separately for various doping concentration. Arrows in the figure indicate the modified portion of the Fermi surfaces.

the FS as evident from this figure. As a matter of fact electron doped 122 SCs also have maximum T_c at around 10% Co doping. Therefore, both the hole doped as well as electron doped compounds exhibit a close connection between superconductivity and LT in Fe-based SCs. It should also be noted here that contrary to the hole doped Ba122 compounds, LT occurs in the electron doped compounds in the hole like bands around Γ point. Our findings are very much consistent with the previous experimental findings [200].

Now we move to the case of isovalently doped Ba122 compounds. We study the FSs and band structures of $BaFe_2(As_{1-x}P_x)_2$ compounds for various P doping concentrations as well as in two different structural phases and at two different temperatures (low temperature orthogonal phase and high temperature tetragonal phase) using experimentally measured temperature and doping dependent structural parameters (a, b, c and z_{As}). In

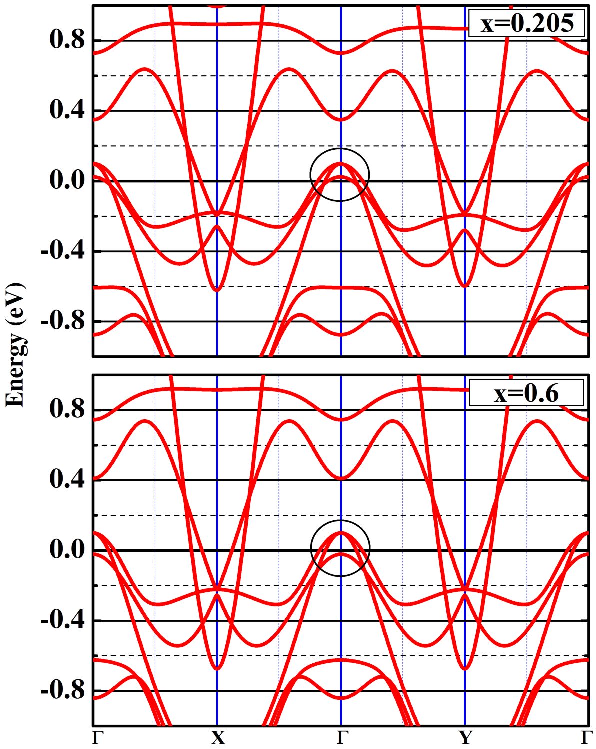

Figure 7.20: Calculated band structure of BaFe$_2$(As$_{1-x}$P$_x$)$_2$ in the low temperature orthorhombic phase for (a) x = 0.205 and (b) x = 0.6 respectively along the $\Gamma - X - \Gamma - Y$ direction. Modifications in the band structure around Γ point have been highlighted by black circular envelope.

Fig.7.19, we demonstrate the calculated FSs of the BaFe$_2$(As$_{1-x}$P$_x$)$_2$ compounds in the low temperature phase for various doping concentrations, indicated in the figure. It is very clear from the right column of Fig.7.19 that topology of one of the hole like FS is getting modified with increasing P doping concentration. Our calculated band structure shown in Fig.7.20 also reflect the signature of LT, as a result of which at higher doping concentration, one of the bands namely d$_{xy}$ around Γ point situated well above the Fermi level goes below the Fermi level. In order to provide a clear and lucid picture, we show orbital resolved band structures of BaFe$_2$(As$_{1-x}$P$_x$)$_2$ compounds in the low temperature phase (1st row of Fig.7.21) as well as in the high temperature tetragonal phase (2nd row of Fig.7.21) for various P doping concentrations. In both the cases with increasing doping concentration LT occurs but not at the same doping concentration. In both the phases (10 K and 300 K), d$_{xy}$ band around Γ point goes below the Fermi level at doping concentra-

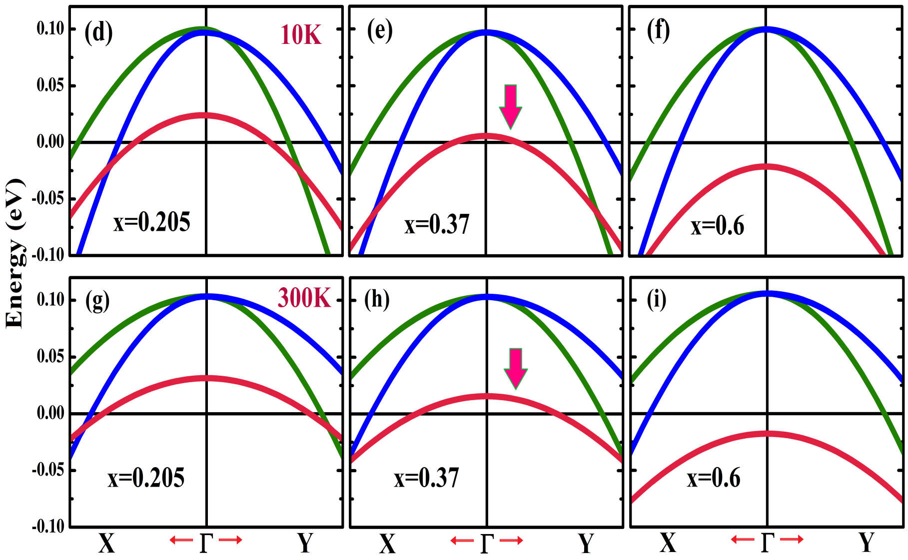

Figure 7.21: Calculated band structure of $BaFe_2(As_{1-x}P_x)_2$ compound in the low temperature orthorhombic phase (first row) as well as high temperature tetragonal phase (second row) with $x = 0.205$, $x = 0.37$ and $x = 0.6$ around Γ point. Various colours are used to indicate different orbital resolved bands presented in the figure. Topological transition in the d_{xy} band is observed as this d_{xy} band situated well above the Fermi level ($x = 0.205$) goes below the Fermi level for higher P doping concentration ($x = 0.6$). But there is notable differences in the calculated electronic band structure in the orthorhombic (10 K) and tetragonal phases (300 K).

tion $x = 0.6$. But a closer look at the band structures of $BaFe_2(As_{1-x}P_x)_2$ for $x = 0.37$ at 10 K and at 300 K, reveal that there are important differences in the band structures. In case of the electronic band structure of orthorhombic phase (10 K) (which is in superconducting phase), the d_{xy} band is about to cross the Fermi level (Lifshitz point) but on the other hand in case of non-superconducting tetragonal phase (300 K) d_{xy} lies above the Fermi level. This give rise to an indication to the influence of temperature and structural phases on topological transitions (ETT/LT). In this case also LT occurs at a doping concentration where superconducting T_c is maximum. Clearly, as a consequence of temperature effect, curvatures of bands become different leading to lower effective mass in the superconducting orthorhombic phases (also contrast Fig. 7.23). In case of Ru doped Ba122 compounds we also find LT (not shown here for brevity) at very higher Ru doping concentration (>50% Ru doping) where superconducting T_c reaches its maximum. This is consistent with the finding of some earlier theoretical work on Sr122 compounds

[216]. We found significant moderation of shape and relative positions of the bands near Fermi level for $BaFe_2(As_{1-x}P_x)_2$ compounds as a result of increasing doping concentration. From Fig.7.21 one can see that the positions of d_{xz} and d_{yz} are hardly affected by P doping at As site, but d_{xy} bands are very sensitive to doping concentration. One of the reasons for this fact may arise from the structural modification, caused by P doping in place of As (Fe-As hybridization can change anion height which is closely related to electronic structures of these compounds).

7.3.3 Temperature induced Lifshitz transition

It is well established that electronic structure of these Fe-based Ba122 compounds is highly sensitive to temperature [29, 30, 135]. It should also be noted here that the structural parameters which essentially controls the electronic structures of these systems, has significant temperature dependencies [29, 100, 142, 143].

We also study the temperature effect in the electronic structures of the undoped parent compound $BaFe_2As_2$ and 5% Ru doped Ba122 compounds. We use temperature dependent experimental lattice parameters a, b, c and z_{As} to simulate the electronic structures (band structures and FSs) at various temperatures. We found that in the undoped compound there is no LT/ETT but in 5% Ru doped Ba122 compounds ($BaFe_{2-x}Ru_xAs_2$ with $x = 0.1$) temperature dependent LT occurs. In Fig.7.22, we display explicitly calculated FSs of 5% Ru doped Ba122 compounds at various temperatures. In the right column of the Fig.7.22, we show a particular FS where LT take place. In Fig.7.23, we depict the band structures of this compound around Γ point. From Fig.7.23 one can clearly see that the d_{xy} band near FL goes below FL as temperature decreases from 120 K to 90 K, which bears the signature of LT. Temperature induced LT is not very common but observed in some other compounds experimentally. To find the root cause of temperature dependent LT, we have carried out further calculations on undoped Ba122 system using experimental lattice parameter [18] by varying z_{As} (one of the important structural parameter as discussed

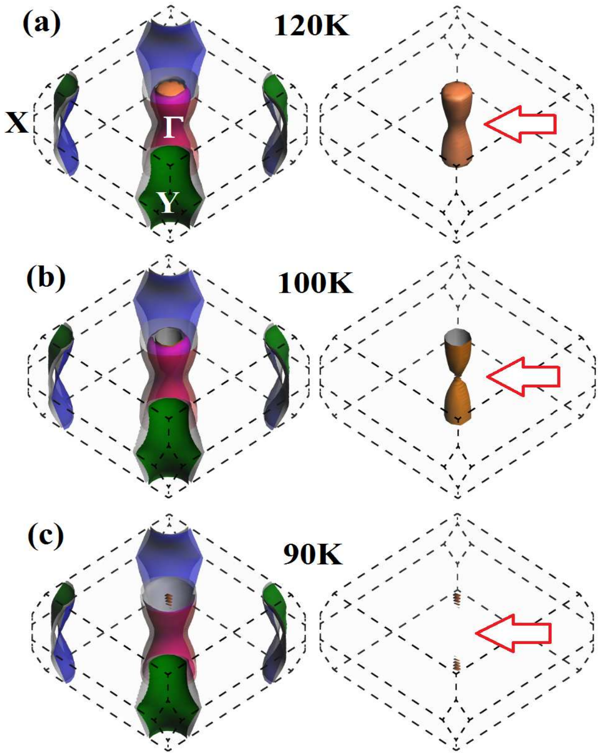

Figure 7.22: Calculated Fermi surfaces of $BaFe_{2-x}Ru_xAs_2$ compounds with $x = 0.1$ for (a) 120 K, (b) 100 K and (c) 90 K. In the left column all the FSs around Γ (hole like), X and Y (electron like) points are shown using different colours. In the right column topologically modified FS is shown separately for various temperatures. Arrows in the figure indicate the modified portion of the Fermi surfaces.

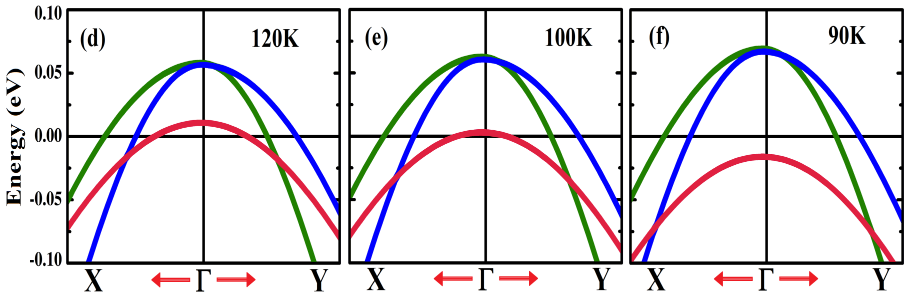

Figure 7.23: Calculated electronic band structure of $BaFe_{2-x}Ru_xAs_2$ compound for $x = 0.1$ for (a) 120 K, (b) 100 K and (c) 90 K temperatures magnified around Γ point. Various colours are used to indicate different orbital resolved bands presented in the figure. Topological transition in the d_{xy} band is observed as this d_{xy} band situated just above the Fermi level at 120 K goes below the Fermi level as the temperature is lowered to 90 K.

earlier). We calculate FSs and band structures of undoped Ba122 in the orthorhombic phase by tuning z_{As} only and all other structural parameters are kept constant. In Fig.7.24 and Fig.7.25 we present the FSs and band structures of the undoped Ba122 system for

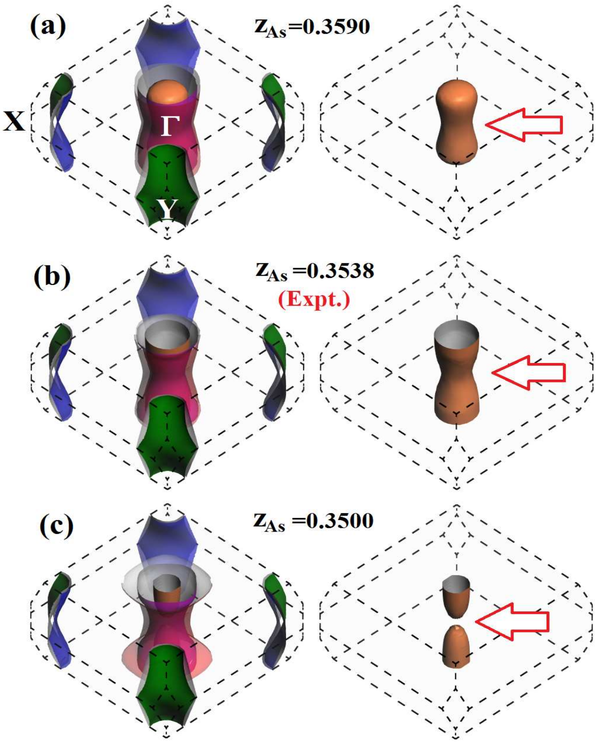

Figure 7.24: Calculated Fermi surfaces of $BaFe_2As_2$ in the low temperature orthorhombic phase for different z_{As} (a) 0.3590, (b) 0.3538 (experimental) and (c) 0.3500. In the left column all the FSs around Γ (hole like), X and Y (electron like) points are shown using different colours. In the right column topologically modified FS is shown separately for different z_{As}s. Arrows in the figure indicate the modified portion of the Fermi surfaces.

different z_{As}. Essentially we find that electronic structure very near to the FL is heavily influenced by z_{As}. From Fig.7.24 one can see that LT can occur with slight change in the z_{As} (see right column of the Fig.7.24). With slight lowering in the values z_{As} the d_{xy} band near FL goes below the FL causing LT. On the other hand, there is not much influence to the other bands near the FL due to the variation of z_{As}. On the whole, structural parameters of Ba122 system are highly sensitive to impurity, doping, temperature and pressure. As a result of variations of these external parameters, the structural parameters specially z_{As} and can lead to LT/ETT in these compounds.

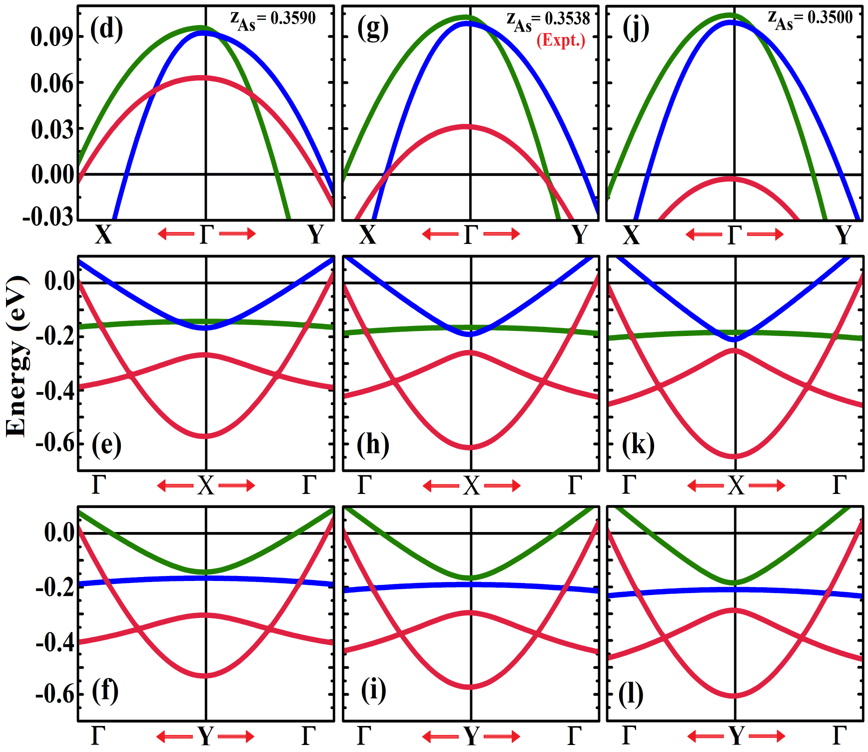

Figure 7.25: Calculated band structure of $BaFe_2As_2$ compound in the low temperature orthogonal phases with different z_{As} (a) 0.3590, (b) 0.3538 (experimental) and (c) 0.3500. Various colours are used to indicate different orbital resolved bands denoted in the figure. Topological transition in the d_{xy} band around Γ point is observed as this d_{xy} band situated well above the Fermi level (for z_{As} = 0.3590) goes below the Fermi level as a result of lowering of z_{As} (0.3500). There is no sign of any electronic topological transitions observed around X/Y points.

7.3.4 Probing of Lishitz transition through Fermi surface area

In order get better insight into these doping induced LT/ETT in Fe-based SCs, we present the evolution of Fermi surface area as a function of doping concentration for various 122 Fe-based SCs. In Fig.7.26 we present the variation of FS area with doping concentration for different kinds of doping. In the first row, we display all the five FS areas (FSA) as a function of various kinds of doping concentrations, for example, Co doping (electron doping), K, Na doping (hole doping) and P doping (iso-electronic doping) in the parent Ba-122 compound respectively. In case of electron doped system (Co doped Ba122) area of electron FSs increases with increasing doping concentration and exactly opposite trend is observed in the case of hole FSs. This is what one expect in the case of electron doping as clarified from Fig.7.26b and Fig.7.26c. In the second row we display sum of electron and hole Fermi surface areas as a function of various kinds of doping. One can also see from Fig.7.26c that sum of all the Fermi surface areas (all the electron and hole FS areas) almost shows no variation with doping concentration. In case of P

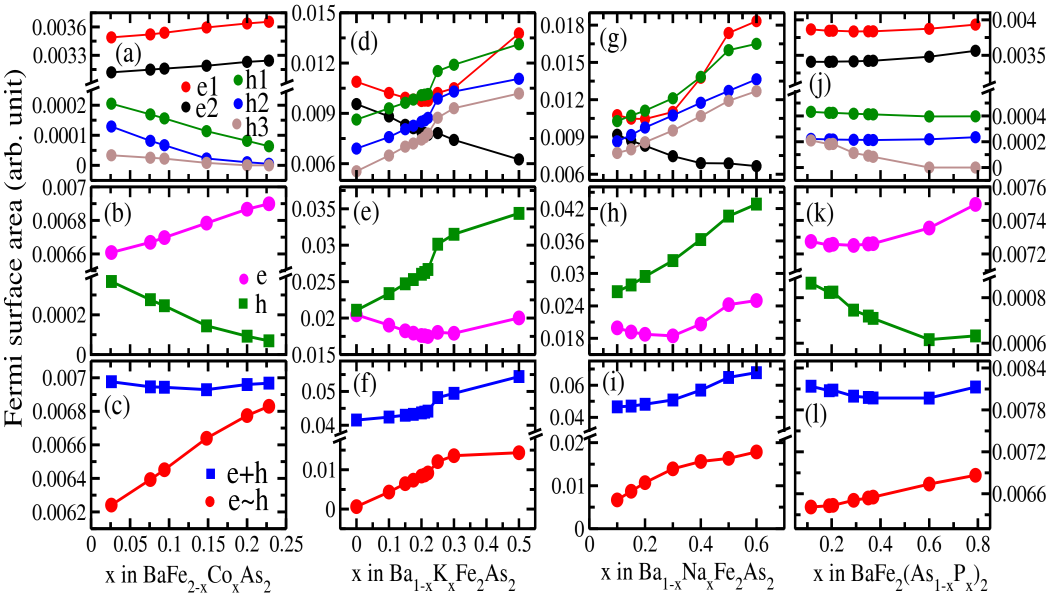

Figure 7.26: Fermi surface area of various doped 122 Fe-based SCs namely Co doped (1st column), K doped (2nd column), Na doped (3rd column) and P doped (4th column) Ba122 systems as a function of doping concentration. Evolution of area of each FS (total five) with doping is shown in the first row. Contribution of electron and hole FS areas as a function of doping are displayed in the second row. Total area of all the FSs and the difference in the FS areas of electron and hole FSs are shown in the last row.

doped Ba122 system (iso-electronically doped), most of the FSAs are nearly independent of doping (*cf.*) Fig.7.26j. But with higher P doping concentration one of the hole FS areas becomes vanishingly small as a result of LT. Although P doping in As site is an iso-electronic substitution, overall it gives the impression of electron doping to the system as far as Fig.7.26k and Fig.7.26l are concerned. On the other hand, in case of the hole doped Ba122 compounds (K and Na doping), areas of the hole FSs increases and that of the electron FSs shrinks. But as an artefact of LT/ETT one of the electron FS which converts to hole FS its area increases with doping (after the occurrence of ETT). So sum total hole FS area increases with hole doping but the sum total electron FS area decreases with doping upto certain doping concentration where ETT take place. But after the topological transition takes place, electron FS area increases with doping. This results in an overall inclination of total FS area (electron and hole) as a function of doping concentration for these hole doped Ba122 systems.

FSAs as a function of various kinds of doping shown in Fig.7.26 can be experimentally measured and turns out to be a unique way of identifying ETT/LT. Normally, hole doping would enlarge (reduce) hole (electron) FSA in contrast to electron doping that would enlarge (reduce) electron (hole) FSA. But in case of any particular FS undergoing topological transition it would follow against the above and such signatures are remarkably visible in Figs.7.26(d),(e),(g),(h),(k)). The red curves in Fig.7.26 (d,g) suggest electron-FSA initially gets reduced with hole doping but increases after certain hole doping because that FS undergoes topological modification from electron like to hole like. This has caused sudden increase in the FSAs of hole-FSs see *e.g*, green, blue, pink curves of Fig.7.26 (d,e) around the LT. Thus FSA are found to carry sensitivity of topological modifications more acutely than the band structures and can be used as a better experimental tool to identify ETT/LT. The difference in FSAs of hole and electron FSs indicate net electronic charge density which increases with doping (*cf* red curves in Fig.7.26 (c,f,i,l)) as expected, but the slope of the curves are different for different materials. This is consistent with experiments [217]. The charge density vary differently below and above the LT, much slowly above the LT indicating less effective doping above LT (*cf* Fig.7.26 (i,f,l))); along with this absence of a particular FS due to LT also reduces density of states at FL and thereby would limit T_c [218].

7.4 Conclusions

In this chapter we have studied in details the topological transition induced by impurity, doping as well as temperature in a number of 122 family of Fe-based materials. We have studied the effect of Sn impurity on the electronic structures of 122 systems

($BaFe_2As_2$, $SrFe_2As_2$ and $CaFe_2As_2$) using VCA method for introducing Sn impurity into the 122 crystal structures. Presence of Sn impurity modifies the electronic structures of Ba122 remarkably, which in turn results in certain changes in the physical properties like reduction of structural and magnetic transition temperatures as well as superconducting transition temperature. On the contrary, Sn impurity does not have much impact on the electronic structures of Sr122 and Ca122 systems as reflected in the experimental evidence of robustness of structural, magnetic and superconducting transition temperatures [213, 219]. In Ba122 system, we observe Sn impurity induced Lifshitz transition around Γ point that dictates several changes in the electronic structures near Fermi level including degradation of FS nesting contrasting the case of Sr122 and Ca122 systems. Orbital ordering between d_{yz} and d_{xz} bands around X and Y points, which is responsible for structural transition, remains unaltered in case of Sr122 and Ca122 systems but is substantially modified in case of Ba122 system in presence of Sn impurity. This work thus not only provide a detailed description of electronic structures of Sn contaminated 122 systems but also provides a possible explanation to the various observed anomalies in the physical properties that are not well understood so far.

We have systematically shown in a variety of high T_c Fe-based SCs that SC occurs at the verge of LT/ETT where magnetism disappears. This is achieved through detailed evaluation of FSs through first principles simulations with experimental structural parameters as a function of doping (temperature) as inputs and detailed demonstrations of LT/ETT. The doping induced net charge density is found to be suppressed at the LT/ETT. This definitely indicates the intriguing heed to the inter-relationship between SC and LT in Fe-based SCs. We have also provided a new way of detecting LT/ETT, through evaluation of FSA as a function of doping or temperature as the case may be which can be experimentally performed and is applicable in general to any system. This may modify the experimental phase diagram of Fe-SCs as far as the location of ETT/LT are concerned. We have presented a rare case of temperature induced LT in Ru doped $BaFe_2As_2$. We believe our work will open up many theoretical as well as experimental research activities in this direction.

Chapter 8

Summary and outlook

In this chapter, we briefly summarize the essence of the works carried out in the thesis and discuss the scope for further extension of the work reported in this thesis. The discovery of the iron-based superconductors modified the notion of uniqueness of high temperature superconductivity in cuprates. It is interesting even after eight years of its discovery not only because they have the ability to exhibit superconductivity at very high transition temperatures, but also because it provides a rich prototype interplay of various degrees freedom ; the lattice and the electronic charge, spin as well as orbital degrees of freedom all have intriguing roles. Apart from issues like proximity of superconductivity to magnetism, unusual Fermi surface topology, existence of orbital order, structural transition, nematic phase, role of Lifshitz topological transition in superconductivity and magnetism etc., are still under substantial debate. Fe based SCs specially 122 family not only posses a very rich phase diagram with lots of exciting physical properties but also capable of practical applications due to its low anisotropy, rather high T_c, significantly higher value of upper critical field, reduced thermal fluctuations and intrinsic pinning mechanisms and promises to show a great potential as a next generation of superconductor. One of the most interesting aspects of these Fe-based (SCs) from a fundamental point of view, is that superconductivity may arise from magnetic fluctuation or orbital fluctuation. However the glue to the electron-electron attraction or more precisely pairing mechanism in these Fe-based SCs is far from being settled. The main purpose of this thesis is to develop a better and conclusive understanding regarding these issues which are discussed briefly in Chapter 1. In this thesis some of the above mentioned problems (described in Chapter 1) are studied using two methodologies, model study and first principles density functional theory based approach. In Chapter 2, basics of this two approaches are described briefly.

In chapter 3, we mainly focused on various superconducting state properties like BCS characteristic ratio, electronic specific heat of Fe-based SCs, calculated using simplistic two band model. The model comprises of spin density wave (SDW), orbital density wave (ODW) arising due to nested pieces of the electron and hole like Fermi surfaces; together with superconductivity of different pairing symmetries around electron and hole like Fermi surfaces. Our first concern is to explain the existence of a single transition temperature in a multi band, multi-gapped system like Fe-based superconducting materials. It is explicitly shown that the inter-band pairing is essential in Fe-based materials having multiple gaps to produce a single global T_c. We also proclaim that either only intra or only inter band pairing is insufficient to describe some of the experimental results like large to small gap ratio, thermal behaviour of electronic specific heat jump etc. We found that the combined intra-inter band pairing mechanism produces the specific heat jump to superconducting transition temperature ratio proportional to square of the transition temperature as observed in experiments. This remains valid both in the electron and hole doped regime, for sign changing $s^{\pm}$ wave symmetry which takes the form of d+s pairing symmetry in two band model. Our work presented in this chapter thus demonstrates the importance of combined intra-inter band pairing irrespective of the pairing mechanism. Although approximated two band model is very much effective to explain certain important physical properties of Fe based SCs but it overlooks many important features which are integral part of Fe-based superconductivity. Thus one should look up for a more realistic theoretical approach which consider all the five d-bands contributing at the Fermi level. We opt for more realistic density functional theory based approach which is in principle an exact theory, to explain some of the salient normal state features of Fe based SCs like origin of structural transition, nematic order, unusual Fermi surface topology and the role of Lifshitz topological transition.

In chapter 4, we discuss the origin of magneto-structural transition in 122 Fe-based superconductors using experimentally determined temperature and doping dependent structural parameters of $BaFe_{2-x}Ru_xAs_2$ through first principles electronic structure calculations. Close intimacy of structural parameters (like z_{As}) to the electronic structures are established. We showed quantitatively that the structural transition in this system is electronic in origin and the suppression of the concurrent magnetic transition is due to loss of temperature dependent nesting of Fermi surface. Direct quantitative correlations between the orbital order and orthorhombicity is further achieved in a number of Fe-based superconductors of 122 family. The former (orbital order) is calculated from first principles simulations using doping and temperature dependent structural parameters while the latter (the orthorhombicity) is taken from already established experimental studies; when normalized, both the above quantities quantitatively corresponds to each other in terms of their doping as well as temperature variations. This proves that the structural transition in Fe-based materials is electronic in nature due to orbital ordering. An universal correlations among various structural parameters and electronic structure are also obtained. Most remarkable among them is the mapping of two Fe-Fe distances in the low temperature orthorhombic phase, with the band energies $E_{d_{xz}}$, $E_{d_{yz}}$ at the high symmetry points of the Brillouin zone. The fractional co-ordinate z_{As} of As atom which essentially determines anion height is inversely (directly) proportional to Fe-As bond distances (with exceptions of K doped $BaFe_2As_2$) for hole (electron) doped materials as a function of doping. On the other hand, Fe-As bond-distance is found to be inversely (directly) proportional to the density of states at the Fermi level for hole (electron) doped systems. Nematic phase is another exotic phase that appears in the phase diagram of Fe-based SCs near magnetic and structural transitions but the origin of this phase in this SCs is unclear. In the next chapter, we study whether orbital order, magnetic order and nematic order are coupled or not.

Through detailed electronic structure simulations we show that the electronic orbital ordering (between d_{yz} and d_{xz} bands) takes place due to local breaking of in-plane symmetry that generates two non-equivalent a, b directions in 122 family of Fe-based superconductors. Orbital ordering is strongly anisotropic and the temperature dependence of the corner zone orbital order maps to that of the orthorhombicity parameter. Orbital anisotropy results in two distinct spin density wave nesting wave vectors and causes inter-orbital charge and spin fluctuations. Temperature dependence of the orbital order is proportional to the nematic order and it sets in at a temperature where magnetic fluctuation starts building as observed in experiments. Orbital ordering becomes strongly spin dependent in presence of magnetic interaction. Occupation probabilities of all the Fe-d-orbitals exhibit temperature dependence indicating their possible contribution in orbital fluctuation. This need to be contrasted with the usual definition of nematic order parameter ($n_{d_{xz}}$-$n_{d_{yz}}$). Relationship among orbital fluctuations, magnetism and nematicity are established and this is the central theme of chapter 5. All these important orders (magnetic, orbital, nematic) including superconductivity are essentially governed by electronic structure near the Fermi level. Therefore, Fermi surface topology of these SCs carries a wealth of information which is discussed in the next two chapters.

Fermiology of various 122 systems (doped as well as undoped) are studied through first principles simulation and presented in chapter 6. In case of electron and hole doping, sizes of the electron and hole Fermi pockets evolve oppositely with increasing doping concentration. Isovalent Ru substitution up to certain doping concentration shows no visible alteration in the electron and hole like FSs but in case of 32% P doping there are visible modifications in the hole FSs. However, 100% Ru substitution modifies the hole FSs significantly (transform completely to three dimensional). A dimensional cross-over, in theoretically computed FS topologies of various Fe-based materials of “122" family are observed with various kinds of doping. From our calculations, it is very clear that two dimensionality of FSs may favour electron pair scattering between quasi-nested FSs which has important bearings in various orders (magnetic, orbital, superconducting) present in

Fe-based superconductors. Occurrence of Lifshitz topological transition is also experimentally observed in some of these 122 family of Fe-based materials. In the forthcoming chapter we depicted the role of Lifshitz topological transition in various phases including superconductivity

Our findings of chapter 6 that in case of electron and hole doping, sizes of the electron and hole Fermi pockets evolve oppositely with increasing doping concentration remains reasonable only in absence of topological transition. In chapter 7, we have presented our theoretical study of impurity, doping and temperature induced Lifshitz transition (LT) in 122 Fe-based systems. We show that only a few percentage of Sn doping at the Ba site of $BaFe_2As_2$, can cause electronic topological transition, namely, the LT. A hole like d_{xy} band of Fe undergoes electron like transition due to 4% Sn doping. LT is found in $BaFe_2As_2$ system around all the high symmetry points. Our detailed first principles simulation predicts absence of any LT in other 122 family compounds like $SrFe_2As_2$, $CaFe_2As_2$. This work bears practical significance due to the facts that a few percentage of Sn impurity is in-built in tin-flux grown single crystals method of synthesizing 122 materials and inter-relationship among the LT, magnetism and superconductivity. Doping as well as temperature driven LT are also predicted from *ab-initio* simulations in a variety of Fe based superconductors that are consistent with experimental findings. In case of doping dependent LT all the studied compounds the LTs are consistently found to take place at a doping concentration where superconductivity is known to acquire the highest T_c and magnetism disappears. This indicates the intriguing heed to the inter-relationship between superconductivity and Lifshitz transition in Fe-based 122 materials. Systematically, the LT occurs (above certain threshold doping) in some of the electronic Fermi surfaces for hole doped 122 compounds, whereas in hole Fermi surfaces for electron as well as some iso-electronic doped 122 compounds. Temperature driven Lifshitz transition is found to occur in the iso-electronic Ru-doped $BaFe_2As_2$ compounds.

Experimentally, in all iron chalcogenides/pnictides (also in phosphides) the chalcogen/pnictogen tetrahedron is found very close to regular tetrahedron. First principles density functional theory using LDA and GGA result in z-direction compressed tetrahedron by 0.1 to 0.15Ådifference. This is a structural mystery that remains unsolved even eight years after its discovery. We have emphasized this aspect through out the thesis and as a result we resort to experimentally determined structural parameters as a function of temperature and doping as inputs of our first principles simulation. This is more so because even finite temperature molecular dynamic simulation together with density functional study has failed this aspect and can not subtly obtain tetragonal to orthorhombic transition. We have shown in details while establishing the correlation between structural parameters and electronic structure as well as FS evolution that the relaxed geometry optimized structure is far from experimental situations. Quantitatively the underestimation of z_As leads to mutual shifts in the Fe-3d bands upto 0.25 eV or slightly more which causes completely different behaviours in the structural parameters and huge difference in the FS from experimental situation. In this respect, consideration of LDA and GGA exchange correlation functional do not make any difference. However, there are no systematic studies involving molecular dynamics coupled with density functional theory using modern exchange correlation functional like B3LYP, sX, sX-LDA, hybrid functional *etc.* available to our knowledge. A systematic study using different exchange correlation function may shed important clue on this subject.

Bibliography

[1] Onnes, H. K. *Leiden Comm.* **1911**, *120b, 122c, 124c.*

[2] Meissner, W.; Ochsenfeld, R. *Naturwissenschaften* **1933**, *21*, 787–788.

[3] Ray, P. J. Master's thesis: Structural investigation of La(2-x)Sr(x)CuO(4+y) - Following staging as a function of temperature. 2016; `https://figshare.com/articles/Structural_investigation_of_La_2_x_Sr_x_CuO_4_y_Following_staging_as_a_function_of_temperature/2075680`.

[4] Ginzburg, V. L.; Landau, L. D. *Zh. Eksp. Teor. Fiz.* **1950**, *20*, 1064.

[5] J. Bardeen, L. N. C.; Schrieffer, J. R. *Phys. Rev.* **1957**, *108*, 1175.

[6] Bednorz, J. G.; Müller, K. A. *Zeitschrift für Physik B Condensed Matter* **1986**, *64*, 189–193.

[7] Schilling, A.; Cantoni, M.; Guo, J. D.; Ott, H. R. *Nature* **1993**, *363*, 56–58.

[8] Chu, C. W.; Gao, L.; Chen, F.; Huang, Z. J.; Meng, R. L.; Xue, Y. Y. *Nature* **1993**, *365*, 323–325.

[9] Yoichi Kamihara, M. H., Takumi Watanabe; Hosono, H. *Journal of the American Chemical Society* **2008**, *130*, 3296–3297.

[10] Mani, A.; Ghosh, N.; Paulraj, S.; Bharathi, A.; Sundar, C. S. *EPL (Europhysics Letters)* **2009**, *87*, 17004.

[11] Park, T.; Park, E.; Lee, H.; Klimczuk, T.; Bauer, E. D.; Ronning, F.; Thompson, J. D. *Journal of Physics: Condensed Matter* **2008**, *20*, 322204.

[12] Alireza, P. L.; Ko, Y. T. C.; Gillett, J.; Petrone, C. M.; Cole, J. M.; Lonzarich, G. G.; Sebastian, S. E. *Journal of Physics: Condensed Matter* **2009**, *21*, 012208.

[13] Sefat, A. S.; Jin, R.; McGuire, M. A.; Sales, B. C.; Singh, D. J.; Mandrus, D. *Phys. Rev. Lett.* **2008**, *101*, 117004.

[14] Leithe-Jasper, A.; Schnelle, W.; Geibel, C.; Rosner, H. *Phys. Rev. Lett.* **2008**, *101*, 207004.

[15] Li, L. J.; Luo, Y. K.; Wang, Q. B.; Chen, H.; Ren, Z.; Tao, Q.; Li, Y. K.; Lin, X.; He, M.; Zhu, Z. W.; Cao, G. H.; Xu, Z. A. *New Journal of Physics* **2009**, *11*, 025008.

[16] Sharma, S.; Bharathi, A.; Chandra, S.; Reddy, V. R.; Paulraj, S.; Satya, A. T.; Sastry, V. S.; Gupta, A.; Sundar, C. S. *Phys. Rev. B* **2010**, *81*, 174512.

[17] Han, F.; Zhu, X.; Cheng, P.; Mu, G.; Jia, Y.; Fang, L.; Wang, Y.; Luo, H.; Zeng, B.; Shen, B.; Shan, L.; Ren, C.; Wen, H.-H. *Phys. Rev. B* **2009**, *80*, 024506.

[18] Rotter, M.; Tegel, M.; Johrendt, D.; Schellenberg, I.; Hermes, W.; Pöttgen, R. *Phys. Rev. B* **2008**, *78*, 020503.

[19] Huang, Q.; Qiu, Y.; Bao, W.; Green, M. A.; Lynn, J. W.; Gasparovic, Y. C.; Wu, T.; Wu, G.; Chen, X. H. *Phys. Rev. Lett.* **2008**, *101*, 257003.

[20] Mizuguchi, Y.; Hara, Y.; Deguchi, K.; Tsuda, S.; Yamaguchi, T.; Takeda, K.; Kotegawa, H.; Tou, H.; Takano, Y. *Superconductor Science and Technology* **2010**, *23*, 054013.

[21] Ganguli, A. K.; Prakash, J.; Thakur, G. S. *Chem. Soc. Rev.* **2013**, *42*, 569–598.

[22] Lee, C.; Kihou, K.; Iyo, A.; Kito, H.; Shirage, P.; Eisaki, H. *Solid State Communications* **2012**, *152*, 644 – 648, Special Issue on Iron-based Superconductors.

[23] Zhao, J.; Yao, D.-X.; Li, S.; Hong, T.; Chen, Y.; Chang, S.; Ratcliff, W.; Lynn, J. W.; Mook, H. A.; Chen, G. F.; Luo, J. L.; Wang, N. L.; Carlson, E. W.; Hu, J.; Dai, P. *Phys. Rev. Lett.* **2008**, *101*, 167203.

[24] Shirage, P.; Miyazawa, K.; Ishikado, M.; Kihou, K.; Lee, C.; Takeshita, N.; Matsuhata, H.; Kumai, R.; Tomioka, Y.; Ito, T.; Kito, H.; Eisaki, H.; Shamoto, S.; Iyo, A. *Physica C: Superconductivity* **2009**, *469*, 355 – 369, Superconductivity in Iron-Pnictides.

[25] Lee, C.-H.; Iyo, A.; Eisaki, H.; Kito, H.; Fernandez-diaz, M. T.; Kumai, R.; Miyazawa, K.; Kihou, K.; Matsuhata, H.; Braden, M.; Yamada, K. *Journal of the Physical Society of Japan* **2008**, *77*, 44–46.

[26] Zhao, J.; Huang, Q.; de la Cruz, C.; Li, S.; Lynn, J. W.; Chen, Y.; Green, M. A.; Chen, G. F.; Li, G.; Li, Z.; Luo, J. L.; Wang, N. L.; Dai, P. *Nat Mater* **2008**, *7*, 953–959.

[27] LeBoeuf, D.; Doiron-Leyraud, N.; Levallois, J.; Daou, R.; Bonnemaison, J.-B.; Hussey, N. E.; Balicas, L.; Ramshaw, B. J.; Liang, R.; Bonn, D. A.; Hardy, W. N.; Adachi, S.; Proust, C.; Taillefer, L. *Nature* **2007**, *450*, 533–536.

[28] Kasinathan, D.; Ormeci, A.; Koch, K.; Burkhardt, U.; Schnelle, W.; Leithe-Jasper, A.; Rosner, H. *New Journal of Physics* **2009**, *11*, 025023.

[29] Sharma, S.; Bharathi, A.; Vinod, K.; Sundar, C. S.; Srihari, V.; Sen, S.; Ghosh, H.; Sinha, A. K.; Deb, S. K. *Acta Crystallographica Section B* **2015**, *71*, 61–67.

[30] Sen, S.; Ghosh, H.; Sinha, A. K.; Bharathi, A. *Superconductor Science and Technology* **2014**, *27*, 122003.

[31] Mazin, I. I.; Singh, D. J.; Johannes, M. D.; Du, M. H. *Phys. Rev. Lett.* **2008**, *101*, 057003.

[32] Singh, D. J. *Phys. Rev. B* **2008**, *78*, 094511.

[33] Zhang, L.; Singh, D. J. *Phys. Rev. B* **2009**, *79*, 174530.

[34] Yin, Z. P.; Lebègue, S.; Han, M. J.; Neal, B. P.; Savrasov, S. Y.; Pickett, W. E. *Phys. Rev. Lett.* **2008**, *101*, 047001.

[35] Mazin, I. I.; Johannes, M. D.; Boeri, L.; Koepernik, K.; Singh, D. J. *Phys. Rev. B* **2008**, *78*, 085104.

[36] Tsuei, C. C.; Kirtley, J. R.; Chi, C. C.; Yu-Jahnes, L. S.; Gupta, A.; Shaw, T.; Sun, J. Z.; Ketchen, M. B. *Phys. Rev. Lett.* **1994**, *73*, 593–596.

[37] Kontani, H.; Onari, S. *Phys. Rev. Lett.* **2010**, *104*, 157001.

[38] Fernandes, R. M.; Schmalian, J. *Phys. Rev. B* **2010**, *82*, 014521.

[39] Evtushinsky, D. V. et al. *New Journal of Physics* **2009**, *11*, 055069.

[40] Bud'ko, S. L.; Ni, N.; Canfield, P. C. *Phys. Rev. B* **2009**, *79*, 220516.

[41] Kim, J. S.; Stewart, G. R.; Kasahara, S.; Shibauchi, T.; Terashima, T.; Matsuda, Y. *Journal of Physics: Condensed Matter* **2011**, *23*, 222201.

[42] Kogan, V. G. *Phys. Rev. B* **2009**, *80*, 214532.

[43] Kogan, V. G. *Phys. Rev. B* **2010**, *81*, 184528.

[44] Zaanen, J. *Phys. Rev. B* **2009**, *80*, 212502.

[45] Vavilov, M. G.; Chubukov, A. V.; Vorontsov, A. B. *Phys. Rev. B* **2011**, *84*, 140502.

[46] Liu, D. et al. *Nature Communications* **2012**, *3*, 931.

[47] Chubukov, A. *Physica C: Superconductivity* **2009**, *469*, 640 – 650, Superconductivity in Iron-Pnictides.

[48] Mazin, I. I. *Phys. Rev. B* **2011**, *84*, 024529.

[49] Christianson, A. D.; Goremychkin, E. A.; Osborn, R.; Rosenkranz, S.; Lumsden, M. D.; Malliakas, C. D.; Todorov, I. S.; Claus, H.; Chung, D. Y.; Kanatzidis, M. G.; Bewley, R. I.; Guidi, T. *Nature* **2008**, *456*, 930–932.

[50] Lumsden, M. D. et al. *Phys. Rev. Lett.* **2009**, *102*, 107005.

[51] Lebègue, S. *Phys. Rev. B* **2007**, *75*, 035110.

[52] Ding, H. et al. *EPL (Europhysics Letters)* **2008**, *83*, 47001.

[53] Paglione, J.; Greene, R. L. *Nat Phys* **2010**, *6*, 645–658.

[54] Chu, J.-H.; Analytis, J. G.; De Greve, K.; McMahon, P. L.; Islam, Z.; Yamamoto, Y.; Fisher, I. R. *Science* **2010**, *329*, 824–826.

[55] Ni, N.; Bud'ko, S. L.; Kreyssig, A.; Nandi, S.; Rustan, G. E.; Goldman, A. I.; Gupta, S.; Corbett, J. D.; Kracher, A.; Canfield, P. C. *Phys. Rev. B* **2008**, *78*, 014507.

[56] Chu, J.-H.; Analytis, J. G.; Kucharczyk, C.; Fisher, I. R. *Phys. Rev. B* **2009**, *79*, 014506.

[57] Luetkens, H. et al. *Nat Mater* **2009**, *8*, 305–309.

[58] Parker, D. R.; Smith, M. J. P.; Lancaster, T.; Steele, A. J.; Franke, I.; Baker, P. J.; Pratt, F. L.; Pitcher, M. J.; Blundell, S. J.; Clarke, S. J. *Phys. Rev. Lett.* **2010**, *104*, 057007.

[59] Margadonna, S.; Takabayashi, Y.; McDonald, M. T.; Kasperkiewicz, K.; Mizuguchi, Y.; Takano, Y.; Fitch, A. N.; Suard, E.; Prassides, K. *Chem. Commun.* **2008**, 5607–5609.

[60] McQueen, T. M.; Williams, A. J.; Stephens, P. W.; Tao, J.; Zhu, Y.; Ksenofontov, V.; Casper, F.; Felser, C.; Cava, R. J. *Phys. Rev. Lett.* **2009**, *103*, 057002.

[61] Imai, T.; Ahilan, K.; Ning, F. L.; McQueen, T. M.; Cava, R. J. *Phys. Rev. Lett.* **2009**, *102*, 177005.

[62] Chandra, P.; Coleman, P.; Larkin, A. I. *Phys. Rev. Lett.* **1990**, *64*, 88–91.

[63] Fang, C.; Yao, H.; Tsai, W.-F.; Hu, J.; Kivelson, S. A. *Phys. Rev. B* **2008**, *77*, 224509.

[64] Xu, C.; Müller, M.; Sachdev, S. *Phys. Rev. B* **2008**, *78*, 020501.

[65] Qi, Y.; Xu, C. *Phys. Rev. B* **2009**, *80*, 094402.

[66] Fernandes, R. M.; VanBebber, L. H.; Bhattacharya, S.; Chandra, P.; Keppens, V.; Mandrus, D.; McGuire, M. A.; Sales, B. C.; Sefat, A. S.; Schmalian, J. *Phys. Rev. Lett.* **2010**, *105*, 157003.

[67] Cano, A. *Phys. Rev. B* **2011**, *84*, 012504.

[68] Fernandes, R. M.; Chubukov, A. V.; Knolle, J.; Eremin, I.; Schmalian, J. *Phys. Rev. B* **2012**, *85*, 024534.

[69] Fanfarillo, L.; Cortijo, A.; Valenzuela, B. *Phys. Rev. B* **2015**, *91*, 214515.

[70] Sen, S.; Ghosh, H. *Journal of Alloys and Compounds* **2016**, *675*, 416 – 422.

[71] Krüger, F.; Kumar, S.; Zaanen, J.; van den Brink, J. *Phys. Rev. B* **2009**, *79*, 054504.

[72] Lee, C.-C.; Yin, W.-G.; Ku, W. *Phys. Rev. Lett.* **2009**, *103*, 267001.

[73] Chen, C.-C.; Maciejko, J.; Sorini, A. P.; Moritz, B.; Singh, R. R. P.; Devereaux, T. P. *Phys. Rev. B* **2010**, *82*, 100504.

[74] Lv, W.; Krüger, F.; Phillips, P. *Phys. Rev. B* **2010**, *82*, 045125.

[75] Onari, S.; Kontani, H. *Phys. Rev. Lett.* **2012**, *109*, 137001.

[76] Zhai, H.; Wang, F.; Lee, D.-H. *Phys. Rev. B* **2009**, *80*, 064517.

[77] Boeri, L.; Dolgov, O. V.; Golubov, A. A. *Phys. Rev. Lett.* **2008**, *101*, 026403.

[78] Cao, C.; Hirschfeld, P. J.; Cheng, H.-P. *Phys. Rev. B* **2008**, *77*, 220506.

[79] Singh, D. J.; Du, M.-H. *Phys. Rev. Lett.* **2008**, *100*, 237003.

[80] Haule, K.; Shim, J. H.; Kotliar, G. *Phys. Rev. Lett.* **2008**, *100*, 226402.

[81] Xu, G.; Ming, W.; Yao, Y.; Dai, X.; Zhang, S.-C.; Fang, Z. *EPL (Europhysics Letters)* **2008**, *82*, 67002.

[82] Putzke, C.; Coldea, A. I.; Guillamón, I.; Vignolles, D.; McCollam, A.; LeBoeuf, D.; Watson, M. D.; Mazin, I. I.; Kasahara, S.; Terashima, T.; Shibauchi, T.; Matsuda, Y.; Carrington, A. *Phys. Rev. Lett.* **2012**, *108*, 047002.

[83] Analytis, J. G.; Chu, J.-H.; McDonald, R. D.; Riggs, S. C.; Fisher, I. R. *Phys. Rev. Lett.* **2010**, *105*, 207004.

[84] Kuroki, K.; Onari, S.; Arita, R.; Usui, H.; Tanaka, Y.; Kontani, H.; Aoki, H. *Phys. Rev. Lett.* **2008**, *101*, 087004.

[85] Gastiasoro, M. N.; Hirschfeld, P. J.; Andersen, B. M. *Phys. Rev. B* **2014**, *89*, 100502.

[86] Raghu, S.; Qi, X.-L.; Liu, C.-X.; Scalapino, D. J.; Zhang, S.-C. *Phys. Rev. B* **2008**, *77*, 220503.

[87] Ghosh, H.; Purwar, H. *EPL (Europhysics Letters)* **2012**, *98*, 57012.

[88] *A Chemist Guide to Density Functional Theory*, 2nd ed.; Wiley-VCH Verlag GmbH, 2001.

[89] *Energy Density Functional Theory of Many-Electron Systems*; Springer Netherlands, 1990.

[90] Hohenberg, P.; Kohn, W. *Phys. Rev.* **1964**, *136*, B864–B871.

[91] *Density Functional Theory and the Family of (L)APW-methods: a step-by-step introduction*; 2004.

[92] *Density-Functional Theory of Atoms and Molecules*; Oxford University Press, 1989.

[93] Kohn, W.; Sham, L. J. *Phys. Rev.* **1965**, *140*, A1133–A1138.

[94] Zhao, Y.; Truhlar, D. G. *The Journal of Chemical Physics* **2008**, *128*.

[95] Perdew, J. P.; Burke, K.; Ernzerhof, M. *Phys. Rev. Lett.* **1996**, *77*, 3865–3868.

[96] Clark, J.; Segall Matthew, D.; Pickard Chris, J.; Hasnip Phil, J.; Probert Matt, J.; Keith, R.; Payne Mike, C. *zkri*; 2005; Vol. 220; Chapter First principles methods using CASTEP, p 567, 5/6.

[97] Anisimov, V. I.; Zaanen, J.; Andersen, O. K. *Phys. Rev. B* **1991**, *44*, 943–954.

[98] Cococcioni, M.; de Gironcoli, S. *Phys. Rev. B* **2005**, *71*, 035105.

[99] Dudarev, S. L.; Botton, G. A.; Savrasov, S. Y.; Humphreys, C. J.; Sutton, A. P. *Phys. Rev. B* **1998**, *57*, 1505–1509.

[100] Avci, S.; Allred, J. M.; Chmaissem, O.; Chung, D. Y.; Rosenkranz, S.; Schlueter, J. A.; Claus, H.; Daoud-Aladine, A.; Khalyavin, D. D.; Manuel, P.; Llobet, A.; Suchomel, M. R.; Kanatzidis, M. G.; Osborn, R. *Phys. Rev. B* **2013**, *88*, 094510.

[101] Lucarelli, A.; Dusza, A.; Pfuner, F.; Lerch, P.; Analytis, J. G.; Chu, J.-H.; Fisher, I. R.; Degiorgi, L. *New Journal of Physics* **2010**, *12*, 073036.

[102] Wang, X. F.; Wu, T.; Wu, G.; Liu, R. H.; Chen, H.; Xie, Y. L.; Chen, X. H. *New Journal of Physics* **2009**, *11*, 045003.

[103] Thaler, A.; Ni, N.; Kracher, A.; Yan, J. Q.; Bud'ko, S. L.; Canfield, P. C. *Phys. Rev. B* **2010**, *82*, 014534.

[104] Nandi, S.; Kim, M. G.; Kreyssig, A.; Fernandes, R. M.; Pratt, D. K.; Thaler, A.; Ni, N.; Bud'ko, S. L.; Canfield, P. C.; Schmalian, J.; McQueeney, R. J.; Goldman, A. I. *Phys. Rev. Lett.* **2010**, *104*, 057006.

[105] Kasahara, S.; Shibauchi, T.; Hashimoto, K.; Ikada, K.; Tonegawa, S.; Okazaki, R.; Shishido, H.; Ikeda, H.; Takeya, H.; Hirata, K.; Terashima, T.; Matsuda, Y. *Phys. Rev. B* **2010**, *81*, 184519.

[106] Nordheim, L. *Ann. Phys. (Leipzig)* **1931**,

[107] Marzari, N.; de Gironcoli, S.; Baroni, S. *Phys. Rev. Lett.* **1994**, *72*, 4001–4004.

[108] Saitta, A. M.; de Gironcoli, S.; Baroni, S. *Phys. Rev. Lett.* **1998**, *80*, 4939–4942.

[109] Payne, M. C.; Teter, M. P.; Allan, D. C.; Arias, T. A.; Joannopoulos, J. D. *Rev. Mod. Phys.* **1992**, *64*, 1045–1097.

[110] Ramer, N.; Rappe, A. *Journal of Physics and Chemistry of Solids* **2000**, *61*, 315 – 320.

[111] Bellaiche, L.; Vanderbilt, D. *Phys. Rev. B* **2000**, *61*, 7877–7882.

[112] Pulikkotil, J. J.; Schwingenschlögl, U. *Phys. Rev. Lett.* **2010**, *104*, 177006.

[113] Stewart, G. R. *Rev. Mod. Phys.* **2011**, *83*, 1589–1652.

[114] Chen, H.; Ren, Y.; Qiu, Y.; Bao, W.; Liu, R. H.; Wu, G.; Wu, T.; Xie, Y. L.; Wang, X. F.; Huang, Q.; Chen, X. H. *EPL (Europhysics Letters)* **2009**, *85*, 17006.

[115] Tsuei, C. C.; Kirtley, J. R. *Rev. Mod. Phys.* **2000**, *72*, 969–1016.

[116] Van Harlingen, D. J. *Rev. Mod. Phys.* **1995**, *67*, 515–535.

[117] Ghosh, H. *Phys. Rev. B* **2001**, *63*, 226502.

[118] Barzykin, V.; Gorkov, L. P. *JETP Letters* **2008**, *88*, 131–135.

[119] Chubukov, A. V.; Efremov, D. V.; Eremin, I. *Phys. Rev. B* **2008**, *78*, 134512.

[120] Yanagi, Y.; Yamakawa, Y.; Ōno, Y. *Phys. Rev. B* **2010**, *81*, 054518.

[121] Dolgov, O. V.; Mazin, I. I.; Parker, D.; Golubov, A. A. *Phys. Rev. B* **2009**, *79*, 060502.

[122] Sunagawa, M. et al. *Scientific Reports* **2014**, *4*, 4381.

[123] Sen, S.; Ghosh, H. *Physics Letters A* **2015**, *379*, 843 – 847.

[124] Evtushinsky, D. V. et al. *Phys. Rev. B* **2014**, *89*, 064514.

[125] Podolsky, D.; Kee, H.-Y.; Kim, Y. B. *EPL (Europhysics Letters)* **2009**, *88*, 17004.

[126] Ghosh, H.; Purwar, H. *AIP Conference Proceedings* **2012**, *1461*.

[127] Gofryk, K.; Sefat, A. S.; Bauer, E. D.; McGuire, M. A.; Sales, B. C.; Mandrus, D.; Thompson, J. D.; Ronning, F. *New Journal of Physics* **2010**, *12*, 023006.

[128] Davis, J. C.; Hirschfeld, P. J. *Nat Phys* **2014**, *10*, 184–185, News and Views.

[129] Fernandes, R. M.; Chubukov, A. V.; Schmalian, J. *Nat Phys* **2014**, *10*, 97–104, Review.

[130] Nakajima, M.; Ishida, S.; Tomioka, Y.; Kihou, K.; Lee, C. H.; Iyo, A.; Ito, T.; Kakeshita, T.; Eisaki, H.; Uchida, S. *Phys. Rev. Lett.* **2012**, *109*, 217003.

[131] Jiang, S.; Jeevan, H. S.; Dong, J.; Gegenwart, P. *Phys. Rev. Lett.* **2013**, *110*, 067001.

[132] Chu, J.-H.; Kuo, H.-H.; Analytis, J. G.; Fisher, I. R. *Science* **2012**, *337*, 710–712.

[133] Yi, M.; Lu, D.; Chu, J.-H.; Analytis, J. G.; Sorini, A. P.; Kemper, A. F.; Moritz, B.; Mo, S.-K.; Moore, R. G.; Hashimoto, M.; Lee, W.-S.; Hussain, Z.; Devereaux, T. P.; Fisher, I. R.; Shen, Z.-X. *Proceedings of the National Academy of Sciences* **2011**, *108*, 6878–6883.

[134] Backes, S.; Jeschke, H. O. *Phys. Rev. B* **2013**, *88*, 075111.

[135] Dhaka, R. S.; Hahn, S. E.; Razzoli, E.; Jiang, R.; Shi, M.; Harmon, B. N.; Thaler, A.; Bud'ko, S. L.; Canfield, P. C.; Kaminski, A. *Phys. Rev. Lett.* **2013**, *110*, 067002.

[136] Hirschfeld, P. J.; Korshunov, M. M.; Mazin, I. I. *Reports on Progress in Physics* **2011**, *74*, 124508.

[137] Reid, J.-P.; Tanatar, M. A.; Juneau-Fecteau, A.; Gordon, R. T.; de Cotret, S. R.; Doiron-Leyraud, N.; Saito, T.; Fukazawa, H.; Kohori, Y.; Kihou, K.; Lee, C. H.; Iyo, A.; Eisaki, H.; Prozorov, R.; Taillefer, L. *Phys. Rev. Lett.* **2012**, *109*, 087001.

[138] Aktürk, E.; Ciraci, S. *Phys. Rev. B* **2009**, *79*, 184523.

[139] Lifshitz, I. M. *Sov. Phys. JETP* **1960**,

[140] Yildirim, T. *Phys. Rev. Lett.* **2008**, *101*, 057010.

[141] Seo, K.; Bernevig, B. A.; Hu, J. *Phys. Rev. Lett.* **2008**, *101*, 206404.

[142] Avci, S.; Chmaissem, O.; Chung, D. Y.; Rosenkranz, S.; Goremychkin, E. A.; Castellan, J. P.; Todorov, I. S.; Schlueter, J. A.; Claus, H.; Daoud-Aladine, A.; Khalyavin, D. D.; Kanatzidis, M. G.; Osborn, R. *Phys. Rev. B* **2012**, *85*, 184507.

[143] Allred, J. M.; Taddei, K. M.; Bugaris, D. E.; Avci, S.; Chung, D. Y.; Claus, H.; dela Cruz, C.; Kanatzidis, M. G.; Rosenkranz, S.; Osborn, R.; Chmaissem, O. *Phys. Rev. B* **2014**, *90*, 104513.

[144] Hosono, H.; Tanabe, K.; Takayama-Muromachi, E.; Kageyama, H.; Yamanaka, S.; Kumakura, H.; Nohara, M.; Hiramatsu, H.; Fujitsu, S. *Science and Technology of Advanced Materials* **2015**, *16*, 033503.

[145] Wu, J. J.; Lin, J.-F.; Wang, X. C.; Liu, Q. Q.; Zhu, J. L.; Xiao, Y. M.; Chow, P.; Jin, C. *Proceedings of the National Academy of Sciences* **2013**, *110*, 17263–17266.

[146] Wilson, S. D.; Yamani, Z.; Rotundu, C. R.; Freelon, B.; Bourret-Courchesne, E.; Birgeneau, R. J. *Phys. Rev. B* **2009**, *79*, 184519.

[147] Allan, M. P.; Chuang, T.-M.; Massee, F.; Xie, Y.; Ni, N.; Bud/'ko, S. L.; Boebinger, G. S.; Wang, Q.; Dessau, D. S.; Canfield, P. C.; Golden, M. S.; Davis, J. C. *Nat Phys* **2013**, *9*, 220–224.

[148] Dusza, A.; Lucarelli, A.; Sanna, A.; Massidda, S.; Chu, J.-H.; Fisher, I. R.; Degiorgi, L. *New Journal of Physics* **2012**, *14*, 023020.

[149] Song, C.-L.; Wang, Y.-L.; Cheng, P.; Jiang, Y.-P.; Li, W.; Zhang, T.; Li, Z.; He, K.; Wang, L.; Jia, J.-F.; Hung, H.-H.; Wu, C.; Ma, X.; Chen, X.; Xue, Q.-K. *Science* **2011**, *332*, 1410–1413.

[150] Baek, S.-H.; Efremov, D.; Ok, J.; Kim, J.; Brink, J. v. d.; Büchner, *Nat Mater* **2015**,

[151] Avci, S. et al. *Nat Commun* **2014**, *5*.

[152] Shimojima, T. et al. *Science* **2011**, *332*, 564–567.

[153] Fernandes, R. M.; Schmalian, J. *Phys. Rev. B* **2010**, *82*, 014521.

[154] Lawler, M. J.; Fujita, K.; Lee, J.; Schmidt, A. R.; Kohsaka, Y.; Kim, C. K.; Eisaki, H.; Uchida, S.; Davis, J. C.; Sethna, J. P.; Kim, E.-A. *Nature* **2010**, *466*, 347–351.

[155] Hinkov, V.; Haug, D.; Fauqué, B.; Bourges, P.; Sidis, Y.; Ivanov, A.; Bernhard, C.; Lin, C. T.; Keimer, B. *Science* **2008**, *319*, 597–600.

[156] Daou, R.; Chang, J.; LeBoeuf, D.; Cyr-Choiniere, O.; Laliberte, F.; Doiron-Leyraud, N.; Ramshaw, B. J.; Liang, R.; Bonn, D. A.; Hardy, W. N.; Taillefer, L. *Nature* **2010**, *463*, 519–522.

[157] Fujita, K.; Kim, C. K.; Lee, I.; Lee, J.; Hamidian, M. H.; Firmo, I. A.; Mukhopadhyay, S.; Eisaki, H.; Uchida, S.; Lawler, M. J.; Kim, E.-A.; Davis, J. C. *Science* **2014**, *344*, 612–616.

[158] Fernandes, R. M.; Maiti, S.; Wölfle, P.; Chubukov, A. V. *Phys. Rev. Lett.* **2013**, *111*, 057001.

[159] Zhang, P.; Qian, T.; Richard, P.; Wang, X. P.; Miao, H.; Lv, B. Q.; Fu, B. B.; Wolf, T.; Meingast, C.; Wu, X. X.; Wang, Z. Q.; Hu, J. P.; Ding, H. *Phys. Rev. B* **2015**, *91*, 214503.

[160] Sen, S.; Ghosh, H. *AIP Conference Proceedings* **2016**, *1728*.

[161] Dai, P.; Hu, J.; Dagotto, E. *Nat Phys* **2012**, *8*, 709–718.

[162] Sen, S.; Ghosh, H. *Journal of Alloys and Compounds* **2015**, *618*, 102 – 109.

[163] Shimojima, T.; Ishizaka, K.; Ishida, Y.; Katayama, N.; Ohgushi, K.; Kiss, T.; Okawa, M.; Togashi, T.; Wang, X.-Y.; Chen, C.-T.; Watanabe, S.; Kadota, R.; Oguchi, T.; Chainani, A.; Shin, S. *Phys. Rev. Lett.* **2010**, *104*, 057002.

[164] Stoner, E. C. *Proceedings of the Royal Society of London A: Mathematical, Physical and Engineering Sciences* **1938**, *165*, 372–414.

[165] Wang, G.; Qian, Y.; Xu, G.; Dai, X.; Fang, Z. *Phys. Rev. Lett.* **2010**, *104*, 047002.

[166] Yan, J.-Q.; Kreyssig, A.; Nandi, S.; Ni, N.; Bud'ko, S. L.; Kracher, A.; McQueeney, R. J.; McCallum, R. W.; Lograsso, T. A.; Goldman, A. I.; Canfield, P. C. *Phys. Rev. B* **2008**, *78*, 024516.

[167] Matan, K.; Morinaga, R.; Iida, K.; Sato, T. J. *Phys. Rev. B* **2009**, *79*, 054526.

[168] Luo, H.; Wang, M.; Zhang, C.; Lu, X.; Regnault, L.-P.; Zhang, R.; Li, S.; Hu, J.; Dai, P. *Phys. Rev. Lett.* **2013**, *111*, 107006.

[169] Lu, X.; Park, J. T.; Zhang, R.; Luo, H.; Nevidomskyy, A. H.; Si, Q.; Dai, P. *Science* **2014**, *345*, 657–660.

[170] Lu, D. H.; Yi, M.; Mo, S.-K.; Erickson, A. S.; Analytis, J.; Chu, J.-H.; Singh, D. J.; Hussain, Z.; Geballe, T. H.; Fisher, I. R.; Shen, Z.-X. *Nature* **2008**, *455*, 81–84.

[171] Malaeb, W.; Yoshida, T.; Fujimori, A.; Kubota, M.; Ono, K.; Kihou, K.; Shirage, P. M.; Kito, H.; Iyo, A.; Eisaki, H.; Nakajima, Y.; Tamegai, T.; Arita, R. *Journal of the Physical Society of Japan* **2009**, *78*, 123706.

[172] Evtushinsky, D. V.; Zabolotnyy, V. B.; Harnagea, L.; Yaresko, A. N.; Thirupathaiah, S.; Kordyuk, A. A.; Maletz, J.; Aswartham, S.; Wurmehl, S.; Rienks, E.; Follath, R.; Büchner, B.; Borisenko, S. V. *Phys. Rev. B* **2013**, *87*, 094501.

[173] Wang, F.; Lee, D.-H. *Science* **2011**, *332*, 200–204.

[174] Mazin, I.; Schmalian, J. *Physica C: Superconductivity* **2009**, *469*, 614 – 627, Superconductivity in Iron-Pnictides.

[175] *Tranport Phenomena in Strongly Correlated Fermi Liquids*; Springer, Heidelberg, New York, 2013.

[176] Nekrasov, I. A.; Pchelkina, Z. V.; Sadovskii, M. V. *JETP Letters* **2008**, *88*, 144–149.

[177] Graser, S.; Kemper, A. F.; Maier, T. A.; Cheng, H.-P.; Hirschfeld, P. J.; Scalapino, D. J. *Phys. Rev. B* **2010**, *81*, 214503.

[178] Pan, L.; Li, J.; Tai, Y.-Y.; Graf, M. J.; Zhu, J.-X.; Ting, C. S. *Phys. Rev. B* **2013**, *88*, 214510.

[179] Dhaka, R. S.; Liu, C.; Fernandes, R. M.; Jiang, R.; Strehlow, C. P.; Kondo, T.; Thaler, A.; Schmalian, J.; Bud'ko, S. L.; Canfield, P. C.; Kaminski, A. *Phys. Rev. Lett.* **2011**, *107*, 267002.

[180] Brouet, V.; Rullier-Albenque, F.; Marsi, M.; Mansart, B.; Aichhorn, M.; Biermann, S.; Faure, J.; Perfetti, L.; Taleb-Ibrahimi, A.; Le Fèvre, P.; Bertran, F.; Forget, A.; Colson, D. *Phys. Rev. Lett.* **2010**, *105*, 087001.

[181] Ren, Z.; Tao, Q.; Jiang, S.; Feng, C.; Wang, C.; Dai, J.; Cao, G.; Xu, Z. *Phys. Rev. Lett.* **2009**, *102*, 137002.

[182] Ye, Z. R.; Zhang, Y.; Chen, F.; Xu, M.; Ge, Q. Q.; Jiang, J.; Xie, B. P.; Feng, D. L. *Phys. Rev. B* **2012**, *86*, 035136.

[183] Xu, N.; Qian, T.; Richard, P.; Shi, Y.-B.; Wang, X.-P.; Zhang, P.; Huang, Y.-B.; Xu, Y.-M.; Miao, H.; Xu, G.; Xuan, G.-F.; Jiao, W.-H.; Xu, Z.-A.; Cao, G.-H.; Ding, H. *Phys. Rev. B* **2012**, *86*, 064505.

[184] Yoshida, T.; Nishi, I.; Ideta, S.; Fujimori, A.; Kubota, M.; Ono, K.; Kasahara, S.; Shibauchi, T.; Terashima, T.; Matsuda, Y.; Ikeda, H.; Arita, R. *Phys. Rev. Lett.* **2011**, *106*, 117001.

[185] Xie, W.; Bao, M.; Zhao, Z.; Liu, B.-G. *Phys. Rev. B* **2009**, *79*, 115128.

[186] Jiang, S.; Xing, H.; Xuan, G.; Wang, C.; Ren, Z.; Feng, C.; Dai, J.; Xu, Z.; Cao, G. *Journal of Physics: Condensed Matter* **2009**, *21*, 382203.

[187] Kordyuk, A. A. *Low Temperature Physics* **2012**, *38*.

[188] Benhabib, S.; Sacuto, A.; Civelli, M.; Paul, I.; Cazayous, M.; Gallais, Y.; Méasson, M.-A.; Zhong, R. D.; Schneeloch, J.; Gu, G. D.; Colson, D.; Forget, A. *Phys. Rev. Lett.* **2015**, *114*, 147001.

[189] Norman, M. R.; Lin, J.; Millis, A. J. *Phys. Rev. B* **2010**, *81*, 180513.

[190] Xu, S.-Y. et al. *Phys. Rev. B* **2015**, *92*, 075115.

[191] Kim, B.; Liu, P.; Ergnenc, Z.; Toschi, A.; Khmelevskyi, S.; Franchini, C. *arXiv:1601.03310* **2016**,

[192] Okamoto, Y.; Nishio, A.; Hiroi, Z. *Phys. Rev. B* **2010**, *81*, 121102.

[193] Hackl, A.; Vojta, M. *Phys. Rev. Lett.* **2011**, *106*, 137002.

[194] Chen, K.-S.; Meng, Z. Y.; Pruschke, T.; Moreno, J.; Jarrell, M. *Phys. Rev. B* **2012**, *86*, 165136.

[195] Lemonik, Y.; Aleiner, I. L.; Toke, C.; Fal'ko, V. I. *Phys. Rev. B* **2010**, *82*, 201408.

[196] Varlet, A.; Bischoff, D.; Simonet, P.; Watanabe, K.; Taniguchi, T.; Ihn, T.; Ensslin, K.; Mucha-Kruczyński, M.; Fal'ko, V. I. *Phys. Rev. Lett.* **2014**, *113*, 116602.

[197] Liu, C.; Kondo, T.; Fernandes, R. M.; Palczewski, A. D.; Mun, E. D.; Ni, N.; Thaler, A. N.; Bostwick, A.; Rotenberg, E.; Schmalian, J.; Bud/'ko, S. L.; Canfield, P. C.; Kaminski, A. *Nat Phys* **2010**, *6*, 419–423.

[198] Khan, S. N.; Johnson, D. D. *Phys. Rev. Lett.* **2014**, *112*, 156401.

[199] Ni, N.; Thaler, A.; Kracher, A.; Yan, J. Q.; Bud'ko, S. L.; Canfield, P. C. *Phys. Rev. B* **2009**, *80*, 024511.

[200] Liu, R. H.; Luo, X. G.; Zhang, M.; Wang, A. F.; Ying, J. J.; Wang, X. F.; Yan, Y. J.; Xiang, Z. J.; Cheng, P.; Ye, G. J.; Li, Z. Y.; Chen, X. H. *EPL (Europhysics Letters)* **2011**, *94*, 27008.

[201] Xu, N.; Richard, P.; Shi, X.; van Roekeghem, A.; Qian, T.; Razzoli, E.; Rienks, E.; Chen, G.-F.; Ieki, E.; Nakayama, K.; Sato, T.; Takahashi, T.; Shi, M.; Ding, H. *Phys. Rev. B* **2013**, *88*, 220508.

[202] Liu, Y.; Lograsso, T. A. *Phys. Rev. B* **2014**, *90*, 224508.

[203] de la Cruz, C.; Huang, Q.; Lynn, J. W.; Li, J.; II, W. R.; Zarestky, J. L.; Mook, H. A.; Chen, G. F.; Luo, J. L.; Wang, N. L.; Dai, P. *Nature* **2008**, *453*, 899–902.

[204] Chubukov, A. *Annual Review of Condensed Matter Physics* **2012**, *3*, 57–92.

[205] Wu, Y.; Jo, N. H.; Ochi, M.; Huang, L.; Mou, D.; Bud'ko, S. L.; Canfield, P. C.; Trivedi, N.; Arita, R.; Kaminski, A. *Phys. Rev. Lett.* **2015**, *115*, 166602.

[206] Quader, K.; Widom, M. *Phys. Rev. B* **2014**, *90*, 144512.

[207] Ghosh, H.; Sen, S. *Journal of Alloys and Compounds* **2016**, *677*, 245 – 251.

[208] Wang, Y.; Gastiasoro, M. N.; Andersen, B. M.; Tomić, M.; Jeschke, H. O.; Valentí, R.; Paul, I.; Hirschfeld, P. J. *Phys. Rev. Lett.* **2015**, *114*, 097003.

[209] Rotter, M. High-Temperature Superconductivity in Doped $BaFe_2As_2$. Ph.D. thesis, Ludwig-Maximilians-Universität München, 2010.

[210] Tegel, M.; Rotter, M.; Weiß, V.; Schappacher, F. M.; Pöttgen, R.; Johrendt, D. *Journal of Physics: Condensed Matter* **2008**, *20*, 452201.

[211] Goldman, A. I.; Argyriou, D. N.; Ouladdiaf, B.; Chatterji, T.; Kreyssig, A.; Nandi, S.; Ni, N.; Bud'ko, S. L.; Canfield, P. C.; McQueeney, R. J. *Phys. Rev. B* **2008**, *78*, 100506.

[212]

[213] Su, Y.; Link, P.; Schneidewind, A.; Wolf, T.; Adelmann, P.; Xiao, Y.; Meven, M.; Mittal, R.; Rotter, M.; Johrendt, D.; Brueckel, T.; Loewenhaupt, M. *Phys. Rev. B* **2009**, *79*, 064504.

[214] Colombier, E.; Torikachvili, M. S.; Ni, N.; Thaler, A.; Bud'ko, S. L.; Canfield, P. C. *Superconductor Science and Technology* **2010**, *23*, 054003.

[215] Kim, J. S.; Kim, E. G.; Stewart, G. R. *Journal of Physics: Condensed Matter* **2009**, *21*, 252201.

[216] Wang, G.; Zheng, L.; Zhang, M.; Yang, Z. *Phys. Rev. B* **2010**, *81*, 014521.

[217] Ideta, S. et al. *Phys. Rev. Lett.* **2013**, *110*, 107007.

[218] Thirupathaiah, S.; Stürzer, T.; Zabolotnyy, V. B.; Johrendt, D.; Büchner, B.; Borisenko, S. V. *Phys. Rev. B* **2013**, *88*, 140505.

[219] Sun, G. L.; Sun, D. L.; Konuma, M.; Popovich, P.; Boris, A.; Peng, J. B.; Choi, K.-Y.; Lemmens, P.; Lin, C. T. *Journal of Superconductivity and Novel Magnetism* **2011**, *24*, 1773–1785.